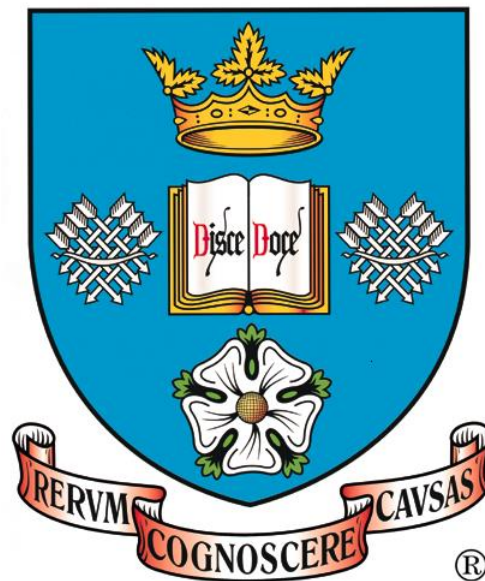


**Towards a Micromechanistic Understanding of
Imparted Subsurface Deformation During Machining
of Titanium Alloys**

Pete Crawforth

Department of Materials Science and Engineering

The University of Sheffield



Thesis submitted for the degree of Doctor of Philosophy

September 2014

“Good metallurgists are not born, they are made with the ample money of the companies which hire them, and since they usually make their mistakes on a grand scale, they are the nightmares of business managers.”

W.J. Kroll

Summary

Current surface integrity practice, generally applied by mechanical engineers, characterises macroscopic features such as surface tearing, chip smearing and general deformation of grains in the direction of cutting; with little emphasis placed on subsurface microstructure damage. However, through the exploitation of electron backscatter diffraction (EBSD) it has been possible to show the role microstructure plays during metal removal and further quantify the level of deformation that remains after the component has been machined. From the significant amount of data acquired, it has been possible to construct a mechanistic model, which can predict subsurface deformation during machining. Titanium manufacturers such as Timet are in the process of developing alloys that offer their customers cost savings via an improvement in the material's inherent machinability, whilst offering comparable (or improved) in-service properties. For example, Timetal® 54M (Ti-54M) is currently being marketed as a direct alloy replacement for components that are currently manufactured out of Ti-6Al-4V. The cost benefits for the use of Ti-54M through improved tool wear characteristics at higher machining rates have been documented, however, the reasons for this improvement are still under investigation. Through material supply from Timet UK a significant emphasis of the PhD programme was based on using this new alloy. Further studies have shown the potential deleterious effects of induced deformation features imparted during turning on the important titanium alloy, Ti-834, which due to its good mechanical properties at high temperature is currently used for blades, rings and discs in the compressor stages of an aero-engine. Here machining damage in the form of mechanical twins, which until this point, had not been observed in machined Ti-834 material, provided nucleation sites for silicide precipitation during thermal exposure at 750°C, indicating that creep strength could be locally reduced at the surface. The microtexture developed during the complex multi-step forging route can produce a highly anisotropic billet that has consequences for service performance. All critical aerostructural titanium alloys will be machined following forging and furthermore, will be machined using high-speed practices to meet aircraft build targets. As microtexture heavily influences mechanical performance such as fatigue, there is a growing need to understand how the upstream forging steps influence the machining process and determine the severity of induced microstructure damage. Here machining trials were undertaken whilst using force dynamometers; fluctuations in the recorded force have been subsequently attributed to variation in the workpiece's crystallographic texture. The texture of the billet that has evolved during the primary breakdown forging steps acts as a 'finger print' of the forging process and has a lasting legacy, which can have a significant influence not only on the machining process but also the materials' in-service performance.

Contents

Summary	ii
Contents	iii
Acknowledgements	vii
List of figures	viii
List of tables	xxii
Nomenclature	xxiii
Preface	1
Thesis outline	3
Chapter 1 Literature review	5
1.1 Alloy classification	5
1.1.1 α alloys	6
1.1.2 Near α alloys.....	7
1.1.3 $\alpha + \beta$ alloys	8
1.1.4 Near β alloys	9
1.1.5 β alloys	9
1.2 Thermomechanical processing	10
1.2.1 The $\beta \rightarrow \alpha$ phase transformation and texture development during forging ..	11
1.3 Deformation Mechanisms	14
1.3.1 Slip	14
1.3.2 Mechanical twinning.....	15
1.3.3 The sensitivity of deformation to microstructure variations in polycrystalline materials.	18
1.3.4 Deformation characteristics related to material grain size.....	18
1.3.5 The role of the applied stress/strain in conjunction with the underlying crystallographic orientation on the resulting deformation.	19
1.4 Summary	23
Chapter 2 - The mechanics of machining	24
2.1 Cutting force relationships	24
2.2 Material response of the workpiece during machining	26
2.3 The influence of cutting parameters on fatigue life /residual stress	32
2.4 Metallurgical analysis of machined components	32
2.5 Deformation characteristics within the workpiece during machining	42
2.6 Microstructure deformation sensitivities to changes in machining parameters	49
2.6.1 The response to cutting speed	53
2.6.2 The response to machining feed	55

2.7 The “size effect” in metal cutting	58
2.8 Microstructure response to variable feed rate and further machining induced microstructure damage	66
2.9 Role of crystallographic texture during machining.....	69
2.10 Tool contact	72
2.10.1 Crater wear.....	73
2.10.2 Flank wear.....	73
2.10.3 Built up edge	74
2.11 Taylor relationship of tool wear	75
2.12 The role of alloy chemistry in machining	77
2.13 Summary.....	79
Chapter 3 - Material analysis procedures	80
3.1 Introduction.....	80
3.2 Specimen Preparation	80
3.2.1 Precision sample sectioning.....	80
3.3 Surface Preparation.....	81
3.3.1 Metallographic polishing	81
3.4 Imaging and analysis	83
3.4.1 Microstructure optical imaging.....	83
3.4.2 Scanning Electron Microscopy (SEM)	83
3.4.3 Electron backscatter diffraction (EBSD)	84
3.5 EBSD data representation.....	92
3.5.1 Euler transformation	92
3.5.2 All Euler OIM	93
3.5.3 Inverse pole figure OIM.....	94
3.5.4 Noise reduction	95
3.5.5 Band contrast OIM.....	96
3.5.6 Twinning delineation	97
3.6 Pole figures	98
3.7 Slip trace analysis.....	99
3.7.1 Crystallographic orientation mathematical methodology	99
3.7.2 Schmid factor	104
3.7.3 Pole figure plots and trace chord delineation for slip planes of interest ..	105
3.7.4 Slip trace analysis	107
3.7.5 Determining the K_1	111
3.8 Summary.....	112
Chapter 4 - Subsurface microstructure deformation during precision turning of Ti-834	113

4.1 Introduction.....	113
4.2 Experimental methods.....	114
4.2.1 As received material	114
4.2.2 Machining trials	115
4.2.3 Tool wear	116
4.2.4 Surface roughness	118
4.2.5 Hardness profiling.....	118
4.2.6 Microstructure analysis	118
4.2.7 Heat treated samples	119
4.3 Results and discussion	120
4.3.1 Tool Wear	120
4.3.2 Surface Roughness.....	123
4.3.3 Hardness profiling.....	124
4.3.4 Microstructure analysis	129
4.3.5 Thermal exposure to machined workpiece	136
4.4 Further Ti-834 billet characterisation identification of ‘i-type’ twin	140
4.5 Summary.....	142
Chapter 5 - Identifying critical machining parameters for subsurface damage in high speed machined titanium	143
5.1 Introduction.....	143
5.2 Experimental methods.....	143
5.2.1 As received material	143
5.2.2 Machining trials	144
5.2.3 Microstructure Analysis.....	145
5.3 Results and discussion	146
5.3.1 Material response of Ti-54M after high speed machining.....	146
5.3.2 Backscatter election image analysis of machined Ti-54M	147
5.3.3 Electron backscattered diffraction analysis of machined Ti-54M	152
5.4 Microstructure analysis of material following a machining dwell.	166
5.5 Summary.....	173
Chapter 6 - Quantifying the cutting forces as a function of material chemistry and billet forging route.....	174
6.1 Introduction.....	174
6.2 Experimental methods.....	174
6.2.1 As received material	174
6.2.2 Microstructure analysis	175
6.2.3 Machining trials	176
6.2.4 Parametric orthogonal cutting trials.....	179

6.2.5 The mechanics of machining	181
6.2.6 Orthogonal cutting trails for microstructure correlation	183
6.2.7 Ultrasound analysis	184
6.3 Results and discussion	185
6.3.1 Characterisation of Ti-54M Billet.....	185
6.3.2 EBSD analysis	185
6.3.3 Microstructure analysis	191
6.4 Data handling of orthogonal cutting trials.	197
6.4.1 Machining force response during variable feed orthogonal cutting trials	198
6.4.2 The size effect	199
6.4.3 Cutting force analysis and tool engagement behaviour	201
6.4.4 Machining force response during variable speed orthogonal cutting trials	215
6.5 Orthogonal cutting trials and microstructure correlation.....	217
6.5.1 Force data processing.....	218
6.5.2 Ultrasound analysis	222
6.6 Application of the plane simple shear stress state model and the role of forging route on the resulting induced machining damage.	223
6.7 Summary.....	227
Conclusions.....	228
Recommendations for further work.....	229
References.....	235
Appendix.....	251

Acknowledgements

Firstly, I would like to thank my supervisors Dr Martin Jackson, Dr Brad Wynne and Dr Sam Turner for their invaluable support. Their continuous encouragement, guidance and patience assisted me throughout this work and without whom this research would not have been possible.

I am particularly grateful for the opportunities that were given to me and allowed me to present my findings at international conferences.

Numerous members of staff as part of the Department of Materials Science and Engineering and at the AMRC have helped me to carry out the experimental and analysis work. I would particularly like to thank Dr Peter Korgul, Dr Chris Taylor, Dr Pete Osborne and John Mann for their technical support. I would also like to thank fellow researchers Dr Meurig Thomas and Dr Magda Lopez-Pedrosa for their help with my work.

I would like to extend thanks to both Dr Matthew Thomas and Yvon Millet at Timet for their support and technical input throughout the project.

I would like to give special thanks to all my D1 compatriots and wish them all great success in their future careers.

Finally, I would like to thank my parents Pip and Paul for their continued support and I dedicate this thesis to them.

List of figures

	Page
Figure 1.1 Schematic binary phase diagrams illustrating the effect of increasing proportions of α , β and neutral stabilizing alloying additions in titanium alloys [6].	5
Figure 1.2 Pseudo titanium phase diagram containing both α and β stabilising solute elements and illustrating the relative position of α alloys, near α alloys, $\alpha + \beta$ alloys, near β alloys and β alloys [11].	6
Figure 1.3 Composite optical micrographs illustrating the design rationale of Ti-834 (formerly IMI 834) whereby through careful control during heat treatments the desired in-service bimodal microstructure can be achieved [13].	7
Figure 1.4. Schematic processing route diagram illustrating the 4 processing steps required during production to produce bimodal microstructure for $\alpha+\beta$ titanium alloys [4].	10
Figure 1.5 Proposed orientation of the initial rectangular cross-section of the intermediate billet with respect to position of the final round billet. Coloured lines indicate the regional average crystallographic alignment of the basal plane in the transverse plane [19].	12
Figure 1.6 Basal $\langle a \rangle$ (0002), prismatic $\langle a \rangle \{10\bar{1}0\}$, pyramidal $\langle a \rangle \{10\bar{1}1\}$ slip systems, and second-order pyramidal $\langle c + a \rangle \{11\bar{2}2\}$ slip systems in HCP materials [4].	14
Figure 1.7 Schematic illustration demonstrating the association between the parent material and that of the twin, using the relationship between a reference sphere and twinning ellipsoid with each sharing a common plane K1. After Hall [26].	15
Figure 1.8 Histogram comparing the distribution of all grains (white bars) and twinned grains (gray bars) as a function $\{10\bar{1}2\}$ type twinning, with the Schmid factor for each grain determined by in EBSD. The marks represent the ratio between the gray and white bars as well as indicating the fraction of twinned grains, after [44].	20
Figure 1.9 Frank–Read or Köhler source creating a pile-up at a grain boundary thus acting as a nucleolus for further deformation to occur within a neighbouring grain [35].	22
Figure 2.1 Schematic illustrating the key machining features of an orthogonal cutting arrangement. After Dieter [49].	24
Figure 2.2 Schematic diagrams of the simple two-dimensional orthogonal steady state cutting operation illustrating (a) the key dimensional parameters and (b) the resulting stress components acting within the arrangement. After	25

Dieter [49].

Figure 2.3 The effect of surface roughness on number of cycles to failure for aluminium fatigue test specimens [55]. 27

Figure 2.4 Representative optical micrographs of Ti-64 specimens with the resulting microstructure deformation, following a turning operation using (a) new tool and (b) prepared ‘worn’ tool geometries [56]. 27

Figure 2.5 Deformed surface microstructure of Ti-64 following a machining operation at a cutting speed of 100 m.min⁻¹, feed rate 0.25 mm.rev⁻¹ micrographs obtained are representative of material following (a) 10 seconds and (b) 120 seconds of machining time (worn tool), under a dry cutting environment [57]. 28

Figure 2.6 Microhardness profiles beneath the machined surface when machining Ti-64 with 883 insert at a surface speed of 100 mm.min⁻¹ with a variable feed rate under dry cutting conditions [57]. 30

Figure 2.7 Back scatter electron micrograph taken in cross section of a deformed Inconel 718 subsurface microstructure following micro drilling trials, demonstrating significant grain refinement in the near surface region [77]. 33

Figure 2.8 Following machining on brass test specimens (a) TEM micrographs illustrating the similarities in grain refinement that occur within the chip and in the near surface regions of the workpiece, (b) EBSD OIM of the machined brass substrate demonstrating the severe amount of grain refinement at the surface of the material with further imparted deformation occurring at depths > 50 µm from the machined surface [78]. 34

Figure 2.9 Deformation map illustrating the effect on microstructure as a result of variable machining parameters for copper test specimens [79]. 35

Figure 2.10 Backscattered electron micrograph of a drilled Ti-64 test specimen representative of the near the surface condition using a worn tool following the completion of the 128th hole. The two delineated regions A and B demonstrate the presence of two distinct deformed layers remaining following machining; high shear zone (A) and plastically deformation region (B) [60]. 37

Figure 2.11 Schematic diagrams illustrating the common operational preparations used to achieve an (a) orthogonal cut using either b (i) outer diameter or (ii) facing arrangement preparation. 38

Figure 2.12 Comparative evaluation of (a) acquired simulated chip morphologies to (b) experimentally obtained Ti-64 chips, using chip maximum and minimum height as a reference [87]. 39

Figure 2.13 Experimental and numerical chip formation of Ti-64 using (a) new tool and (b) worn tool geometry Rake angle 0° Clearance angle 11° Cutting 41

speed 60 m.min-1 [96].

Figure 2.14(a) cross sectional optical micrograph of red annealed brass using a microgrid grid pattern to demonstrate the severity of the imparted strain following machining, (b) graphical representation of the total plastic subsurface strain imparted following a machining pass [99]. 43

Figure 2.15 Cross sectional optical micrographs of machined CP titanium (a) resulting microstructure following a halted quick stop test (b) As machined material, which can be divided into three distinct regions; the uppermost layer indicating a region that has become highly refined following intense shear, the twinned region within ~150 μm of the surface and the undeformed bulk microstructure [102]. 44

Figure 2.16 In-situ machine monitoring using (a) Particle image velocimetry (PIV) and (b) infrared (IR) thermography imagery measuring the deformation and temperature fields respectively [103]. 45

Figure 2.17 Band contrast OIM with special boundary delineation of the deformed CP titanium microstructure following a halted machining operation[103]. 46

Figure 2.18 Cross sectional backscattered electron micrographs showing varying severity in induced deformation in the form of intense slip bands following high-speed machining in (a) Ti-64 and (b) Ti-834. (c) illustrates further regional non-uniformity of deformation observed in Ti-64 [105]. 47

Figure 2.19 EBSD OIMs of milled Ti-834 following a high-speed cutting operation (200 m min-1). (a) Crystal disorientation OIM referenced against individual grain average orientation; (b) pattern quality (band contrast) OIM of the region delineated in (a). the corresponding slip trace analysis demonstrating the identification of $\{0002\}$ and $\{10\bar{1}1\}$ type slip [105]. 48

Figure 2.20 Cross sectional backscatter electron micrograph following machining of Ti-64 with a surface speed $V_c = 260 \text{ m.min}^{-1}$, the delineated regions P1, P2 and P3 relate to the bulk material, plastically deformed material and severely deformed tertiary shear material respectively [107]. 51

Figure 2.21 Band contrast OIM of machined Ti-64 following a turning operation, the image demonstrates the diminishing severity of the deformation away from the machined surface [107]. 51

Figure 2.22 Resulting plastic deformation depth as a function of cutting speed for turned Ti-64 as determined using EBSD data to identify the interface between the bulk and deformed material [107]. 53

Figure 2.23 Resulting cutting force profile as a function of cutting speed for orthogonally turned Ti-64 [90]. 54

Figure 2.24 Resulting relationship of cutting and thrust forces as a function of 56

feed rate for machined Ti-64 samples in a mill annealed (MA) and solution heat and aged (STA) condition [124].

Figure 2.25 Resulting relationship of cutting and thrust forces as a function of feed rate for orthogonally machined titanium samples, illustrating the effect of chemical composition using test specimens of; Ti-64, Ti-54M and Ti-6246 [126]. 57

Figure 2.26 Typical resulting ‘size effect’ relationship of specific cutting energy as a function of uncut chip thickness [129]. 58

Figure 2.27 Schematic illustrating Shaw’s approach to shear band formation relying upon the coalescence of microcracks that are generated at sites of stress concentration, after Shaw [131]. 59

Figure 2.28 The typical friction coefficient relationship with uncut (undeformed) chip thickness during orthogonal machining of 7075 T6 aluminium cut at 10 and 150 m.min⁻¹ [137]. 60

Figure 2.29 Typical feed-force relationship illustrating a cross over point occurring at an uncut chip thickness of ~0.09 mm, below which the values of thrust force are higher than the experienced cutting force, after Armendia [138]. 61

Figure 2.30 Schematic illustrations of a orthogonal machining arrangement when cutting using a tool that has an (a) infinitely sharp cutting edge and (b) cutting with a tool that has a edge radius (r) greater than the uncut chip thickness (t₁), after Ng [137]. 62

Figure 2.31 Schematic diagram of an orthogonal cutting arrangement where the edge radius is approximately equal to that of the uncut chip thickness and a stable built up edge has formed ahead of the tool, thus changing the effect tooling geometry [139]. 63

Figure 2.32 Resulting relationship of specific cutting energy and uncut chip thickness for orthogonal machining trials with each data set for variable tooling approach angles represented by a solid and dashed line; the solid line indicates the typical ‘size effect’ relationship prior to removing the ploughing forces and the dashed line represented the corresponding relationship once the ploughing forces have been removed [142]. 64

Figure 2.33 Cutting F_c and thrust F_t force relationship with uncut chip thickness t₁, for a range of rake angles $\alpha = 0^\circ, 10^\circ$ and 30° . With components P1 and P2 representing the ploughing force for F_c and F_t respectively [143]. 64

Figure 2.34 Resulting relationship of friction and uncut chip thickness for orthogonal machining trials with each data set for variable tooling approach angles represented by a solid and dashed line; the solid line indicates the typical ‘size effect’ relationship prior to removing the ploughing forces and the dashed line represented the corresponding relationship once the ploughing 65

forces have been removed [142].

Figure 2.35 Resulting depth of imparted mechanically induced twinning in beryllium as a function of depth of cut for machining operations undertaken at varying temperatures [148]. 67

Figure 2.36(a) Light micrographs of a fractured thin walled beryllium surface demonstrating large facets adjacent to surface A and small facets adjacent to surface B, (b) corresponding polarized light micrograph of a representative region of the thin walled beryllium sample demonstrating significantly more twins in the region adjacent to surface B [147]. 68

Figure 2.37 Machining arrangement for machining single crystal samples using; (a) planing configuration, (b) plunge-turning configuration, and (c) in-plane machining [155]. 69

Figure 2.38 The resulting variation in specific cutting energy as a function of crystallographic orientation as determined via a plunge turning configuration [159]. 70

Figure 2.39 The relationship of (a) elastic modulus (E), (b) yield stress ($\sigma_{0.2}$) and reduction in area (RA(%)) as a function of loading direction in relation to the average orientation of Ti-64 test specimens [4]. 71

Figure 2.40(a) Cross-section schematic of a worn cutting tool showing the effect of crater wear on the tool rake angle and flank wear (VB) (b) schematic illustrating the regions of tool wear on the rake, flank and nose of the cutting insert [166], [167]. 73

Figure 2.41 Typical wear profile of a cutting insert as a function of cutting time with key wear regions identified after, after Taylor [176]. 74

Figure 2.42 Taylor relationship of tool wear determined following a series of tool life trials used to determine tool life as a function of cutting speed [176]. 75

Figure 2.43 Wear rate map for Ti-64, determined through a series of parametric outer diameter machining trials using H13A uncoated carbide cutting inserts [177]. 76

Figure 3.1 Typical sample orientations for microstructure analysis relative to the workpiece. The normal (ND) –cutting (CD) – feed direction (FD) and corresponding EBSD sample dimensions. 80

Figure 3.2 Principle components of an EBSD system, after Oxford Instruments [186]. 85

Figure 3.3(a) The Bragg condition is satisfied when the backscattered electrons from the diffracting planes are reflected in phase (b) Schematic diagram illustrating how the diffracted electron cones are projected on to the phosphor screen allowing identification, after Wilkinson *et al.* [187]. 86

Figure 3.4 Fundamental processing steps during the acquisition of orientation data; following the capture, processing and analysis of an EBSD with its associated Hough space representation and MAD.	87
Figure 3.5 EBSD job database saved as a common transfer file (.ctf).	92
Figure 3.6 Schematic illustrating the Euler transformations where (a) ϕ_1 equals the rotation around z-axis, (b) Φ equals the rotation about e_2 axis, (c) ϕ_2 equals rotation about the e_3 axis.	92
Figure 3.7 All Euler orientation image map and corresponding legend, colouring set parallel to the viewing plane.	93
Figure 3.8 Inverse pole figure and corresponding legend, colouring set parallel to the viewing plane.	94
Figure 3.9 Inverse pole figure orientation image map after a noise reduction function has been applied.	95
Figure 3.10 Band contrast image map of a cross section taken of a machined titanium alloy surface. Enlarged region (i) showing the highly deformed subsurface region beneath the machined surface.	96
Figure 3.11 Inverse pole figure orientation image map after a noise reduction and $\{10\bar{1}2\}$ twin delineation function has been applied. Enlarged region (i) showing the highly deformed subsurface region beneath the machined surface with the identification of $\{10\bar{1}2\}$ type twins within an individual grain.	97
Figure 3.12(a) Inverse pole figure orientation image map after a noise reduction with a subset taken from within an individual grain. (b) Graphical representation of the average orientation of the HCP crystal within the highlighted subset, including the corresponding Euler angles. (c) Pole figure representation of highlighted subset with corresponding contour plot (d).	98
Figure 3.13 The crystal coordinate system for hexagonal materials is defined by the starting orientation of the initial HCP crystal. The two possible orientations are defined by the x-axis being either parallel or perpendicular to the $\{10\bar{1}0\}$ axis as shown in (a) and (b) respectively.	100
Figure 3.14 Composite pole figure plot, displaying the relative location of the basal and prismatic planes when $\phi_1 = 0$, $\Phi = 0$, $\phi_2 = 0$.	107
Figure 3.15 Application of the slip trace tool used to determine the available deformation planes for a specified region of material. After a Schmid factor filter of $m = 0.6$ is applied this allows the user to more easily identify the coincidence of the deformed plane, which for this example can be aligned to fit the $\{0002\}$ basal plane.	110
Figure 3.16 Inverse pole figure orientation image map after a noise reduction	111

and twin delineation. Using the deformed grains average Euler angles for the parent and the twin material the corresponding location of their nearest neighbours are shown on the $\{10\bar{1}2\}$ pole figure. Here the location of the determined K1 plane displays clear coincidence to the normal orientation of the twin trace.

Figure 4.1 Backscatter electron micrograph of the as-forged Ti-834 114
microstructure.

Figure 4.2(a) Photograph of the roughly turned stepped Ti-834 billet 115
workpiece prior to the outer diameter precision turning trials; (b) Schematic illustrating the cutting process and typical subsurface microstructure deformation, sectioned parallel to the cutting direction.

Figure 4.3 (a) Schematic diagram illustrating the tools orientation relative to 117
the workpiece during precision turning. (b) Image of a Sandvik CNMG 120408-23 H13A cutting insert illustrating the location of the flank face, rake face, leading edge and nose.

Figure 4.4 Light micrographs of the flank nose cutting edge for a Sandvik 117
CNMG 120408-23 H13A cutting inserts (a) Unworn tool (b) worn tool.

Figure 4.5 Hardness indent array at 10 μm intervals from the machined surface 118

Figure 4.6 Image of a Sandvik CNMG 120408-23 H13A uncoated carbide 120
cutting insert demonstrating the position of the (a) rake and (b) flank edges at the nose of the tool and the typical wear pattern appearance on each of the faces following 90 seconds of machining at 50 m.min⁻¹.

Figure 4.7 tool wear profiles for the (a) average (b) maximum tool wear, 122
VBmax, for rake and flank wear at the nose of the tool as a function of machining speed. The error bars indicate the true spread in the recorded data.

Figure 4.8 Roughness profiles of the workpiece material as a function of 123
machining speed using, a centre Line Average approach, Ra. The included error bars indicate the true spread in the recorded data

Figure 4.9 Cross-sectional backscatter electron micrograph of outer diameter 126
turned Ti-834 and corresponding microhardness profile for (a) 50 m.min⁻¹ and (b) 70 m.min⁻¹. The error bars indicate the true spread in the recorded data.

Figure 4.10 Cross-sectional backscatter electron micrograph of outer diameter 127
turned Ti-834 and corresponding microhardness profile for (a) 80 m.min⁻¹ and (b) 95 m.min⁻¹. The error bars indicate the true spread in the recorded data.

Figure 4.11 Cross-sectional backscatter electron micrograph of outer diameter 128
turned Ti-834 and corresponding microhardness profile for (a) 105 m.min⁻¹ and (b) 120 m.min⁻¹. The error bars indicate the true spread in the recorded data.

- Figure 4.12 Electron backscatter images of the machined surface with increasing surface speed. The delineated line signifies the interface between the undeformed bulk material and the average depth of deformation assessed using beta distortion at 10 μm intervals across approximately 2000 μm of surface material. 130
- Figure 4.13 Cross-sectional backscattered electron micrographs of turned Ti-834 at surface speeds of (a) 50 m.min⁻¹, (b) 80 m.min⁻¹ and (c) 105 m.min⁻¹ with adjacent enlarged micrographs highlighting imparted deformation. 132
- Figure 4.14 EBSD inverse pole figure (IPF) OIMs of the outer diameter turned Ti-834 surface material with increasing surface speed. The dashed black delineated line signifies the interface between the non-deformed bulk material and the average depth of damage. The dashed red delineated line signifies the interface between the non-deformed bulk material and the maximum depth of damage. 134
- Figure 4.15 Graph illustrating the effect of surface speed on the depth of surface deformation assessed by measuring beta distortion using backscatter electron images and EBSD. 135
- Figure 4.16 Cross-sectional backscatter electron micrograph of 80 m.min⁻¹ turned Ti-834, following a 1600 hour thermal exposure at 750°C. Silicide precipitates form in the vicinity of apparent twin boundaries and throughout a grains interior. 137
- Figure 4.17 Cross-sectional backscatter electron micrographs of high speed turned Ti-834 (95 m.min⁻¹). a) Following thermal exposure at 750°C for 1600 hours mechanically induced deformation generated during the machining process promotes silicides to precipitate adjacent to; a (i) mechanical twin boundaries, a (ii) along slip planes. b) Cumulative disorientation profile illustrating lattice rotation across transect x to y. 139
- Figure 4.18(a) Representative EBSD inverse pole figure (IPF) OIMs of as-forged Ti-834 illustrating the presence of twin features distributed throughout the material, enlarged region (i) shows their appearance with a transect across the delineated boundaries. (b) The corresponding disorientation profile for the transect given in (i) shows the relative disorientation across the boundary displaying a regular 64° rotation, satisfying the features of the “i” twin. 140
- Figure 5.1 Backscatter electron micrograph of the Ti-54M mill annealed microstructures. 144
- Figure 5.2 Schematic diagram of the outer diameter turning process to illustrate the sample coordinates; Normal direction (ND); Feed direction (FD) and Cutting direction (CD), and a schematic arrangement of the obtained EBSD data orientated parallel and perpendicular to the cutting direction. 145
- Figure 5.3 Composite image of the outer diameter turned material using a secondary electron detector for the surface combined with a backscatter 146

electron detector for the subsurface.

Figure 5.4 Cross sectional backscatter electron micrograph of outer diameter turned Ti-54M sectioned perpendicular to the cutting direction, the image illustrates the presence of mechanically induced subsurface deformation in the form of (a) slip and (b) twinning. 149

Figure 5.5 Cross sectional backscatter electron micrograph of outer diameter turned Ti-54M sectioned parallel to the cutting direction, the image illustrates evidence of mechanically induced subsurface deformation within primary α grains, manifesting in a substantial channelling contrast image effect. (a) Uppermost deformed primary α grain surrounded by colony α , (b) Deformed neighbouring primary α grains. 150

Figure 5.6 Cross sectional backscatter electron micrograph of turned Ti-54M with a machining induced surface defect identified. High magnification micrograph of subsection (i) shown in inset image. 151

Figure 5.7 Cross sectional EBSD OIMs of outer diameter turned Ti-54M (a) IPF coloured OIM with corresponding (b) pattern quality OIM, delineated region i and ii in (a) indicate two macrozone regions with the corresponding pole figures for both regions presented in (c). Region iii has been enlarged in (d) and (e) with $\{10\bar{1}2\}$ twin boundary delineation and slip trace analysis. 154

Figure 5.8 Resulting $\{10\bar{1}2\}$ pole figure projection for the activated twins illustrating the position of the assumed activated K1 plane for each parent twin pair. Note further lattice rotation between parent and twin has caused some deviation of both planes. 155

Figure 5.9 Pole figure projections of the $\{0002\}$ and $\{10\bar{1}2\}$ for the parent material for each grain displaying evidence of twinning, following filtering to remove rogue twined grain orientations. 156

Figure 5.10 Pole figure projections of the $\{0002\}$ for the parent material for each grain displaying evidence of twinning, the data presented has been filtering to remove rogue orientations and divided into two discrete opposing groups as labelled. 157

Figure 5.11(a) Composite backscatter electron image illustrating the forward and reverse simple shear components ahead and behind the tool with the corresponding inclined HCP crystal, (b) The application of the plane simple shear model and its interaction with the HCP crystal; $\pm 38^\circ$ and $\pm 52^\circ$ correspond to the optimal orientation of the HCP crystal for both the forward and reverse condition. 158

Figure 5.12 Pole figure projections of the $\{0002\}$ and $\{10\bar{1}2\}$ for the parent material for each grain displaying evidence of twinning, following filtering and dividing into discrete groups. 159

Figure 5.13(a) IPF coloured, with respect to FD, OIM of outer diameter turned 161

Ti-54M illustrating the orientation of the parent grains that contain $\{1012\}$ twins via (i) forward and (ii) reverse simple shear. (b) Corresponding $\{0002\}$ and $\{1012\}$ stereographic pole figure projections.

Figure 5.14(a) IPF coloured, with respect to FD, OIM of outer diameter turned Ti-54M illustrating the orientation of abnormally orientated parent grain that contain $\{1012\}$ twins (b) Corresponding $\{0002\}$ and $\{1012\}$ stereographic pole figure projections. 162

Figure 5.15 Histogram comparing the distribution of the relative frequency of the calculated Schmid factor for $\{10\bar{1}2\}$ twinning for each that has twinned to that of all of the grains within 100 μm of the surface. Schmid factor calculated assuming plane simple shear. 163

Figure 5.16 bulk material surface, orientation of parent grains which have twinned, theoretical orientation Figure 5 (a) The crystallographic texture of all material within 100 μm of the surface, (b) orientation of the parent grains that have deformed via $\{10\bar{1}2\}$ twinning, (c) theoretical orientation of grains that are most favourably orientated for $\{10\bar{1}2\}$ twinning assuming plane simple shear. 165

Figure 5.17 Secondary electron micrograph of an inclined machined Ti-54M surface following a machining tool dwell. The shoulder highlighted within the area between the two delineated lines locates the dwell zone. 166

Figure 5.18 Cross sectional backscatter electron micrographs of outer diameter turned Ti-54M, sectioned parallel to the cutting direction from within the dwell region. The images illustrate the typical gross mechanically induced subsurface deformation, manifesting in twins and intense slip that have developed into severe cracking. (a) Has captured a primary α grain that has appeared to resist deformation, (b) severe cracking progressing unimpeded through neighbouring primary α grains and through grain boundary β . 169

Figure 5.19 Cross sectional backscatter electron micrograph of outer diameter turned Ti-54M sectioned parallel to the feed direction within the dwell region, the images illustrate the occurrence of a residual white layer at the surface interface, the enlarged micrograph (i) shows evidence of slip progressing unimpeded through the residual grain boundary β . 170

Figure 5.20 (a) IPF coloured, with respect to FD, OIM of outer diameter turned Ti-54M illustrating the occurrence of mechanically induced $\{1012\}$ tension type twins within the dwell zone (b) Corresponding $\{0002\}$, 1010 and $\{1012\}$ stereographic pole figure projections of the bulk region indicating strong alignment of the basal plane along CD and FD. 172

Figure 6.1 Backscatter electron micrograph of Ti-54M, with an as-forged microstructure. 175

Figure 6.2 (a) Photograph showing the orientation of the arbitrary Ti-54M billet axis with the cardinal points scribed onto the billet cross section (b) 176

location and orientation of the sectioned microstructure analysed samples.	
Figure 6.3 Ti-54M billet position held in a MAG Cincinnati Hawk lathe prepared for an orthogonal cutting trial.	177
Figure 6.4 Ti-54M Workpiece and tool arrangement following an orthogonal cutting trial.	178
Figure 6.5 Schematic diagram illustrating the orientation of the Cartesian planes used when recording the force feedback data.	178
Figure 6.6 Schematic diagram of a simple two-dimensional orthogonal steady state cutting operation illustrating the resulting stress components acting within the arrangement.	181
Figure 6.7 Shallow notch grooved onto the orthogonal cutting surface of Ti-54M.	183
Figure 6.8 DEFORM-3D finite element software simulation identifying the total strain distribution within a Ti-54M billet, following a typical multi-stage cogging process performed by TIMET. Data supplied courtesy of TIMET UK, note scale bar not included with colour distribution to be used only as a guide for relative strain variance.	185
Figure 6.9 Composite image comprising of a quarter cross section taken of the Ti-54M billet, positioned between East and south on the arbitrary billet axis. Representative basal stereographic pole figure projections, each presented as a contour plot illustrating the average bulk texture for each region. The location of the samples analysed correspond to the position of two concentric rings of diameter ~ 223 mm and ~83 mm with two additional samples taken from the centre and midpoint of R2.	187
Figure 6.10 Composite image illustrating how the varying crystallographic orientation of the billet has evolved as a result of the forging procedure. (a) Quarter cross section with regional average orientation pole figures, adjacent to each pole figure the corresponding effective rolling axis inclination indicates to what angle the region has undergone an effective plane strain environment. The subsequent removal of this angle from the data gives rise to the resulting pole figure demonstrating a typical plain strain type texture indicative of a rolled morphology, as demonstrated by the surrounding stereographic pole figures. (b) The plot shows how much the effective rolling axis inclination varies circumferentially around the billet and throughout its interior. (c) Reference image after Lütjering [4] illustrates how the typical rolled type microstructure can vary as a function of the deformation temperature.	189
Figure 6.11 Proposed orientation of the initial rectangular cross-section of the intermediate billet with respect to the arbitrary coordinates, the weighted lines indicate the average microstructure alignment of the bulk material in the transverse plane.	190

- Figure 6.12 Representative backscatter electron micrographs illustrating the microstructure variation across a quarter cross section of a 250 mm Ø Ti-54M billet in the as-forged condition. (a-e) illustrate the circumferential microstructure variation taken at 223 mm Ø, (f) corresponds to a midpoint parallel to R1 at 150 mm Ø, Micrographs (g-i) taken at 75 mm Ø, (j) centre. Inset average {0002} crystallographic orientation image to be used as a reference when analysing the microstructure. 193
- Figure 6.13 Representative backscatter electron micrographs illustrating the microstructure variation within a 250 mm Ø Ti-54M billet in the as-forged condition across the R2 axis. 194
- Figure 6.14 Representative backscatter electron micrographs illustrating the microstructure variation within a 250 mm Ø Ti-54M billet in the as-forged condition taken; (a) parallel to the R2 axis, (b) at 45° and (c) parallel to the R1 axis. 195
- Figure 6.15 Representative backscatter electron micrographs illustrating the microstructure variation within a 250 mm Ø Ti-54M billet in the as-forged condition taken; (a) at 22.5° to the R2 axis and (b) at 67.5° to the R2 axis. With enlarged region (i) illustrating the presence of potential α'' precipitates. 196
- Figure 6.16 Resulting cutting force data along the x, y and z planes, the acquired data monitors a complete cutting cycle with the corresponding cutting regions identified; start, contact, steady state and finish. 197
- Figure 6.17 Compiled steady state thrust (y) and cutting (z) force data for each feed rate analysed, with additional regression line for each dataset. 198
- Figure 6.18 A series of plots demonstrating the typical ‘size effect’ for the (a) coefficient of friction (μ), (b) specific cutting energy (F'_y , F'_z) and (c) apparent shear stress of the material (τ_{app}) in relation to the applied feed rate 200
- Figure 6.19 Schematic illustrating the resulting tool path into the workpiece during a single rotation, assuming the billet has been faced prior to machining resulting in a planar finish. 201
- Figure 6.20 Compiled steady state thrust (y) and cutting (z) force data for each feed rate analysed, with additional regression line for each dataset. Superimposed onto the plot, the 0.25 mm.rev-1 initial contact data with its position and thus effective feed equalling the tools corresponding displacement. 201
- Figure 6.21 Compiled initial contact data for each machining trial with the resulting forces plotted in relation to the total displacement of the tool into the workpiece. (a) Thrust forces and (b) cutting forces, Enlarged regions (i) and (ii) illustrate the common inflection point occurring at ~0.06 mm. 203
- Figure 6.22 Compiled steady state thrust (y) and cutting (z) force data for each 204

feed rate analysed, with additional regression line for each dataset. Superimposed onto the plot, the 0.25 mm.rev-1 initial contact data with its position taking into account the initial offset of ~0.06 mm, following this offset the effective feed equals that of the tools corresponding displacement.

Figure 6.22 Compiled steady state thrust (y) and cutting (z) force data for each feed rate analysed, with additional regression line for each dataset. Superimposed onto the plot, the 0.25 mm.rev-1 initial contact data with its position taking into account the initial offset of ~0.06 mm, following this offset the effective feed equals that of the tools corresponding displacement. 206

Figure 6.23 Composite images illustrating the proposed root causes of the data offset. (a) Assumed ideal contact scenario with the tool approaching the workpiece in parallel, (b) non parallel contact, thus resulting in an offset. (c) Role of edge radius of the cutting edge in relation to the uncut chip thickness (equal to feed rate during orthogonal cutting) (d) force data plot illustrating how the culmination of the edge radius and the tool approaching the workpiece at an angle results in a total offset of ~0.06 mm. 207

Figure 6.24 Compiled initial contact data for each machining trial with the resulting forces plotted following the removal of the initial offset, the thrust and cutting data plots have been determined using an effective feed rate calculated in relation to the tools displacement into the workpiece. The calculated regression line acquired during the steady state trials has also been included as a reference. 208

Figure 6.25 Typical resulting thrust (y) and cutting (z) force relationship with respect to feed rate acquired using a non-compiled individual 0.2 mm.rev-1 initial data following the removal of the offset data. 208

Figure 6.26 Illustrates the proportion of the total force for both the thrust (y) and cutting (z) that is accounted for by the initial ploughing forces, which remain constant throughout and offer no further contribution to the chip removal process. 209

Figure 6.27 Resulting thrust (y) and cutting (z) force relationship with respect to feed rate acquired using a non-compiled individual 0.2 mm.rev-1 cutting trial following the removal of the ploughing forces each dataset pass through the origin. The gradient has been determined using a linear fit regression relationship for both the thrust and cutting forces, with the corresponding R2 value. 210

Figure 6.28 Resulting effective friction of the cutting environment as determined using the single cut initial contact filtered 15 Hz signal data (solid line), black dashed line denoting the filtered signal compiled average and the red dashed line representing resulting effective friction as calculated using the linear fit regression relationship. 212

Figure 6.29 The resulting specific cutting energy of the cutting environment for thrust force (y) in blue and the cutting force (z) in red. As determined using 213

the single cut initial contact filtered 15 Hz signal data (thick solid line), thin solid line denoting the filtered signal compiled average and the dashed line representing resulting specific cutting energy as calculated using the linear fit regression relationship.

Figure 6.30 Resulting apparent shear stress of the cutting environment as determined using the single cut initial contact filtered 15 Hz signal data (solid blue line), black dashed line denoting the filtered signal compiled average and the red dashed line representing resulting apparent shear stress as calculated using the linear fit regression relationship. 214

Figure 6.31 Resulting thrust (y) and cutting (z) force relationship with respect to cutting speed obtained during orthogonal cutting trials (a) individual run raw data (b) compiled average data for each individual speed. 215

Figure 6.32 Resulting signal cutting (z) force, showing both the raw and 15 Hz Fourier transformed low band pass filtered data. 217

Figure 6.33 Identification of a single rotation using reference notch index mark manifesting as a spike in the resulting fixed (x) thrust (y) cutting (z) force data, a, b and c respectively, included for each forces both the raw and 15 Hz Fourier transformed low band pass filtered data. The enlarged plot i for the z force data illustrates the nature of the index mark. 219

Figure 6.34 Aligned filtered thrust (y) and cutting (z) force data transposed on to circle plots aligning with the corresponding cross sectional quadrant of the billet with the related basal pole figures for each region. 221

Figure 6.35 Composite signal plot illustrating the repeating “M” within the thrust (y) force using the raw and filtered data. Superimposed onto the plot is the corresponding Young’s modulus as determined via ultrasound analysis, its position determined using the arbitrary billet axis and the prior notch index mark. 222

Figure 6.36 (left and right) Representative stereographic contoured $\{0002\}$ pole figures for region A and region B respectively. (Centre) corresponding photograph illustrating the location of region A and region B. 224

Figure 6.37 Representative polarised light micrographs at the machined surface of region A and region B, illustrating the occurrence of mechanically induced twins beneath the machined surface. The delineated lines represent transects used when calculating the frequency of the induced twins at a depth of 30 and 60 μm beneath the machined surface. The enlarged region (i) show the high density of induced twins that can be found within region A. 225

Figure 6.38 Histogram comparing the distribution of the relative frequency of the calculated Schmid factor for $\{10\bar{1}2\}$ twinning for region A and region B. Schmid factor calculated assuming plane simple shear. 225

Figure 6.39 Histogram comparing the distribution, within region A and region 226

B, of the absolute number of grains to that of the number of grains that have twinned using a transect method at a depth of 30 and 60 μm beneath the machined surface. The overlaid points signify the frequency of the twins within each region at each specified depth.

List of tables

	Page
Table 1.1 Slip systems of titanium [4].	14
Table 1.2 Twinning systems in α titanium [28], [29].	16
Table 3.1 Summary of metallographic analysis preparation stages for titanium alloy EBSD samples.	82
Table 3.2 Operating parameters for the Inspect F FEG SEM.	83
Table 3.3 Sirion FEG SEM EBSD Acquisition parameters and advisory guidelines.	89
Table 3.4 Calculated orientations for the slip direction and plane in sample space, when $\phi_1 = 0$, $\Phi = 0$, $\phi_2 = 0$.	106
Table 4.1 Billet composition of the near-alpha titanium alloy Ti-834 (wt. %).	115
Table 4.2 Machining parameters and workpiece geometry.	116
Table 5.1 Billet composition of the $\alpha+\beta$ titanium alloy Ti-54M (wt. %).	144
Table 6.1 Billet composition of the $\alpha+\beta$ titanium alloy Ti-54M (wt. %).	175
Table 6.2 Tooling required for orthogonal cutting force trials.	177
Table 6.3 Machining parameters for feed variable orthogonal cutting trials and workpiece geometries.	179
Table 6.4 Machining parameters for speed variable orthogonal cutting trials and workpiece geometries.	180
Table 6.5 Machining parameters for orthogonal cutting trials and workpiece geometries for microstructure correlation.	183

Nomenclature

“i” twin	Irrational twinning mode
BC	Band contrast (pattern quality)
BCC	Body centred cubic
BS	Band slope
BUE	Built up edge
CCD	Charge coupled device
CFCs	Cutting force coefficients
CP	Commercially pure
CRSS	Critically resolved shear stress
DIC	Digital image correlation
E	Young’s modulus (elastic modulus)
EB	Electron beam
EBSD	Electron back scatter diffraction
EBSP	Electron back scatter pattern
EDM	Electric discharge machining
FCC	Face centred cubic
FEG-SEM	Field emission gun scanning electron microscope ()
FEM	Finite element modeling
HCP	Hexagonal close packed
Hv	Vickers hardness
IMI	Imperial Metal Industries
IPF	Inverse pole figure
IR	Infrared
m	Schmid factor
$m_{Tensile}$	Schmid factor in a tensile environment
$m_{Compressive}$	Schmid factor in a compressive environment
MA	Mill annealed
MAD	Mean angular deviation
MUD	Multiples of uniform density
OIM	Orientation image map
PIV	Particle image velocimetry
RA	Reduction in area as a percentage
Ra	Average surface roughness value
Rt	Maximum surface roughness value
SCL	Spiral cut length
SEM	Scanning electron microscope
SIMS	Secondary ion mass spectrometry
SPD	Severely plastically deformed
STA	Solution heat treated and aged
TEM	Transmission electron microscope
TMP	Thermomechanical processing
UTS	Ultimate tensile strength
VAR	Vacuum arc re-melting
X-EDS	X-ray energy dispersive spectroscopy
XRD	X-ray diffraction
α	Hexagonal close packed alpha phase
α_p	Equiaxed primary α
β	Body centred cubic beta phase

k	Shear flow stress
σ	Stress
σ_y	Maximum yield stress (Ultimate tensile strength)
\emptyset	Diameter

Sample and material orientations

B	Basal texture relative to a rolling direction
CD	Cutting direction
N	‘North’ Cardinal point
ND	Macroscopic normal direction
R1	Arbitrary axis in the plane perpendicular to the billet axis
R2	Axis in the plane perpendicular to the billet axis and perpendicular to R1
T	Transverse texture relative to a rolling texture
TD	Macroscopic transverse direction

Tool parameters and cutting coefficients

DOC	Depth of cut
FR	Feed rate.
P1	Related to the bulk undeformed material
P2	Plastically deformed material
P3	Severely deformed tertiary shear material
SPE	Specific cutting energy
r	Edge radius
t_1	Uncut chip thickness
t_2	Chip thickness
VB	Flank wear land average
VB_{max}	Maximum tool wear
V_c	Cutting speed
x, y, z	Normal direction, feed direction and cutting direction coordinates
F_x	Normal direction normal force (orthogonal -facing)
F_y	Feed direction thrust force (orthogonal -facing) (alt. term F_f)
F_z	Cutting direction cutting force (orthogonal -facing) (alt. term F_c)
F_s	Resultant shear plane force
F'_y	Thrust specific cutting energy
F'_z	Cutting specific cutting energy
F'_s	Resultant shear plane force
K_c	Oxley cutting edge coefficient
K_f	Oxley feed edge coefficient
k_{c1}	Specific cutting energy needed to cut a chip area of 1 mm ² that is 1 mm thick
P_1	Cutting contribution to the ploughing force

P_2	Thrust contribution to the ploughing force
Q_1	Component of force in the direction of the tool motion
Q_2	Component of force perpendicular to the direction of the tool motion
α	Rake angle
θ	Angle
ϵ_{xx}	Total subsurface plastic strain horizontal
ϵ_{yy}	Total subsurface plastic strain vertical
γ_{xy}	total shear strain
σ	Stress
τ	Shear strength of the material
τ_Q	Shear strength of the material as calculated following the removal of the ploughing forces
ϕ	Shear angle
θ	Relief angle
ω	Width of orthogonal cut
μ	Coefficient of friction
μ_Q	Effective coefficient of friction following the removal of the ploughing forces

Bragg equation

n	Integer
λ	Wavelength of the electrons
d	Diffracting plane spacing
θ	Angle of incidence

EBSP conversion

(x, y)	EBSP coordinates
(ρ, θ)	Hough space coordinates

Taylor Tool life relationship

V	Cutting speed
T	Tool life time
C	Taylor tool life constants
n	Taylor tool life constants

Ultrasound analysis

E	Young's modulus;
v	Sound wave velocity;
V_T	Shear (transverse) velocity;
V_L	Longitudinal velocity
V_L	Longitudinal velocity
ρ	Material density

ν Poisons ratio

Lattice parameters

a	Lattice parameter, length HCP 2.95
b	Lattice parameter, length HCP 2.95
c	Lattice parameter, length HCP 4.72
α	Lattice parameter, angle HCP 90°
β	Lattice parameter, angle HCP 90°
γ	Lattice parameter, angle HCP 120°
$[a\ b\ c]$	Zone axis coordinates
$[L]$	Transformation matrix
$[g]$	Rotation matrix
$[g]^{-1}$	Inverse rotation matrix
(x, y, z)	Orthonormal arrangement
$\{h, k, i, l\}$	HCP Miller–Bravais
$\{h', k', l'\}$	Miller indices
$\{x'_{sp}, y'_{sp}, z'_{sp}\}$	Slip plane orthorhombic axes
$\langle x'_{sd}, y'_{sd}, z'_{sd} \rangle$	Slip plane direction orthorhombic axes
$\{x_{norm\ sp}, y_{norm\ sp}, z_{norm\ sp}\}$	Normal slip plane with orthonormal axes
$\langle x_{norm\ sd}, y_{norm\ sd}, z_{norm\ sd} \rangle$	Normal slip direction with orthonormal axes
$\{x_{sp}, y_{sp}, z_{sp}\}$	Slip plane in sample space
$\langle x_{sd}, y_{sd}, z_{sd} \rangle$	Slip direction in sample space
$\{x_{sp}, y_{sp}, z_{sp}\}$	Specific slip plane within the macroscopic sample space
$\langle x_{sd}, y_{sd}, z_{sd} \rangle$	Specific direction within the macroscopic sample space
(x_T, y_T, z_T)	Tensile loading direction in sample space
(x_C, y_C, z_C)	Compressive loading direction in sample space
$\{x_{sp}, y_{sp}, z_{sp}\}$	Slip plane orientation in sample space
(x_{trace}, y_{trace})	Slip trace coordinates for graphic use
(x_n, y_n)	Northern hemisphere pole figure plot
(x_s, y_s)	Southern hemisphere pole figure plot
ϕ_1	First Euler angle
Φ	Second Euler angle
ϕ_2	Third Euler angle

Twin planes and directions

K_1	Twinning equatorial plane
K_2	Prior twinning plane (undistorted)
K_2'	Post twinning plane (undistorted)
η_1	Twin shear direction
η_2	Prior twinning plane (undistorted) shear direction
η_2'	Post twinning plane (undistorted) Twin shear direction

Lattice parameters - Definitions

Misorientation angle

A specific angle of rotation about a common axis between two adjoining crystal systems.

Depending on the symmetry of the crystal there could be up to; 24 combination for a BCC system and 12 combinations for HCP.

Disorientation angle

Represents the minimum rotation that is required of all available axes to give an equivalent orientation, i.e. an angle of rotation about a family of axes rather than a specific axis.

Preface

The initial motivation for the project was to investigate the impact of high speed machining on titanium alloys. However, the fundamental material principles associated with traditional machining practices are little understood, especially those regarding titanium alloys for which high speed machining during turning relates to cutting speeds greater than $100 \text{ m}\cdot\text{min}^{-1}$. Here we seek to identify a link between fundamental material properties, which are controlled by a material's composition and microstructure, and their role during the machining process.

The aerospace industry remains the primary market for titanium metal, which in 2012 accounted for a buy-in weight of ~60,000 tonnes of material [1]. Over the coming 20 years there is an expected 4.7% annual growth in the global fleet of aircraft, requiring ~30,000 new passenger aircraft and freighters to be constructed, at a value of approximately US \$4.4 trillion [2]. For the next generation of aircraft such as the A380 and A350 from Airbus and the B787 from Boeing, in order to achieve improvements in fuel efficiency and noise reduction there is a drive to use ever increasing quantities of carbon fibre reinforced polymers (CFRPs) within the airframe. Due to its inherent favourable compatibility with CFRPs over aluminium, this ensures titanium's position as a key material in the manufacture of aircraft is assured. In response to this increase in demand and the economic drive for efficiency savings, the exploitation of high speed machining techniques is vital for the competitiveness of the UK advanced manufacturing sector, where high value manufacturing accounts for ~35% of all UK exports, contributing £151bn to the UK economy [3].

Machinists regard titanium as a 'difficult to machine alloy'. Unfortunately, the very properties that make titanium a popular engineering alloy also lead to difficulties during machining; low thermal conductivity and significant retention of mechanical strength at high temperatures, leads to excessive tool wear and prohibitive manufacturing costs. Machining of wrought product is a costly process and accounts for 60% of the total cost of critical titanium aerospace components, in most part due to approximately 95% of the starting material being removed as swarf [4] [5]. To minimise costs, the advanced manufacturing community are developing techniques to machine at higher rates. Up until now, the majority of high speed machining research has focussed on optimising the dynamics of the process and minimisation of tool wear for maximum productivity. Typically research into the fundamental processes that govern machining has traditionally been the domain of mechanical engineers who strive for efficiency gains through the optimisation of the cutting process using the

‘mechanical’ parameters which are at their disposal (cutting speed, depth of cut, rake angle, tooling geometry etc). Through the use of finite element modelling, researchers have provided a greater understanding of chip formation mechanics during the machining of titanium alloys.

This study identifies a fundamental knowledge gap between the role of machining and the resultant subsurface plastic deformation and microstructure modifications and links them.

This project has applied a multidisciplinary approach combining mechanical engineering and metallurgy methods to address key machining issues, which often lie out of the remit of the two disciplines. Traditionally the term machinability is used as a broad measure of machining efficiency, typically referring to aspects of inherent tool wear or maximum achievable cutting speeds. This investigation has however highlighted the need for a reassessment to be carried out on the fundamental understanding of machinability, taking into account surface and subsurface condition of the workpiece. In essence there is little point in machining a structurally critical component faster if it has poor in-service properties.

Precision turning is an energy intensive, yet important machining operation for critical aero-structural titanium alloy components. Current surface integrity practice generally applied by mechanical engineers characterises macroscopic features such as surface tearing, chip smearing and general deformation of grains in the direction of cutting; with little emphasis placed on subsurface microstructure damage. Through the use of high-resolution electron backscatter diffraction, microstructure subsurface damage has been identified in the form of mechanical twins, which until now, had not been observed in turned $\alpha + \beta$ titanium alloys. It was also revealed that there was an increase in induced subsurface deformation with an increase in machining surface speed. The occurrence of this deformation contradicts observations made when applying standard surface integrity techniques. The deformation features identified throughout this study could prove to have serious consequences on in-service properties, as, under certain stress conditions, the components resistance to fatigue crack initiation may be severely degraded. Subsurface microstructure damage such as mechanical twins and intense slip bands have also been shown to provide nucleation sites for silicide precipitation within the structurally critical alloy Ti-834 during thermal exposure at 750°C, indicating that creep and fatigue strength could be locally reduced at the machined surface. The microstructure subsurface damage reported during this study has significant industrial implications since there is a current strategy of increasing surface speeds to improve productivity in addition to the need

to review the effectiveness of current surface integrity analysis methods for determining the nature of deformation for machined titanium alloys

It has been demonstrated that microstructure variations across a billet's cross-section, which occurs as a result of a multiple cogging procedure, has a profound impact on the material's performance during machining. Following investigatory turning trials using the development alloy Ti-54M, the conditions required for the formation of subsurface $\{10\bar{1}2\}$ twins in the workpiece was determined. Twins were mostly observed in two orientation clusters at approximately $\pm 45^\circ$ to CD, which is attributed to a plane simple shear state that operates in a forward mode ahead of the tool and in reverse behind the tool. This observation means upstream processing, through the development of specific crystallographic texture components, has a direct impact on the level of subsurface damage caused by machining. This offers the possibility for material suppliers to develop upstream processing routes that generate material that complements the machining process, thus minimising the imparted damage, leading to enhanced in-service performance. Product designers may also be able to incorporate the crystallographic distribution of the billet into their designs, stipulating that critical areas or facets of a component are positioned such that they are away from a region that may have a high predisposition for mechanically induced damage. It would be in the interest of the machinist to pursue machining strategies that consider the underlying crystallographic orientation of the workpiece material, through the development of machining practices that either minimise the amount of imparted damage for finishing purposes or in the case of roughing may wish to maximise the amount of imparted damage.

A novel approach for acquiring cutting force coefficients and cutting force material data has also been detailed and could be considered to be analogous to using the lathe as an effective high strain rate material test. Capturing key material performance values such as the apparent cutting friction and shear stress of the material.

Thesis outline

Chapter 1 is a literature review that includes a general overview on titanium metallurgy and fundamental deformation characteristics.

Chapter 2 Reviews the mathematical methods that are used throughout this investigation, detailing the mechanics of machining. This chapter also introduces the fundamental metallurgical response characteristics of machined components, with respect to the deformation characteristics of the workpiece and the role of crystallographic texture during machining.

Chapter 3 covers the experimental methods and analysis procedures that were applied throughout this study, further experimental method subsections are included prior to each subsequent investigation detailing more the specific techniques that were used which were specifically related to each particular trial.

Chapter 4 uses high-resolution electron backscatter diffraction on machined Timetal® 834 to reveal an increase in induced subsurface deformation with increasing surface speed, contradicting observations when applying standard surface integrity techniques. Subsurface microstructure damage such as mechanical twins and intense slip bands provide nucleation sites for silicide precipitation during thermal exposure at 750°C, indicating that creep and fatigue strength could be locally reduced at the machined surface.

Chapter 5 reports how subsurface layer (~10-60 µm) of turned Timetal® 54M shows a significant proportion of alpha grains containing $\{10\bar{1}2\}$ twins. Quantitative analysis via EBSD of the deformed subsurface material has shown that most twinned grains have parent c-axes at approximately $\pm 45^\circ$ to the cutting direction (CD) in the plane containing CD and the workpiece normal, with twin planes parallel and perpendicular to CD. Schmid factor analysis of the twin planes identified the stress state to be approximately plane simple shear with a forward sense ahead of the tool and a reversal behind.

Chapter 6 investigates the material aspects that influence the machining process during variable parameter orthogonal cutting trials, through the analysis of the resulting cutting forces. Further analysis of the cutting force data reveals how the variation in feedback level appears directly linked to processing history. For both the thrust and cutting forces, higher forces are required in regions where the billet has received greater amounts of total strain. This suggests microstructure and/or crystallographic texture variations generated by varying strain path histories have a direct impact on the machining response of titanium and, therefore, its machinability. A final impact case study concludes this chapter through the application of some of the key findings that have been made throughout this investigation and pursues their potential impact for industrial applications.

Chapter 7 completes this study, with the principle observations made throughout the study drawn as conclusions, with a final further work subsection detailing the author's suggested areas of further research.

Chapter 1 Literature review

1.1 Alloy classification

Titanium is an allotropic metal exhibiting a phase transition from alpha (α) to beta (β); the α phase exists as a hexagonal close packed (HCP) crystal structure, and the β phase as a body centred cubic (BCC) crystal structure. In pure titanium, the α phase is stable at room temperature, with the allotropic phase transformation (β transus) to the high temperature β phase occurring at 882°C [4]. Through the addition of alloying elements, the stability of the two phases can be engineered to suit necessary properties, as shown in the simplified schematic binary phase diagrams in Figure 1.1.

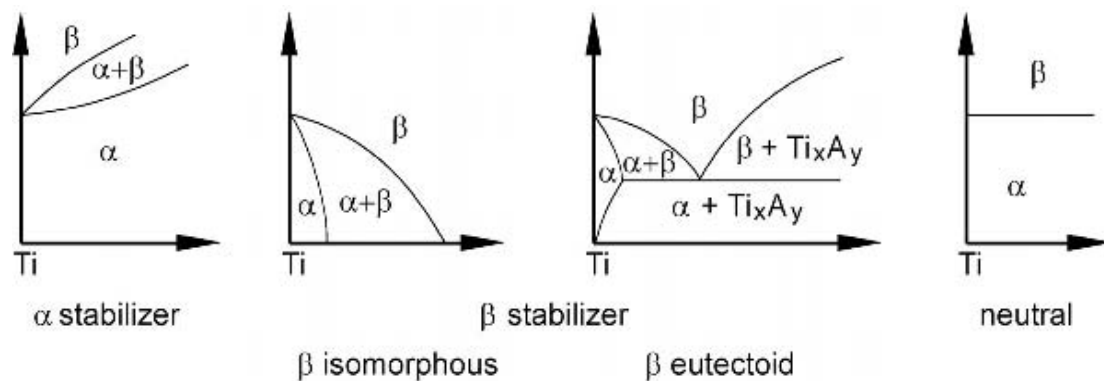


Figure 1.1 Schematic binary phase diagrams illustrating the effect of increasing proportions of α , β and neutral stabilizing alloying additions in titanium alloys [6].

Alloying elements in titanium are classified as being either α or β stabilizing additions, depending on whether they increase or decrease the β transus temperature. Al, O, N, and C are common α stabilising elements and raise the β transus temperature. Mo, V, W, Nb and Ta are traditionally categorised as isomorphous β stabilisers and continuously depress the β transus temperature, as illustrated in the schematic in Figure 1.1. Isomorphous β stabilisers must also be added as part of an aluminium masteralloy due to their high melting points and densities, and are relatively high-cost additions. In addition to the typical β stabilising elements, Fe, Mn, Cr, Ni, Cu, Si and H also depress the β transus until a compound is formed through a eutectoid reaction and are relatively low cost additions and can be added elementally. Eutectoid β stabilisers such as Fe tend to have a wide freezing range; hence, they segregate strongly. Compounded by their relatively large effect on β transus temperature, segregation can result in isolated regions having a significantly lower β transus values than the bulk. Conversely isomorphous β stabilisers such as Mo tend to have narrower freezing ranges and segregate less [7]. Zr and Sn are also commonly

used alloying additions serving as enhancers for solid solution strengthening of both the α and β phases, with their addition having minimal effect on the β transus temperature and are therefore regarded as being neutral [8].

It is to be noted that the systems designated previously as traditionally being isomorphous β (Mo and W), are not so in reality, exhibiting a miscibility gap in which the β phase separates into two bcc phases ($\beta'+\beta$) outside the $(\alpha+\beta)$ phase field [9]. For Mo the miscibility gap occurs at ~20% (the maximum molybdenum content present in conventional titanium alloys being ~15%) [10].

Through the additions of a combination of alloying elements (Figure 1.2) allows the production of different alloys, of which there are five classifications, in increasing β alloying additions: α alloys, near α alloys, $\alpha + \beta$ alloys, near β alloys/metastable β alloys and β alloys .

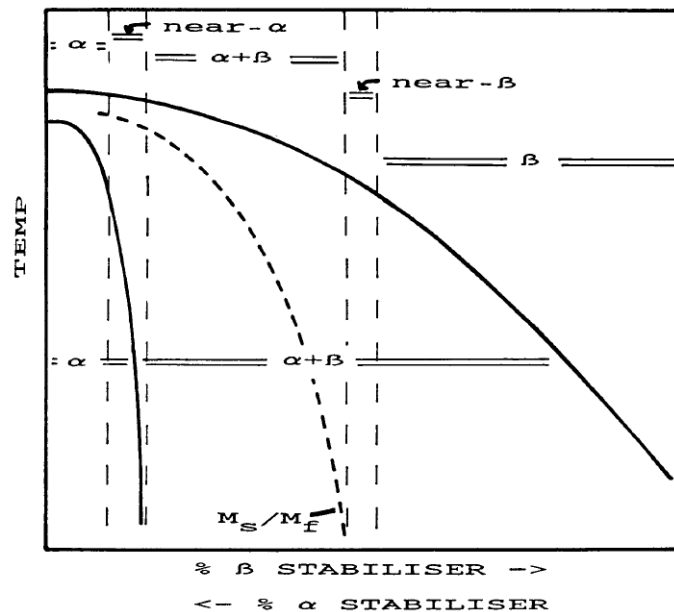


Figure 1.2 Pseudo titanium phase diagram containing both α and β stabilising solute elements and illustrating the relative position of α alloys, near α alloys, $\alpha + \beta$ alloys, near β alloys and β alloys [11].

1.1.1 α alloys

Commercially pure titanium (CP-Ti), Ti-2.5Cu and Ti-5Al-2.5Sn are examples of α alloys. α alloys are solution treated within the β region as shown in Figure 1.2 and subsequently quenched to give a fully martensitic α (HCP) microstructure. These alloys are unable to be subsequently heat treated however they can be strengthened via the addition of solution strengtheners (O, Al), or by controlled grain refinement following the Hall-Petch relationship using a cold working process [12]. The main properties of α alloys include excellent corrosion resistance and high weldability, α

alloys also do not exhibit a ductile to brittle transition and are therefore widely used as part of cryogenic systems and desalination.

1.1.2 Near α alloys

Alloys that have a small amount of retained β at equilibrium within their microstructure at room temperature are classed as near α alloys. The small amount of β phase within the system further expands and stabilises the $\alpha + \beta$ phase field and allows for improved workability when the alloys are being forged. Timetal® 834 (Ti-834) of nominal composition Ti-5Al-4Sn-3.5Zr-0.7Nb-0.5Mo-0.35Si-0.06C, is regarded as being one of the most advanced titanium alloys that is currently used within the aerospace industry, with superior high temperature fatigue and creep performance. Ti-834 gains its superior properties by careful prior processing that ensures the final microstructure consists of 15% remaining as primary α with 85% being derived from transformed β . Ti-834 has been engineered to possess a wide heat treatment window such that this critical ratio can be easily achieved during forging. Figure 1.3 describes the design rationale behind Ti-834 (formerly IMI 834). An optimal proportion of both α and β phases in a bi-modal structure allows Ti-834 to possess; high fatigue resistance, acceptable ductility, high creep resistance, fracture toughness, crack propagation resistance and temperature stability.

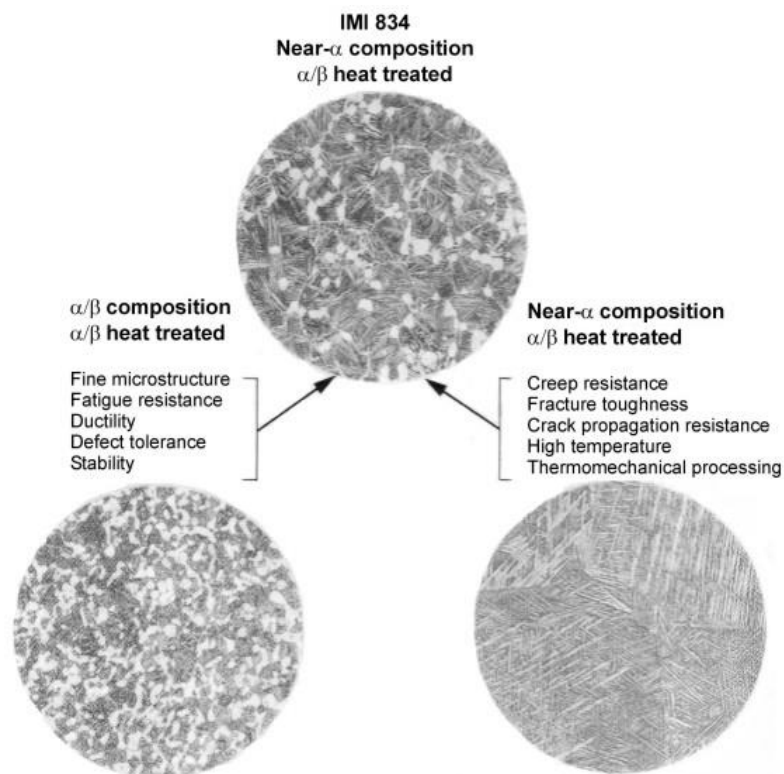


Figure 1.3 Composite optical micrographs illustrating the design rationale of Ti-834 (formerly IMI 834) whereby through careful control during heat treatments the desired in-service bimodal microstructure can be achieved [13].

1.1.3 $\alpha + \beta$ alloys

Ti-6Al-4V (Ti-64) is the most tested and developed titanium alloy in production and is widely used within the aerospace industry. For the last 60 years bulkheads, which are found within the middle section of military aircraft, are commonly constructed from a single piece of Ti-64 that is initially forged to shape and then extensively machined (>95% material is removed) [4]. $\alpha + \beta$ alloys are very versatile materials and can be used in conditions up to 300°C. A wide range of microstructures can be produced, depending on their processing route. Thermomechanical treatment with respect to the β transus has the most dominant effect as discussed below.

- Super β transus forge:
 - Followed by a slow furnace cool; this cooling process gives time for α grains to grow at prior β grain boundaries in a lamellar type formation. Consisting of solute rich retained β separated by intergranular α plates all within the shape of the prior β grains.
 - Slow air cool; due to the uneven nature of air cooling less grain boundary α forms and the lamellar structure grows with more variation within each prior β grain.
 - Medium air cool; leads to the formation of a basket weave structure of lamellar α .
 - Rapid air cool; results in a Widmanstatten array of α plates in prior β grains
 - Water quench; creates a fully martensitic structure
- Sub β transus forge:

This forging process take place within the $\alpha + \beta$ two phase region. Since the β transus temperature has not been crossed the material the retains its primary α grains which pin the β grains, preventing excessive growth

- Forge temperature high in $\alpha + \beta$ region followed by an air cool will result in a ‘bimodal’ structure consisting of primary α and transformed β . The volume fraction of primary α is reduced significantly due to the high forging temperature the transformed prior β grain regions forms into fine secondary lamellar α and solute enriched β .
- A medium forging temperature within the $\alpha + \beta$ region and followed by an air cool results in an equiaxed 50:50 structure of primary α and fine transformed β structure.

A medium forging temperature route is used for $\alpha + \beta$ alloys used for superplastic forming operations since a suitably fine grain microstructure can be created.

1.1.4 Near β alloys

Near or metastable β alloys have compositions to the right of martensitic start/finish (M_s/M_f) (Figure 1.2). Near β alloys are widely used within the aerospace industry for structurally critical components due to their high strength capabilities, created by age hardening steps which produce a fine scale α precipitate within the β phase matrix. Landing gear forgings for aircraft are constructed out of near β alloys and are required to have high strength, exemplary resistance to fatigue crack propagation and high fracture toughness. Common near β alloys are Ti-10-2-3 (Ti-10V-2Fe-3Al) and Ti-5553 (Ti-5V-5Mo-5Al-3Cr). If a near β alloy is processed above the β transus ($>\sim 800^\circ\text{C}$), this leads to the dissolution of α and promotes excessive β grain growth and the structure becomes fully β . On quenching, even though the M_s line is not crossed, through a combination of residual stresses and low stability of β additions can lead to the formation of stress induced martensite during quenching. Processing at a lower forging temperature ($\sim 20^\circ\text{C}$ lower) below the β transus, the presence of a small volume fraction of primary α prevents excessive β grain growth. Near β alloys have high fracture toughness and high strength giving excellent properties against crack initiation and propagation. After formation, the retained β is metastable and with subsequent aging in the range $450\text{-}550^\circ\text{C}$ a fine α scale can be precipitated giving enhanced strength properties.

1.1.5 β alloys

While β alloys offer the highest strength-to-weight ratio of any titanium alloy, they are nonetheless higher in density compared to other alloys, with typical densities in the order of $4.7\text{-}4.98\text{ g/cc}$ with ultimate tensile strength levels in the range of $1517\text{ - }1586\text{ MPa}$ [7]. β titanium alloys such as Ti-13V-11Cr-3Mo have been available since the 1950s, the most notable application being the SR-71 Blackbird (service from 1964 to 1998) in which 93% of the aircraft was fabricated from titanium alloys, with the majority being β alloys. More recently, the most significant applications of β alloys is for biomedical applications where low-modulus β alloys have been developed specifically for orthopaedic application, their aim being to decrease the elastic modulus difference between natural bone ($10\text{-}30\text{ GPa}$) and the implant material, thereby promoting load sharing between the bone and the implant [14]. β alloys are generally not considered for cryogenic or elevated temperature applications since they exhibit a ductile to brittle transition below $\sim 0^\circ\text{C}$ and have poor creep capabilities, especially at high temperature [15]. One disadvantage is that they are unweldable. The mechanical properties of β alloys are substantially influenced by the underlying microstructure, with grain size or effective structural size (β colony) determining the materials strength as seen for α alloys. Interstitial elements act as potent solid solution strengtheners (O, N, C) and are deleterious to ductility.

1.2 Thermomechanical processing

Thermomechanical processing (TMP) of titanium alloys can be divided into two groups;

- (1) Primary working and secondary mill operations; Ingot breakdown with hot rolling or forging for producing usable shapes.
- (2) The optimization of mechanical properties, through microstructure control during the different stages of TMP [16].

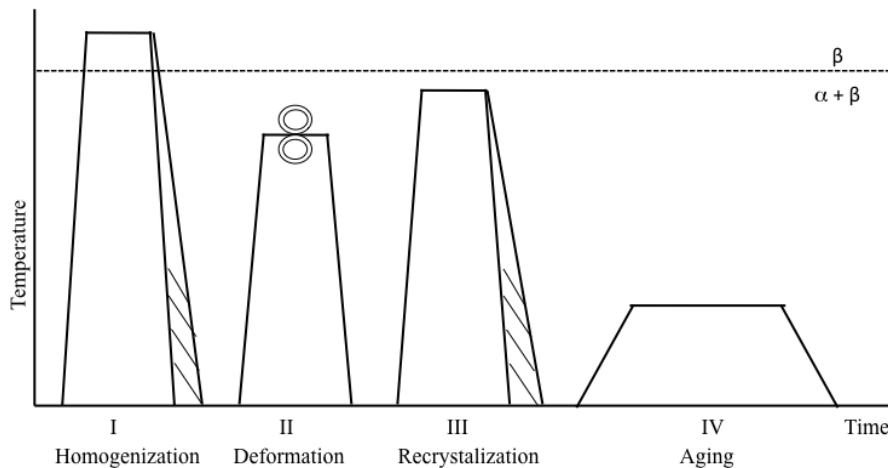


Figure 1.4. Schematic processing route diagram illustrating the 4 processing steps required during production to produce a bimodal microstructure for $\alpha + \beta$ titanium alloys [4].

The schematic shown in Figure 1.4 outlines the typical processing route for a bimodal microstructure, which begins with **homogenization** that occurs after the remelting process, this occurs well above the β transus temperature resulting in a fully β microstructure. Due to the high temperatures associated with their formation β grains can grow to the order of several millimeters. The size and crystallographic orientation of these large β grains behave as a type of ‘finger print’ for the alloys since the formation α colonies grow at β grain boundaries and are influenced by the β grain orientation. For some alloys this effect is prevalent and can be observed as macrozones [17]. The transformation step from α to β is controlled by the Burgers relationship. **Deformation** usually occurs below the β transus within the $\alpha + \beta$ region, the lamellar structure is plastically deformed. The deformation promotes grain refinement and allows for the material to be processed into bar stock material, which is of suitable size for the customer. For these alloys that are susceptible to forming macrozones the deformation stage will also be carried out above the β transus to allow the breakdown of these large grains. Stages I and II are carried out by the material

supplier during the primary forging steps. The material at this stage is categorised as being in the ‘as-forged’ condition.

During the **recrystallization** step it is important to optimise the operational temperature in order to precisely control the volume fraction of recrystallized equiaxed primary α (α_P), which grow from ‘triple-points’ between the β grains. The nature of the cooling rate will also determine the width of the individual α lamellar as well as the colony size of α lamellar structure, which form within the prior β grains. The control of operating time and temperature of the material through the final **ageing** is step is essential since this step establishes the material properties. The fracture toughness of $\alpha + \beta$ alloys is controlled by the size of the α grains within the α colonies, fracture toughness can be enhanced by increasing the quantity of α -lamellar due to crack growth being hindered by the presence of multiple grain boundaries [18].

1.2.1 The $\beta \rightarrow \alpha$ phase transformation and texture development during forging

During TMP when α , near α and $\alpha + \beta$ alloys are cooled from above the β transus temperature, a number of phase transformations can take place. These cooling transformation are dictated the chemical composition of the β phase and the cooling rate from above the β transus temperature. As a result of these factors, the transformation from β to α may involve either singularly or a combination of the following; a rapid martensitic transformation, or massive mechanisms of diffusion driven grain nucleation and growth. In many cases the BCC β phase transforms to the HCP α phase whilst obeying the following Burgers orientation relationship [17].

$$\begin{aligned} (0001)\alpha // \{110\}\beta \\ \langle 1\bar{2}10 \rangle \alpha // \langle 111 \rangle \beta \end{aligned} \qquad \text{Equation 1.1}$$

During a Burgers type transformation, a single β orientation will give rise to a maximum of 12 distinct α orientations or variants. This range of inherited α orientations is a feature of the transformed microstructure and it has been shown, through the use of software developed at the University of Sheffield, that prior β grain orientations, can be subsequently reconstructed. Davies [19] was able to further illustrate using the “ β reconstruct” software how the development of the crystallographic texture is determined by a type of material “DNA” that is set during the prior forging steps.

During forging, generally occurring within $\alpha + \beta$ region, the billet is subjected to a multiple step cogging procedure that sees the billets cross sectional area being reduced considerably thus ensuring the adequate refinement of the microstructure. Cogging involves the material being passed through a variable open die forge which

can accommodate the many shape changes that are required during refinement. The resulting billet is therefore subjected to a non-uniform strain distribution. For example, Wilson *et al.* [20] showed via finite element modelling of Ti-64 that cogging produces strain as high as 2 near the surface, decreasing to about 1 in the centre, which had a direct impact on the fraction of recrystallized α . In addition Davies *et al.* [21] and Nasserri [22], using EBSD and neutron diffraction on Ti-834 billet and Ti-6246 billets respectively, showed that crystallographic texture also varied throughout the cross-section and showed significant sensitivities to the forging operation.

Analysis of the orientation data obtained by Davies [19] and Nasserri [22] shows that there are regional texture variations across the billet, generated during the forging stages. These variations are caused by the anisotropy of the HCP crystal, which when loaded parallel to the HCP c-axis displays the highest elastic modulus and in turn the highest resistance to plastic deformation. During forging the microstructure changes allow for the c-axis to re-orientate such that it is positioned perpendicular to the maximum applied load, thus allowing deformation to occur more easily. The orientation of the c-axis' alignment is governed by the non-equal strains imposed around the billet axis during the forging process. To accommodate the reduction in cross section, the near β alloy Ti-6246 [22] adopts an extruded core and compressive mandrel morphology, similar to that observed in Ti-64 [23]. The core and mandrel condition is however not displayed in the near α alloy Ti-834 [19], the schematic shown in Figure 1.5 shows a resulting orientation alignment of Ti-834, which throughout its interior is significantly dominated by the reduction of the historical long axis of the prior billet.

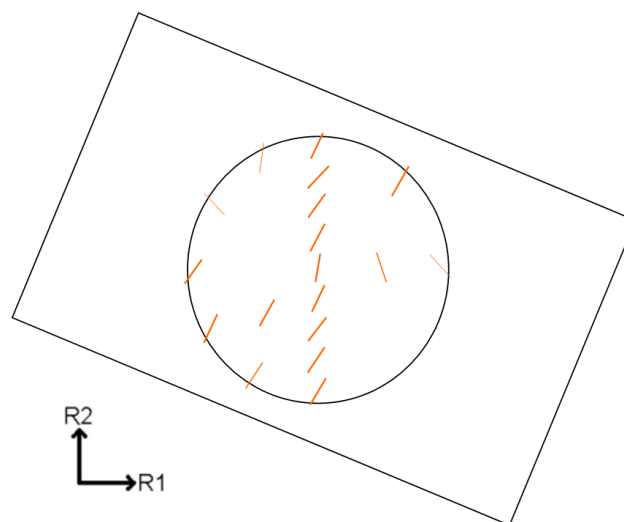


Figure 1.5 Proposed orientation of the initial rectangular cross-section of the intermediate billet with respect to position of the final round billet. Coloured lines indicate the regional average crystallographic alignment of the basal plane in the transverse plane [19].

Microstructure analysis of a billet cross section carried out by Bescond *et al.* [24] revealed using ultrasonic imaging two high noise bands separated by 90°. These features corresponded to the location of macrozones of similarly orientated material. The process history of the material analysed by Bescond *et al.* [24] had been forged from a square section to a circular billet, thus resulting in the two equally strong signal peaks.

During the production of high quality titanium alloys for structurally critical aerospace components, the material will have originated from ingots that have undergone multiple vacuum arc re-melting (VAR) steps. This process, which is time and energy consuming, ensures the material is free of unwanted impurities and inclusions which if undetected could pose a serious risk to a component's life. Furthermore, to ensure the material has the desired microstructure and crystallographic properties throughout the billets cross section, the VAR ingots are cast to be of sufficient enough size such that after forging the material is large enough to accommodate the component and that enough strain can imparted which drives grain refinement and reorientation. Lower cost or development materials are commonly produced through a single electron beam (EB) melt route. EB ingots are commonly smaller than those of full production VAR ingots and as such the material will inherently undergo a different strain path resulting in a reduced strain penetration. It is therefore important when studying billet material to have a clear understanding as to which processing routes have been used.

1.3 Deformation Mechanisms

Due to its inherent low symmetry as a result of the hexagonal close packed (HCP) crystal structure, the deformation modes of α -Ti are highly anisotropic. Deformation is consequently accommodated by the activation of a multitude of complex slip and twinning modes.

1.3.1 Slip

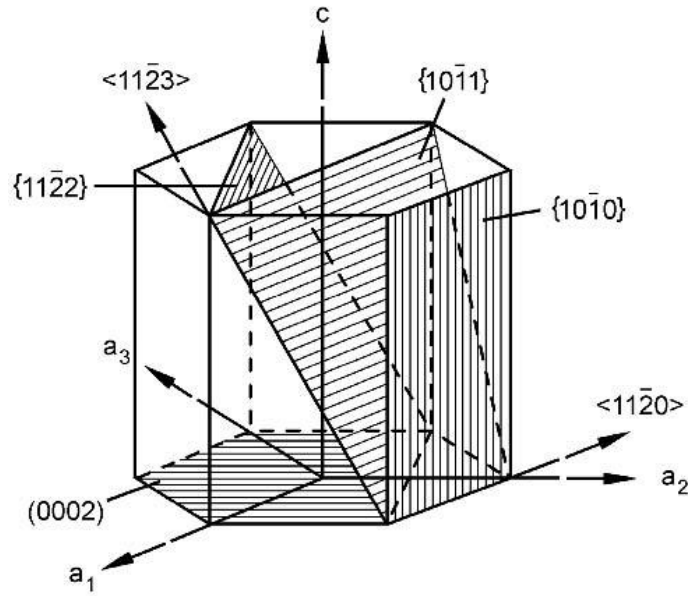


Figure 1.6 Basal $\langle a \rangle$ (0002), prismatic $\langle a \rangle$ $\{10\bar{1}0\}$, pyramidal $\langle a \rangle$ $\{10\bar{1}1\}$ slip systems, and second-order pyramidal $\langle c + a \rangle$ $\{11\bar{2}2\}$ slip systems in HCP materials [4].

The schematic HCP crystal given in Figure 1.6 illustrates the different slip planes and corresponding directions for α -Ti these are also given in Table 1.1. For homogeneous plastic deformation to occur the von Mises criterion states that a minimum of five independent slip systems are required [25]. Titanium however, for which the principal deformation mechanisms are $\langle a \rangle$ type, basal (0002), prismatic $\{10\bar{1}0\}$ and pyramidal $\{10\bar{1}1\}$ all slip with along the $\langle 11\bar{2}0 \rangle$ Burgers vector, which can only produce a total of 4 independent slip systems thus falling short of the prerequisite. Therefore to fulfil this requirement a $\langle c + a \rangle$ Burgers vector needs to be activated.

Table 1.1 Slip systems of titanium [4].

Slip system type	Burgers vector type	Slip direction	Slip plane	No. of slip systems	
				Total	Independent
1	\bar{a}	$\langle 11\bar{2}0 \rangle$	(0002)	3	2
2	\bar{a}	$\langle 11\bar{2}0 \rangle$	$\{10\bar{1}0\}$	3	2
3	\bar{a}	$\langle 11\bar{2}0 \rangle$	$\{10\bar{1}1\}$	6	4
4	$\bar{c} + \bar{a}$	$\langle 11\bar{2}3 \rangle$	$\{11\bar{2}2\}$	6	5

Titanium's secondary phase β can deform much more homogeneously compared to α due to β having a body centred cubic (BCC) structure. The major deformation modes exhibited by the β are; slip, twinning and stress induced martensite. Similarly to α -Ti, twinning may occur in addition to slip, though this is limited to the single phase state [4] with slip becoming the only observed deformation mechanism at high solute contents.

1.3.2 Mechanical twinning

Under an imposed strain the formation of a twin within a HCP metal arises due to an inadequate number of available slip systems. The nucleation of a twin is not thermally activated; rather, it will occur at a point of high stress concentration, however once a twin has nucleated it has been shown that there is a significant temperature range over which twins grow more readily than slip can propagate. This is due to partial or twinning dislocations not becoming as readily immobilised as lattice dislocations [4]. Therefore twinning can be regarded as a more regulated process than is slip.

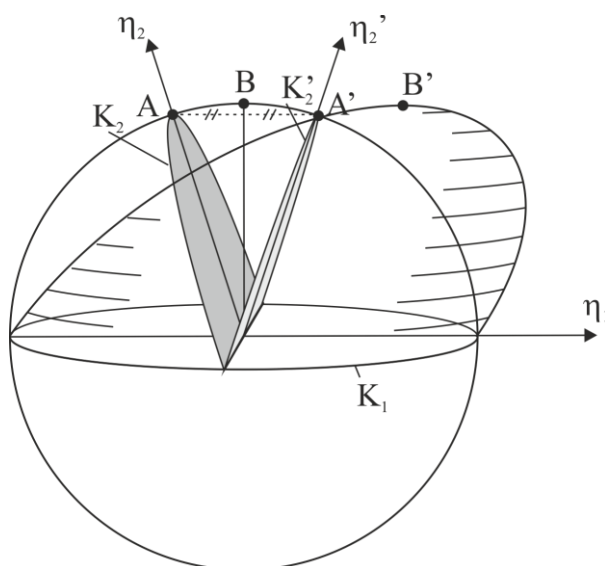


Figure 1.7 Schematic illustration demonstrating the association between the parent material and that of the twin, using the relationship between a reference sphere and twinning ellipsoid with each sharing a common plane K_1 . After Hall [26].

The process by which a twin is formed can be described using an example of a deformed sphere, as illustrated in Figure 1.7. The northern hemisphere represents the twinned material and the southern the parent. Through shear, the northern hemisphere is displaced about the equatorial plane and is referred to as the K_1 . The K_1 plane remains undistorted and is shared by both the northern and southern hemispheres. The shearing process remains homogenous with the atomic planes which are parallel to the K_1 forming reflections of one another. After shearing has occurred, another plane also remains undistorted and is referred to as the K_2 prior to the formation of the twin

and the K_2' after the twin has formed. Illustrated by the translation of point A to point B, the direction of shear during twinning occurs parallel to the K_1 along the line that is normal to the intersection of the K_1 and K_2 planes. The shear direction is referred to as η_1 [26].

Twins are most commonly defined by their K_1 shear plane, however to confidently identify a specific mode via a quantitative analysis method, such as EBSD, requires the prior knowledge of the relationship between the twin and its parent phase. This can be characterized by an angle of rotation about a specific axis. The relationships given in Table 1.2 have each been spatially confirmed (and indexed) by transmission electron microscopy (TEM) which allows the identification of the misorientation angle and the plane on which the axis of rotation occurs [27]–[29].

Table 1.2 Twinning systems in α titanium [28], [29].

Twin Plane	Shear Direction	Misorientation θ About $\langle uvw \rangle$	Twinning type
$\{10\bar{1}2\}$	$\langle \bar{1}011 \rangle$	$84.78^\circ \langle 2\bar{1}\bar{1}0 \rangle$	tension
$\{11\bar{2}1\}$	$\langle \bar{1}126 \rangle$	$35.1^\circ \langle 10\bar{1}0 \rangle$	tension
$\{11\bar{2}2\}$	$\langle \bar{1}123 \rangle$	$64.62^\circ \langle 10\bar{1}0 \rangle$	compression
$\{10\bar{1}1\}$	$\langle \bar{1}012 \rangle$	$57.42^\circ \langle 2\bar{1}\bar{1}0 \rangle$	compression (above 400°C)
$\{1\bar{1}24\}$	$\langle \bar{2}243 \rangle$	$76.66^\circ \langle 10\bar{1}0 \rangle$	-
$\{11\bar{2}3\}$	$\langle \bar{1}122 \rangle$	$86.98^\circ \langle 10\bar{1}0 \rangle$	-
$\{5\bar{6}1\bar{3}\}$	$\langle 41\bar{5}3 \rangle$	$65^\circ \langle 33\bar{6}3 \rangle$	“i” twin tension

For the given twinning types reviewed in Table 1.2 the corresponding description for each twin system refers to whether the activation of the mode accommodates either an extension or compression along the c-axis, not the applied stress that has activated the twin system. Diiorio *et al.* [29] documented the existence of the $\{5\bar{6}1\bar{3}\}$ tension type twin when analysing Ti–64 at 20 K under monotonic loading, by virtue of its K_1 plane being of such high order it is deemed to be irrational [30] and as such Diiorio *et al.* [29] referred to them as “i” twins. “i” twins were attributed to being a major damage precursor at a microscopic scale with $\{10\bar{1}1\}$ twins being identified within the interior

of the $\{5\bar{6}1\bar{3}\}$ twins. These secondary twins subsequently accommodated 10% strain, this was observed to lead to further internal stresses which promoted the $\{5\bar{6}1\bar{3}\}$ twin plane debonding from the matrix forming microcracks and voids. Diiorio *et al.* [29] reported that this was first time the $\{5\bar{6}1\bar{3}\}$ twin had been experimentally observed, which under such circumstances is correct. Previous work undertaken by Thomas [31] and later Davies [19] studying the forging characteristics of Ti-834 also identified non-standard twins through EBSD analysis, though were unable to completely confirm their characteristics using TEM and as such the twins remain unresolved. On reflection of Thomas' [31] and Davies' [19] data using the twinning relationship given in Table 1.2 for the "i" twin, the author has identified that their non-standard twins were in fact "i" twins.

Within the literature, studies that characterise the deformation characteristics of HCP polycrystalline materials most commonly detail the behaviour seen in a single-phase condition, which for titanium can be obtained using commercially pure (CP) titanium. A fundamental knowledge gap does however exist, covering the microstructure dependencies on the resulting deformation behaviour of multiphase ($\alpha+\beta$) material, when subjected to deformation.

Studies have shown an unsurprising link between the starting microstructure of a metallic system and its behavioural characteristics, during and after (being subjected to) deformation. However, knowing specifically which parameters play the most significant role in determining the severity and type of resulting deformation is still unclear and is currently being debated. Under a suitable loading environment, α titanium may deform via a number of deformation modes, the activation of which is intimately connected to dislocation activity; slip requires dislocation movement along a specific plane whilst twinning requires the cooperative movement of dislocations in planes parallel to the twinning plane.

A significant proportion of this investigation will concentrate on the mechanisms involved during the formation of mechanically induced twins. Within the literature, twinning is generally studied at comparatively lower strain rates to those experienced during machining, this is due to system limitations associated with data acquisition during high strain rate experiments. However, a common method used to encourage twin formation in a laboratory environment involves deformation at high strain rates and low temperatures, thus reducing the amount of time and driving force available for long-range dislocation movement. For HCP materials such as titanium, lowering the operating temperature can have a substantial effect on the resulting deformation behaviour, due to their inherent sensitivity to high strain-rate and temperature [32]–[35]. Twinning is a prominent deformation mode in pure titanium though its

propensity can be significantly reduced with appropriate α stabilising alloying additions, such as Al.

1.3.3 The sensitivity of deformation to microstructure variations in polycrystalline materials.

It is important to understand what microstructure factors influence the resulting deformation. There are common characteristics shared across many different metallic system types, body centred cubic (BCC), face centred cubic (FCC) and hexagonal close packed (HCP), that similarly dictate the type, size, shape and frequency of activated deformation modes. Twinning, the mechanics of which are outlined previously (§1.3.2), plays an important role in permitting further deformation to occur via slip. It has been observed for titanium that the presence of activated twinning contributes little to the total plastic strain within the material. However, this is not true for all HCP materials such as magnesium, which deforms readily via twinning and the activation of which can contribute a substantial shape change to the system [36], [37]. The deformation characteristics of titanium show common behavioural trends to those observed within BCC systems where twinning usually occurs prior to macro-yielding. For BCC metals, which have a much lower strain-rate sensitivity (but higher work hardening ability), twinning often occurs after significant plastic deformation, and in turn further raises the corresponding stress level [35].

1.3.4 Deformation characteristics related to material grain size

Armstrong *et al.* [38] identified for BCC materials a size effect relationship between the dimension of the parent grain and the propensity for twin formation. This relationship has however been contested for other metallic systems, with contradictory observations being made throughout the literature relating grain size and twin formation. For a twin to nucleate, a dislocation source is required, in many cases grain boundaries act as a prime location for twins to be generated, since they possess a high density of dislocations. Qualitative observations reported by Ghaderi *et al.* [37] state that for titanium, a consistent trend showed that larger grains possess a greater area of grain boundaries upon which twins can nucleate. The author does however dispute this justification, since the ratio of grain boundary surface area to grain volume will in fact increase with decreasing grain size. A more quantitative investigation carried out by Capolungo studying the nucleation and growth of twins in zirconium [39], showed there was a weak dependence of grain size on the propensity of twins occurring. Capolungo concluded that large and small grains were equally likely to undergo twinning. Grain size was also shown to have no effect on the resultant twin thickness. It was however reported that a larger number of individual twins were observed within larger grains, suggesting that grain crystallographic

orientation plays a significant role in determining both the deformation type and severity.

1.3.5 The role of the applied stress/strain in conjunction with the underlying crystallographic orientation on the resulting deformation.

Constitutive models describing the flow behaviour of metallic systems have been constructed and further modified over recent years. These studies are generally focused on describing the multiple processes that are taking place whilst the material undergoes deformation, permitting the development of constitutive equations that can more accurately predict behaviour. As a first order approximation, the models generated by Zerilli and Armstrong [40] demonstrated that the constitutive response of BCC materials could be used to represent the behaviour of α titanium (HCP structure). Extended modified Zerilli-Armstrong models have since been adapted to account for the shear instabilities that are observed during the deformation of HCP structures [41]. Constitutive equations such as these are used as the foundation for computational finite element simulations. Generally once a constitutive model has been created, the material is often considered to be a 'black box' whose behaviour is determined using macroscopic behavioural trends. For the next generation of computational finite element simulations to offer the user a greater insight into the mechanisms that are taking place on a microscopic level, an understanding needs to be developed addressing how the underlying microstructure relates to the resulting deformation.

The most significant influencing factor relating the microstructure to the resulting deformation is that of the local underlying crystallographic orientation and its relative position to the applied stress. It has been shown that the formation of a twin is governed by the texture of its parent grain. Song *et al.* [42] found whilst studying the stress-strain response of zirconium over a range of strain rates that the nucleation of a twin always started within a grain having a K_1 plane close to the maximum local stress plane. The relationship between crystallographic orientation and an applied stress is often investigated under controlled monotonic loading conditions, allowing the user to apply a controlled load to a sample of known orientation. The relative coincidence between the position and direction of an applied macroscopic loading condition to that of a specific deformation plane is measured in terms of a Schmid factor [43]. Schmid factors can be used as a first order approach for determining how likely it is for a specific deformation mode to activate, with higher values relating to a condition that satisfies deformation along a specific plane of interest. A detailed explanation covering the principles and methodology used throughout this investigation to calculate Schmid factors is provided in §3.7.2.

The work presented in Figure 1.8, obtained by Beyerlein *et al.* [44], does show how a significant number of grains display twinning even though their respective Schmid factor values, calculated using an assumed macroscopic stress state, are comparatively low. The histogram shown in Figure 1.8 compares the calculated Schmid factor within all grains and for individual grains displaying evidence of twinning. For the grains that display $\{10\bar{1}2\}$ type twinning, the majority have a Schmid factor approaching the maximum value of 0.5. Considering Beyerlein *et al.* [44] used highly textured material, which evidently showed a predisposition for twinning with a significant proportion of all of the grains showing high Schmid factor values. The increasing resulting fraction of deformed grains however, shows how the activation of a twin is governed by the specific orientation of the underlying grain and that the twinning is not a random occurrence.

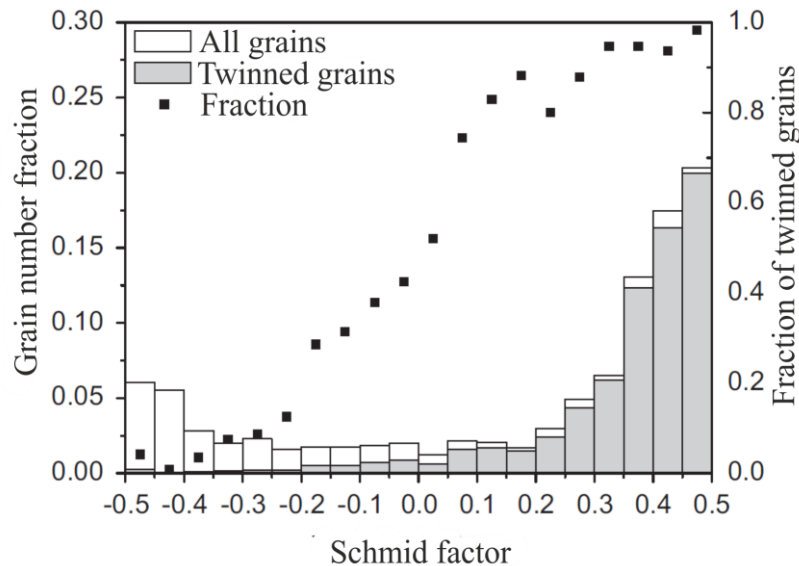


Figure 1.8 Histogram comparing the distribution of all grains (white bars) and twinned grains (gray bars) as a function $\{10\bar{1}2\}$ type twinning, with the Schmid factor for each grain determined by in EBSD. The marks represent the ratio between the gray and white bars as well as indicating the fraction of twinned grains, after [44].

It is important to note that twin variants that become detectable using EBSD are only discernible following significant growth has occurred following nucleation, therefore, the two processes cannot be individually investigated using visual type inspection. The work presented by Beyerlein *et al.* [44] and further supported by Capolungo *et al.* [39] suggests that the nucleation and growth of a twin are governed by different stress states; whereby nucleation and variant selection are governed by localized stress states between grain boundaries, whereas growth is dictated by the macroscopic stress state. Consequently grain orientation affects twin growth more strongly than twin nucleation. As a result of this, additional twins displaying a lower Schmid factor (that

happened to have nucleated due to localized high stresses) are not likely to grow as thick as the higher rank variants. Owing to the time dependent kinetics of twin growth, it has been shown that needle like twins are generated within a high strain rate environment [45], [46].

Localised variation in stress state caused by potential miss-matching of neighbouring grain orientations was investigated by Capolungo *et al.* [39] to determine whether or not specific neighbour disorientations altered the propensity for twins to nucleate. The rationale being, that grain boundaries with relatively high disorientation would typically possess a higher density of dislocations. This part of the investigation by Capolungo *et al.* [39] proved inconclusive, with increasing disorientation differences displaying a minimal preference to twin nucleation; a further contradictory observation suggested more twins had nucleated at grain boundaries with smaller disorientation angles. However, as Beyerlein [44] demonstrated, the local crystallographic orientation relative to the macroscopic stress state has a significant effect in determining whether or not a grain will deform. Grains that have low disorientation grain boundaries with their neighbours must by definition be similarly orientated. Since twins are observed, their parent grain must therefore be favourably orientated for twin activation and would be expected to twin regardless of the presence of the grain boundary.

Meyers *et al.* [35] presented the following constitutive twinning model, as shown in Figure 1.9, by which deformation may transfer across a grain boundary; for this to occur, a dislocation source is required. For this example, dislocations are generated within a grain from a Frank-Read or Köhler source and subsequently pile-up at a grain boundary. The magnitude of the dislocation pile-up is determined by the distance between the source and barrier, and the applied stress. The pile-up will generate a stress concentration at the grain boundary that will increase as the pile-up gets longer. The local stress concentration that is generated in front of the barrier is equal to the product of the applied stress and the number of piled up dislocations exists. If the energy for twin nucleation is less than that required for dislocations to overcome the grain boundary, the dislocation pile-up will provide the energy necessary to nucleate a twin in the adjacent grain. The amount of energy required to nucleate a twin will strongly depend on the crystallographic orientation of that specific grain.

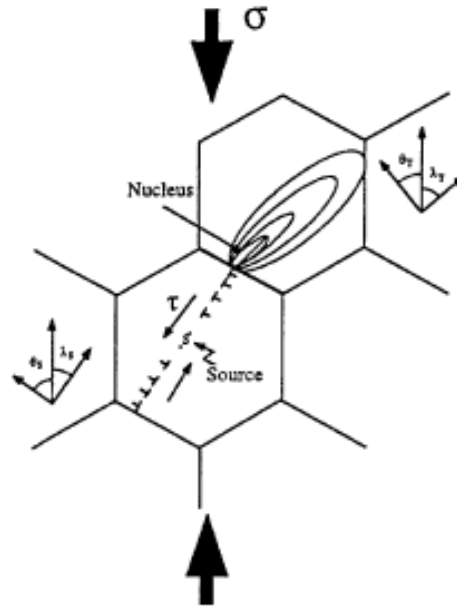


Figure 1.9 Frank–Read or Köhler source creating a pile-up at a grain boundary thus acting as a nucleolus for further deformation to occur within a neighbouring grain [35].

Meyer’s model [35] was originally quoted as a theory for a BCC system, however deformation features have been observed within a HCP system following a similar type of behaviour. Wang *et al.* [47] observed the presence of twins whose nucleation had been attributed to the transfer of slip across grain boundaries in CP titanium. Here it was found that prismatic slip within a grain can stimulate $\{10\bar{1}2\}$ type twins in neighbouring grains. Critical grain disorientation combination requires each of the two deformation systems to have their plane normal and Burgers vector close to one another, thus facilitating deformation transmission across the grain boundary. Within the analysed samples slip-stimulated twinning was estimated to account for a third of the total induced twins. In a further study, Wang *et al.* [48] also observed the nucleation of paired twins at grain boundaries in CP titanium. Here the presence of twin pairs at a grain boundaries was attributed to be either from; a twin impacting a grain boundary thus stimulating the nucleation of an accommodating twin in the neighbouring grain, or from slip-stimulated twinning. Or alternatively, their formation may be the result of a condition that encouraged twins to mutually nucleate at the same location on the grain boundary and grow into their respective parent grains.

1.4 Summary

Within this section the metallurgical background into titanium has been introduced detailing alloy classification, the role of common alloying additions, thermomechanical processing routes and the crystallographic characteristics of Ti-834, Ti-64 and Ti-6246. A significant proportion of this investigation will concentrate on the deformation characteristics of titanium during machining. Therefore, the fundamental deformation mechanisms have been introduced. These include slip and mechanical twinning. A fundamental knowledge gap does however exist, covering the microstructure dependencies on the resulting deformation behaviour of multiphase ($\alpha+\beta$) materials when subjected to deformation.

Chapter 2 - The mechanics of machining

2.1 Cutting force relationships

Generally for the purpose of ease of modelling and force calculation, the mechanics behind metal removal are commonly simplified for both turning and milling to a basic model of two-dimensional machining (orthogonal cutting), as shown in Figure 2.1. During milling however, which employs the use of a rotating tool, the size of the chip is immediately governed by the speed of rotation and the feed per tooth. For turning, which will be the focus of this investigation, the tool remains in constant contact with the workpiece and an unbroken chip may be formed. The key features of the machining operation that are highlighted in Figure 2.1 are outlined as follows; **cutting direction** dictates the forward progression of the tool, usually at a fixed speed (V_c) relative to the test **workpiece**, commonly for modelling and force calculations the **Tool** is usually of fixed geometry and is unaffected by tool wear and has an assumed tool edge radius that is infinitely sharp, the **rake face** is the forward portion of the tool that is in contact with the chip, the contact length of the chip against the rake face can change depending on the workpiece material and machining parameters, the **flank face** of the tool remains in sliding contact with the workpiece and is susceptible to wear at the cutting tip, the **chip** is removed from the workpiece during the machining operation and can adopt a range of chip types; continuous, discontinuous and segmented, the **chip thickness** is dictated by the shear plane angle, the force imposed by the tool onto the workpiece create intense shearing action on the metal ahead of the tool that becomes concentrated within the **shear plane** thus accommodating the shape change into the chip, during orthogonal cutting trials the **uncut chip thickness** relates to the instantaneous feed rate of the cut relative to the surface of the proceeding material ahead of the tool.

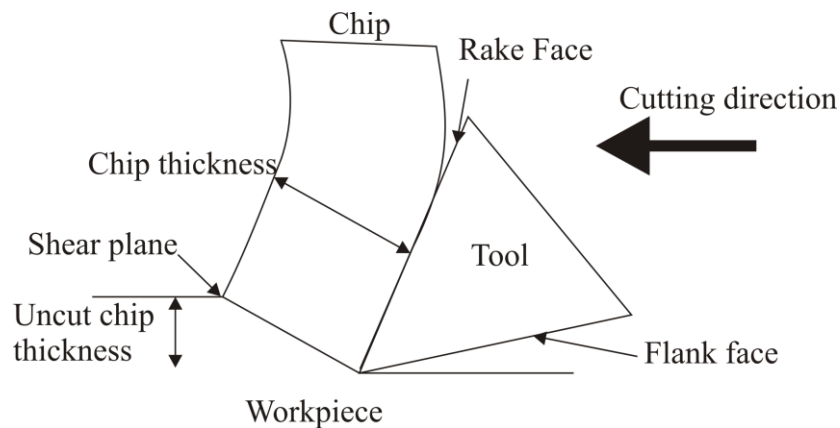


Figure 2.1 Schematic illustrating the key machining features of an orthogonal cutting arrangement. After Dieter [49].

A simple model of two-dimensional machining (orthogonal cutting) is shown in Figure 2.2(a), during the cutting operation the tool progresses over the workpiece at a constant cutting speed (V_c). Whilst in contact with the material the metal in the chip is severely deformed within a localized shear plane region in the vicinity of AO, which is inclined with a shear angle (ϕ). The relationship between the uncut chip thickness (t_1) and the shear angle (ϕ) dictates the chip thickness (t_2), cutting with a large shear angle (ϕ) will therefore result in a thin chip. The chip thickness ratio, also known as the cutting ratio $r = t_1 / t_2$ can be determined and typically equals $\sim r = 0.5$. The clearance angle, also known as the relief angle (θ) of the flank face and the rake angle (α) are controlled by the tool holder (θ). Considering in reality all two-dimensional orthogonal cutting trials must have a fixed third-dimension, (ω) corresponds to the depth of cut (DOC) / the width of the cutting material.

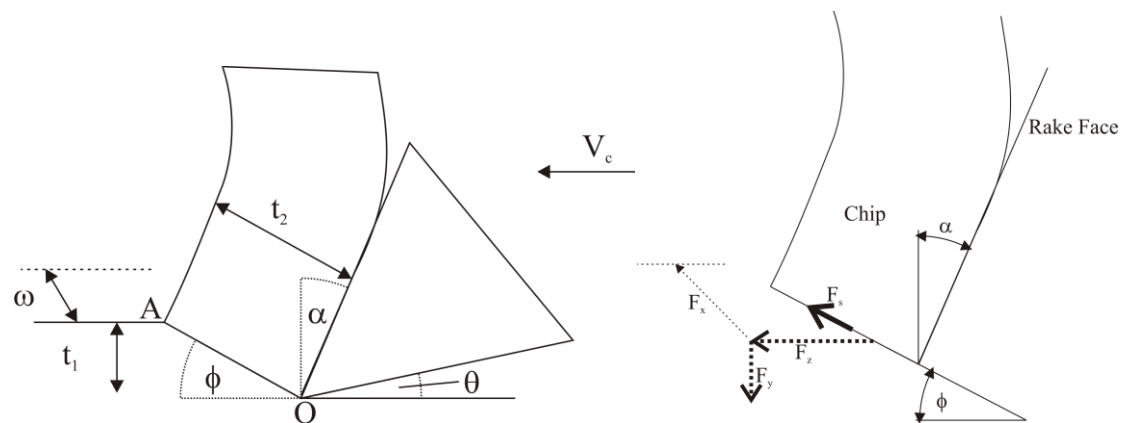


Figure 2.2 Schematic diagrams of the simple two-dimensional orthogonal steady state cutting operation illustrating (a) the key dimensional parameters and (b) the resulting stress components acting within the arrangement. After Dieter [49].

The schematic in Figure 2.2(b) illustrates the resulting stress components acting within the orthogonal arrangement. During orthogonal trials the instantaneous cutting forces recorded and defined as acting within the plane of the DOC - normal direction are; the normal force (F_x), the feed direction thrust force (F_y) and the cutting direction cutting force (F_z). Using these resolved forces in conjunction with the known machining parameters it is possible to determine, using empirical machining formulae as outlined by Merchant [50]–[52], the effective coefficient of friction (μ) (Equation 2.1) for the cutting environment, the resultant shear plane force (F_s) (Equation 2.2) and the average shear stress (τ) (Equation 2.3) of the material acting on the shear plane.

The coefficient of friction, (μ) ;

$$\mu = \frac{F_y + F_z \tan \alpha}{F_z - F_y \tan \alpha} \quad \text{Equation 2.1}$$

The resultant force occurring parallel to the shear plane (F_s) may be resolved as such;

$$F_s = F_z \cos \phi - F_y \sin \phi \quad \text{Equation 2.2}$$

Using the resultant shear plane force F_s the average shear stress of the material, (τ);

$$\tau = \frac{F_s + \sin \phi}{\omega t_1} \quad \text{Equation 2.3}$$

2.2 Material response of the workpiece during machining

Parametric machining trials generally fall to the realm of mechanical engineers who often employ a limited approach to workpiece integrity analysis. The most commonly used techniques for surface analysis stem from the methods detailed in manufacturing standards. Such standards indicate a pass/fail type criterion for values such as arithmetic mean surface roughness (Ra) or the presence (or size) of features such as cracks. Surface roughness measurements are typically acquired using stylus based or confocal laser scanning methods and surface cracks are usually assessed optically through the use of dye penetrant [53]. These analysis methods are non-destructive in nature and can be carried out on a component following manufacture prior to being put into service. The quality of a component's surface finish has been shown to directly influence its in-service performance with troughs and scratches offering sites that can accelerate fatigue crack initiation [54]. Bayoumi *et al.* [55] observed using aluminium fatigue test specimens a reduction in fatigue life with an increase in surface roughness (Figure 2.3) with samples of increase roughness being attributed to offer a larger number of sites for crack initiation. During their trials Bayoumi *et al.* [55] stated that fatigue is a surface-sensitive process and cracks will preferentially nucleate from the free surfaces of cyclically loaded material at stress raiser sites such as notches. Whilst using a displacement transducer to monitor the fatigue test regime Bayoumi *et al.* [55] was able to identify the respective number of cycles that were required for cracks to initiate, propagated and eventually rupture. The author feels it is important to note that Bayoumi *et al.* [55] did not include any further explanation into the mechanisms the microcracks formed nor included microstructural analysis into their properties.

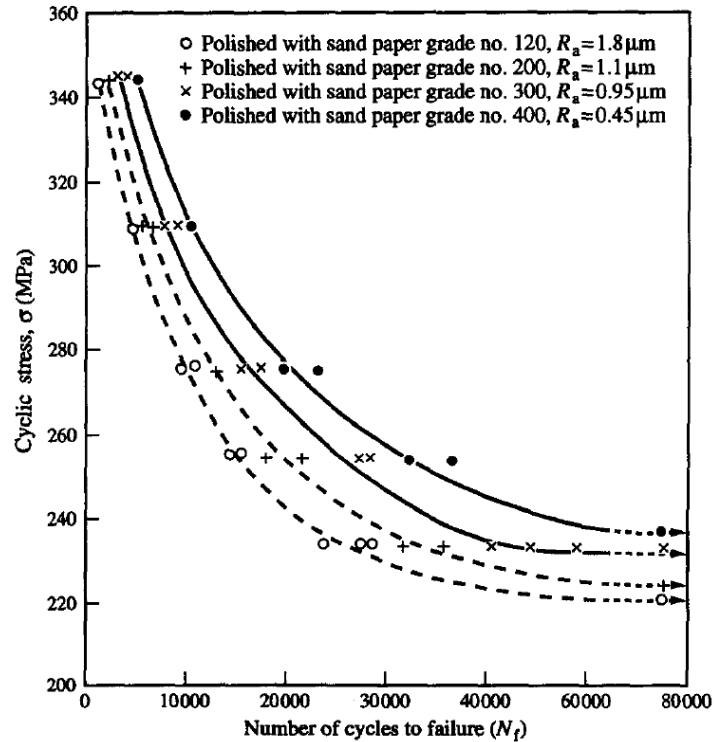


Figure 2.3 The effect of surface roughness on number of cycles to failure for aluminium fatigue test specimens [55].

Further ‘classical’ techniques used to characterise the subsurface material following machining, often employ the use of low magnification light microscopy or secondary/backscatter electron microscopy.

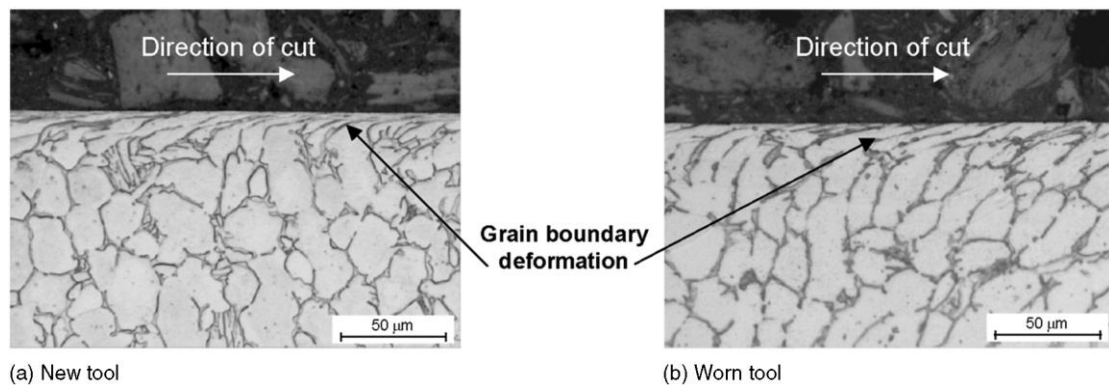


Figure 2.4 Representative optical micrographs of Ti-64 specimens with the resulting microstructure deformation, following a turning operation using (a) new tool and (b) prepared ‘worn’ tool geometries [56].

The light micrographs presented in Figure 2.4 are taken from an investigation carried out by Hughes *et al.* [56]; the images illustrate the resulting microstructure deformation typical of machined $\alpha+\beta$ titanium alloys. The characteristic plastic

flow-like swept microstructure offers the reader a clear visual representation of the magnitude of the imparted strain, with the severity of the deformation diminishing towards the bulk. As part of their investigation Hughes *et al.* [56] attempted to demonstrate how changes in cutting insert geometry influence the integrity of the workpiece. Through the use of new and pre prepared ‘worn’ inserts the severity of the imparted deformation was quantified.

The images shown in Figure 2.4 show indiscernible or at best vague differences between the two cutting environments, Hughes *et al.* offer no explanation for this nor do they present the differences between the two cutting geometries. The images do however demonstrate how the induced plastic deformation causes the microstructure to become almost indistinguishable at the uppermost layer of the material at this resolution. Within this region a common feature is often observed, shared between differing titanium alloy types and is also found when machining other metallic systems it takes a name coined by machinists due to its obvious nature “white layer”.

a 10 seconds

b 120 seconds

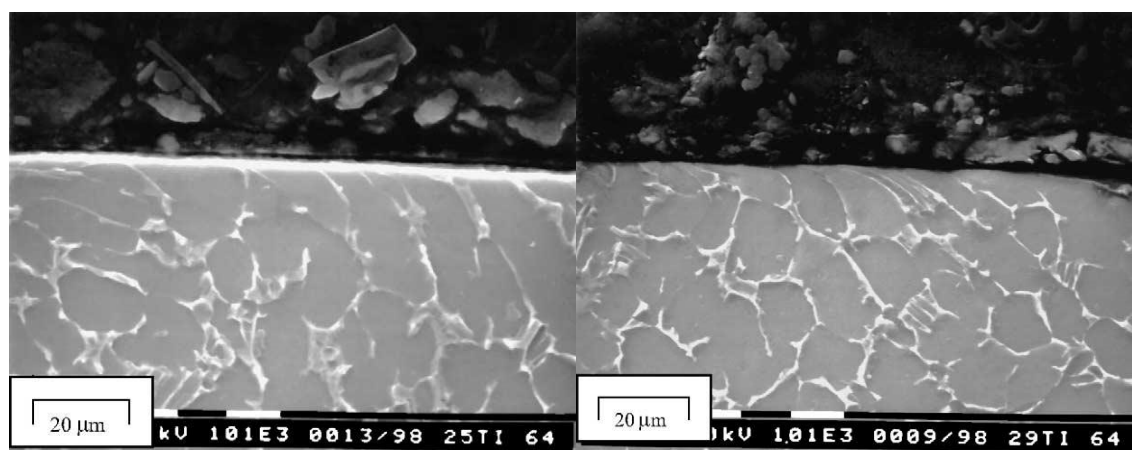


Figure 2.5 Deformed surface microstructure of Ti-64 following a machining operation at a cutting speed of $100 \text{ m}\cdot\text{min}^{-1}$, feed rate $0.25 \text{ mm}\cdot\text{rev}^{-1}$ micrographs obtained are representative of material following (a) 10 seconds and (b) 120 seconds of machining time (worn tool), under a dry cutting environment [57].

The backscatter electron micrographs in Figure 2.5 illustrate the deformation characteristics of Ti-64 following a high speed cutting regime ($100 \text{ m}\cdot\text{min}^{-1}$) under dry conditions and with a feed rate of $0.25 \text{ mm}\cdot\text{rev}^{-1}$. The images in Figure 2.5(a-b) are representative of the microstructure deformation after 10 and 120 seconds respectively [57]. Similarly to the work presented by Hughes *et al.* [56], Che-Haron *et al.* [57] demonstrated that the total amount of plastic deformation remains constant when comparing the effect of a new or worn tools. There are however other clear

differences with the resulting workpiece integrity. After 10 seconds the workpiece micrograph shows the presence of an immediate white layer plus a substantial amount of plastic deformation to a depth $\sim 20 \mu\text{m}$; the surface of the workpiece also appears smooth. Following 120 seconds of cutting it was reported that the tool appeared considerably worn and the trial was stopped, as previously noted the severity of the subsurface deformation appears similar to that seen after 10 seconds. However the workpiece surface is notably rougher, plus the white layer is absent. It is important to reiterate however that the trials conducted by Che-Haron *et al.* [57] were undertaken dry – with zero coolant or lubricant and dry cutting is considered to generate an more abusive cutting environment [58]–[60] compared to cutting with coolant as examined by Hughes *et al.* [56].

The phenomenon of white layer development (and the properties thereof) has drawn the attention of researchers and machinists who have well documented its existence. Knowledge of its formation is limited, though it is generally associated with higher speed (and therefore higher temperature) cutting regimes. The absence of a white layer in Figure 2.5(b) does introduce further confusion, however this could well be justified by the white layer spalling. What is known of its properties is that it consists of a recast hardened layer often only $5 \mu\text{m}$ thick, the presence of which is generally regarded as being detrimental to workpiece properties, since it can promote microcracking between itself and the bulk [61].

The influence of the machining process on the subsurface microstructure is commonly assessed using micro-hardness profiles. The hardness profiles presented in Figure 2.6 for the material cut with a $0.25 \text{ mm}\cdot\text{rev}^{-1}$ correlate with the micrographs in Figure 2.5. The surface hardness values were obtained by measuring the hardness directly on the machined surface, with the hardness-depth profile constructed in $\sim 50 \mu\text{m}$ increments in cross section, parallel to the cutting direction. The profiles demonstrate the subtle changes in micro-hardness found beneath the high-speed machined surface with each profile following a similar trend. Whereby following a rapid increase in hardness at the surface a substantial decrease has been recorded this is followed by a further abrupt increase in hardness, which as the profile progresses further towards the bulk then falls towards an average value. This phenomenon is usually attributed to a combination in thermal softening and work hardening of the workpiece material, whilst dry cutting the softening component can become more pronounced [57]. Work hardening generated by impingement of mobile dislocations either through the introduction of a further large number of dislocations or by the formation of mechanically induced twin boundaries [62]. Further explanations refer to the evolution of a severely plastically deformed (SPD) layer that can promote the

formation of a fine granular substructure [63], which in turn can affect the material's localized hardness. Other investigations for titanium have sought to ascertain whether or not a phase change has occurred within this region, driven by the high temperatures and high strain [64].

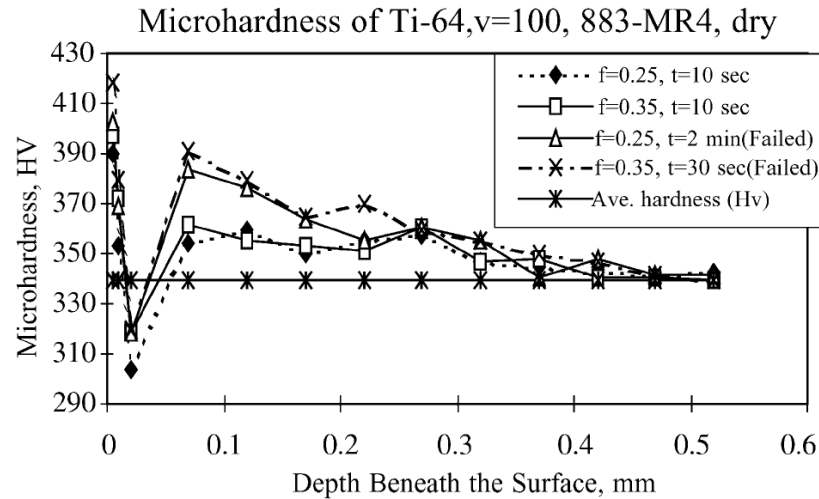


Figure 2.6 Microhardness profiles beneath the machined surface when machining Ti-64 with 883 insert at a surface speed of $100 \text{ mm} \cdot \text{min}^{-1}$ with a variable feed rate under dry cutting conditions [57].

The significant variation between the hardness values taken at the surface to those obtained just below the surface of the material, question the occurrence of the softening effect that has been widely reported. Warren *et al.* [65] investigated this phenomenon and found that the low microhardness values were the result of a systematic misinterpretation caused by an “edge effect” on the surface during a microhardness testing rather than surface softening. The edge effect occurs as a consequence of being too close to the edge of the test specimen, therefore resulting in the interaction volume of the indenter with the workpiece being reduced giving rise to reduced values in hardness. This was confirmed through the use of further nanohardness measurements on the very top and subsurface. It is important when analysing microhardness profile data such as the profiles presented in Figure 2.6 to appreciate the other inherent sources of error that are associated with the hardness data. Hardness testing apparatus relies upon the response of the workpiece material to the load applied via the indenter. When undertaking micro or nanohardness measurements the recorded values become increasingly more sensitive to material variables such as grain shape, grain size, volume fraction of phases and crystallographic texture. This gives rise to an inherently large amount of spread in the data, the profiles shown in Figure 2.6 that are typical of hardness profiles found in literature, only display average hardness values with little regard to how much spread

is actually generated by the sensitivities to the microstructure. This is inherently problematic when drawing conclusions, especially if the data has a wide spread. Rugg *et al.* [66] discussed the influence of crystallographic texture when collecting nanoindentation hardness profiles for mechanically ground Ti-64 samples; here it was found that if the orientation effect was ignored, there was a ~20% (± 1 GPa) variation in hardness. Thus by correlating the hardness profiles with the localized crystallographic texture a normalized profile can be created that demonstrates a more representative profile showing the effect of mechanical processing. The hardness values obtained will be indicative of the residual stress within the workpiece, with higher hardness values signifying a greater amount of imparted deformation which has resulted in work hardening; it can therefore be assumed that the residual stress within this region ought to also be greater. However the amount of residual stress can only be implied since for a given material (and corresponding condition) their specific work hardening rates may vary.

Many components before being put into service will often undergo further surface treatments such as shot peening or ball burnishing. These processes induce compressive residual stresses that reduce the rate at which a fatigue crack can propagate. It has been identified however, that a small compressive surface residual stress can remain following the machining of titanium alloys using typical machining parameters [67]. The progression towards high speed and high feed machining has drawn the attention of researchers investigating whether or not the machining environment can be tailored to also impart a compressive fatigue crack resistive layer [68], removing the need for further manufacturing processing steps. Furthermore machinists consider the role of imparted residual stress to be important when fabricating products with thin wall sections or parts with high dimensional tolerances, in order to reduce the effect of machining induced distortion. Through the use of finite element models cutting regimes can be simulated [69] to predict the amount of residual stress remaining. Complex cutting cycles can also be recreated in order to predict the amount a component may distort following machining [70], [71], allowing the machinist to tailor the cutting process. In order to obtain quantifiable residual stress data, profiling through X-ray diffraction (XRD) is most commonly used [72]. Other techniques are also used such as the method outlined by Wyatt *et al.* [68] that monitors the shape change of microhardness indentations, which occurs upon relief of residual stress manifesting in the form of thermal deformation, mechanical deformation or combined thermal and plastic deformation.

2.3 The influence of cutting parameters on fatigue life /residual stress.

It has been demonstrated that the fatigue life of a component is governed by many differing factors, as a result of this there is currently no reliable model that exists which can predict fatigue life that encompasses all of these variables. The relationship between a component's residual stress and the size of surface defects has been demonstrated for steel fatigue specimens where it was found that in the absence of a residual stress if the surface roughness values were in between 0.1 -2.5 $\mu\text{m Ra}$ the size of the defects would have a strong influence on the specimens fatigue life. If the surface had a $\text{Ra} < 0.1 \mu\text{m}$, cracks initiate predominately during a fatigue cycle at grain boundaries or at persistent slip bands. When workpiece surface roughness values are between 2.5–5 $\mu\text{m Ra}$, residual stress becomes a significant factor in determining fatigue life [71]. For machined samples, studies have shown that a compressive stress can always be generated below the surface [73] and that its magnitude increases with cutting speed. Sun *et al.* [74] showed for a series of milling trials on Ti-64 that the residual stress exhibited a maximum at $\sim 80 \text{ m}\cdot\text{min}^{-1}$ with a reduction at higher cutting speed being attributed to higher cutting temperatures, which leads to significant thermal softening countering the dominant strain hardening behaviour. The compressive residual stresses were also shown to decrease with feed. The influence of tooling parameters has been shown to influence the residual stress with an increase of the edge radius resulting in a decrease of the compressive residual stresses [75]. The use of negative rake angle has been shown to induce a higher compressive stress, as well as a deeper affected zone below the surface. With increased positive rake angles, the maximum stress position is moved further into the material. Dahlam *et al.* [73] showed that, by controlling the feed and rake angle, it is possible to generate tailor-made stresses in the product.

However it is important to have an appreciation of how the material will behave considering its operational environment once commissioned, since it has been shown that the deformation required to impart a lasting residual stress can end up being detrimental to its in-service performance. This has been reported for shot peened Ti-834 subjected to a prolonged thermal exposure; here the imparted dislocations serve as sites for the formation of silicide precipitates, which have a significant deleterious consequence on fatigue life [76].

2.4 Metallurgical analysis of machined components

Even though the field of surface and subsurface integrity analysis is well established, it has however maintained a comparatively narrow scope with thorough microstructure damage investigations being seldom explored. The machinability of a

material is generally assessed in terms of chip formation characteristics, cutting forces, tool life and surface condition, with no detailed examination or quantification of the subsurface microstructure. There is however, a growing body of evidence that demonstrates how subsurface microstructure deformation generated during machining is sensitive to both the underlying microstructure of the workpiece and fundamental machining parameters (cutting speed, feed rate etc.). There is also an awareness within the literature that the resulting imparted deformation can be regarded as ‘damage’, since its presence has been shown to have a deleterious effect. The following section will cover a broad range of machining investigations that have adopted a more metallurgical approach to subsurface integrity analysis. It details the types of mechanically induced deformation that are commonly observed during machining for a selection of metallic systems, describing how similarities remain across many different material types, plus underlining the fact that the specifics of titanium machining remains limited. As will also be made clear, many investigations fall short on explaining the mechanisms of the imparted deformation or how such microstructure features may affect a component’s in-service performance.

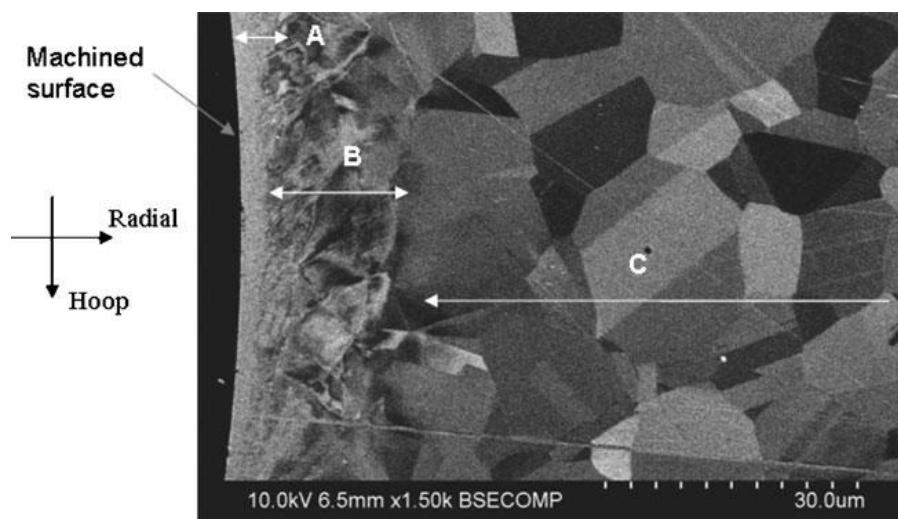


Figure 2.7 Back scatter electron micrograph taken in cross section of a deformed Inconel 718 subsurface microstructure following micro drilling trials, demonstrating significant grain refinement in the near surface region [77].

Away from using the more standard practices, through the use of high resolution electron microscopy techniques, microstructure features such as those in Figure 2.7 can be more easily defined. Imran *et al.* [77], during micro drilling trials of Inconel 718, identified through the use of backscattered electron microscopy the significant amount of microstructure disruption that occurs during machining. Regions A and B, as shown in Figure 2.7, represent material that has undergone a substantial amount of microstructure development. Material closest to the machined surface, region A, has

experienced the highest levels of imparted stress and strain resulting in a SPD ultrafine granular structure, which is unresolvable at the given magnification. Region B denotes microstructure that has undergone a significant amount of grain refinement and lattice rotation. The severity of the microstructure alterations can be seen to diminish towards the bulk, where region C signifies undeformed material that remains in the as received condition. In Figure 2.7, the significant number of subsurface twins within region C are annealing twins that were formed during the heat treatment and have not been imparted by the machining trial.

Parametric studies undertaken by Guo *et al.* [78]–[80], investigating the sensitivities of machined copper and brass substrates, showed the processes by which the subsurface can become more refined. Copper and brass samples are commonly used for such studies, due to their typically large starting granular structures, which have a high propensity for further grain refinement when subjected to high strain/ strain rate.

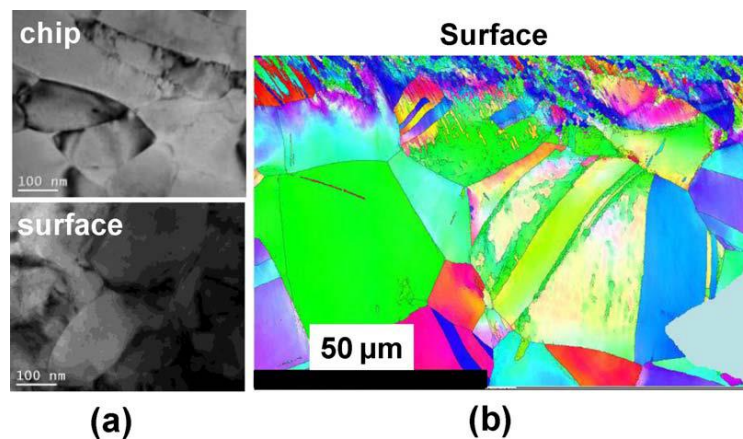


Figure 2.8 Following machining on brass test specimens (a) TEM micrographs illustrating the similarities in grain refinement that occur within the chip and in the near surface regions of the workpiece, (b) EBSD OIM of the machined brass substrate demonstrating the severe amount of grain refinement at the surface of the material with further imparted deformation occurring at depths $> 50 \mu\text{m}$ from the machined surface [78].

Guo *et al.*[78] were able to demonstrate how the cutting process influences the resulting microstructure. The TEM micrographs and EBSD OIM shown in Figure 2.8 illustrate the significant grain refinement that occurs within both the chip and the surface for machined brass. Qualitative analysis of TEM micrographs (Figure 2.8(a)) shows how the microstructures within both the chip and surface undergo a similar amount of refinement. The EBSD OIM (Figure 2.8(b)) illustrates how the amount of grain refinement reduces away from the machined surface with deeper subsurface grains deforming extensively via mechanically induced twinning, occurring up to $\sim 80 \mu\text{m}$ beneath the surface. The varying deformation modes were attributed to a

reduction in the magnitude of the experienced shear strain, which was observed to reduce as a function of distance away from the cut surface.

The deformation map presented in Figure 2.9 published by Guo *et al.* [79] shows the effect of varying cutting conditions on the resulting microstructure and the subsequent hardness (proportional to the materials strength) for machined copper. These observations further corroborate the notion that through controlled machining, a scaled subsurface strain distribution could be adapted to create a graded surface microstructure, which could complement a components application. A noteworthy observation of the work reported by Guo *et al.* [78]–[80] is that the changes in microstructure are simply referred to as being deformation and not “damage”.

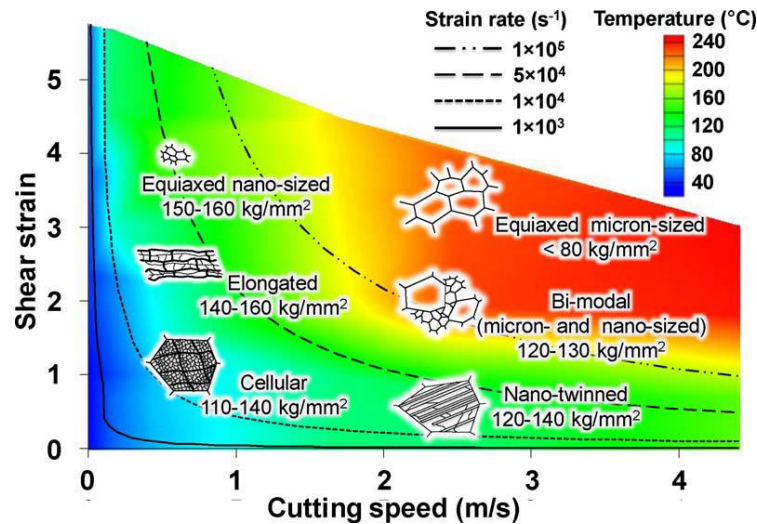


Figure 2.9 Deformation map illustrating the effect on microstructure as a result of variable machining parameters for copper test specimens [79].

The deformation map presented in Figure 2.9 by Guo *et al.* [79] shows the interactive effects of process parameters on microstructure and hardness and was derived from machining experiments that were undertaken using cutting tools with increasing rake angles that imparted a controlled increased level of shear strain. Guo *et al.* [78]–[80] demonstrated how individual machining cutting parameters, in this case cutting speed, can have a significant effect on the workpiece material. The trials were undertaken within a slow cutting regime in order to minimise the effect of temperature on the available deformation modes within the workpiece. However, with an increase in experienced strain rate, the material undergoes a significant amount of heating, which has resulted in grain growth and the induced twins are annealed out from the structure.

Under more severe machining conditions it has been shown that $\alpha+\beta$ titanium alloys can also display similar deformation characteristics to brass and copper with the formation of SPD layer. The SEM micrograph in Figure 2.10 shows the resulting subsurface microstructure of Ti-64 following a series of 50 m.min⁻¹, 0.07 mm.rev⁻¹ dry drilling trials (cutting undertaken without the addition of a lubricant or coolant fluid). These trials were undertaken using such an environment as to accelerate the mechanisms of tool wear, as part of the investigation a series of holes were created with tool wear measurements being taken between each cut. The micrograph shown in Figure 2.10 is representative to material that has been cut using a heavily worn tool, following this final cut, the tool was deemed to have failed using a maximum tool wear threshold. Analysis of the worn tool using SEM imaging and X-ray energy dispersive spectroscopy (X-EDS) showed that the tool had undergone excessive amounts abrasive and chipping type wear, as well as chemical wear that had resulted in the transfer of material from the workpiece into the tooling itself and a loss of tungsten and nitrogen from the tooling surface. The mechanisms of tool wear will be covered in greater detail in section §2.10 with examples of tool wear included in the Appendix.

As for the deformation behaviour of titanium under these atypical cutting conditions, the micrograph in the Figure 2.10 displays two regions as denoted by A and B, that possess contrasting microstructures. Region A, positioned closest to the drilled surface, has a width of ~125 μm and has been experienced a large amount of strain, which has resulted in a highly refined microstructure with grains that cannot be resolved at this magnification. The vertical striations that are positioned parallel to the cut surface suggest a substantial amount of material movement also occurs during the cutting process, emphasizing the severity of the imparted plastic strain. In Figure 2.10 Cantero *et al.* [60] do not clarify the transition point as to when region B begins since the two regions appear to be separated. However, region B can be characterized as being material that has undergone a significant amount of plastic deformation, but has largely retained its original grain size. The material within region B can be seen to have adopted a swept type microstructure, which has aligned itself with the movement of the driller tool. Under these cutting conditions the severe cutting environment has been exacerbated through the use of an already substantially worn tool, this has resulted in a deformed region that has affected material up to ~450 μm away from the cut surface. Similarly to the examples shown for brass and copper, the resulting microstructure changes offer the reader insight into how the tool is interacting with the workpiece and how external variables such as tool wear can have a compounding influence on a material's deformation.

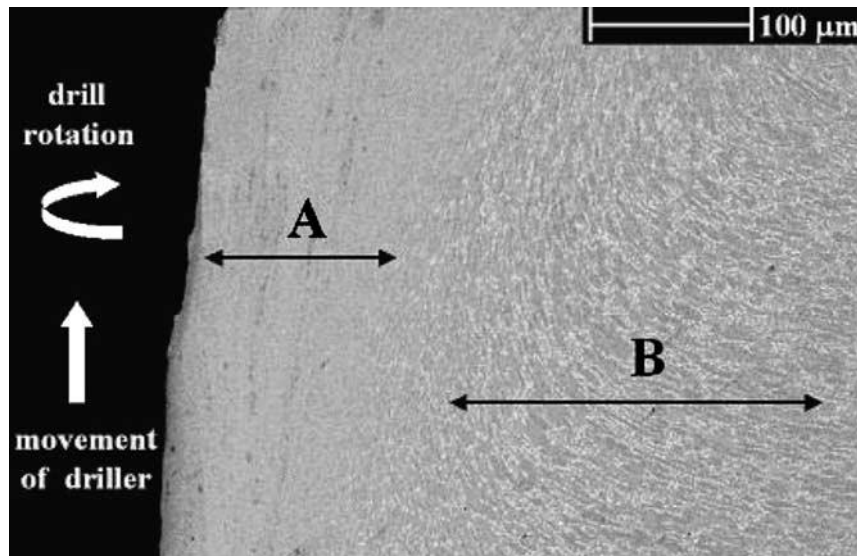


Figure 2.10 Backscattered electron micrograph of a drilled Ti-64 test specimen representative of the near the surface condition using a worn tool following the completion of the 128th hole. The two delineated regions A and B demonstrate the presence of two distinct deformed layers remaining following machining; high shear zone (A) and plastically deformation region (B) [60].

It is important when analysing and drawing conclusions from machined samples to have a prior understanding on how the material is expected to behave when subjected to mechanical loading and thermal cycling. During such dry machining trials it is expected that more heat will be generated at the tool chip interface, when compared to cutting when coolant is present. However, it is of the opinion of the author that Cantero *et al.* [60] has a contradictory and poorly supported view as to what effect this imparted heat has on the resulting microstructure. They attributed an observed increase in microhardness within region A to the formation of a proposed α case layer. An α case may form through the uptake of oxygen or nitrogen both of which stabilize and strengthen α phase within the uppermost layer of the workpiece [81]. α case layers are encouraged to form when exposed to a hot environment over the course of a prolonged period, this time at temperature exposure aids the diffusion of oxygen or nitrogen into the matrix. However the fine nano-sized grains found within region A do not support this claim considering any prolonged period at elevated temperature (which for titanium would be expected to be as high as ~ 700 - 1100°C [82]) would encourage further grain growth. This nano-size grain structure could however be directly attributed to the increase in hardness using a Hall-Petch relationship, where an increase in grain-boundary surface area (smaller grain size) strengthen the material by impeding dislocation propagation [12]. Without the use of further quantitative analysis techniques such as Secondary Ion Mass Spectrometry (SIMS) [83], it is not possible to deconvolute the potential causes of hardening due to

α grain refinement and or oxygen uptake. Machining induced deformation was also claimed to occur as a consequence of temperature gradients within the workpiece. However, no explanation was included as to how these deformation features manifested and to what form they had. It is plausible that Cantero *et al.* [60] are alluding to the potential impact machining induced residual stresses may have on a component as previously discussed in §1.3, imparted residual stresses can be used to benefit a components fatigue performance. However when machining thin walled components with high dimensional tolerance, the part may experience severe distortion following a machining pass. The effect and causes of these residual stresses have been extensively studied using finite element modeling (FEM) software packages in order to design machining programs that can mitigate their effect [71]. To prevent machining induced product distortion, machinists often employ high surface cutting speeds at very low depth of cut and reduced feed rates [84]–[86].

In order to study in detail the effect of machining and the dynamic changes that are occurring at the tool/chip interface, either through the use of FEM or during real machining trials, a simplified machining apparatus is often employed adopting an orthogonal cutting arrangement Figure 2.11. During orthogonal cutting the tool is limited to only move within a two dimensional plane and replicates the cutting behaviour occurring during a steady state cut. Using these simplified investigations material and cutting characteristics can be determined which can be applied to more complex cutting arrangements, such as drilling, milling and outer diameter turning.

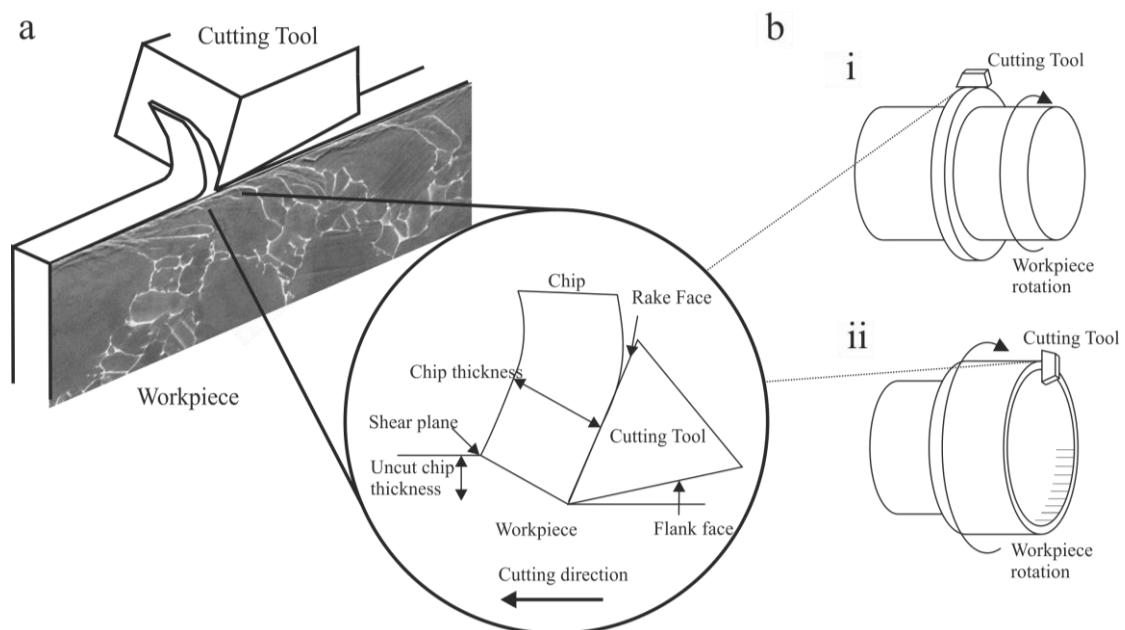


Figure 2.11 Schematic diagrams illustrating the common operational preparations used to achieve an (a) orthogonal cut using either b (i) outer diameter or (ii) facing arrangement preparation.

Using an orthogonal cutting arrangement as shown in Figure 2.11(a) it is possible to easily reproduce successive cutting trials allowing a precise method to compare and analyse the cutting performance of differing workpiece materials, cutting tools (shape, size, geometry and material), lubricant types, lubricant delivery and machining variables such as cutting surface speed, depth of cut and feed rate. The two schematics shown in Figure 2.11(b i-ii) illustrate how the cutting arrangement is limited to two Cartesian planes, with movement only occurring along the cutting direction and the feed direction with zero movement observed in the remaining plane parallel to the depth of cut.

Orthogonal cutting arrangements, such as the ones outlined in Figure 2.11, allow for improvements to be made during finite element simulations. Such simplified studies can be modelled more easily (less computing power) and in more detail (more elements per unit area) than normal cutting operations, due to the simulations only needing to be undertaken within a two dimensional plane. Comparative studies such as the one presented in Figure 2.12 compare simulated results (Figure 2.12(a) to those obtained via experimentation (Figure 2.12(b)) [87]. From these results it is possible to ascertain whether or not the material data, incorporated within the software packages, is giving rise to realistic outputs allowing for further modifications to be made [88], [89].

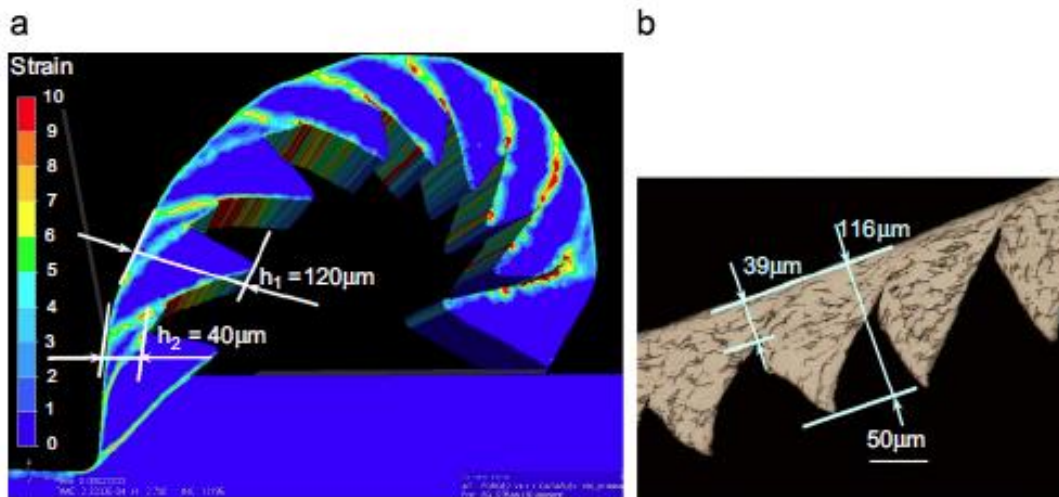


Figure 2.12 Comparative evaluation of (a) acquired simulated chip morphologies to (b) experimentally obtained Ti-64 chips, using chip maximum and minimum height as a reference [87].

There is a growing body of research focused on creating and improving finite element simulations concentrating on the behaviour of how a chip is generated during the machining of titanium [90]. Such investigations help characterize the types of chip

that are generated; for example, investigations studying the differences between continuous and discontinuous chip types and possible controlling factors which dictate their formation [91], [92]. Results obtained via finite element simulation rely upon the use of material constitutive equations that have been obtained via experimentation and subsequently dictate how the simulated material will behave. Simulations, such as those undertaken by Shivpuri *et al.* [93] use numerical models that incorporate known material changes into the phenomenological behaviour of the chip. Such models are then calibrated by comparing results with experimental measurements at different cutting speeds and feeds and by making modifications to the material's constitutive models [94], [95]. Finite element simulations can also be used to replicate how the dynamics of a cut can change as the tool begins to wear. Calamaz *et al.* [96] compared the effect of cutting a Ti-64 sample with a new tool geometry to that of a worn tool geometry. The cut was undertaken using the following cutting parameters; rake angle 0° , clearance angle 11° , cutting speed $60 \text{ m}\cdot\text{min}^{-1}$. The results, shown in Figure 2.13, are presented alongside experimentally acquired cross sectional chip micrographs, to serve as a reference for the simulated data. In both instances, the simulated chip bears a close, but noticeably non-exact resemblance to its corresponding experimental example, with an observed increase in the shear band spacing when using the worn tool. The results presented do not, however, discuss how much variation there is between each data set, considering only a single measurement has been taken for both the new and worn data sets. The simulated images do however illustrate how, when cutting using a worn tool geometry, a larger area of material experiences the maximum level of plastic strain both within the chip and into the remaining workpiece (maximum values of strain relative to the given scale bar, may have risen higher than 2). The images shown for the worn tool geometry in Figure 2.13(b) demonstrate a larger amount of strain penetration into the remaining material, and therefore show deeper subsurface material experiencing higher strain levels.

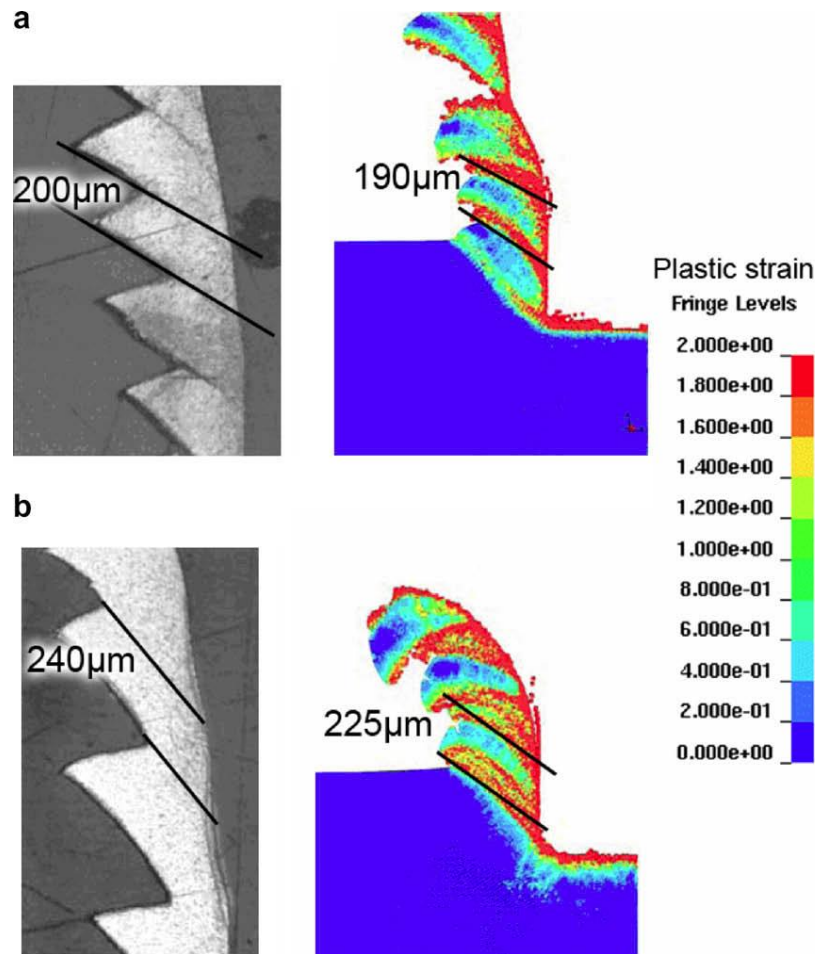


Figure 2.13 Experimental and numerical chip formation of Ti-64 using (a) new tool and (b) worn tool geometry Rake angle 0° Clearance angle 11° Cutting speed $60 \text{ m}\cdot\text{min}^{-1}$ [96].

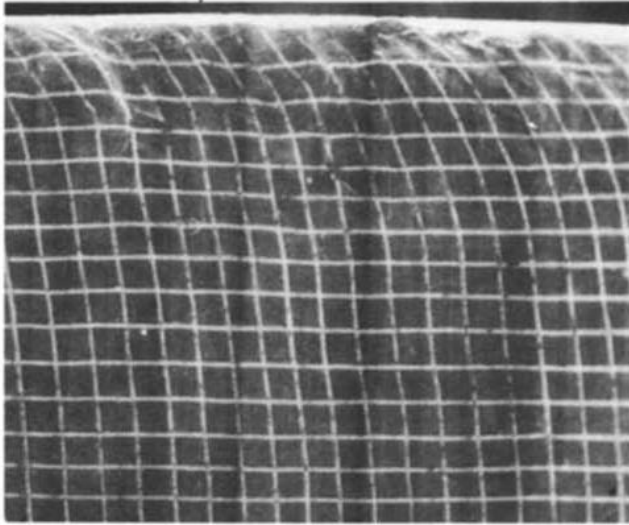
In addition to the typical compromises associated with all finite element models, such as deciding upon the right balance between element mesh size, computing power and available time to run the simulation, machining simulations are inherently plagued with further difficulties. Machining simulations are especially difficult due to the associated high strain rate environment that is generated within the shear band and at the tool chip interface. Material data used during simulations will have been originally obtained and adapted from experimentally acquired data. Representative flow stress data for a broad range of material types will be typically included as part of the FEM package; these datasets are subsequently extrapolated to suit the predicted simulation. However during a simulation such as the one outlined in Figure 2.13 many assumptions are often made; most commonly, the tool will remain ridged often with no thermal or elastic capacity [97]. The workpiece material will also obey simplified conditions regarding the contact friction with the tool as well as the whole structure adopting nominal bulk material properties. Currently there still remain a very limited

number of studies that have attempted to recreate the machining characteristics of either multiphase or polycrystalline materials. The ability to recreate real world materials is seen as an important engineering development for software designers [98]. However, since the knowledge base surrounding the deformation behaviour of any machined material is very complex, multiphase simulations at this stage are at best speculative and are generally created to demonstrate software capability rather than as a method of predicting material behaviour.

2.5 Deformation characteristics within the workpiece during machining.

Material samples prepared for microstructure analysis are typically sectioned parallel to the machining direction; using this orientation it is possible to capture the magnitude of the imparted strain in relation to the loads that have been applied within the plane of the cutting direction. The cross sectional optical micrograph shown in Figure 2.14(a) demonstrates a primitive method of determining the total amount of plastic strain imparted following a machining pass. Prior to conducting an orthogonal type cut a grid pattern had been drawn onto the side of the red brass sample. By measuring the displacement of points from their original positions Jeelani *et al.* [99] was able to determine the induced subsurface plastic strain distribution within both the horizontal and vertical directions as illustrated graphically in Figure 2.14(b). Total subsurface plastic strain in x and y and total shear strain are denoted by ϵ_{xx} , ϵ_{yy} and γ_{xy} respectively. This method offers the reader a clear visual representation of the severity of the resulting deformation imparted into the substructure following the machining operation. The micrograph and corresponding graphical strain distribution plot demonstrates how for this particular machining condition, surface speed $7.6 \text{ m}\cdot\text{min}^{-1}$, feed rate $0.25 \text{ mm}\cdot\text{rev}^{-1}$ in conjunction with using large positive rake angle tooling 20° resulted in deformation to a depth to $\sim 90 \text{ }\mu\text{m}$. Towards the machined surface the imparted plastic strain can be observed to be largely negative for both the horizontal (ϵ_{xx}) and vertical (ϵ_{yy}) orientations with a vertical negative peak at $\sim -15\%$ with further significant fluctuations with a positive peak of $\sim 5\%$ vertical strain at a depth of $40 \text{ }\mu\text{m}$ beneath the surface. Horizontally the plastic strain can be observed to progressively increase to a maximum of $\sim -5\%$ at the machined surface. The total shear strain can be observed to also increase linearly to a positive maximum level of $\sim 35\%$.

a



b

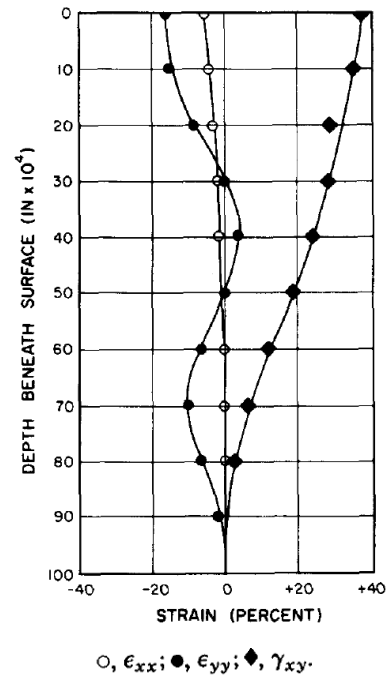


Figure 2.14(a) cross sectional optical micrograph of red annealed brass using a microgrid grid pattern to demonstrate the severity of the imparted strain following machining, (b) graphical representation of the total plastic subsurface strain imparted following a machining pass [99].

It is important when evaluating cross sectional micrographs such as the one presented in Figure 2.14(a) to have an appreciation of the complex deformation regime that material has undergone. Since by itself, analysis of the remaining material can only illustrate a proportion of the complete mechanics, considering a significant proportion of the deformed material is subsequently removed as chip, as the tool traverses over the workpiece. In order to capture the in-cut deformation mechanics it is necessary to employ the use of a quick stop method, whereby the tool is released from its holder effectively freezing the cutting process. Early work undertaken by Turley *et al.* [100] and Doyle [101] developed the technique for characterising chip formation and calculating shear strains for both turning and grinding. The optical micrographs shown in Figure 2.15(a-b) were captured following a quick stop trial and illustrate the large amount of deformation ahead of and beneath the tool/workpiece interface. Shankar *et al.* [102] were able to identify a fan shaped deformation zone that manifests itself ahead of the tool, here CP titanium samples where machined in an orthogonal arrangement at a surface speed of $0.6 \text{ m}\cdot\text{min}^{-1}$, a cutting width of 3 mm and feed rate $0.3 \text{ mm}\cdot\text{rev}^{-1}$, whilst using a tool with a negative rake angle of -20° . The quick stop method allows the reader to easily identify how the workpiece material is

interacting with the tool, with the fan shaped deformation zone penetrating forward $\sim 500 \mu\text{m}$ into the workpiece. Figure 2.15(a) illustrates how as the tool approaches the density of the induced deformation within the workpiece increases to a point of saturation within the region identified as the zone of localized severe deformation, commonly referred to as the shear band. Beyond the shear band, the chip is subsequently removed and does not undergo any further discernable microstructure changes.

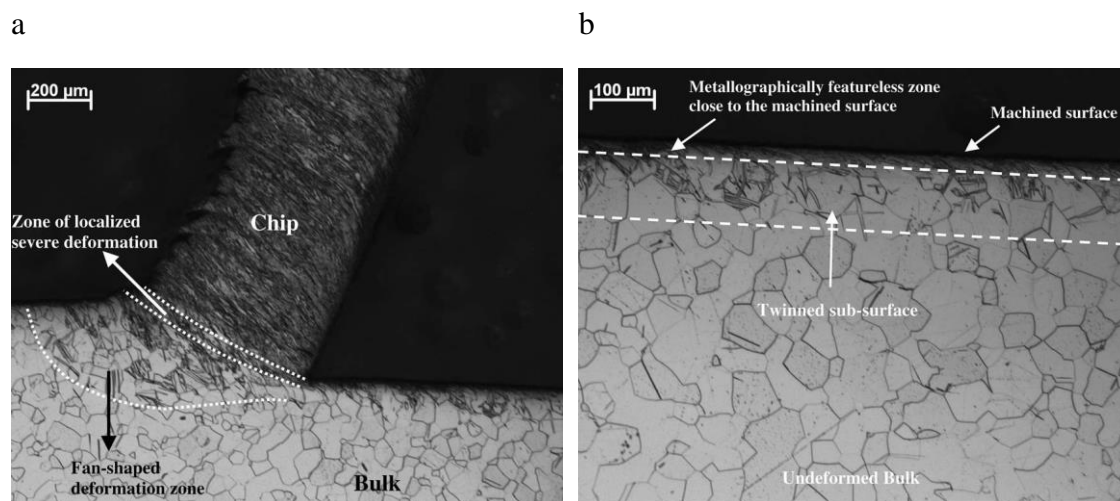


Figure 2.15 Cross sectional optical micrographs of machined CP titanium (a) resulting microstructure following a halted quick stop test (b) As machined material, which can be divided into three distinct regions; the uppermost layer indicating a region that has become highly refined following intense shear, the twinned region within $\sim 150 \mu\text{m}$ of the surface and the undeformed bulk microstructure [102].

The cross sectional optical micrographs shown in Figure 2.15(b) illustrate the severity of the residual subsurface deformation that remains following a machining pass. Due to the deformation kinetics of CP titanium, plastic deformation is predominantly accommodated by the generation of mechanical twins [4]. The delineated line signifies the maximum depth to which the deformation occurs with twins being identified within the first $\sim 150 \mu\text{m}$ of material from the machined surface, with all grains that border the machined surface showing evidence of mechanically induced twinning.

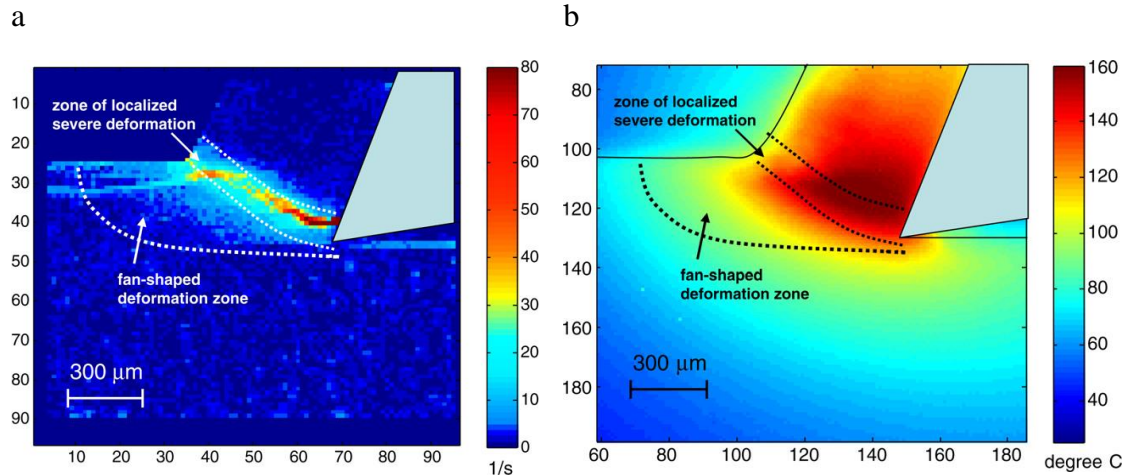


Figure 2.16 In-situ machine monitoring using (a) Particle image velocimetry (PIV) and (b) infrared (IR) thermography imagery measuring the deformation and temperature fields respectively [103].

As a progression to the investigation carried out by Shankar *et al.* [102] work undertaken within the same group by Huang *et al.* [103] was able to capture direct observational data utilizing particle image velocimetry (PIV), known also as digital image correlation (DIC) - and infrared (IR) thermography, to measure the deformation and temperature fields respectively, whilst machining under the same parameters. Using these techniques it is possible to observe the significant amount of shape change that occurs within both the chip and the deformation zone. The images shown in the Figure 2.16(a-b) illustrate the strain rate distribution and recorded temperature profile taken whilst the machining under a steady state cutting condition. Huang *et al.* [103] reported that the maximum strain within the chip rises to values ~ 1.5 (150% plastic strain) as estimated by PIV, with no further indication as to the strain in the remaining material. The strain rate distribution map illustrates both the close concentration and severe increase in strain rate across the material with the largest values of strain rate approaching $\sim 80 \text{ s}^{-1}$ within the shear band. The presented temperature profile also show a recorded temperature rise up to $\sim 1000 \mu\text{m}$ beneath the tool edge, with a maximum temperature also recorded in the region of the shear band, of 160°C . Interestingly, this temperature falls well below any thermal softening threshold or the beta transus temperature even though the trials were undertaken under dry cutting conditions. The author feels that such temperature recordings need to be considered with caution since they fall well short of anticipated cutting ‘flash’ temperatures (of $\sim 700\text{-}1100^\circ\text{C}$), as simulated by Umbrello [82] and $\sim 825^\circ\text{C}$, as recorded by Sutter [104]. The images shown in Figure 2.16 demonstrate how the precise nature of the materials deformation route is closely controlled by its location relative to tool/workpiece interface, with the remaining material immediately below

the machined surface undergoing a complex deformation cycle as the tool is progressed across the surface.

To capture the microstructure development within the deformation zone, Huang *et al.* [103] conducted EBSD analysis on a machined sample at the point where the machining process had been stopped abruptly. The band contrast Orientation Image Map (OIM) with special boundary delineation shown in Figure 2.17 illustrates the extensive amount of mechanically induced twinning present within the microstructure, as well as the significant amount of grain refinement occurring within the shear band. Note the chip appears to have broken away from the workpiece. Qualitative analysis indicates the majority of twins formed ahead of the tool are $\{10\bar{1}2\}$ tension type twins, as denoted by an $\sim 86^\circ$ rotation about the $\langle 1\bar{2}10 \rangle$ axis, with further evidence of compressive $\langle 11\bar{2}2 \rangle$ twins ($\sim 65^\circ$ rotation about the $\langle \bar{1}010 \rangle$ axis) with a further limited number of tension $\{11\bar{2}1\}$ twins ($\sim 30^\circ$ rotation about the $\langle \bar{1}010 \rangle$ axis). Due to the large amount of grain refinement occurring within the shear band, this results in a substantial amount of un-indexed regions as signified by the large amount of zero (black) data points. Both studies carried out by Shankar *et al.* [102] and Huang *et al.* [103] did not include quantitative metallography analysis, with regard to identifying the point at which the residual deformation remaining in the workpiece has been induced. The fan shaped deformation zone shown in Figure 2.15(a) and Figure 2.16(a) ahead of the tool can be seen to spread beneath the tool tip; however, qualitatively it would appear that the density of twins within this region increases after the tool tip has passed over. This observation suggests further sensitivities of the workpiece's microstructure to induced deformation.

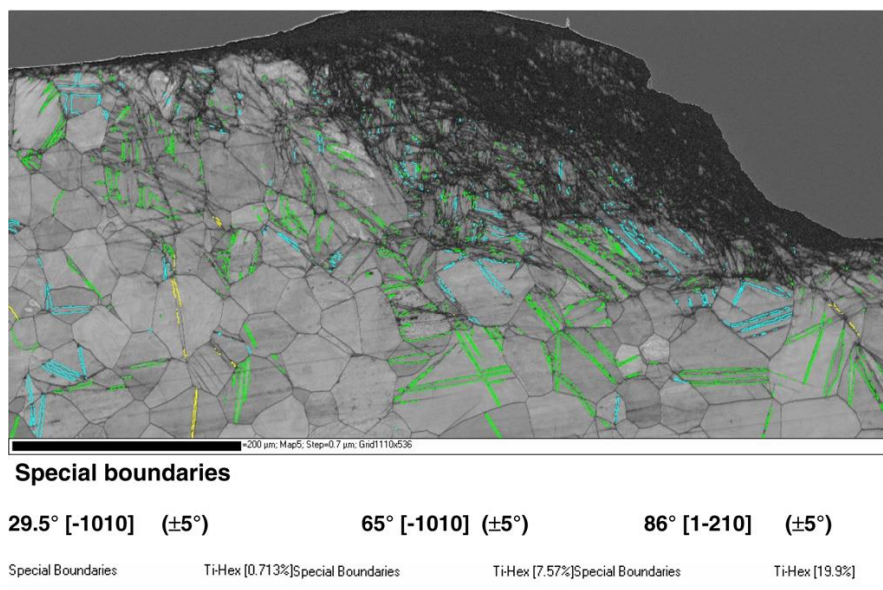


Figure 2.17 Band contrast OIM with special boundary delineation of the deformed CP titanium microstructure following a halted machining operation[103].

The findings of Huang *et al.* [103] are important as they are amongst first to have exploited the use of quantifiable orientation imaging methods to characterise machining induced deformation. Through the use of EBSD the deformed microstructure layer has been characterised and for machined CP titanium an abundance of both tension and compressive twins has been identified. Since turning involves the tool being in constant contact with the workpiece, the stress state within this region will have remained largely consistent throughout. Therefore, the variation in deformation types amongst grains further illustrates the critical relationship between the underlying microstructure and the specific deformation environment that is imparted during machining.

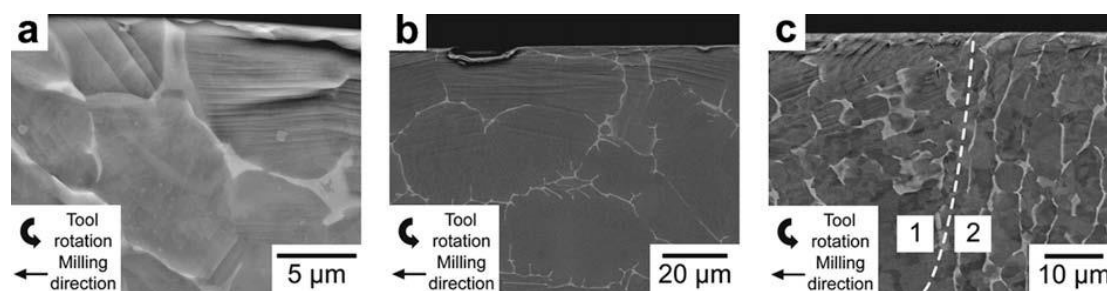


Figure 2.18 Cross sectional backscattered electron micrographs showing varying severity in induced deformation in the form of intense slip bands following high-speed machining in (a) Ti-64 and (b) Ti-834. (c) illustrates further regional non-uniformity of deformation observed in Ti-64 [105].

The high resolution cross sectional backscatter electron micrographs shown in Figure 2.18 were obtained by Thomas *et al.* [105] following a series of milling trials on the near α titanium alloy Timetal® 834 and the $\alpha+\beta$ alloy Ti-64. Due to the intermittent nature of the milling process the impact on the subsurface microstructure is often considered to be less disruptive than that of turning. However as shown in the micrographs in Figure 2.18, the extensive amount of induced subsurface deformation following milling suggests otherwise. Thomas *et al.* [105] were able to show how localised variation in crystallographic orientation had a direct effect on the induced slip band characteristics as shown in Figure 2.18(a) where neighbouring grains in a Ti-64 sample demonstrates variation in slip intensity, including slip band spacing. Figure 2.18(b) illustrates how the depth to which slip bands can be observed varies across the subsurface layer of a milled Ti-834 sample, with grains displaying evidence of slip bands occurring at a maximum depth of $\sim 50 \mu\text{m}$ from the machined surface. The α colonies separated by the delineated boundary in Figure 2.18(c) display an example of non-uniform deformation typically observed along the subsurface machined layer of Ti-64. The texture of each α colony is determined by the burgers relationship during the β -to- α transformation on cooling, which results in the α laths

within each colony adopting a similar crystallographic orientation, thus creating an effective single structural unit [106]. Due to the limited number of active slip systems, in HCP crystal structures, the crystallographic orientation of the α phase within each colony will govern its deformation characteristics. Again, the variation in deformation response suggests that the material within α colony 1 is more favourably orientated for induced deformation.

Using EBSD, Thomas *et al.* [105] were able to identify and characterize the imparted deformation features. Figure 2.19(a-b) shows a relative disorientation composite image and corresponding band contrast OIM of high speed ($200 \text{ m}\cdot\text{min}^{-1}$) milled Ti-834 substructure respectively.

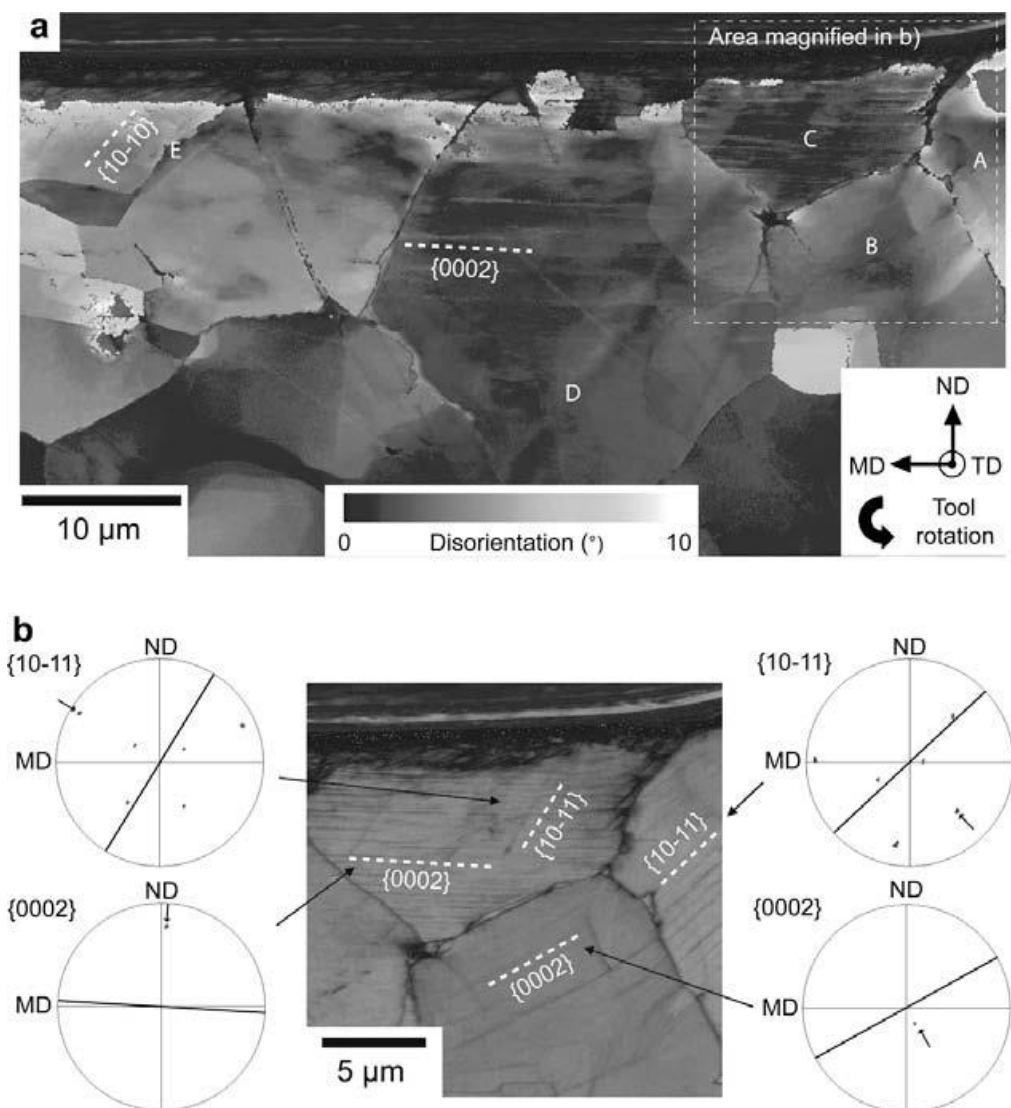


Figure 2.19 EBSD OIMs of milled Ti-834 following a high-speed cutting operation ($200 \text{ m}\cdot\text{min}^{-1}$). (a) Crystal disorientation OIM referenced against individual grain average orientation; (b) pattern quality (band contrast) OIM of the region delineated in (a). the corresponding slip trace analysis demonstrating the identification of $\{0002\}$ and $\{10\bar{1}1\}$ type slip [105].

Within the regions analysed there is zero evidence of mechanically induced twins, rather plastic deformation has been accommodated by the activation of various slip systems. Using a slip trace analysis method, slip has been identified to $\{10\bar{1}1\}$ have occurred along the basal, pyramidal and prismatic planes ($\{0002\}$, $\{10\bar{1}1\}$ and $\{10\bar{1}0\}$ respectively). Corresponding Schmid factor values were calculated using a first order approximation of the macroscopic stress state, this assumed a loading direction of 45° to the machined surface, leading to a state of shear occurring parallel to the milling direction. This estimation gave Schmid factor values approaching 0.5, suggesting the highest probability of activation, for the identified modes of slip within grains adjacent to the machined surface. Considering the high values of Schmid factor, this gives validity to the first order approximation for the assumed macroscopic stress state. Contrasting results occurring within grains that are positioned further from the machined surface such as within grain B, as shown in upper right of Figure 2.19(a), here the identified activated $\{0002\}$ slip has a lower corresponding Schmid factor of 0.3. This variation has been attributed to either (i) the complex nature of the milling process - having a significant varying effect on neighbouring grains, or (ii) localised heating, which could result in a reduction in the critically resolved shear stress - required for the activation of a specific mode of deformation. From the abundance of multiple types of activated slip systems that have been identified, the results show that, for α -rich titanium alloys, the underlying grain orientation, with respect to the machining direction, plays a significant role in determining the degree of damage that can be generated.

2.6 Microstructure deformation sensitivities to changes in machining parameters

The increasing use of large monolithic titanium alloy components in the next generation of civil aircraft, has led to a drive for higher production rates. Machining is a costly process and accounts for 60% of the total cost of critical titanium aerospace components [15], in most part due to approximately 95% of the starting material being removed as swarf [5]. To minimize costs, the advanced manufacturing community is developing techniques to machine titanium products at higher rates. For milling and turning, this equates to higher surface speeds, and thus higher strain rates at tool/workpiece interfaces. To facilitate this progression towards high speed machining it is important to gain a metallurgical understanding on how such changes in parameters affect the underlying microstructure of the workpiece and in turn what effect this may have on the products in-service properties. The work presented by Thomas *et al.* [105] in Figure 2.19 illustrates the typical subsurface microstructure changes occurring within Ti-834 using these emerging high speed ($200 \text{ m}\cdot\text{min}^{-1}$)

methods. As previously discussed it has been shown for Ti-64 that, when the machining surface speed is increased to $\sim 80 \text{ m}\cdot\text{min}^{-1}$, a peak in compressive residual stress can be imparted into the uppermost layers of the workpiece, after which any further increase in surface cutting speed results in a reduction in compressive stress [74]. This decrease in residual stress could be attributed to the activation of a significant number of slip systems similar to that observed in Figure 2.19, rather than as suggested by Sun *et al.* [74] as an effect primarily caused by an increase in the cutting temperatures leading to thermal softening. Considering the financial benefits that high speed machining will bring for component manufacturers, this gives a significant amount of motivation to gain a better understanding of the sensitivities of the microstructure in order to minimise any detrimental effect they may bring.

The following section is intended to bridge a gap that has manifested as a result of the methodologies employed by two distinct research factions, which are used when assessing the machining characteristics of a material. Using broad generalisations; assessment undertaken by groups from a more mechanical engineering background usually concentrate on acquiring unequivocal data often employing the use of force feed-back type equipment that can obtain results whilst a cut is underway. Whereas the metallurgical approach is to concentrate on the relationship between the workpiece interface with the tool and how the materials are responding within the cutting environment. This can be directly, i.e. chemical interactions or strain rate sensitivities that may lead to changes in the flow stress behaviour, or indirectly, i.e. relating not just how the material is responding during the cut but in what condition the material is in post machining. For the purpose of this review both parties methodologies are considered to be equally important and it is of the opinion of the author that when combined they present a more complete understanding of the mechanisms that are taking place. As previously discussed in §2.5, researchers/engineers will usually relate damage to more easily observable macroscopic large scale deformation rather than the activation of sub-grain features such as twins or slip. Therefore damage depth is usually defined using standard imaging techniques, such as backscatter imaging, to a point at which no discernable distortion can be observed and representative of the bulk. Following a series of parametric dry turning trials of Ti-64, Velásquez *et al.* [107] proposed a technique to more accurately classify the transitional boundaries within the deformed turned material. As depicted in the backscatter electron micrograph in Figure 2.20 the delineated areas P1, P2 and P3 relate to the bulk material, plastically deformed material and severely deformed tertiary shear material respectively. Using backscatter imaging to identify the boundary between the bulk and effected material (P1 and P2) poses some difficulties as it is an ambiguous feature: The observer is required to subjectively decide whether

or not the material has been distorted without prior knowledge as to what form the microstructure had prior to machining.

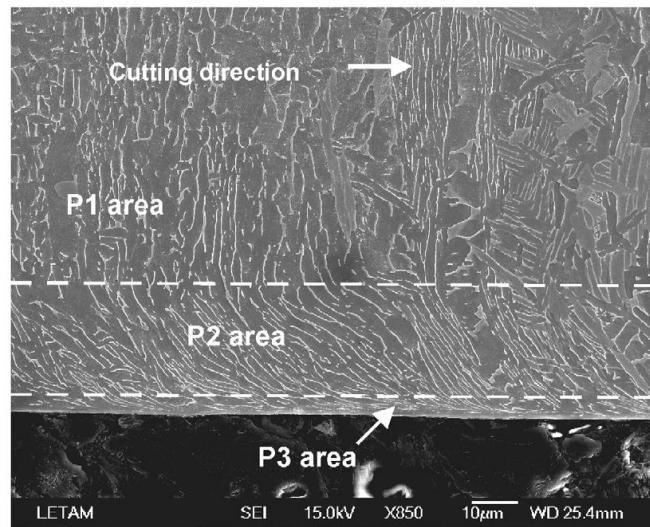


Figure 2.20 Cross sectional backscatter electron micrograph following machining of Ti-64 with a surface speed $V_c = 260 \text{ m}\cdot\text{min}^{-1}$, the delineated regions P1, P2 and P3 relate to the bulk material, plastically deformed material and severely deformed tertiary shear material respectively [107].

Therefore to gain a deeper understanding of the deformation history of the material, it is necessary to use a quantifiable analysis technique such as EBSD. By presenting the acquired data in the form of a band contrast OIM, as shown in Figure 2.21, the nature of the transition between the P1 and P2 areas can be more easily defined.

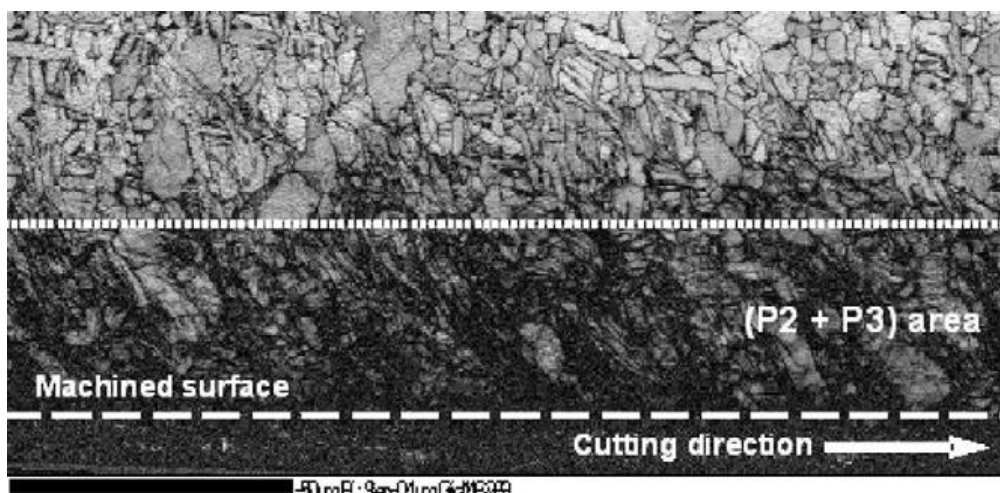


Figure 2.21 Band contrast OIM of machined Ti-64 following a turning operation, the image demonstrates the diminishing severity of the deformation away from the machined surface [107].

From the band contrast OIM, low band contrast data points, that appear as dark regions, are indicative of material containing a high density of dislocations that are disrupting the diffraction pattern. (NB the precise relationship between the true intensity of a band contrast data point and the underlying dislocation density or relationship with other plastic defects is not fully understood). Here Velásquez *et al.* [107] defined the boundary between the P1 and P2 areas as being a position within an area containing both low and high band contrast data points. No further explanation is given as to what density of high and low band contrast data points was chosen to define this boundary nor how many measurements were taken when calculating its average depth. The data presented in Figure 2.21 clearly illustrates how the boundary between these two areas must be considered to be occurring over a graduated zone rather than appearing abruptly; in addition, the deformation depth and density fluctuates significantly along the machined surface. This work further demonstrates that the type and magnitude of the imparted deformation is sensitive to the underlying microstructure of the workpiece.

Within the literature there are conflicting arguments on how a components subsurface microstructure is expected to respond when machined at elevated surface cutting speeds. Unsurprisingly it has been shown that when using more ‘abusive’ cutting conditions; such as high feed rates, large depths of cut, a dry cutting environment, and in particular when using a worn cutting tool, greater levels of subsurface deformation will be observed [57], [67], [108]–[113]. However, the resulting effect of independently increasing the cutting speed seems less well defined. As highlighted in the deformation map in Figure 2.9, the machined subsurface microstructure shows significant sensitivities to the associated stress state. It has been shown that when machining at an increased cutting speed, the deformation behaviour changes in response to the increased imparted strain rates [79]. However, what still remains under debate is whether the imparted deformation can be regarded as being more or less severe. As discussed in section §2.2 complete quantification of the deformed microstructure is uncommon for machined material. Most investigations see subsurface damage in single and multiphase materials in the form of plastic deformation, with grains aligning with the cutting direction parallel to the machined surface. The severity of the deformation is usually determined using microstructure assessment methods such as; EBSD band contrast OIM [107], micro-grid deformation [114] or deformation depth measurements [108], [113] these results may be supplemented with further surface roughness measurements [55] and or residual stress analysis [72]. Results may also be reported using optical or backscatter electron micrographs alongside an approximate qualitative assessment from the author, with no further supporting evidence [57], [59], [67].

2.6.1 The response to cutting speed

Parametric investigations studying the effect of cutting at increased surface speeds have reported contradicting results regarding the depth to which the deformation can be observed. Independent studies using the previously listed methodologies, have shown for titanium alloys, when machining with an increasing surface speed, the depth of the accompanying workpiece sub-surface deformation can be seen to either increase [107], [113], [115] decrease [59], [67], [116] or show zero trend [57], [108]. In all of these cases there is no corresponding discussion that could help address this confusion. The investigations that report an increase in the depth of the imparted deformation with increasing machining speed follow a comparable trend to plot recorded by Velásquez *et al.* [107] as shown in Figure 2.22. Here the plot demonstrates an approximate linear relationship between the depth of deformation with surface cutting speed, during orthogonal cutting trials of Ti-64. The trials carried out by Narutaki [67] and Ginting *et al.* [59] whose findings used qualitative analysis methods, reported a reduction in the depth of the deformation layer with increasing surface speed. In each of these instances the trials were undertaken using a small depth of cut (0.5 mm) and feed rate ($0.1 \text{ mm}\cdot\text{rev}^{-1}$). As previously discussed in section §2.5, the complete interaction volume of material being removed plays a significant role in determining the deformation kinetics. The investigations carried out by Hughes *et al.* [56] and Che-Haron *et al.* [57] remain inconclusive with regard to the relationship between the deformation depth and machining speed, due to the significant amount spread in their results, which is exacerbated by the limited range of cutting speeds used.

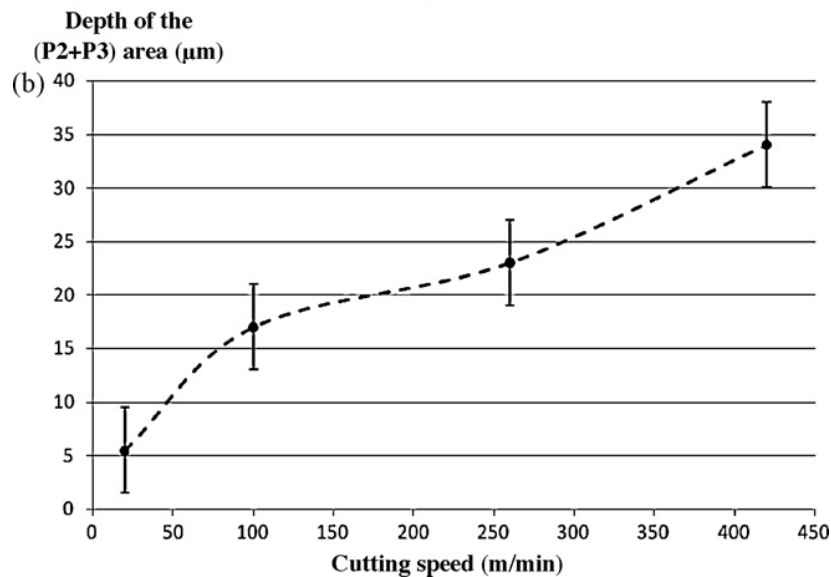


Figure 2.22 Resulting plastic deformation depth as a function of cutting speed for turned Ti-64 as determined using EBSD data to identify the interface between the bulk and deformed material [107].

The plot presented in Figure 2.23 demonstrates the behaviour of the resulting cutting forces (F_c) and feed forces (F_f) that are generated during machining, plotted as a function of the cutting speed V_c . The forces are measured in situ using a dynamometer that holds the tool in place and measures the resultant forces along the three Cartesian planes. The results presented in Figure 2.23 are average values that have been compiled over a broad range of cutting speeds. It can be observed from the plot that the resulting cutting forces (F_c) is the dominant force component, each force can be observed to rapidly decrease as the cutting speed increases to an almost constant value at speeds above 40 $\text{m}\cdot\text{min}^{-1}$. The results presented in Figure 2.23 are typical [96], [116], [117] for machining titanium with the plateau region of force, occurring beyond $\sim 40 \text{ m}\cdot\text{min}^{-1}$. Experimental cutting trials using alternative cutting arrangements, many using customized high strain rate Split Hopkinson bar test type apparatus [87], [118], [119] have demonstrated how the plateau region is maintained at speeds in excess of $\sim 4800 \text{ m}\cdot\text{min}^{-1}$. The results presented in Figure 2.23 demonstrate how the typical reducing force response with speed can be approximated for both the cutting and thrust components of force, however the results do suggest there is significantly more scatter in force response occurring along the feed direction.

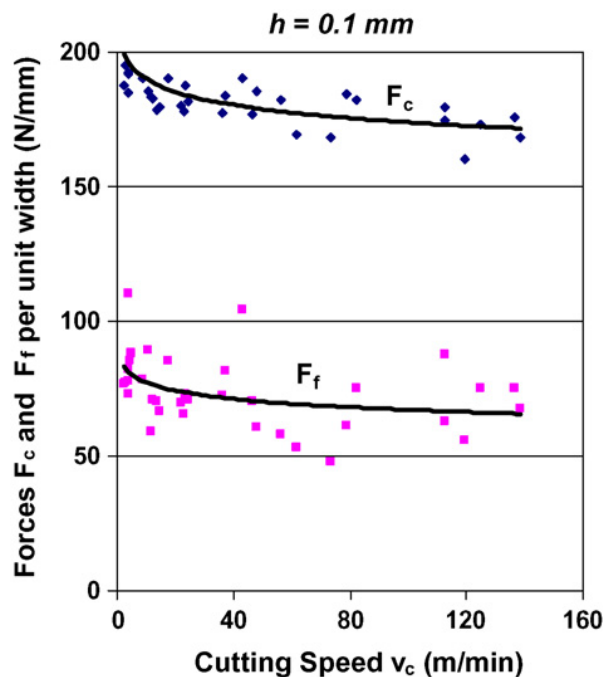


Figure 2.23 Resulting cutting force profile as a function of cutting speed for orthogonally turned Ti-64 [90].

The typical reducing force response with machining speed has been attributed to sensitivities of the shear band angle ahead of the tool, which dictates the total area of the shear plane. It has been observed that as the speed is increased within a low to

moderate range of cutting speeds, the shear angle increases with machining speed, resulting in a reduction of the shear plane. When machining with a high rake angle, an increase in cutting speed can result in the shear angle tending towards a maximum value of 45° thus corresponding to an uncut chip thickness equal to the thickness of the chip ($t_1 = t_2$). At intermediate or high speed, strain-hardening effects in some workpiece materials tend to increase the cutting force while other materials start to undergo adiabatic shear, which further reduces the cutting force. At very high speeds, inertial effects become a significant factor, since the momentum of both the workpiece and of the tool cause the forces to artificially increase [120], [121].

Considering most investigations that evaluate the effect of cutting speed on the workpiece are undertaken at speeds that lie within the force plateau region, assuming the material analysed has been cut using comparable tooling geometries (new tool), fluctuations in the resulting microstructure must therefore be the result of the materials strain rate sensitivity. Such sensitivities could subsequently result in deeper sub-grains deforming under significantly lower total strain environments, or influence the mechanisms of chip generation. Studies have shown how the shear band angle ahead of the tool tip within the chip displays sensitivities to the cutting surface speed [122] as well as variation in segmentation frequency [123], thus resulting in a sensitivity of the chip morphology. From this it can be implied that alterations in the chip morphology could have a significant effect on the stress field surrounding the tool chip interface, resulting in changes in the direction and magnitudes of the experienced loads.

2.6.2 The response to machining feed

In order to gain a more complete understanding of how a material behaves during machining, many investigators adopt a common methodology and study the mechanical response of a material across a range of feed rates. Bearing in mind cutting surface speeds have little effect on the resulting cutting forces above $\sim 40 \text{ m}\cdot\text{min}^{-1}$, feed rate trials are normally undertaken within 'normal' cutting speeds of $40\text{-}60 \text{ m}\cdot\text{min}^{-1}$ as to minimise any additional effect caused by of tool wear.

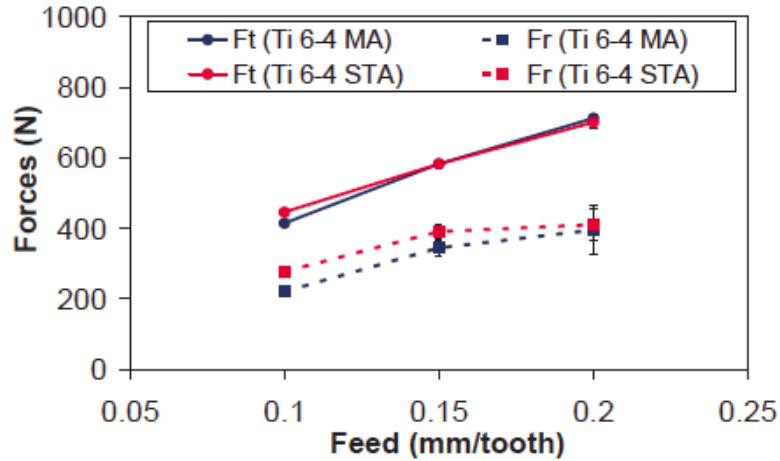


Figure 2.24 Resulting relationship of cutting and thrust forces as a function of feed rate for machined Ti-64 samples in a mill annealed (MA) and solution heat and aged (STA) condition [124].

As shown in the plot in Figure 2.24 [124], the relationship between the resulting cutting and thrust forces with respect to the applied feed rate can be seen to be approximately linear, a relationship identified in the Oxley cutting force model [125]. Through the application of a trend line, Oxley’s model determines cutting force coefficients (CFCs) from the gradient and y-intercept values relating these to “cutting coefficients” and “edge coefficients” respectively, see Equation 2.4 and Equation 2.5.

(Cutting direction) Cutting force $F_z = K_c \cdot \omega \cdot FR + P_1 \cdot \omega$ Equation 2.4

(Feed direction) Thrust force $F_y = K_f \cdot \omega \cdot FR + P_2 \cdot \omega$ Equation 2.5

Where ω is the depth of cut and FR the feed rate. Oxley attributed the cutting and feed cutting coefficients, K_c and K_f , to the amount of force occurring on the shear band and therefore the amount of force required to machine the material and the edge coefficients, P_1 and P_2 , to frictional interactions of the tool with the workpiece.

Since the relationship is linear, the Oxley model [125] allows for a minimal number of incremental feed rate trials to be undertaken to determine their relationship. Armendia *et al.* [126] used the Oxley model to compare the cutting characteristics during orthogonal cutting trials for a selection of $\alpha+\beta$ titanium alloys. The corresponding force results for each individual feed rate are presented in Figure 2.25. Average values are determined from a minimum of two repeat experiments, with a claimed 3% uncertainty; however no further indication as to the spread for all of the values was included.

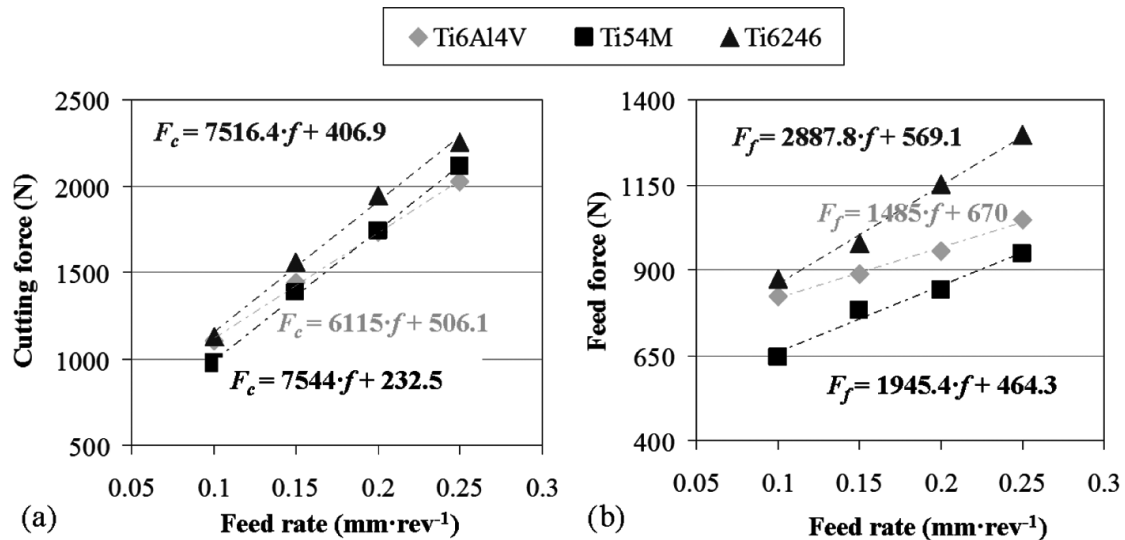


Figure 2.25 Resulting relationship of cutting and thrust forces as a function of feed rate for orthogonally machined titanium samples, illustrating the effect of chemical composition using test specimens of; Ti-64, Ti-54M and Ti-6246 [126].

From this investigation Armendia *et al.* [126] linked the associated poor machining performance of Ti-6246 and improved machining performance of Ti-54M [127]–[129] to the corresponding CFCs. Here the related edge coefficients or “edge effect” for both the thrust and cutting components of force were attributed to have a relationship with the temperature of the cutting environment, with Ti-6246 having an assumed elevated cutting temperature that subsequently led to accelerated tool wear. However the claim regarding the temperature of the cutting environment was not substantiated, nor was any further discussion made discussing the behaviour of the cutting coefficients (gradients) for each of the materials, which showed no correlation to tool wear performance. It is of the opinion of the author that the CFCs obtained using Oxley’s approach need to be taken with some degree of caution. Drawing into question the validity of the edge coefficients, determined via extrapolation, the values of which correspond to a theoretical cut occurring at a zero depth of cut. Furthermore such a relationship implies a value of force can be calculated for a machining operation occurring at a negative depth of cut, a scenario that is obviously impossible. The edge coefficient has become a widely excepted phenomenon, commonly attributed to frictional forces at the tool/workpiece interface occurring when the tool is effectively rubbing along the surface of the workpiece. If this justification is blindly accepted, the size of the edge coefficient lends itself to further paradoxes.

2.7 The “size effect” in metal cutting

It has become widely believed that when metal is removed during machining there is a substantial increase in the specific energy required when there is a decrease in chip size [129]–[137]. This phenomenon has been observed when machining all metallic systems and was first investigated in detail by Backer *et al.* [131] who performed a series of trials in which the shear energy was determined as a function of specimen size, incorporating cutting trials of increasing metal removal rates; grinding, micromilling and turning. To determine the specific cutting energy required during machining it is necessary to normalize the resulting cutting force data with respect to the volume of material being removed. As a result of this, there is a non-linear relationship between the specific cutting energy versus uncut chip thickness (feed rate), as shown in Figure 2.26.

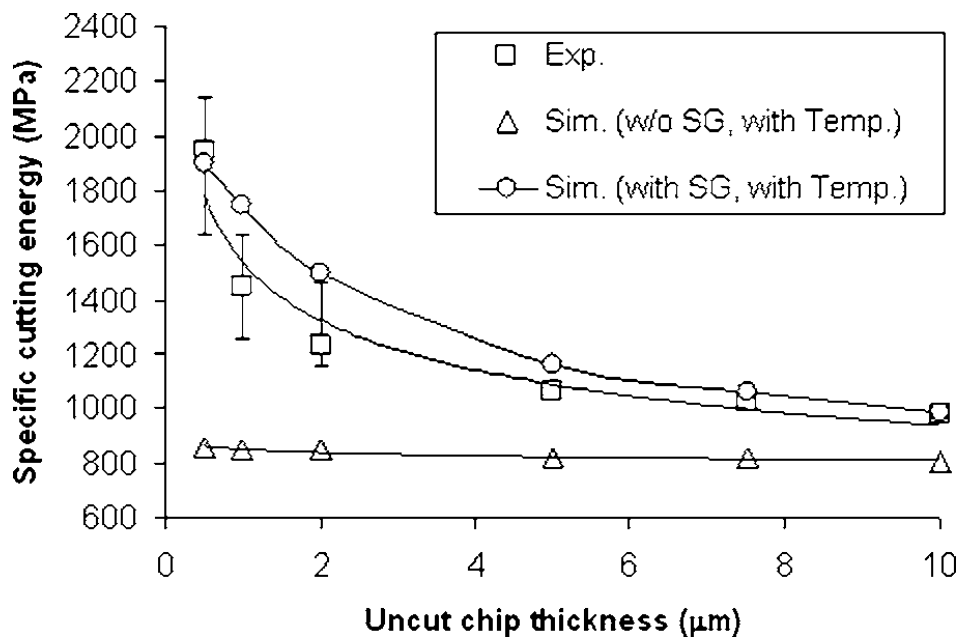


Figure 2.26 Typical resulting ‘size effect’ relationship of specific cutting energy as a function of uncut chip thickness [129].

This paradox is often referred to as the “size effect” with many investigations devoting a substantial amount of time into capturing and attempting to rationalise its properties. Shaw [130], an advocate of the size effect, associated the increase in cutting force with decreasing chip thickness alongside his own theory of shear band formation that relies upon the formation of microcracks. Shaw proclaimed that during machining the tool is constantly encountering stress-reducing microstructure defects, such as grain boundaries, missing atoms or impurity atoms, all of which can create short-range inhomogeneities, which constantly limit the total cutting forces. Therefore if the uncut chip thickness is decreased the probability that the tool encounters a

defect also decreases. Thus creating a condition where the forces steadily rise, reaching a maximum point that corresponds to a theoretical shearing strength of the material. The schematic presented in Figure 2.27 illustrates Shaw's microcrack shear band theory, whilst machining the material is subjected to very large strains giving rise to sites of stress concentration. These develop into sites for microcracks to nucleate and grow. Once a critical number of microcracks have coalesced this gives rise to the development of a shear band [131].

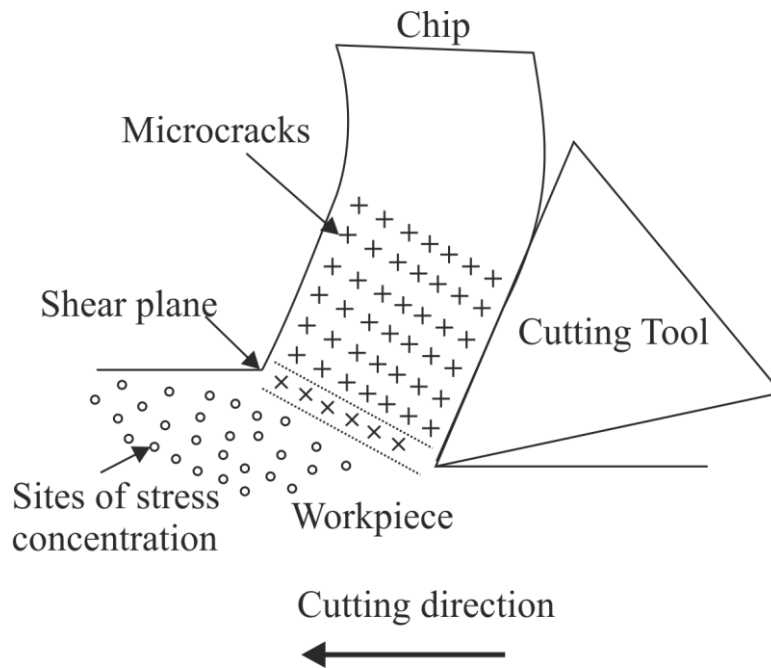


Figure 2.27 Schematic illustrating Shaw's approach to shear band formation relying upon the coalescence of microcracks that are generated at sites of stress concentration, after Shaw [131].

Using the Merchant empirical formula [51] as outlined in §2.1 and implementing the raw resulting force data for orthogonal machining of aluminium 7075 T6 alloy, Ng *et al.* [137] determined the effective friction of the cutting environment across a range of depths of cut. The results shown in Figure 2.28 illustrate a similarly observed size effect type relationship, whereby the coefficient of friction appears to increase significantly with a decrease in the chip thickness.

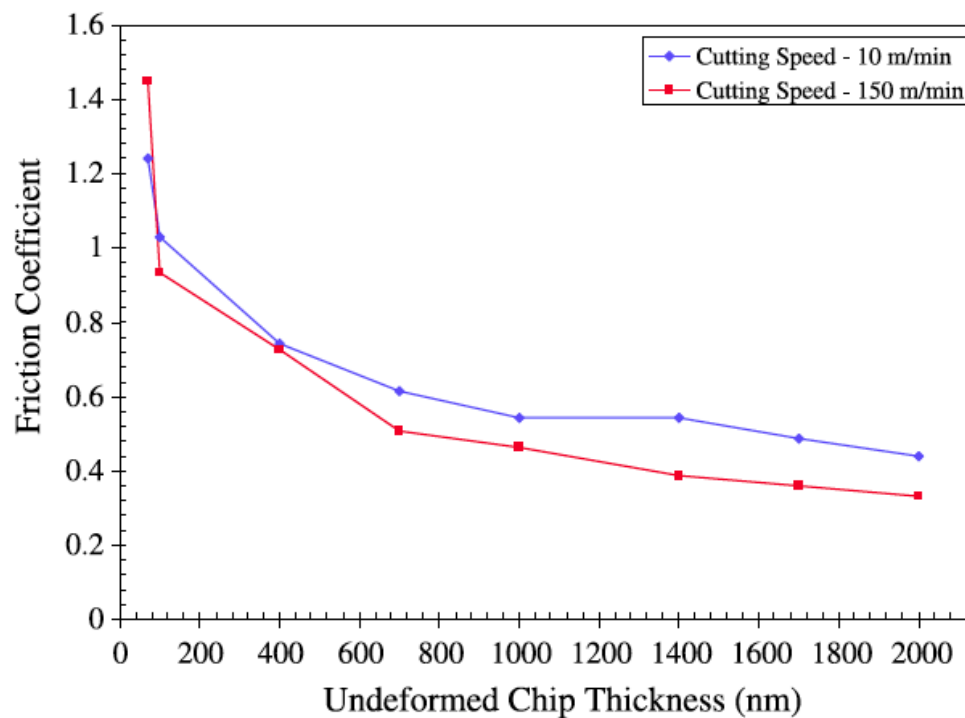


Figure 2.28 The typical friction coefficient relationship with uncut (undeformed) chip thickness during orthogonal machining of 7075 T6 aluminium cut at 10 and 150 $\text{m}\cdot\text{min}^{-1}$ [137].

Ng *et al.* [137] justified the existence of the frictional size effect being a result of the material strengthening by virtue of a decrease in the tool/workpiece interface temperature, in response to the decrease in the total contact area. The author acknowledges that a reduction in the chip thickness may result in a subsequent reduction in the cutting environment temperature, however such induced heating has been shown not have a significant effect on the workpiece material [134]. Further observations of the resultant force feed back data does however help explain how such a phenomenon occurs. The plot shown in Figure 2.29 illustrates the typical force feedback behaviour of a material across a range of feeds during an orthogonal cutting trial (after Armendia *et al.* [138]). Due to the thrust force having a higher offset y-intercept value than the cutting force, this results in the friction coefficient calculation producing the characteristic non linear relationship. In addition, due to the cutting and

thrust force plots intersecting, this results in values for the effective coefficient of friction to be greater than 1 for an uncut chip thickness of less than ~ 0.03 mm.

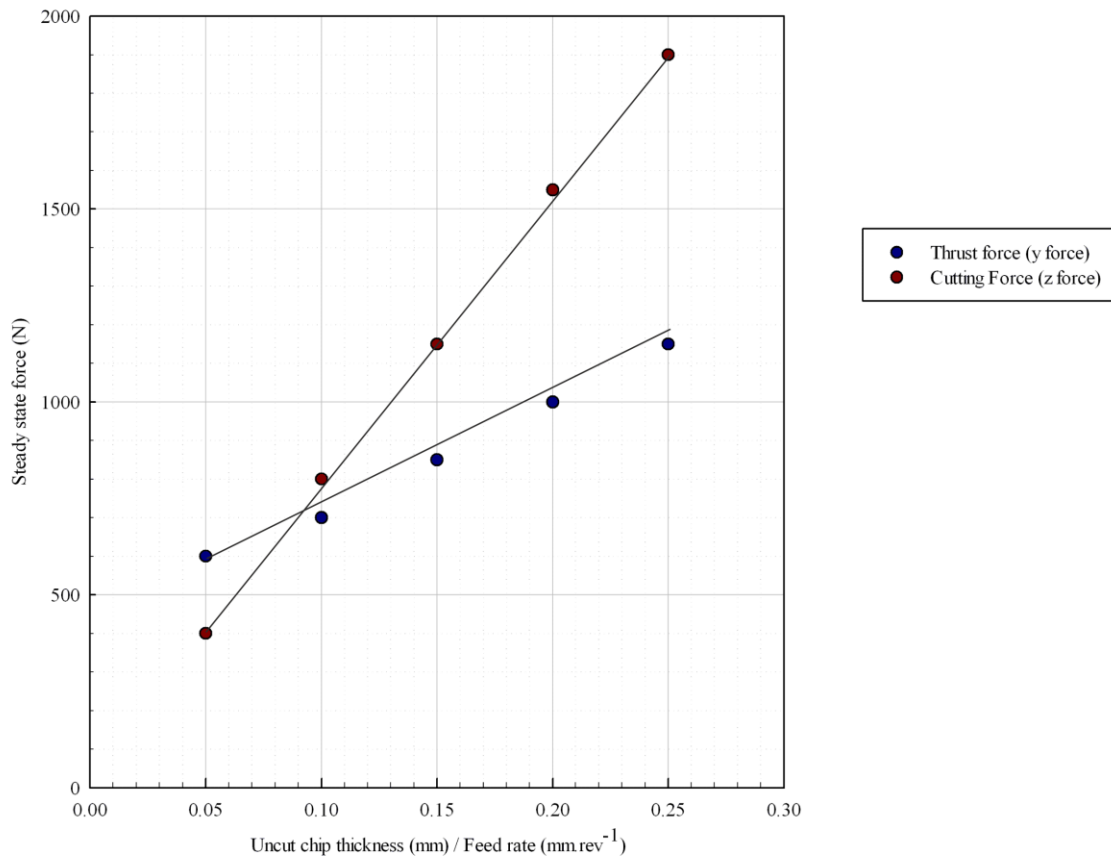


Figure 2.29 Typical feed-force relationship illustrating a cross over point occurring at an uncut chip thickness of ~ 0.09 mm, below which the values of thrust force are higher than the experienced cutting force, after Armendia [138].

As previously illustrated by Figure 2.26 and Figure 2.28 the nature of the size effect is linked to the phenomenon of the edge coefficient y-intercept values. In response to this many independent investigations within literature have been undertaken to rationalise their presence. Studies have shown that as the uncut chip thickness is reduced, the geometry of the tool at the cutting edge becomes a significant determining factor on how the chip is being generated.

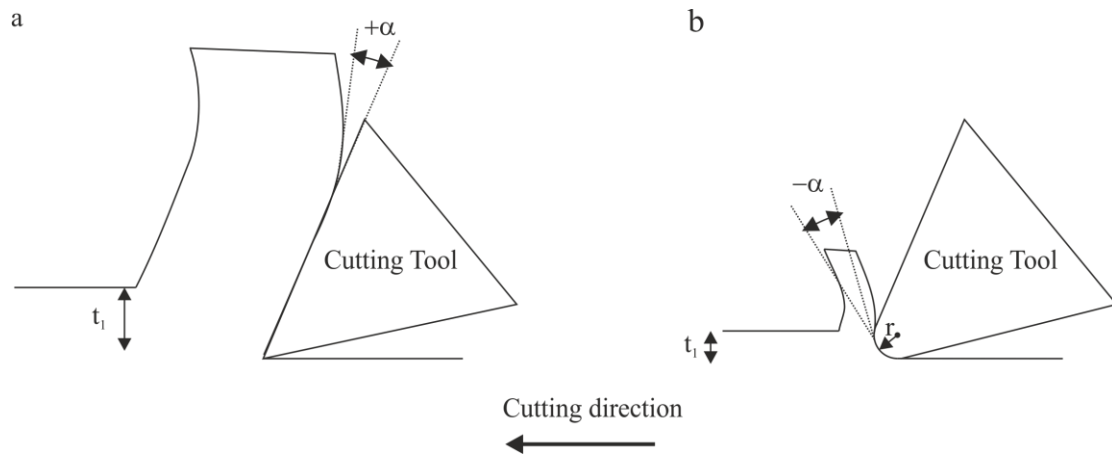


Figure 2.30 Schematic illustrations of a orthogonal machining arrangement when cutting using a tool that has an (a) infinitely sharp cutting edge and (b) cutting with a tool that has a edge radius (r) greater than the uncut chip thickness (t_1), after Ng [137].

The schematics shown in Figure 2.30 illustrate differences in cutting behaviour when using a tool that has an edge radius that is either infinitely sharp/ proportionally insignificant to the size of the uncut chip thickness (Figure 2.30(a)) or has an edge radius of a similar scale to that of the uncut chip thickness (Figure 2.30(b)). When cutting with a large uncut chip thickness, the cutting process follows a traditional cutting behaviour, with the tools corresponding clearance and rake angles being determined by the tools shape and position within the tool holder. However when cutting a small uncut chip thickness or when using a tool with a large edge radius, the effective cutting rake angle becomes negative [137][81]. The effective rake angle is determined by the angle between the vertical axis and the tangent to the contact point between the cutting tool and the uncut chip thickness (t_1).

When machining under conditions similar to those depicted in the schematic in Figure 2.30(b), the process is often referred to as “ploughing” with the corresponding forces labelled “ploughing forces”. Under such conditions the tool can be observed to drag along the surface of the workpiece. In principle, if the uncut chip thickness (t_1) is reduced significantly, the material under the tool will be compressed under the tools cutting edge, resulting in no material being removed as a chip. When the uncut chip thickness is increased to a point where chip can be generated, the chip will begin to form through the shearing of the workpiece. Due to the negative effective rake angle, in conjunction with the small uncut chip thickness, the cutting process generates a steep shear band angle resulting in a significant amount of plastic deformation throughout the chip. It is always worth bearing in mind that during a cutting cycle the dynamics of the cut can be constantly evolving if for example, a built up edge were to form ahead of the tool, as shown in Figure 2.31, this can change the effective rake

angle since the addition of the built up edge will inevitably change the cutting edge's geometry.

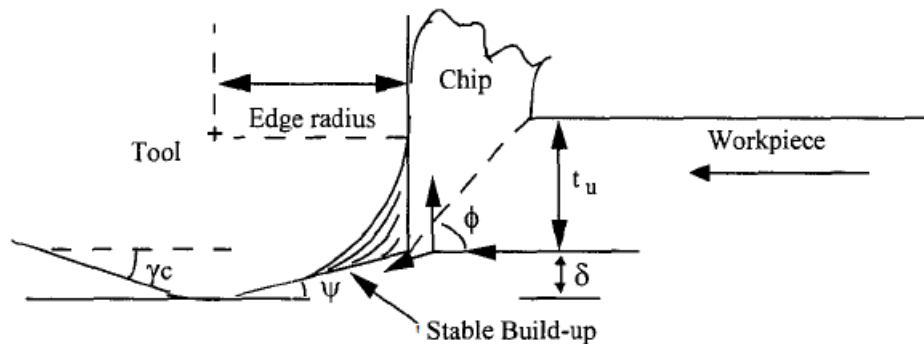


Figure 2.31 Schematic diagram of an orthogonal cutting arrangement where the edge radius is approximately equal to that of the uncut chip thickness and a stable built up edge has formed ahead of the tool, thus changing the effect tooling geometry [139].

Studies investigating the nature of the ploughing forces have shown a further dependency on the edge radius of the tool [137], [140]–[142], whereby through the use of a tool that has an edge radius that is always less than that of the uncut chip thickness (i.e. the use of a sharper tool) can reduce the magnitude of the ploughing forces. In practice this would equate to a reduction in the y-intercept values for the typical force versus feed rate relationship as shown in Figure 2.29. Since the discovery of the size effect by Backer *et al.* [131] in 1952 the phenomenon has been the subject of substantial study. In the following year Masuko [142] published a revised theory that stated that total recorded resulting cutting forces comprised not only the deformation forces required to generate a chip, but also an indentation force generated as the tool penetrates the workpiece. Unbeknown to Masuko's findings Albrecht [143] published a similar report detailing a method of decoupling the ploughing forces from the total force data. (Note Masuko's reference to an indentation force equals that of the ploughing force referred to by Albrecht.) Following their publication, Shaw [144] vehemently rebuffed the claims made by both Masuko [142] and Albrecht [143] making claim that their methodologies required untenable assumptions, namely that the size of the edge radius will always be “insignificant”, a claim not supported by the author. The principles of the findings by Masuko [142] and Albrecht [143] result in a challenging of the size effect phenomenon. The plots shown in Figure 2.32 demonstrate how the force data displayed using the traditional methodology displays the typical non-linear behaviour, following the removal of the indentation force the specific cutting energy shows independence to the uncut chip thickness and remains constant.

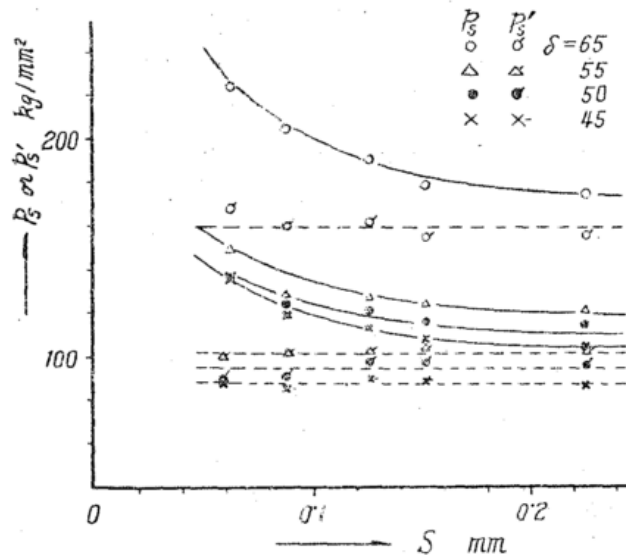


Figure 2.32 Resulting relationship of specific cutting energy and uncut chip thickness for orthogonal machining trials with each data set for variable tooling approach angles represented by a solid and dashed line; the solid line indicates the typical ‘size effect’ relationship prior to removing the ploughing forces and the dashed line represented the corresponding relationship once the ploughing forces have been removed [142].

Albrecht [143] found once the uncut chip thickness was greater than the edge radius of the tool, the relationship between the uncut chip thickness and the resulting force response became linear for both the cutting and thrust components, as shown in Figure 2.33. The corresponding cutting and thrust ploughing forces, P_1 and P_2 respectively, are determined by extrapolating the linear relationship back to the y-intercept.

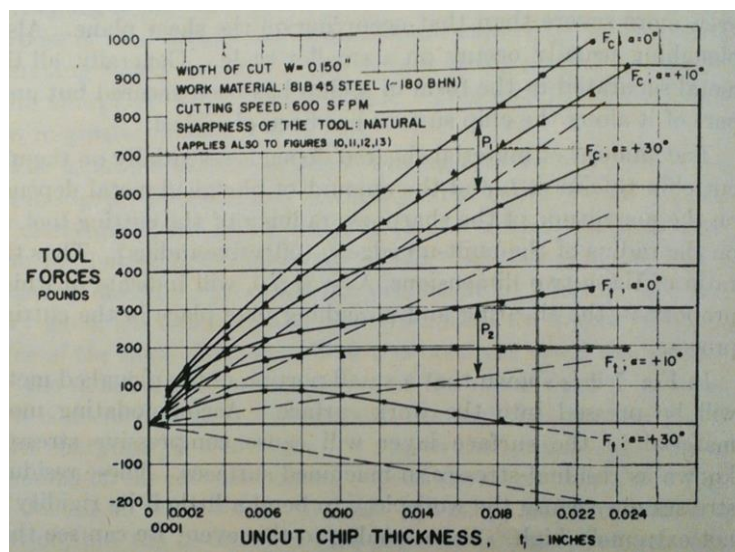


Figure 2.33 Cutting F_c and thrust F_t force relationship with uncut chip thickness t_1 , for a range of rake angles $\alpha = 0^\circ, 10^\circ$ and 30° . With components P_1 and P_2 representing the ploughing force for F_c and F_t respectively [143].

The total resulting cutting force F_z can be written in terms of the ploughing force (P_1) and the component of force in the direction of the tool motion (Q_1), Equation 2.6.

$$F_z = P_1 + Q_1 \quad \text{Equation 2.6}$$

Similarly the total resulting thrust force F_y can be written in terms of the ploughing force (P_2) and the component of force perpendicular to the direction of the tool motion (Q_2), Equation 2.7.

$$F_y = P_2 + Q_2 \quad \text{Equation 2.7}$$

The effective friction coefficient (μ_Q) for the cutting process can therefore be determined by substituting the ploughing forces from the cutting and thrust forces, Equation 2.8.

$$\mu_Q = \frac{(F_t - P_2) + (F_c - P_1) \tan a}{(F_c - P_1) - (F_t - P_2) \tan a} \quad \text{Equation 2.8}$$

The plots shown in Figure 2.34 demonstrate how the frictional performance displayed using the traditional methodology displays the typical nonlinear behaviour (N.B. Masuko [142] has added a straight trend line to the nonlinear plots). Following the removal of the ploughing force, using Equation 2.8, the effective coefficient of friction shows independence to the uncut chip thickness and remains approximately constant.

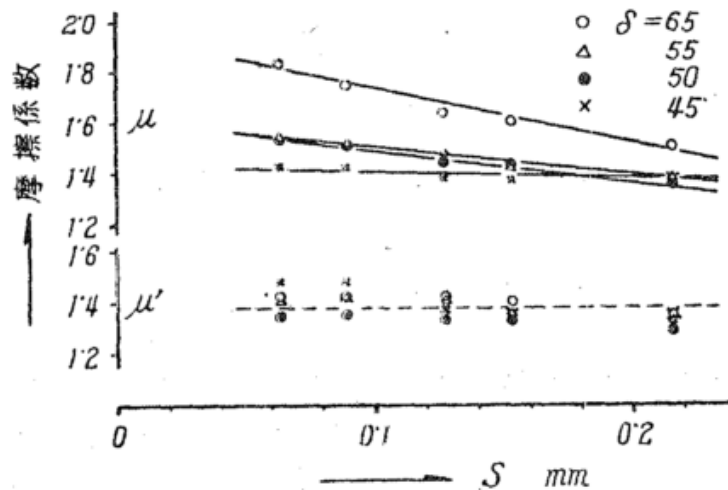


Figure 2.34 Resulting relationship of friction and uncut chip thickness for orthogonal machining trials with each data set for variable tooling approach angles represented by a solid and dashed line; the solid line indicates the typical 'size effect' relationship prior to removing the ploughing forces and the dashed line represented the corresponding relationship once the ploughing forces have been removed [142].

Since their publication Masuko [142] and Albrecht [143] are rarely directly cited in literature in reference to separating the ploughing forces from the total resultant forces. With only occasional further independent 'rediscoveries' that discuss similar fundamental principles, such as by Arsecularatne [133] who also highlighted that the ploughing forces can be considered not to contribute to the chip removal process.

2.8 Microstructure response to variable feed rate and further machining induced microstructure damage

Due to the increase in structurally critical titanium products there is an ever increasing demand to gain a greater understanding as to what impact the machining process is having upon the material. Technical information papers that have been recently released from the Department US Defence and NASA show a similar demand existed during the rise of space exploration, focusing on the use of beryllium. Due to its superior high specific strength (tensile strength/density) beryllium is an attractive material for space flight and military hardware, however due to its damage sensitivities and toxicity its application remains limited. Importantly in reference to this investigation beryllium possess similarities to titanium, being its hexagonal close packed (HCP) structure with a below normal c/a ratio of 1.568 compared to titanium being 1.598, normal equalling 1.633 [145]. In order to minimise the number of mechanically induced twins in beryllium special care is required during machining, since it is claimed that even light abrasion, such as the use of 600 grit emery cloth, can reintroduce twins into the uppermost surface grains [146]. The author wishes to highlight that the following investigations covered within this part of the literature review, that study the machining characteristics of beryllium, are amongst the very few that have identified the presence of machining induced twins in commercially applicable alloys/ components. These studies have also highlighted the significance of having such microstructure features and the potential deleterious effect they may have on the in-service properties a component, with further indication as to how to reduce the amount of twins present following machining or methods of how to remove them from the subsurface layer.

The total shear strain imparted into the material substructure has been shown to be directly proportional to the depth of cut [79], [80], the plot shown in Figure 2.35 further illustrates this relationship with respect to the total depth of machining induced twinning, which increases proportionally at ~10% of the depth of cut [146], [147]. Goldberg [146] also found whilst studying the effect of machining temperature on the depth of twinning that at elevated temperatures 230°C, 290°C and 340°C the depth of twinning becomes insensitive to the depth of cut. Figure 2.35 also demonstrates how the depth of twinning at each respective depth of cut shows a

marginal decrease with an increase in temperature, an observation also made by Rennhack [148] who showed that twinning, microcracking, and residual stress could be eliminated when machining at 400°C. Rennhack [148] linked this behaviour of beryllium to the activation of multiple slip systems that occur whilst machining near its ductile-brittle transition temperature.

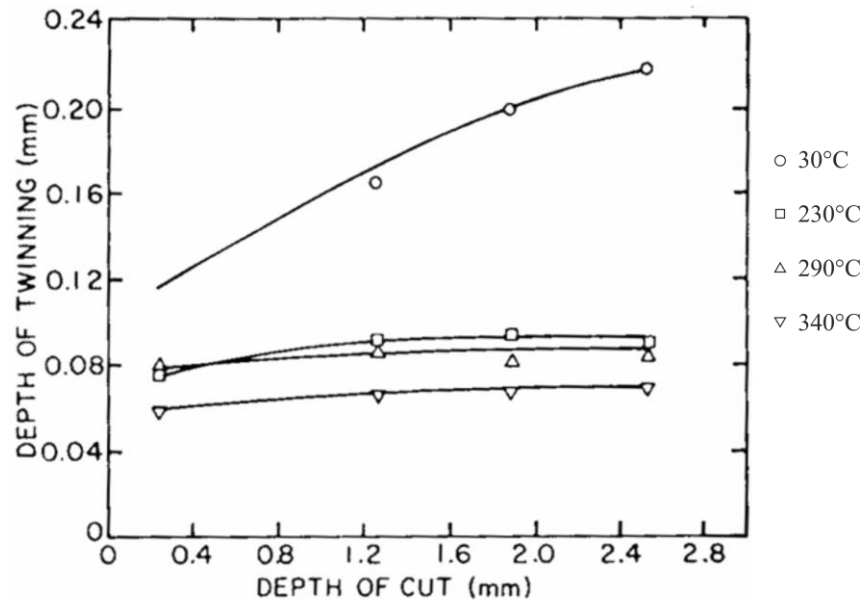


Figure 2.35 Resulting depth of imparted mechanically induced twinning in beryllium as a function of depth of cut for machining operations undertaken at varying temperatures [148].

The plots shown in Figure 2.35 show how that by reducing the depth of cut successively the remaining amount of residual twinning can be reduced, if the trend lines were to be extended to the y-axis it implies a minimum twinning depth value at the contact of the tool for each respective cutting temperature. The author has attributed this characteristic to be the result of the independent ploughing force that precedes the cutting process. It has been shown following extensive research regarding the impact of the machining that when beryllium is subjected to high loads in structural applications, these surface changes can cause premature failures [149], [150].

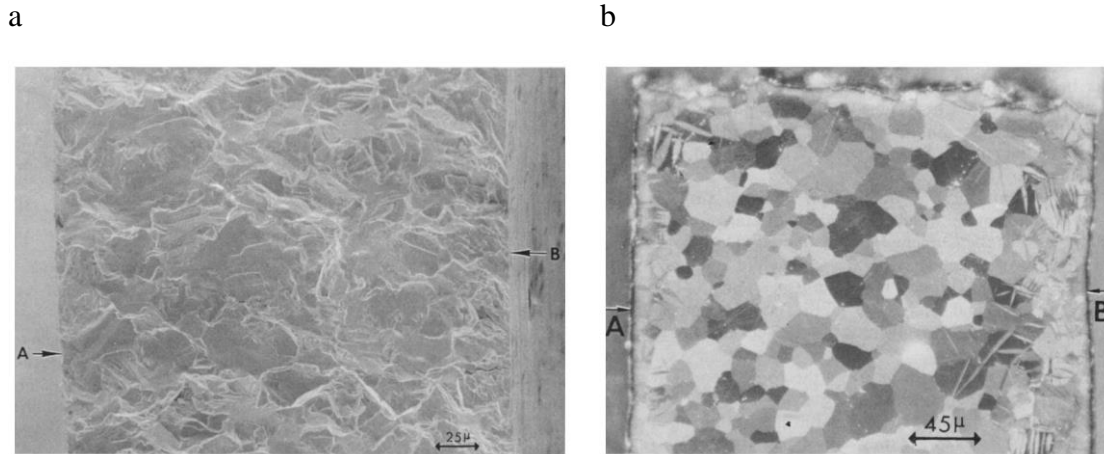


Figure 2.36(a) Light micrographs of a fractured thin walled beryllium surface demonstrating large facets adjacent to surface A and small facets adjacent to surface B, (b) corresponding polarized light micrograph of a representative region of the thin walled beryllium sample demonstrating significantly more twins in the region adjacent to surface B [147].

Moreen [147] whilst investigating the presence of deformation twins in thin walled beryllium samples found a dependency on the nature of the modes of failure in relation to the density of induced twins. The optical micrographs presented in Figure 2.36(a) show the typical deformation characteristics of the failed material. The corresponding polarized light micrograph (Figure 2.36(b)) indicates the severity of the induced twinning with surface A presenting a relatively minimal intensity of fragmentation of cleavage facets whilst surface B shows a heavier layer of fragmented facets. Taylor *et al.* [151] also studied the deleterious effect of twins being present in a component's substructure following a parametric investigation whereby twins were induced via grinding which, similar to turning, is a method commonly used for finishing of aero-structural components. The corresponding sample properties' were further analysed using a series of a bend tests with heavily twinned regions displaying the worst performance. Before entering service it is therefore necessary for machined beryllium parts to have the entire remaining twin damage removed [152], [153]. Common methods of relieving the machining damage include either annealing the material at an elevated temperature or by etching away the uppermost surface material [154], however such methods can affect dimensional tolerances. Goldberg [146] also discussed a link between some aspects of machining induced damage directly with the material's surface condition. It was reported that under optical observations a satin-like appearance corresponded to light machining subsurface damage (0.05 mm depth) with a striated surface corresponding to heavier damage, the

degree of which increases with increased depth of damage, during lathe turning of beryllium.

2.9 Role of crystallographic texture during machining

Machining investigations on single crystal samples, typically aluminium, brass or copper, have shown a dependency on the shear angle and cutting forces with the crystallographic orientations of the metals being cut [155]–[162]. The schematics shown in Figure 2.37 illustrate the common experimental arrangements used to capture the machining dependencies on the crystallographic orientation of the workpiece, them being; planing, plunge-turning and in-plane machining. While planing experiments can provide detailed data in terms of cutting forces, only a single crystallographic orientation can be machined at a time. In addition to the planing configuration (Figure 2.37(a)), the plunge-turning configurations shown in Figure 2.37(b-c) provide data for an entire range of cutting directions within a specific zone axis. The plunge turning experiments can be divided into two types, as illustrated in Figure 2.37(b) that shows how the zone axis $[a b c]$ serves as the axis of rotation and Figure 2.37(c) has the cutting plane normal (in-plane) as the axis of rotation.

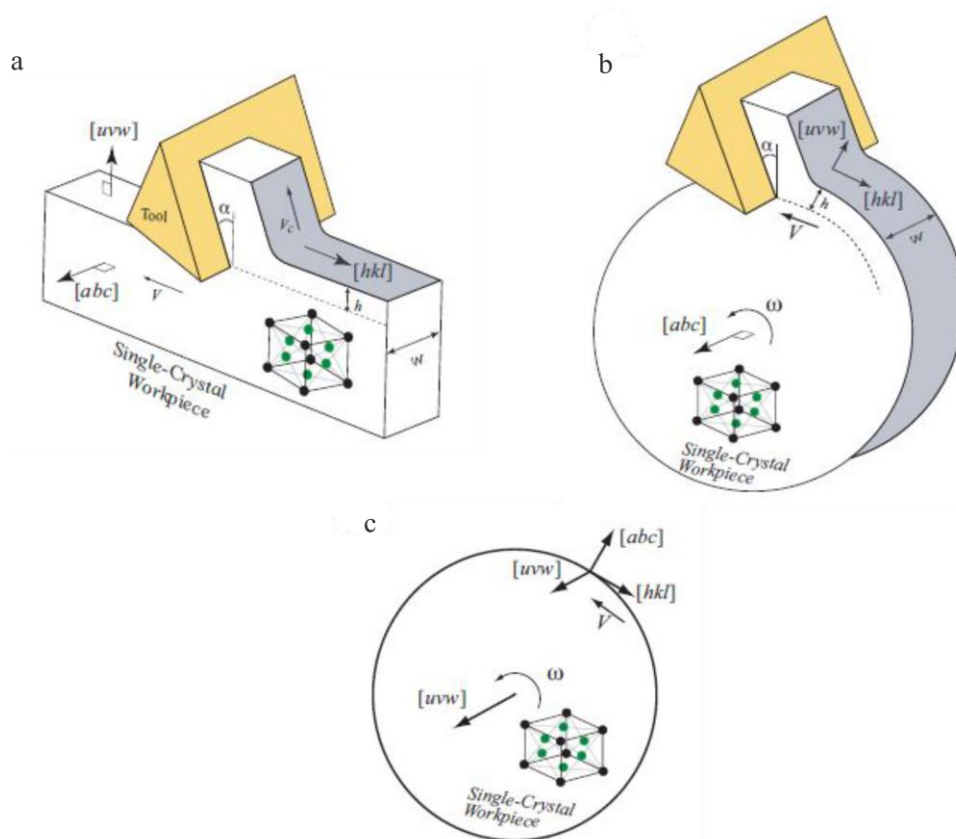


Figure 2.37 Machining arrangement for machining single crystal samples using; (a) planing configuration, (b) plunge-turning configuration, and (c) in-plane machining [155].

Cutting force data collected during such microstructure machining investigations are compiled in order to show the dependencies of the materials cutting properties in relation to the underlying texture. The data plots presented in Figure 2.38 show the resulting relative specific energy variations for plunge-turning of single crystal aluminium samples, at varying incident angles.

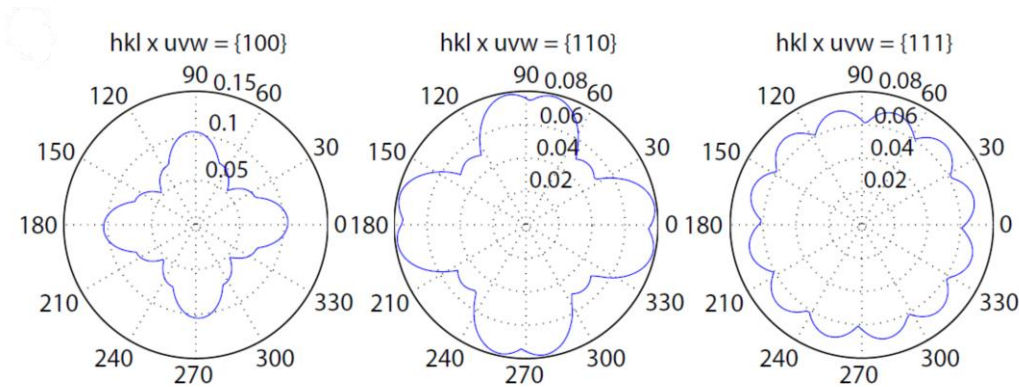


Figure 2.38 The resulting variation in specific cutting energy as a function of crystallographic orientation as determined via a plunge turning configuration [159].

The results shown in Figure 2.38 show the typical relationship of specific cutting forces for an FCC structure, with the cutting forces collected about the $[0\ 0\ 1]$ zone axis ($[a\ b\ c]$ format from Figure 2.37) showing repeatable four-fold symmetry, as related to the crystallographic symmetry of the $[0\ 0\ 1]$ zone axis [159]. Here the variation in relative specific cutting energy has been attributed to the exposure of available slip planes, with specific crystal inclinations permitting an increase in available deformation modes [160], [161].

Whilst investigating the chip formation mechanisms of single crystal β -brass, Ueda *et al.* [162], found that the machined surface integrity of the single crystal is also affected by its underlying crystallographic orientation. Whereby, the machined surface roughness was observed to improve when machined under a favourable cutting direction with respect to the workpiece's crystallographic orientation. Ueda *et al.* [162] observed a relationship between the crystallographic orientation and the resulting chip type, where fluctuations in chip type were observed to impact upon cutting forces and surface roughness. The findings of Ueda *et al.* [162] imply that for specific material type a desirable crystallographic orientation must be selected to obtain an optimised surface finish. Single crystal machining investigations have so far only been undertaken using FCC and BCC structures, however many of the behavioural characteristics can be inferred upon an α -titanium HCP structure. Since for titanium it has been shown through extensive research that the effect of

crystallographic texture on mechanical properties can be significant. This material property dependency was demonstrated by Lütjering *et al.* [4], Bowen [163] and Tromans [164] who showed how the tensile properties of a rolled, fully equiaxed Ti-64 samples exhibited significant property variation as a direct result of the test direction and initial starting texture. The plots shown in Figure 2.39 illustrate property variation for two common textures, these being the transverse (T) texture and the basal/transverse (B/T); in each case both material types follow a similar dependency to the testing orientation as depicted in the adjacent schematics. Note for the B/T texture the basal planes remain parallel to the test direction. The plots in Figure 2.39(a) show how for both the T and B/T texture types the variation of modulus of elasticity (E) is comparable, with the B/T texture showing lower elastic modulus values than the T texture due to the basal (B) plane component having an inherently low elastic modulus during all test orientations. For both material types, the highest value of elastic modulus was achieved when the material was loaded parallel to the HCP c-axis, as the loading direction is rotated the elastic modulus of the HCP crystal reduces. The variation in yield stress as shown in Figure 2.39(b), shows how both T and B/T textures exhibit a minimum in yield stress when tested when orientated at 45° with the highest value of yield stress along the transverse direction (TD).

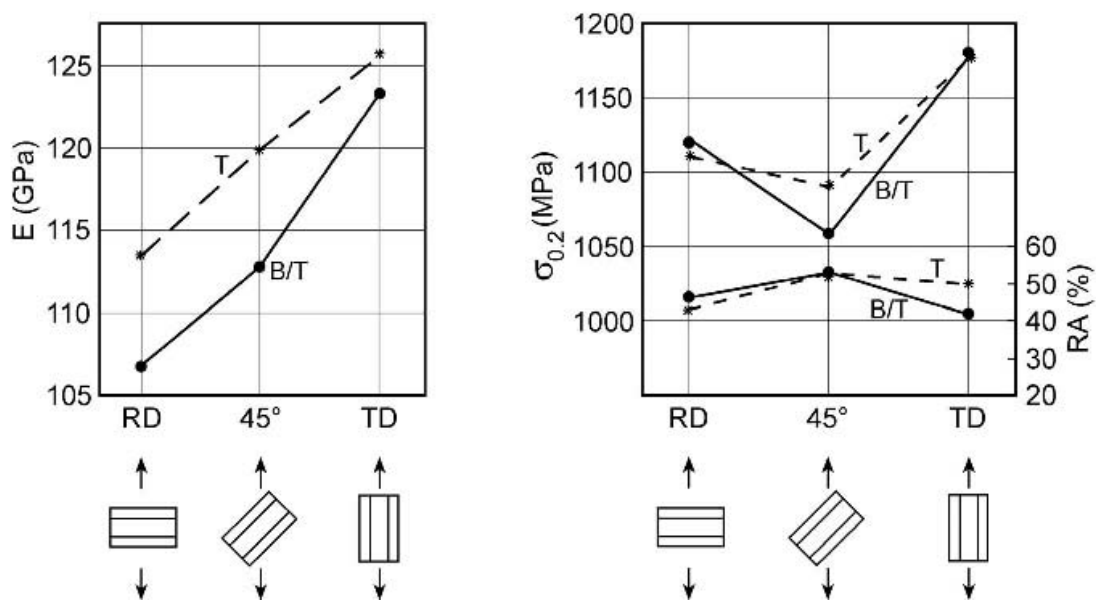


Figure 2.39 The relationship of (a) elastic modulus (E), (b) yield stress ($\sigma_{0.2}$) and reduction in area (RA(%)) as a function of loading direction in relation to the average orientation of Ti-64 test specimens [4].

The highest yield stress values for testing in TD direction due to the restriction of a-type dislocations since a-type dislocations are orientated parallel to the basal plane, which for TD are perpendicular to the testing direction. This results in the shear stress

therefore equalling zero, resulting in the activation in $\langle c + a \rangle$ type dislocations, which require significantly higher stresses to move. For RD and 45° , a-type slip can be more easily activated. At 45° the reported low yield stress value is due to the basal plane being oriented at 45° to the test direction, thus maximising the number of available slip systems. Whereas for RD, only the basal plane remains parallel to the loading direction, resulting in a slight increase in the yield strength.

2.10 Tool contact

The machining of titanium possess a significant number of challenges induced by its inherent high strength and fracture toughness at elevated temperatures, as well as a strong affinity to reactive elements such as oxygen and carbon. During machining the most commonly adopted method of assessing a materials machinability considers the rate of tool wear during operation. With maximum tool life being dictated by a pre-determined threshold. Tool wear can be broadly defined by the following three categories.

Abrasive wear: The removal of particles caused by the rubbing of the tool against the workpiece and the chip resulting in flank wear.

Diffusive wear: Atoms from tool diffuse across into the chip, commonly along the face of the tool resulting in crater wear

Fracture failure: is the result of an abrupt failure of the tool caused by excessive or dynamic loading.

During machining gradual wear mechanisms such as abrasive and diffusive wear are most favorable, since through control of machining variables such as cutting speed and coolant type, tool life can be maximized thus guarding against fracture. However, with the drive to manufacture titanium components at increased manufacturing rate the mechanisms of tool wear needs to be managed. Since any increase in machining speed will inherently result in an elevation in cutting temperature, which will lead to accelerating the abrasive and diffusive wear mechanisms as well as the possibility of further thermal shock fractures [165], [166].

For a concise summary on the modes of tool wear see the Appendix

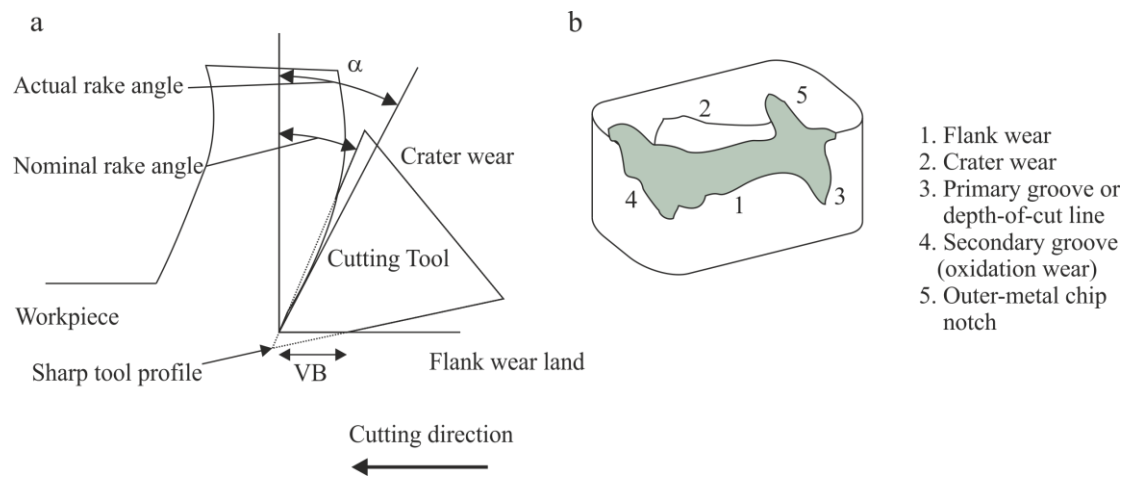


Figure 2.40(a) Cross-section schematic of a worn cutting tool showing the effect of crater wear on the tool rake angle and flank wear (VB) (b) schematic illustrating the regions of tool wear on the rake, flank and nose of the cutting insert [166], [167].

2.10.1 Crater wear

Crater wear most commonly occurs along the face of the cutting insert and is a diffusive wear mechanism that is accentuated by the high temperatures generated at the tool chip interface and is controlled by the chemical affinity of the workpiece and tool materials. The size and shape of the resulting crater can have a substantial influence on the cutting condition by altering the effective rake angle of the insert as shown in Figure 2.40 [165], [168].

2.10.2 Flank wear

Flank wear is an abrasive wear mechanism caused by the insert rubbing against the machining surface [165] resulting in a change in the tools geometry as indicated in Figure 2.40. Most industrial applications utilize the maximum dimension of flank wear (VB) as the main determining indicator for tool replacement [169] since it has a direct influence on the workpiece's surface finish. Therefore a machinist would set a safe limit parameter for VB, which is commonly 0.25 mm average and 0.5 maximum wear for carbide cutting tools [166]. NB. VB safe limit dependent on the dimensional tolerance required of the component.

Typically for titanium, cutting is generally carried out within the region of 60-70 $\text{m}\cdot\text{min}^{-1}$ to maintain a low cutting temperature and for such tooling/workpiece combinations, turning surface speeds in the order of 70 $\text{m}\cdot\text{min}^{-1}$ are recommended for optimum tool life [165], which correlates with the observed minimum depth of induced microstructure damage. At elevated cutting speeds the temperature of the cutting environment begins to rapidly rise. An increase in cutting temperature has been attributed to an increase in the overall chemical reactivity of the system, leading to an increase in chemical attack to the tooling insert [170]. At low speeds however,

the ductile nature of titanium encourages mechanical wear to dominate as a wear mechanism of the tool, promoting galling of the workpiece.

2.10.3 Built up edge

A built up edge (BUE) is a formation ahead of the tool and can create an integral interface between the workpiece and the tool often serving as a protective barrier to flank and crater wear. The size and shape of the BUE can also alter the shape of the leading edge thus changing the effective rake angle [170]. An unstable BUE can lead to irregular wear on cutting edges that can generate a poor surface finish when fragments of the BUE are dragged under the leading edge of the tool [143], [171]–[174]. Due to the highly abusive cutting environment that is inherent when cutting titanium, the mechanics of tool wear are regarded by machinists as perpetually operating within an effective ‘very high speed’ category when aligned with the mechanics of cutting ferrous materials. Kramer [171] acknowledged that if it were not for the ability of titanium to form a stable carbide interlayer which promotes the formation of a stable built up edge, it would be impossible to machine titanium alloys due to high tool wear. There does however seem to be knowledge gap within literature detailing the potential positive properties a BUE may have in further protecting a cutting insert during machining. Since if the formation of a BUE could be controlled and be reproducible, it could be applied within a production environment. This could involve a pre-cut that conditions and protects an insert prior to machining a component. The relationship of VB versus cutting time can be represented as a wear curve as shown in Figure 2.41 with the mechanisms of flank that starts with a break in period where there is a rapid initial wear. Following this there is a steady state wear period where there is a uniform wear rate across the tools cutting edge followed by an abrupt transition to an accelerated wear period that eventually leads to the final failure of the cutting insert. The mechanisms of Crater wear follows a similar growth curve to those shown in Figure 2.41 [172], [175].

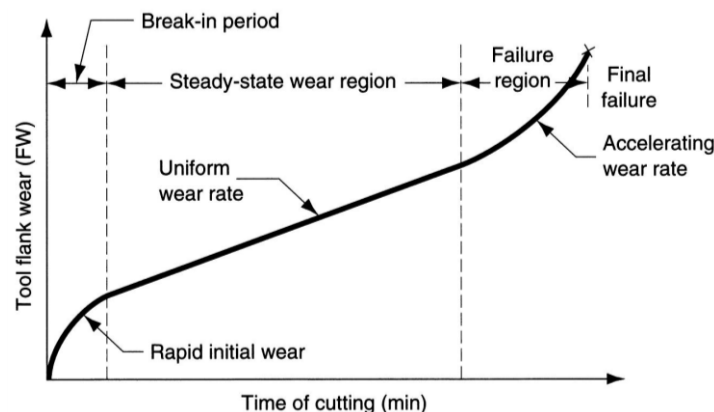


Figure 2.41 Typical wear profile of a cutting insert as a function of cutting time with key wear regions identified after, after Taylor [176].

2.11 Taylor relationship of tool wear

The traditional approach to determining a material's machining performance, with regard to tool wear, requires acquisition of a series of wear curves similar to that shown in Figure 2.41 obtained over a range of machining speeds. Once the predetermined wear limit has been reached for each machining speed, the machining time (tool life) is recorded. Transposing the tool life data onto a log data plot of time and speed gives rise to a linear relationship as shown in Figure 2.42.

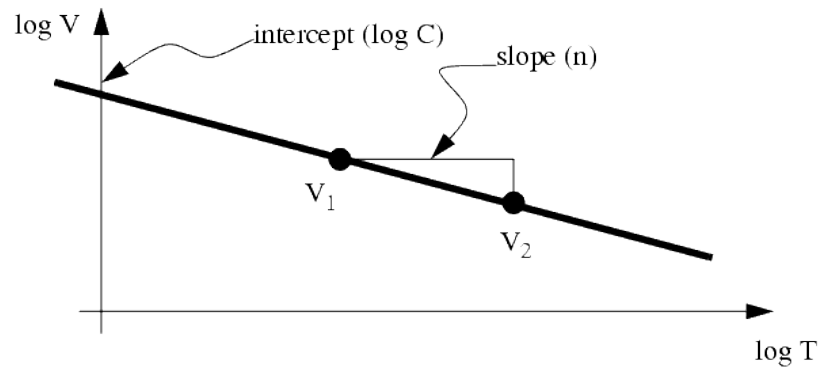


Figure 2.42 Taylor relationship of tool wear determined following a series of tool life trials used to determine tool life as a function of cutting speed [176].

Using the constants from the linear relationship the Taylor equation for tool life expectancy can be determined [176]. The Taylor relationship Equation 2.9 demonstrates how tool life (T) depends on the operation cutting speed (V_c) and the constants (n and C) that represent feed, depth of cut, workpiece material and tooling material. The Taylor equation for tool life expectancy allows machine operators to predict how long a tool will last for a given machining speed (assuming all other machining parameters remain constant).

$$V_c \cdot T^n = C \quad \text{Equation 2.9}$$

Whilst investigating the wear characteristics of uncoated carbide tools during orthogonal machining trials of Ti-64, Jaffery *et al.* [177] constructed a wear map derived from the tool performance over a broad range of speeds and feed rates. Typically prepared for the machining of ferrous alloys [178], [179], wear maps help machine operators identify the most suitable machining parameters.

The wear map presented in Figure 2.43 plots the cutting speed along the x-axis and feed rate along the y-axis. The data shows in addition to cutting speed, the depth of cut can also have a significant effect on wear performance. Most importantly the wear map reveals the presence of two regions of high tool wear in the midst of a moderate

tool wear region. These isolated high wear rate regions are positioned at a feed rate of $\sim 0.17 \text{ mm}\cdot\text{rev}^{-1}$ and surface cutting speed of $\sim 75 \text{ m}\cdot\text{min}^{-1}$ with another smaller region positioned at $\sim 0.14 \text{ mm}\cdot\text{rev}^{-1}$ and surface cutting speed of $\sim 85 \text{ m}\cdot\text{min}^{-1}$. In order to ensure confidence with the results Jaffery *et al.* [177] conducted further repeat trials (see inset enlarged wear map in Figure 2.43). The results obtained from the repeat trials supported the presence of a high tool wear region using comparatively low surface speeds and feed rates.

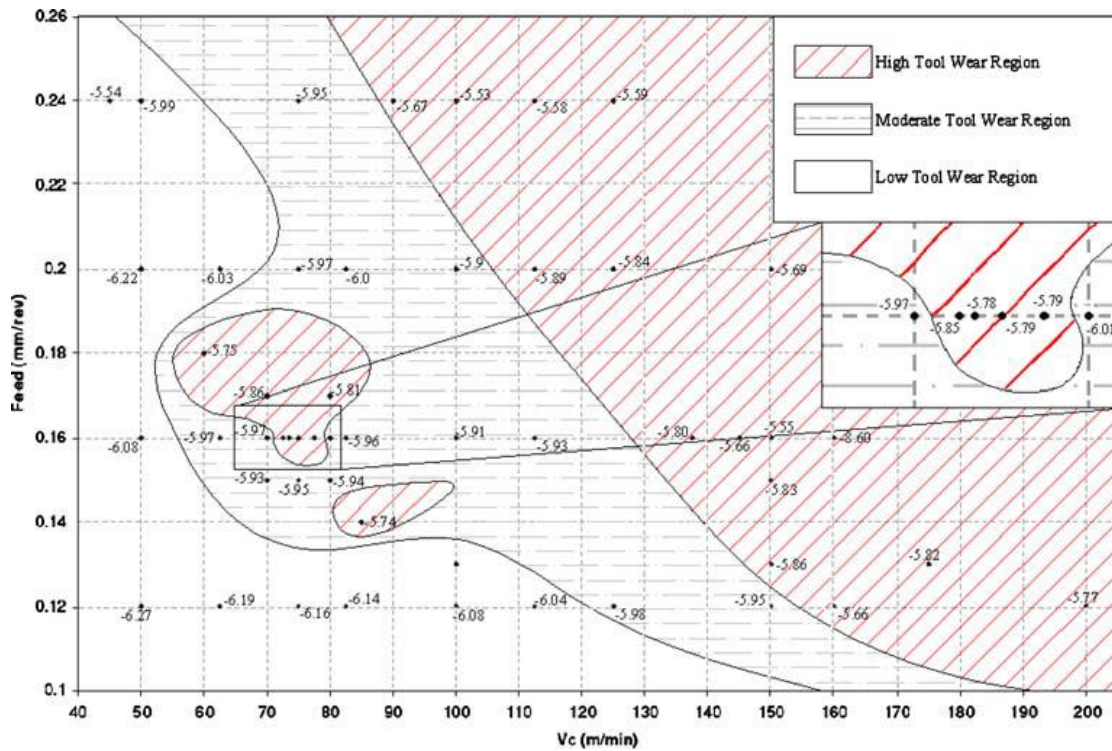


Figure 2.43 Wear rate map for Ti-64, determined through a series of parametric outer diameter machining trials using H13A uncoated carbide cutting inserts [177].

In contrast to the Taylor tool life performance relationship approach a key benefit to developing a tool wear map for a material, is that it offers the reader a more holistic picture offering greater detail into the kinetics of the system. From the tool wear map shown in Figure 2.43 the data shows how the cutting environment of Ti-64 is susceptible to significant changes in wear performance if the surface cutting speed or feed rate is altered. As discussed previously (2.10.3), the stability of the built up edge ahead to the tool can have a significant influence on the tool wear kinetics, offering a barrier to further abrasive and diffusive wear. Since Jaffery *et al.* [177] was unable to conduct further research into the characteristics of the high wear regions the author suggests that the shape, area and location of the high wear regions may be related to the chemical compositions of the tool and workpiece, i.e. the relative chemical stability between the two materials leading to changes in the stability of the protective

BUE. The author does however feel it is important to note that Jaffery *et al.* [177] make no reference to the starting conditions of either the cutting inserts or workpiece material. The effect of starting edge rounding of a cutting insert has been extensively discussed within the scientific literature and has been shown to have a significant effect on the tool wear characteristics [60], [110], [180], [181], with sharper tools often showing improved life [182]; however, they can often be more prone to chipping as a result [183]. Jaffery *et al.* [177] do not discuss the effect on their results of the inevitable variability in starting edge rounding –since, by virtue of the methods used during their manufacture there is a typical variability in edge rounding of $\sim\pm 20\ \mu\text{m}$ [165]. Jaffery *et al.* [177] also do not discuss how microstructural variability within the starting material may also have a profound impact on the resulting wear rates. As discussed in §1.2, forged Ti-64 billets show significant microstructural variability across their cross section. In light of these facts, the author feels that the potential impact caused by this variable starting microstructure should not be ignored. The author also assumes that all of the trials conducted by that Jaffery *et al.* [177] were carried out on material that had received comparable heat treatments and processing routes and therefore had similar mechanical properties.

2.12 The role of alloy chemistry in machining

“Machinability” trials investigating how the underlying chemistry of a workpiece affects its own machining performance are studied using either a predetermined wear threshold over time criterion for turning trials, or for drilling simply a count of the number of holes drilled until catastrophic tool failure. Using such methods allows for maximum speed tests to be undertaken offering an evaluation of machining efficiency. Most commonly, contrasting alloys are chosen for such machinability trials as to emphasise any effect alloying additions may have upon performance, for example comparing the performance of the metastable β alloy Ti-5553 or the near β alloy T-6246 against the machining performance of the $\alpha+\beta$ alloy Ti-64. Such machining trials have observed a systematic trend towards a decrease in machining performance for alloys with an increase in β stabilizers [124], a trend that is challenged by the development alloy Timetal® 54M (Ti-54M) [127]. Ti-54M is being marketed as a replacement for Ti-64 with potential applications including; connecting rods, intake valves and turbocharger compressor wheels. Ti-54M boasts cost savings both during alloy production utilizing existing titanium alloy scrap and low cost alloying elements in addition to exhibiting potential machining efficiency gains. During development Kosaka *et al.* [127] carried out a series of trials on a number of Ti-5Al-4V-Mo/Fe base alloys and investigated their drilling performance, following the trials it was found that Ti-5Al-4V-Mo/Fe base alloys exhibited superior drill

performance compared to a Ti-64 control specimen. Under such drilling conditions the alloys outperformed Ti-64 up to 10x from achieving ~10 holes at a fixed drilling speed to ~100 when drilling the Ti-5Al-4V-Mo/Fe base alloys. Following further refinement the final nominal composition of Ti-54M became fixed at Ti-5Al-4V-0.6Mo-0.4Fe. Many investigations have subsequently reported potential gains in using Ti-54M over Ti-64 with recorded improvements in tool wear at elevated machining speeds. These further trials using both drilling and turning have however only shown marginal gains, in comparison to Ti-64, with only an improvement in performance at speeds $>60\text{m}\cdot\text{min}^{-1}$. Though importantly both alloys see a considerable decrease in machining performance at elevated speeds. Conversely drilling trials carried out by Rahim *et al.* [184] saw Ti-64 possessing superior machinability than Ti-54M during drilling as recorded by better tool life performance as a result of lower flank wear. Further measurements of local tool temperatures in the rake face during orthogonal cutting trials has also revealed that the temperature generated when cutting Ti-64 and Ti-54M were also similar. At this point the majority of studies investigating “machinability” report empirical findings, for example, Ugarte *et al.* [124] attributes the reduction in Ti-5553 machinability to a combination of high dynamic loads as a result from a higher chip segmentation frequency and higher cutting temperatures. Such conclusions offer the reader little metallurgical insight into how the material could be contributing to its machining performance. Arrazola *et al.* [185] did however make an important observation when also comparing the machining performance of Ti-5553 and Ti-64, where the formation of a protective layer of adhered material was observed when machining Ti6Al4V alloy. The size of this layer decreases with increasing speed. As soon as this layer is removed, tool wear increases significantly. No mention was made as to whether or not a protective layer was observed when machining Ti-5553, nor have any other authors reported the formation of a stable protective layer when machining Ti-54M.

2.13 Summary

Within this section the mechanics of machining have been introduced as well as an introduction to (and a critical appraisal of current scientific understanding of) the fundamental metallurgical response of the workpiece during machining, the influence of cutting parameter variability and current practice in surface integrity analysis.

Currently there remains a significant knowledge gap concerning the relationship between both the deformation and cutting force characteristics with the underlying crystallographic morphology of the workpiece material, especially concerning multiphase materials. Consequently, this study will investigate the metallurgical response of multiphase titanium alloys during experimental machining trials in order to quantify and rationalise their mechanical response.

Chapter 3 - Material analysis procedures

3.1 Introduction

Throughout this study, which addresses many different aspects of material behaviour during machining, a number of common experimental procedures were utilised. These included metallographic preparation techniques, optical imagery, scanning electron microscopy (SEM), electron backscatter diffraction (EBSD) and further analytical procedures. In order for the results to be reliable best practice guides were consulted. The following chapter details these procedures and techniques.

3.2 Specimen Preparation

A standard procedure was used to prepare samples for optical microscopy, scanning electron microscopy and EBSD. These techniques remained the same for all the material types investigated. It is important to note the importance of the care required when handling and preparing the specimens for analysis, ensuring the integrity of the surface has been maintained. Prior to metallographic analysis specimens were removed from the machined workpiece. Depending on the nature of the machining trial the sample material was either immediately removed on the lathe using a parting tool or through thickness slices were cut via electric discharge machining (EDM) or a water jet cutter.

3.2.1 Precision sample sectioning

Microstructure analysis samples were sectioned either parallel or perpendicular to the normal (ND) –cutting direction (CD) plane. These directions are defined in Figure 3.1 with respect to common locations relative to the workpiece and the tool.

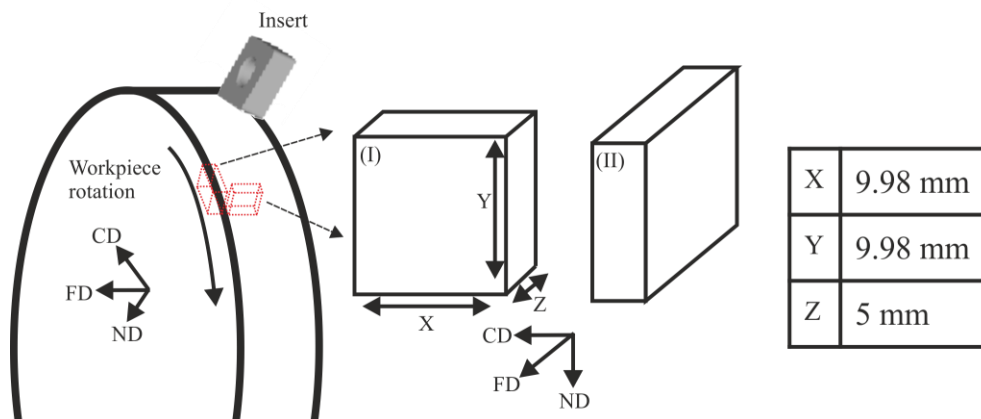


Figure 3.1 Typical sample orientations for microstructure analysis relative to the workpiece. The normal (ND) –cutting (CD) – feed direction (FD) and corresponding EBSD sample dimensions.

All samples were sectioned for EBSD analysis. EBSD requires the sample to fit in a customised sample holder. The critical dimensions for EBSD samples are also given in Figure 3.1.

A manually operated sectioning Buehler Abrasimet with a silicon carbide cut-off blade was occasionally used to quickly reduce the sample dimensions. Allowing the final precision reductions to be carried out using an automated Buehler IsoMet 5000 linear precision saw fitted with a 200 mm diameter, 0.5mm thick non-ferrous specific silicon carbide cutting wheel. For this machine the cutting blade can be positioned to an accuracy of 0.1 mm. To minimise specimen heating, the cutting wheel was advanced with the lowest possible feed rate ($1.2 \text{ mm}\cdot\text{min}^{-1}$) at a constant blade speed of 3000 rpm with a continuous liquid coolant delivery ahead of the cutting wheel. Orientation critical samples were sectioned using EDM on a Mitsubishi FA 20 Wire Eroder. EDM allows samples to be sectioned to an accuracy of 0.01 mm.

3.3 Surface Preparation

3.3.1 Metallographic polishing

In preparation for microstructure analysis, each sample was individually contained within a 32 mm diameter Bakelite resin mount. Prepared in batches of three, the mounted samples were ground and polished using a Struers Abramin automatic polishing machine. Comprising three stages; all samples were ground to a planar finish, ensuring any material that may have been affected during the sectioning stages was subsequently removed; this was then followed by an initial polish using a water based $9 \mu\text{m}$ diamond suspension and then a final $0.05 \mu\text{m}$ polishing stage using a colloidal silica suspension (silco). The silco solution comprises of 90% colloidal silica suspension with the addition of 10% laboratory reagent grade H_2O_2 (30% w/v). In order to prevent the silco from crystallising on the sample surface, the samples and the polishing cloth are rinsed with water. The addition of H_2O_2 reduces the chemical etching affect that can occur when preparing titanium alloys via this method. Any possible surface relief caused by etching is undesirable, especially for EBSD analysis, which requires a perfectly planar surface. Table 3.1 summarises the complete preparation procedure.

Samples required for Scanning Electron Microscopy (SEM) or Electron backscatter diffraction (EBSD) analysis need to be separated from the Bakelite mount once polished. To aid removal prior to the polishing steps grooves are cut into the side of each. With great care the sample can be extracted. To slow the oxidation process the samples need to be immediately submerged in methanol and for best results it is advised to image within the same day of polishing.

Table 3.1 Summary of metallographic analysis preparation stages for titanium alloy EBSD samples.

Stage	Abrasive media	Additions	Time and advisory notes
1. Planar grind	1200 grit silicon carbide grinding paper	Water cooled	Until planar (2- 8 minutes) Replace grinding paper at first sign of excessive wear (4 minutes max)
2. Initial polish	Struers MD-Largo Composite disc	Water based 9µm Diamond suspension and water based lubricant	7 minutes Ensure disc is suitable lubricated use the diamond suspension sparingly
3. Final polish	Struers MD-Chem Porous neoprene disc	Silco solution containing; 90% 0.05µm colloidal silica suspension plus 10% laboratory reagent grade H ₂ O ₂ (30% w/v) Water rinse	5 minute water rinse (including a clean of the cloth with a firm card edge) 5 minute silco → 1 minute water rinse → 5 minute silco → 5 minute water rinse
<p>All stages are carried out with the sample holder moving with a complimentary relative rotation at a constant speed of 150rpm. The applied force also remains constant at 4 N per specimen. For best results it is advised to prepare samples in batches of three ensuring the sample holder is balanced</p>			

3.4 Imaging and analysis

3.4.1 Microstructure optical imaging

The prepared samples were examined under reflected light conditions using a Polyvar light microscope. Cross-polarised filters were inserted to reveal the microstructure of the as prepared samples. The magnified images were acquired using the software KS AxioRun, which allowed for option of graticules to be added to each image.

3.4.2 Scanning Electron Microscopy (SEM)

To study microstructures at higher magnifications, a FEI Inspect F field emission gun scanning electron microscope (FEG SEM) was used. To reduce interference issues, each sample was removed from the Bakelite mounting and held on a metal stub using an adhesive conducting carbon dot. The typical operating parameters for the Inspect F FEG-SEM are outlined in Table 3.2. For imaging the backscatter detector was most commonly employed to enhance the difference between the α and β phases and to resolve deformation features such as twins and slip via channelling contrast.

Table 3.2 Operating parameters for the Inspect F FEG SEM.

Parameter	Typical value
Accelerating voltage	15 keV
Spot size (dimensionless unit specific to Inspect F FEG SEM)	3 (~10 nA probe current)
Working distance	8.00 mm
Detector	Secondary electron and Backscatter detector

See Table 3.3 for detailed descriptions of acquisition parameters and advisory guidelines that are to be followed when using a FEG SEM.

Channelling contrast is generated during backscatter electron imaging, whereby the incident electrons falling on the sample are subject to multiple interactions with lattice planes, which cause the electrons to scatter. These multiple scattering incidents lead to some being emitted from the specimen as backscattered electrons. However, within a deformed specimen containing dislocations, the lattice planes become distorted resulting in a reduction in the number of electrons being backscattered. Grains containing features that possess a high number of dislocations such as twins and or slip disrupt the nature of the backscattered electrons causing tonal variations within the acquired images. These may appear as distinct bands or more subtly as a gradual variation across the grain.

3.4.3 Electron backscatter diffraction (EBSD)

Throughout this investigation extensive use was made of electron backscatter diffraction (EBSD). EBSD can offer great insight into the processing history of material. Through the interpretation of Kikuchi patterns from backscattered electrons, the crystallographic orientation of a specimen's surface can be obtained. Orientation image maps (OIM) comprising logged data points can be constructed to give a more global representation of the crystallographic morphology of a sample.

EBSD formed a critical component of the research and was used to investigate;

1. Specific modes of mechanically induced deformation.
2. The role of the underlying texture and applied stress state in governing which modes of deformation will activate.
3. The texture and microstructure in the as received billet and its subsequent influence on cutting forces during machining.

EBSD analysis was carried out on cross-sectioned specimens taken directly beneath the machined surface. Characterisation of the α and β phase has permitted the identification of mechanically induced deformation, which has been related to the destructive nature of the machining process. Since the material has been received after the machining has occurred the analysis has to be regarded as being a 'post mortem' examination of the machined material. An important aspect of this investigation concerns the post processing of the acquired EBSD.

3.4.3.1 EBSD Equipment description

A FEI Sirion FEG SEM with a retractable Nordlys S detector was used to acquire the EBSD data. Control of the equipment is governed by an HKL Technology EBSD analysis system with an additional control system running the imaging and acquisition software, HKL Channel 5.

3.4.3.2 General Principles of the EBSD System

EBSD requires the sample to be inclined beneath the electron gun to an angle of 70° off horizontal. The EBSD detector is then extended into the chamber via an electric motor where it is locked into position near to the sample. During operation the scan coils within the electron gun are disabled so that the electron beam remains stationary and can be controlled above a specific area of interest. The schematic shown in Figure 3.2 illustrates the components required to perform EBSD.

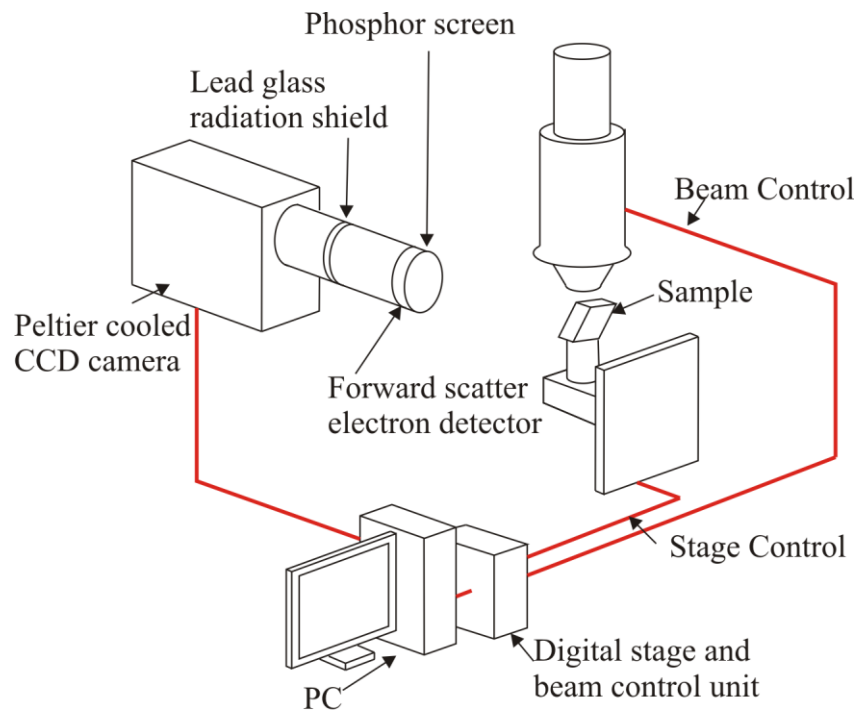


Figure 3.2 Principle components of an EBSD system, after Oxford Instruments [186].

As illustrated in Figure 3.3 the incident beam of electrons interact with the atoms at surface of the specimen, resulting in some of the backscattered electrons to satisfy the Bragg equation (Equation 3.1) where n is an integer, λ is the wavelength of the electrons, d is the spacing of the diffracting planes and θ is the angle of incidence.

$$n\lambda = 2d \sin \theta \quad \text{Equation 3.1}$$

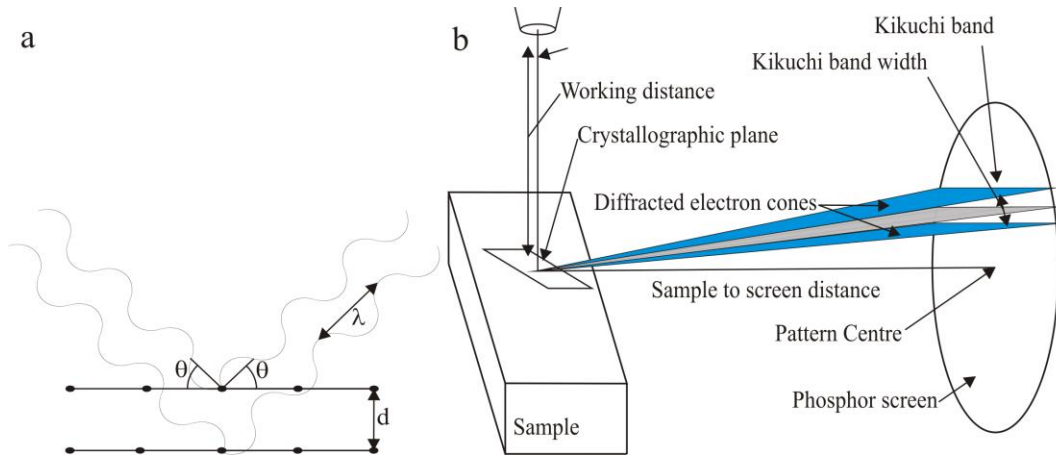
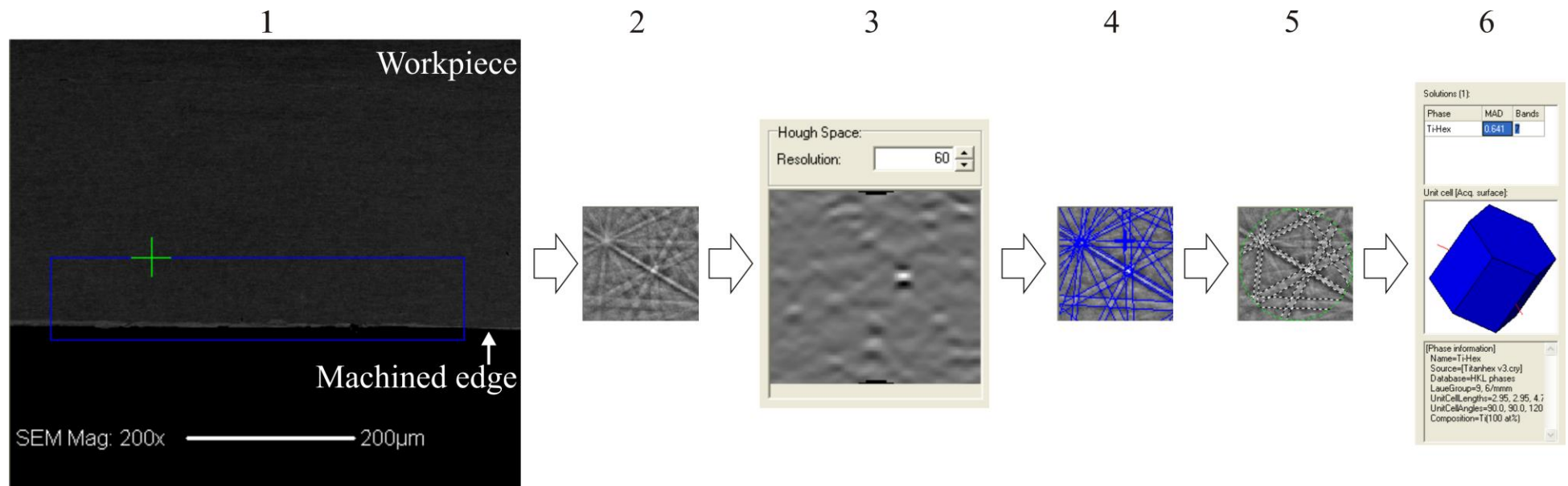


Figure 3.3(a) The Bragg condition is satisfied when the backscattered electrons from the diffracting planes are reflected in phase (b) Schematic diagram illustrating how the diffracted electron cones are projected on to the phosphor screen allowing identification, after Wilkinson *et al.* [187].

The crystallographic backscattered electrons, which satisfy Bragg's law for a given plane, emanate in diffraction cones that correspond to the front and back surface of a specific incident atomic plane. When these cones contact the phosphor screen at the EBSD detector a Kikuchi line is formed that represents a trace of the specific plane from which was created. An electron backscatter pattern (EBSP) comprises of a number of Kikuchi bands and represents the characteristics of the crystal structure and the specific orientation of the region from which it was generated. A charge coupled device (CCD) camera positioned behind the phosphor screen captures the EBSP allowing it to be digitised. The crystal orientation is determined by transforming the positions of the EBSP bands using a Hough transformation (Equation 3.2), which converts the traces into single points within a Hough space. Whereby the EBSP coordinates (x, y) become (ρ, θ) in Hough space. The points represent the perpendicular distance of the trace line from the origin and the angle of the trace line relative to the x-axis.

$$\rho = x \cos \theta + y \sin \theta \quad \text{Equation 3.2}$$

Comparing the angles between the acquired Kikuchi bands to those within a reference database, miller indices can be assigned to each plane. The specific orientation of the crystal lattice with respect to the specimen coordinates can be defined. Figure 3.4 illustrates the capture, processing and analysis of an acquired EBSP pattern. For each indexed data point an associated mean angular deviation (MAD) value is given. MAD represents the relative angular misfit between the acquired bands to those within the reference database. Measured in degrees a MAD value of less than 1° is regarded as being satisfactory.



1. Secondary electron image of the workpiece with an overlaid (blue delineation) 500 μm wide 100 μm tall EBSD scanning area. Note when analysis a machined surface to position the scanning area such that it overhangs the workpiece thus ensuring the edge will be captured. The crosshair mark corresponds to the region of material currently being analysed.
2. Acquired live EBSP pattern
3. Corresponding Hough space for the live EBSP pattern.
4. Visual representation of the band edge detection process whereby all individual bands are identified (software computes this step using the Hough space)
5. Visual representation illustrating which combination of identified bands have been chosen using the minimum/maximum number of critical bands.
6. Resulting final visual representation of the material crystal type and crystallographic orientation.

Figure 3.4 Fundamental processing steps during the acquisition of orientation data; following the capture, processing and analysis of an EBSP with its associated Hough space representation and MAD.

The process of acquiring a Kikuchi pattern and its subsequent indexing can be repeated approximately 25 times per second. By scanning the beam horizontally across the sample and collecting the data an orientation image map (OIM) that represents a scanned area can be constructed. The resolution of the OIM is governed by the beam's step size, a unit length that defines the horizontal and vertical spacing between each of the indexed data points. The HKL Flamenco control software can be programmed to collect a matrix of data points, this is also known as a 'job'. An individual job is limited to an area of approximately 300 x 300 μm on the specimen surface. If the user requires a scan that covers an area larger than 300 x 300 μm , using the stage control system a series of jobs can be collected that can be merged together using a 'mapstitcher' software package, which is also part of the Channel 5 suite.

3.4.3.3 Typical parameters and operational guidelines for EBSD analyses

To facilitate high-resolution EBSD data acquisition the cleanliness and quality of the specimens metallographic preparation is critical. All EBSD samples were prepared using the method detailed in §3.2.1. During the preparation stages, extra care was taken to avoid imparting any mechanical damage, or unwanted surface films through contamination. Having a sound specimen preparation approach allowed for reliable results to be obtained with a low MAD.

Prior to initiating EBSD control it is important to ensure that the microscope gun tilt, lens alignment and astigmatism have been corrected to allow for focusing and thus permitting the calibration of the stage height. Once the microscope has been set up correctly this allows for improved EBSP results. Like most analysis techniques, the accuracy of individual EBSD data points and the resolution of the entire data set are time dependent variables. Therefore, the user must decide prior to setting up the equipment what the requirements are for the individual job. Each specimen has to be treated individually with the parameters detailed in Table 3.3 require careful adjustment. The specimens alloy composition, morphology and process history will further dictate the quality of the acquired EBSP. Once the parameters have been optimised, the user must consider the necessary resolution of the data so that it will possess a sufficient amount of detail. The resolution of an EBSD data set is dictated by the step size, which corresponds to the vertical and horizontal spacing between individual data points. For this investigation, the majority of the EBSD data obtained is presented in the form of high resolution OIMs, these required individual jobs running with a maximum step size of 0.5 μm . To ensure a large enough area of material was analysed these jobs required a running time of 60 hours. In this time upward of 4 million data points can be gathered. It is important to note that the offline data manager cannot process maps containing more than 5 million data points.

Table 3.3 Sirion FEG SEM EBSD Acquisition parameters and advisory guidelines.

	Parameter	Typical value	Guidelines
Microscope	Accelerating voltage	20 keV	For an FEG SEM EBSD system the accelerating Voltages is commonly between 5 and 20 keV. Spatial resolution is reduced outside of upper and lower bounds. High accelerating voltages improve the contrast and sharpness of the obtained patterns, which further improve the acquisition rate and the MAD of indexed data points. However, an increased voltage reduces the band width of the patterns
	Beam spot size (no unit, system specific parameter)	3	The FEG SEM system offers spot sizes in the range of 1-5, for EBSD the smallest spot size that offers the most consistent solvable patterns is desirable. If the pattern quality is weak this can be improved by increasing the spot size. Spot size, also referred to as probe current and is dependent on multiple factors, a spot size of 3 will have a different actual size at 10 keV than at 20 keV, therefore spot size values have no units. Smaller spot size values equate to a smaller dimension of the incident spot size.
	Working distance	14 mm	After ensuring the gun tilt, lens alignment and astigmatism have been suitably corrected a working distance of 14 mm can be accurately set. For the Sirion FEG SEM this distance provides the best EBSP patterns.
	Magnification	200 x	The magnification set by the microscope limits the size of the viewing window and thus the maximum area an individual job can cover. At 200x this equates to area approximately 300 x 300 μm . Any increase in the magnification above 200 x offers no improvement in quality of the obtained data. However, at lower magnifications the beam is required to travel further which can reduce the sampling

			hit rate. To scan an area larger than 300 x 300 μm the automated stage control system can be employed.
	Stage tilt	70°	A tilt angle of 70° is required to reduce the depth to which the beam penetrates the specimen surface and allows the back-scattered electrons easier access to the detection camera.
CCD	Camera extension	166 mm	Attention needs to be made with regard to the cameras proximity to the stage, particularly when analysing the edge of a sample and performing job that requires the stage to automatically move. Note it is possible for the stage and the camera to collide!
	Pixel binning	4x4	The control software can be set to either of the following; No Binning, 2 x 2, 4 x 4, 8 x 8 and 8 x 8- superfast. To increase the acquisition rate it is possible to cluster groups of data points that make up the EBSP, the improvement in sampling rate is however at the expense of angular accuracy. Therefore for this type of investigation it is recommended to use a binning of 4x4 allowing high quality EBSPs to be collected.
	Camera gain	High	Gain is a measure of the cameras sensitivity. At high gain the acquisition time is reduced. However, this may increase the amount of noise within the obtained pattern.
EBSP	Timing per frame	6-10 ms	The timing required to acquire a suitably clear image that is neither too dark or bright is particularly sensitive to the cleanliness of the preparation stages.
	Number of frames averaged	4-6	To further improve the clarity of the acquired pattern an increase in the number of frames required for averaging is required. At the expense of the acquisition rate the hit rate and the spatial resolution is improved.

Calibration	Material database	Ti Hex Ti Cubic	The HKL Channel 5 software is equipped with calibration files for a large selection of materials. These calibration files can be refined to suit the material being analysed to improve the angular accuracy of the obtained data, each refinement can be saved to the user profile. Therefore, it is advised to create separate profiles when studying materials of different alloy composition.
Band detection	Band detection	Band edges	For this study the angular accuracy of the obtained data was deemed more important than acquisition rate. Band edges offer an improved angular accuracy over band centres. Band centres can be employed if the sample has a poorly prepared surface.
	Min/Max number of bands for detection	5/7	The use of a high minimum number of bands required during detection helps avoid the effects of pseudo-symmetry. Further improving the reliability of the obtained data.
	Hough resolution	60	Resolutions can be used in the range of 40-60. This value corresponds to the resolution of the image when it is converted into Hough space.
Resolution and timing	Mapping acquisition rate	0.04 seconds	Once the user is comfortable with the quality of the data being acquired a job can begin. The jobs acquisition rate is the governed by parameters listed above.
	Step size	0.06-5 μ m	The step size corresponds to the desired resolution of the of the acquired data and is independent of all the parameters listed above.

It is important to note that the Euler angles that are assigned to each data point are orientated relative to the SEM chamber and not the sample itself. Therefore, it is important to ensure the sample has been orientated correctly prior to initiating an EBSD run. The Channel 5 software does offer the capability of virtually rotating the dataset if the user requires.

To enable the user to be able to perform textural analysis the EBSD data can be visualised in several different ways, the principles of those employed as part of this study are briefly discussed.

3.5.2 All Euler OIM

All Euler mapping uses a colour representation for each Euler angle component (Figure 3.7). This offers the most realistic representation of the underlying crystallographic orientation. However, the data cannot be easily interpreted, since the displayed colour comprises a combination of the three colour scales.

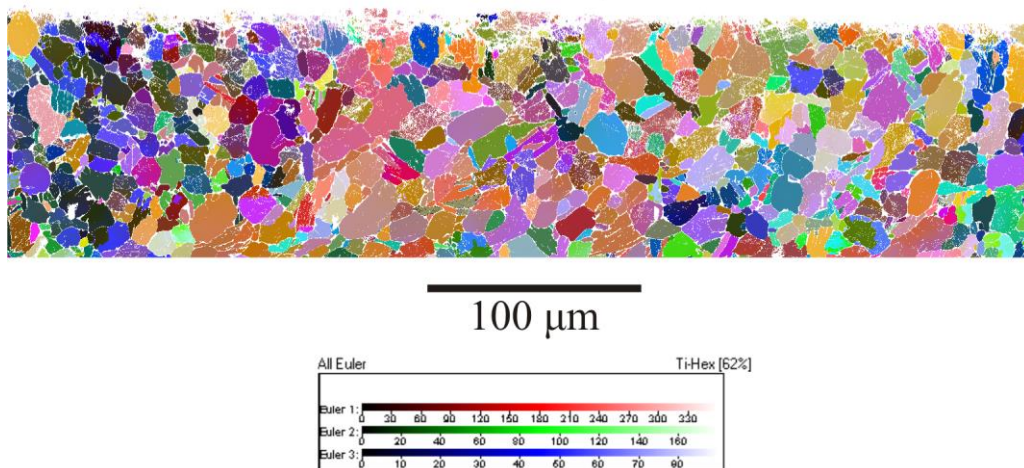


Figure 3.7 All Euler orientation image map and corresponding legend, colouring set parallel to the viewing plane.

3.5.3 Inverse pole figure OIM

Inverse pole figure (IPF) is another colour representation style that allows the user to easily identify the average orientation of a specific data point (Figure 3.8). IPF colouring identifies key crystallographic planes and their orientation relative to the viewing plane. IPF does not however, describe the texture completely since it offers no insight into the specific rotation of the individual data points.

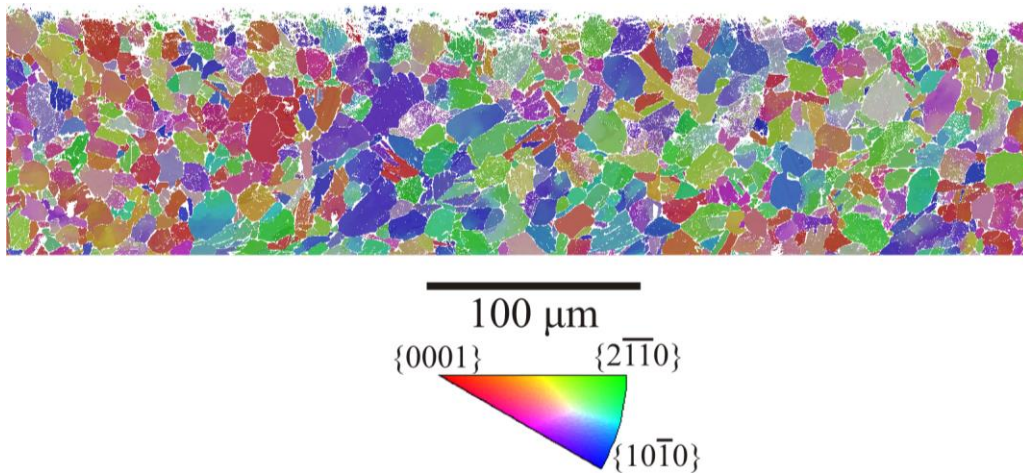


Figure 3.8 Inverse pole figure and corresponding legend, colouring set parallel to the viewing plane.

3.5.4 Noise reduction

The noise reduction tool offered within the HKL Channel 5 software and can be used to ‘clean’ OIM’s. Isolated erroneous data points known as ‘wild spikes’ can be removed and regions containing zero solutions can be filled via an extrapolation method. The OIM data shown in Figure 3.9 has been extrapolated to 24% such that there are only 24% unindexed points remaining. Caution is advised when applying this tool since data points filled using this method are purely theoretical. Therefore, this can lead to misleading results when analysing features such as grain size and/or overall proportion of a specific phase within a dataset.

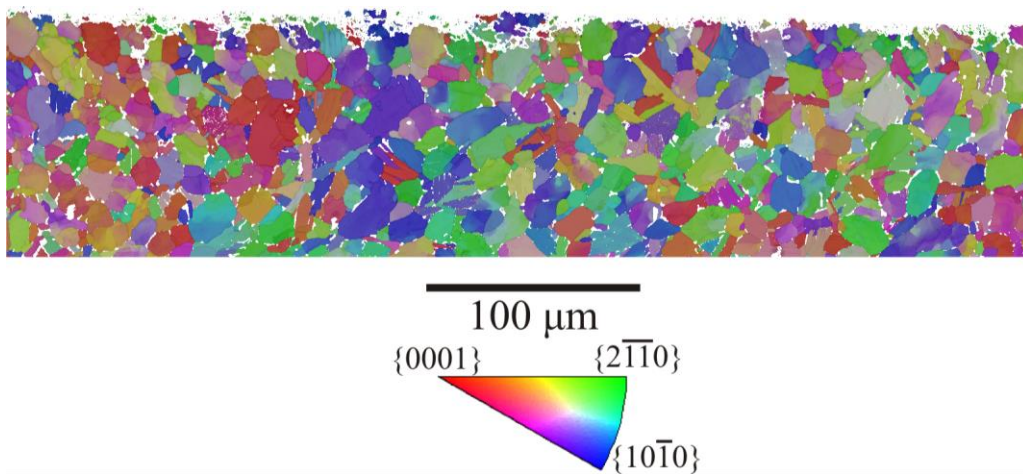


Figure 3.9 Inverse pole figure orientation image map after a noise reduction function has been applied.

3.5.5 Band contrast OIM

A band contrast (BC) value is logged for each recorded data point; band contrast OIMs (also known as pattern quality maps) offer a grey scale representation of the EBSD dataset (Figure 3.10). High BC values correspond to a lighter shade of grey with black representing an unindexed data point. Band contrast OIMs offer a complete image representation of the analysed area, features such as the edge of the sample, deformation bands and grain boundaries can often be more apparent when displayed in this style. As part of this investigation band contrast OIMs are used in conjunction with IPF OIMs, with each map being superimposed onto one another.

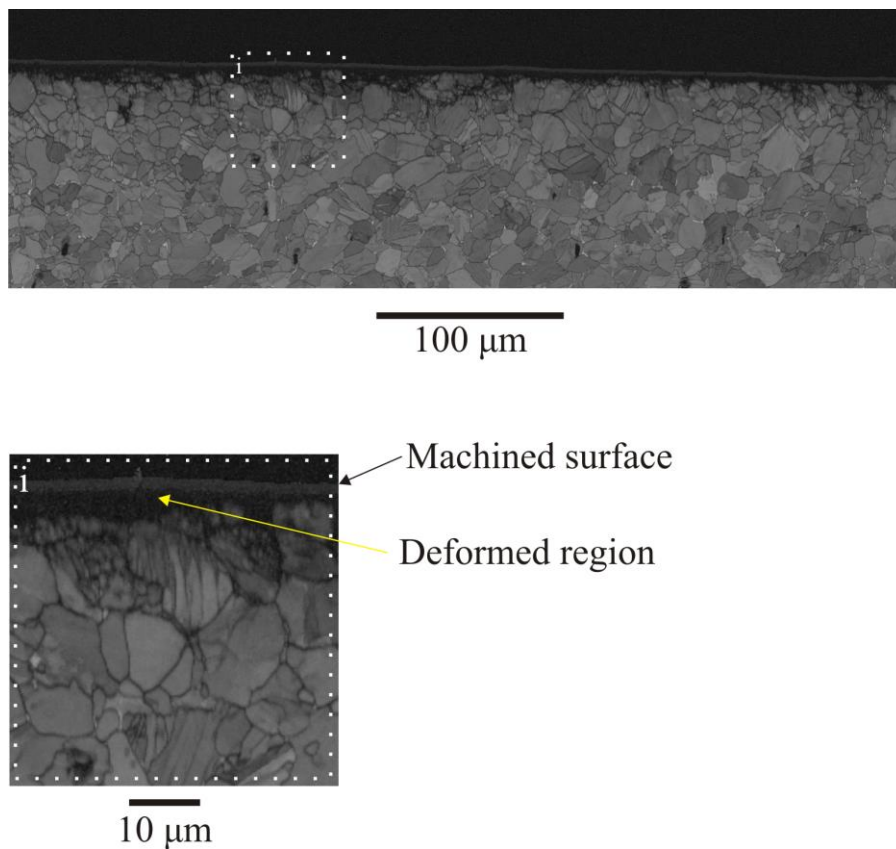


Figure 3.10 Band contrast image map of a cross section taken of a machined titanium alloy surface. Enlarged region (i) showing the highly deformed subsurface region beneath the machined surface.

When attempting to quantify an area using EBSD that contains a high amount of deformation. Defects such as dislocations cause the acquired EBSP to lose its sharpness and can subsequently lead to systematic mis-indexing. Figure 3.10 illustrates the severity to which the mechanically induced deformation can influence the recorded data, with an increase in the number of unindexed data points within the deformed region near the surface.

3.5.6 Twinning delineation

The HKL Channel 5 software offers the user a special boundary function that can be used to delineate grain boundaries that satisfy specific conditions. To identify an individual twin mode, the user is required to input an angle of rotation about a specific plane. Mironov [28] lists a concise account of these identification planes and angles. Figure 3.11 demonstrates the method of the twin delineation process using the example of the $\{10\bar{1}2\}$ tension type twin. Here a specific misorientation rotation angle of 84.78° is specified about the $\langle 1\bar{2}10 \rangle$ axis.

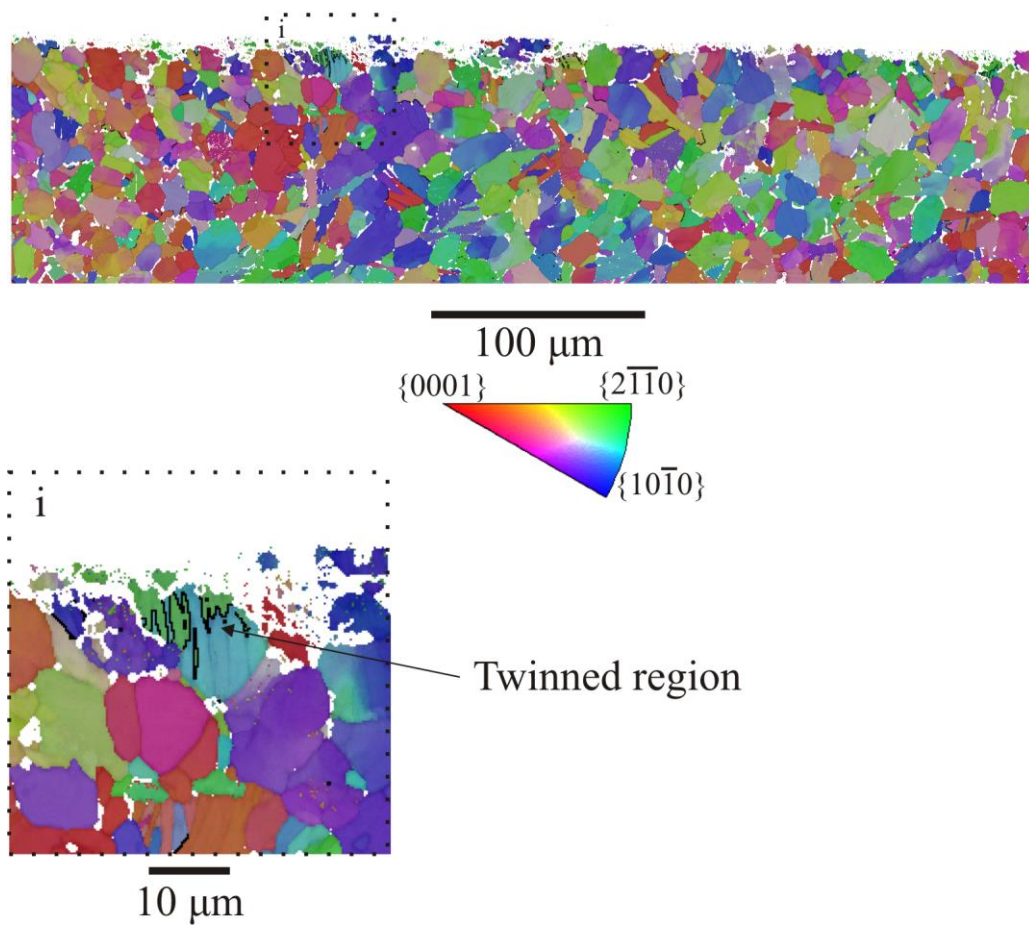


Figure 3.11 Inverse pole figure orientation image map after a noise reduction and $\{10\bar{1}2\}$ twin delineation function has been applied. Enlarged region (i) showing the highly deformed subsurface region beneath the machined surface with the identification of $\{10\bar{1}2\}$ type twins within an individual grain.

3.6 Pole figures

Pole figures offer a projected representation of the orientations within a specified region with each pole figure displaying individual points that correspond to a normal location in the centre of each plane of interest (Figure 3.12). A contour plot can also be applied to a pole figure plot to illustrate any potential clustering that may be occurring, using a scale of multiples of uniform density (mud). Throughout this investigation stereographic projections were used.

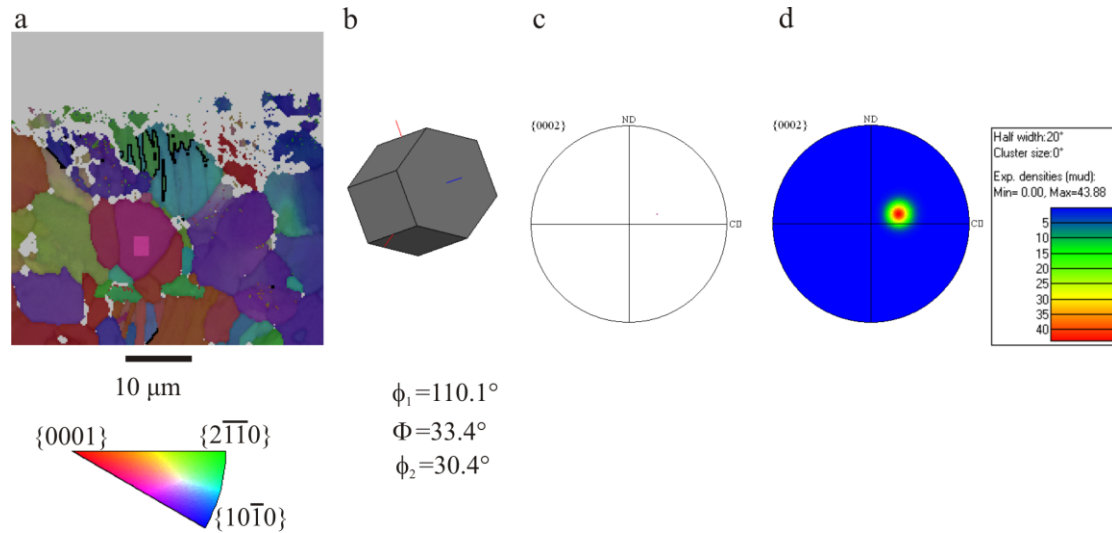


Figure 3.12(a) Inverse pole figure orientation image map after a noise reduction with a subset taken from within an individual grain. (b) Graphical representation of the average orientation of the HCP crystal within the highlighted subset, including the corresponding Euler angles. (c) Pole figure representation of highlighted subset with corresponding contour plot (d).

3.7 Slip trace analysis

A slip trace analysis method for associating observed deformation features with possible slip and twinning modes was presented in §2.2. This manual approach for deformation analysis offers little support to the user for further data handling, plus further examination of the Schmid factor acting upon the planes of interest cannot be accurately determined. To overcome these issues, the following method of data handling was constructed. The following expressions were assembled as part of a series of macro functions in Microsoft Excel.

3.7.1 Crystallographic orientation mathematical methodology

The following procedures were used to identify and characterise mechanically induced deformation within hexagonal close-packed (HCP) alpha grains. Planes and direction within an HCP lattice, are typically expressed as four-index Miller–Bravais indices. Through a series of transformation these planes and directions are expressed in terms of a three-index orthogonal coordinate system that correlates to the global stress state. This allowed for all of the computations to be carried out in terms of a orthogonal system [189].

The first conversion required see the HCP Miller–Bravais $\{h, k, i, l\}$ indices converted into Miller indices $\{h', k', l'\}$. For planes within a hexagonal material the conversion is required to satisfy the following criteria.

$$\{h, k, i, l\} \rightarrow \{h', k', l'\}$$

$$h' = h \quad k' = k \quad l' = l \quad \text{Equation 3.3}$$

$$h = h' \quad k = k' \quad i = -(h' + k') \quad l = l'$$

For directions within a hexagonal material the conversion is required to satisfy the following criteria.

$$\langle u, v, t, w \rangle \rightarrow \langle u', v', w' \rangle$$

$$u' = u - t \quad v' = v - t \quad w' = w \quad \text{Equation 3.4}$$

$$u = \frac{(2u' - v')}{3} \quad v = \frac{(2v' - u')}{3} \quad t = \frac{-(u + v)}{3} \quad w = w'$$

The crystal axes that the miller indices are referring to need to be normalised into an orthonormal arrangement (x, y, z) . The term orthonormal refers to each of the values now representing the same unit length and are in a Cartesian form. To normalising procedure involves pre-multiplying the miller indices by a transformation $[L]$ matrix [190].

When determining the orientation of a HCP crystal, the acquisition software records the necessary Euler transformation steps required to match the orientation of the material to that of a reference crystal. The two possible starting crystal coordinate systems for hexagonal materials are shown in Figure 3.13(a-b), it is important to note precisely which orientation the acquisition software has adopted. The HKL Channel 5 software, used throughout this investigation, has adopted the arrangement illustrated in Figure 3.13(b).

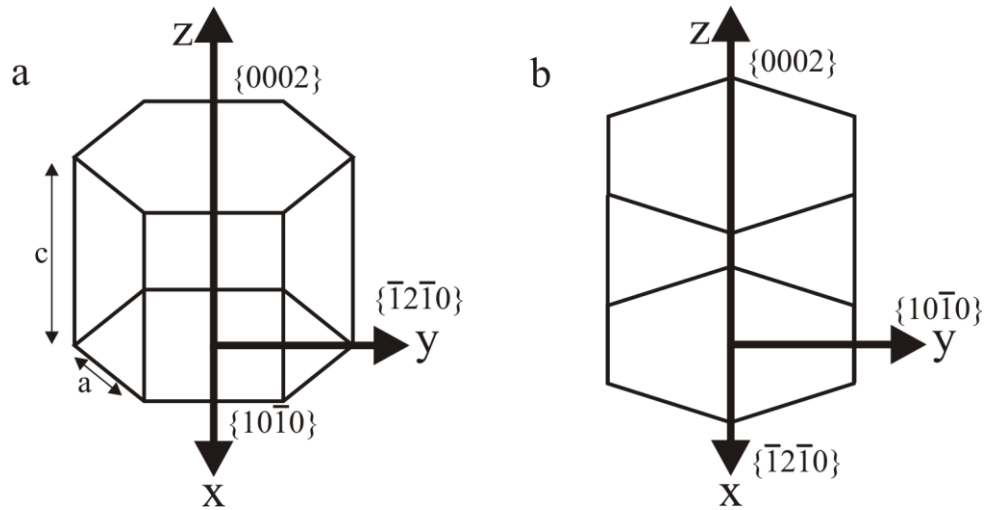


Figure 3.13 The crystal coordinate system for hexagonal materials is defined by the starting orientation of the initial HCP crystal. The two possible orientations are defined by the x-axis being either parallel or perpendicular to the $\{10\bar{1}0\}$ axis as shown in (a) and (b) respectively.

The transformation $[L]$ matrix used takes the following form. Using the titanium HCP lattice parameters $a = b = 2.95$, $c = 4.72$, $\alpha = \beta = 90$, $\gamma = 120$

$$[L] = \begin{bmatrix} sy & 0 & c \cdot c\beta \\ b \cdot cy & a & c \cdot \frac{(c\alpha)(c\gamma)}{(s\gamma)} \\ 0 & 0 & c \cdot \sqrt{\frac{(s\beta^2 s\gamma^2 - c\alpha^2 + 2c\alpha \cdot c\beta \cdot c\gamma - c\beta^2 c\gamma^2)}{s\gamma}} \end{bmatrix}$$

Equation 3.5

Where

$$s\alpha = \sin\left(\alpha \cdot \frac{\pi}{180}\right), s\beta = \sin\left(\beta \cdot \frac{\pi}{180}\right), s\gamma = \sin\left(\gamma \cdot \frac{\pi}{180}\right)$$

$$c\alpha = \cos\left(\alpha \cdot \frac{\pi}{180}\right), c\beta = \cos\left(\beta \cdot \frac{\pi}{180}\right), c\gamma = \cos\left(\gamma \cdot \frac{\pi}{180}\right)$$

Equation 3.6

Note for systems that have adopted the arrangement illustrated in Figure 3.13 (b) it is necessary to alter the resulting $[L]$ matrix to take the following form.

$$(\text{Arrangement } a)[L] = \begin{bmatrix} 11 & 12 & 13 \\ 21 & 22 & 23 \\ 31 & 32 & 33 \end{bmatrix} \rightarrow (\text{Arrangement } b)[L] = \begin{bmatrix} 22 & 21 & 13 \\ 12 & 11 & 23 \\ 31 & 32 & 33 \end{bmatrix}$$

Equation 3.7

Once the $[L]$ matrix has been generated the individual planes and corresponding directions can be converted into orthonormal space with orthorhombic coordinates.

Miller indices conversion into orthorhombic axes for a slip plane.

$$\{x'_{sp}, y'_{sp}, z'_{sp}\} = \{h', k', l'\} \cdot [L] \quad \text{Equation 3.8}$$

Miller indices conversion into orthorhombic axes for a direction along slip plane.

$$\langle x'_{sd}, y'_{sd}, z'_{sd} \rangle = \langle u', v', w' \rangle \cdot [L] \quad \text{Equation 3.9}$$

The slip planes and directions acting normal to the ones calculated above are determined using following conversion.

Normal slip plane with orthonormal axes

$$\{x'_{sp}, y'_{sp}, z'_{sp}\} \rightarrow \{x_{norm\ sp}, y_{norm\ sp}, z_{norm\ sp}\} \quad \text{Equation 3.10}$$

Where

$$\begin{aligned}
 x_{norm\ sp} &= \frac{x'_{sp}}{\sqrt{(x'_{sp}{}^2 + y'_{sp}{}^2 + z'_{sp}{}^2)}} \\
 y_{norm\ sp} &= \frac{y_{sp}}{\sqrt{(x'_{sp}{}^2 + y'_{sp}{}^2 + z'_{sp}{}^2)}} \\
 z_{norm\ sp} &= \frac{z_{sp}}{\sqrt{(x'_{sp}{}^2 + y'_{sp}{}^2 + z'_{sp}{}^2)}}
 \end{aligned}
 \tag{Equation 3.11}$$

Normal slip direction with orthonormal axes.

$$\langle x'_{sd}, y'_{sd}, z'_{sd} \rangle \rightarrow \langle x_{norm\ sd}, y_{norm\ sd}, z_{norm\ sd} \rangle
 \tag{Equation 3.12}$$

Where

$$\begin{aligned}
 x_{norm\ sd} &= \frac{x'_{sd}}{\sqrt{(x'_{sd}{}^2 + y'_{sd}{}^2 + z'_{sd}{}^2)}} \\
 y_{norm\ sd} &= \frac{y'_{sd}}{\sqrt{(x'_{sd}{}^2 + y'_{sd}{}^2 + z'_{sd}{}^2)}} \\
 z_{norm\ sd} &= \frac{z'_{sd}}{\sqrt{(x'_{sd}{}^2 + y'_{sd}{}^2 + z'_{sd}{}^2)}}
 \end{aligned}
 \tag{Equation 3.13}$$

A rotation matrix $[g]$ and inverse rotation matrix $[g]^{-1}$ are generated for each data point from its corresponding Euler angles, $(\varphi_1, \Phi, \varphi_2)$ are given by [190].

$$[g] = \begin{bmatrix} \cos\varphi_{1R}\cos\varphi_{2R} - \sin\varphi_{1R}\sin\varphi_{2R}\cos\phi_R & \sin\varphi_{1R}\cos\varphi_{2R} + \cos\varphi_{1R}\sin\varphi_{2R}\cos\phi_R & \sin\varphi_{2R}\sin\phi_R \\ -\cos\varphi_{1R}\sin\varphi_{2R} - \sin\varphi_{1R}\cos\varphi_{2R}\cos\phi_R & -\sin\varphi_{1R}\sin\varphi_{2R} + \cos\varphi_{1R}\cos\varphi_{2R}\cos\phi_R & \cos\varphi_{2R}\sin\phi_R \\ \sin\varphi_{1R} & \sin\phi_R - \cos\varphi_{1R}\sin\phi_R & \cos\phi_R \end{bmatrix}$$

$$\tag{Equation 3.14}$$

$$[g]^{-1} = \begin{bmatrix} \cos\varphi_{1R}\cos\varphi_{2R} - \sin\varphi_{1R}\sin\varphi_{2R}\cos\phi_R & -\cos\varphi_{1R}\sin\varphi_{2R} - \sin\varphi_{1R}\cos\varphi_{2R}\cos\phi_R & \sin\varphi_{1R}\cdot\sin\phi_R \\ \sin\varphi_{1R}\cos\varphi_{2R} + \cos\varphi_{1R}\sin\varphi_{2R}\cos\phi_R & -\sin\varphi_{1R}\sin\varphi_{2R} + \cos\varphi_{1R}\cos\varphi_{2R}\cos\phi_R & -\cos\varphi_{1R}\sin\phi_R \\ \sin\varphi_{2R}\sin\phi_R & \cos\varphi_{2R}\sin\phi_R & \cos\phi_R \end{bmatrix}$$

Equation 3.15

Where $(\varphi_1, \Phi, \varphi_2)$ have been converted into radians $(\varphi_{1R}, \Phi_R, \varphi_{2R})$

$$\begin{aligned} \varphi_{1R} &= \varphi_1 \cdot \frac{\pi}{180} \\ \Phi_R &= \Phi \cdot \frac{\pi}{180} \\ \varphi_{2R} &= \varphi_2 \cdot \frac{\pi}{180} \end{aligned} \quad \text{Equation 3.16}$$

Pre-multiplying the normal slip plane and slip direction in orthonormal space with the inverse rotation matrix $[g]^{-1}$ aligns the slip plane and slip direction with the macroscopic sample space.

Slip plane in sample space

$$\{x_{sp}, y_{sp}, z_{sp}\} = \{x_{norm\ sp}, y_{norm\ sp}, z_{norm\ sp}\} \cdot [g]^{-1} \quad \text{Equation 3.17}$$

Slip direction in sample space

$$\langle x_{sd}, y_{sd}, z_{sd} \rangle = \langle x_{norm\ sd}, y_{norm\ sd}, z_{norm\ sd} \rangle \cdot [g]^{-1} \quad \text{Equation 3.18}$$

When required, to calculate the corresponding normal slip planes and directions in orthonormal space the slip planes and directions are pre-multiplied with the rotation matrix $[g]$.

3.7.2 Schmid factor

Schmid factor (m) is a geometrical relationship between the deformation mode and the applied direction of force [145]. Values of Schmid factor range from $m = 0 - 0.5$ for a single loading direction and can be used as determine the magnitude of the applied load on an individual slip plane, with $m = 0.5$ representing a maximum load. Here the orientation of a specific slip plane and direction within the macroscopic sample space, $\{x_{sp}, y_{sp}, z_{sp}\}$ and $\langle x_{sd}, y_{sd}, z_{sd} \rangle$ respectively, have been combined with a tensile and compressive loading direction. A total Schmid factor value has been determined through combining both the tensile and compressive loads, thus resulting in a value range of $m = 0 - 1$.

Tensile loading direction in sample space, axis.

$$(x_T, y_T, z_T) \quad \text{Equation 3.19}$$

Tensile Schmid factor

$$m_{Tensile} = \frac{(x_T \cdot x_{sp} + y_T \cdot y_{sp} + z_T \cdot z_{sp})}{\sqrt{(x_T^2 + y_T^2 + z_T^2)} \cdot \sqrt{(x_{sp}^2 + y_{sp}^2 + z_{sp}^2)}} \cdot \frac{(x_T \cdot x_{sp} + y_T \cdot y_{sp} + z_T \cdot z_{sp})}{\sqrt{(x_T^2 + y_T^2 + z_T^2)} \cdot \sqrt{(x_{sd}^2 + y_{sd}^2 + z_{sd}^2)}}$$

$$\text{Equation 3.20}$$

Compressive loading direction, axis.

$$(x_C, y_C, z_C) \quad \text{Equation 3.21}$$

Compressive Schmid factor.

$$m_{Compressive} = \frac{(x_C \cdot x_{sp} + y_C \cdot y_{sp} + z_C \cdot z_{sp})}{\sqrt{(x_C^2 + y_C^2 + z_C^2)} \cdot \sqrt{(x_{sp}^2 + y_{sp}^2 + z_{sp}^2)}} \cdot \frac{(x_C \cdot x_{sp} + y_C \cdot y_{sp} + z_C \cdot z_{sp})}{\sqrt{(x_C^2 + y_C^2 + z_C^2)} \cdot \sqrt{(x_{sd}^2 + y_{sd}^2 + z_{sd}^2)}}$$

$$\text{Equation 3.22}$$

Total Schmid factor.

$$m = m_{Tensile} + m_{Compressive} \quad \text{Equation 3.23}$$

3.7.3 Pole figure plots and trace chord delineation for slip planes of interest.

The following procedure was used to determine the graphical location of slip planes on a stereographic projection pole figure. Each pole figure uses a (x, y) coordinate system with a radius of 2.

Using the pre-determined orientations for the slip planes in sample space.

$$\{x_{sp}, y_{sp}, z_{sp}\} \quad \text{Equation 3.24}$$

Throughout this investigation northern hemisphere projections are used unless otherwise stated. For a plane of interest to be displayed on a northern hemisphere projection $z_{sp} \geq 0$.

Northern hemisphere pole figure plot (x_n, y_n) coordinates.

$$x_n = \frac{2x_{sp}}{1 + z'_{sp}} \quad \text{Equation 3.25}$$

$$y_n = \frac{2y_{sp}}{1 + z_{sp}}$$

If required a southern hemisphere projection can be constructed when $z_{sp} < 0$.

Southern hemisphere pole figure plot (x_s, y_s) coordinates.

$$x_s = \frac{2x_{sp}}{1 - z'_{sp}} \quad \text{Equation 3.26}$$

$$y_s = \frac{2y_{sp}}{1 - z_{sp}}$$

The example presented in Table 3.4 shows the calculated orientations for the slip direction and slip plane with crystallographic coordinates, u, v, t, w and h, k, i, l , with their corresponding slip direction and slip plane in sample space x_{sd}, y_{sd}, z_{sd} and x_{sp}, y_{sp}, z_{sp} respectively. Using the sample space coordinates the stereographic pole figure projection given in Figure 3.14 can be constructed, which demonstrates the relative position of the basal and corresponding prismatic planes for an HCP crystal with Euler angles $\phi_1 = 0, \Phi = 0, \phi_2 = 0$.

Table 3.4 Calculated orientations for the slip direction and plane in sample space, when $\phi_1 = 0$, $\Phi = 0$, $\phi_2 = 0$.

	Slip direction				Slip plane				Slip direction in sample space			Slip plane in sample space			Pole coordinates	
	<i>u</i>	<i>v</i>	<i>t</i>	<i>w</i>	<i>h</i>	<i>k</i>	<i>i</i>	<i>l</i>	x_{sd}	y_{sd}	z_{sd}	x_{sp}	y_{sp}	z_{sp}	x	y
Basal	1	1	-2	0	0	0	0	1	0	0	1	0.8	0.5	0	0	0
Prismatic 1	1	-2	1	0	1	0	-1	0	1	0	0	0	-1	0	2	0
Prismatic 2	-2	1	1	0	0	1	-1	0	0.5	0.8	0	-0.8	0.5	0	1	1.7
Prismatic 3	1	1	-2	0	1	-1	0	0	0.5	-0.8	0	0.8	0.5	0	1	-1.7
Prismatic 4	1	1	-2	0	-1	1	0	0	-0.5	0.8	0	0.8	0.5	0	-1	1.7
Prismatic 5	1	-2	1	0	-1	0	1	0	-1	0	0	0	-1	0	-2	0
Prismatic 6	-2	1	1	0	0	-1	1	0	-0.5	-0.8	0	-0.8	0.5	0	-1	-1.7

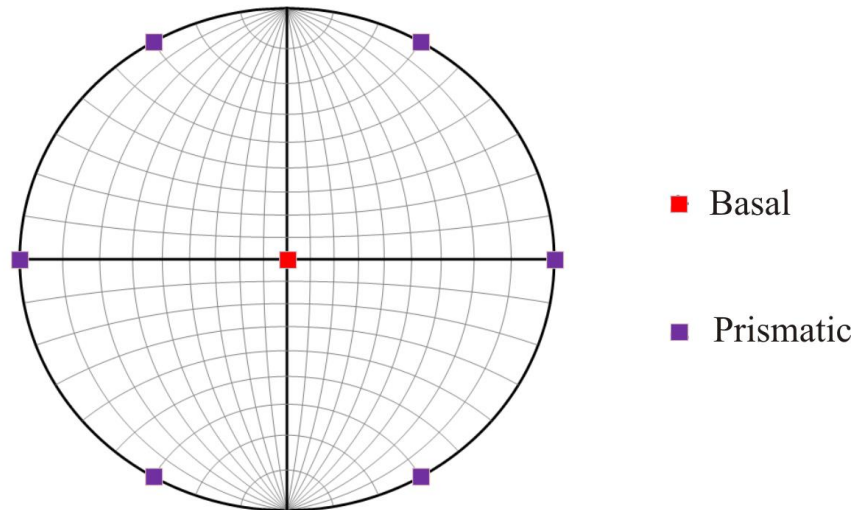


Figure 3.14 Composite pole figure plot, displaying the relative location of the basal and prismatic planes when $\phi_1 = 0$, $\Phi = 0$, $\phi_2 = 0$.

3.7.4 Slip trace analysis

The following method outlines the calculations used during slip trace analysis. Here a graphical tool was generated that illustrated the orientation of slip planes for any given crystallographic orientation. The generated graphic was subsequently overlaid onto an OIM allowing the user to determine which displayed chord most suitably aligns with the observed deformation. Permitting the identification of a particular mode of deformation along with the potential plane for which it has occurred. Firstly it is necessary to determine the angle of the trace chord relative to the OIM. The orientation of the slip planes of interest are calculated using both the northern and southern hemisphere pole figure coordinates (x_n, y_n) and (x_s, y_s) . The orientation of the slip planes occur perpendicular to the orientations displayed in the pole figure. Therefore it is necessary to use the inverse of these values.

For northern hemisphere pole figure data, inverse coordinates.

$$x_{inv} = -y_n \quad \text{Equation 3.27}$$

$$y_{inv} = x_n$$

For southern hemisphere pole figure data, inverse coordinates.

$$x_{inv} = -y_s \quad \text{Equation 3.28}$$

$$y_{inv} = x_s$$

For completeness both the northern and southern hemisphere data is used, this does however create duplicate chords that appear with the same orientation one on top of

the other. This process can therefore only identify pairs of possible activated slip planes. To determine the angle the chord (θ) and therefore the angle of the slip plane the following steps are followed.

If

$$|y_{inv}| = 0 \quad \text{Equation 3.29}$$

Then

$$\delta = 90 \quad \text{Equation 3.30}$$

If

$$|y_{inv}| \neq 0 \quad \text{Equation 3.31}$$

Then

$$\delta = \arctan\left(\frac{x}{y}\right) \cdot \left(\frac{180}{\pi}\right) \quad \text{Equation 3.32}$$

The resulting angle of the chord (θ) is required to remain within the bounds 0-180. Therefore, if δ from Equation 3.32 is larger than 180.

$$\theta = \delta - 180 \quad \text{Equation 3.33}$$

If δ from Equation 3.32 is smaller than 0.

$$\theta = \delta + 180 \quad \text{Equation 3.34}$$

If δ from Equation 3.32 is within the bounds 0-180.

$$\theta = \delta \quad \text{Equation 3.35}$$

The generated slip trace graphic uses the coordinates (x_{trace}, y_{trace}) the axes range -1 - 1 for x and 0 - 1 for y . Using the angle of the chord (θ) the trace coordinates are plotted using the following functions.

Trace x_{trace}

$$x_{trace} = \frac{1}{\sqrt{1 + \left(\tan\left(\theta \frac{\pi}{180}\right)\right)^2}} \quad \text{Equation 3.36}$$

When $\theta > 90$ the negative value of x_{trace} is plotted.

$$x_{trace} = -x_{trace} \quad \text{Equation 3.37}$$

Trace y_{trace}

$$y_{trace} = \sqrt{1 - y'} \quad \text{Equation 3.38}$$

When

$$y' = \frac{1}{\sqrt{1 + \left(\tan\left(\theta \frac{\pi}{180}\right)\right)^2}} \quad \text{Equation 3.39}$$

The flow diagram presented in Figure 3.15 illustrates the slip trace analysis tool in operation, using the above functions in combination with a further Schmid factor filter. Here, for an assumed macroscopic stress state the Schmid factor is used as a first order approach for determining a slip systems propensity for activating. If the orientation of the slip planes in orthonormal space suit a critical Schmid factor criteria the (x_{trace}, y_{trace}) coordinates are plotted. Note this Schmid factor approach for determining the propensity for activating does not take into account the critically resolved shear stress (CRSS) of an individual plane.

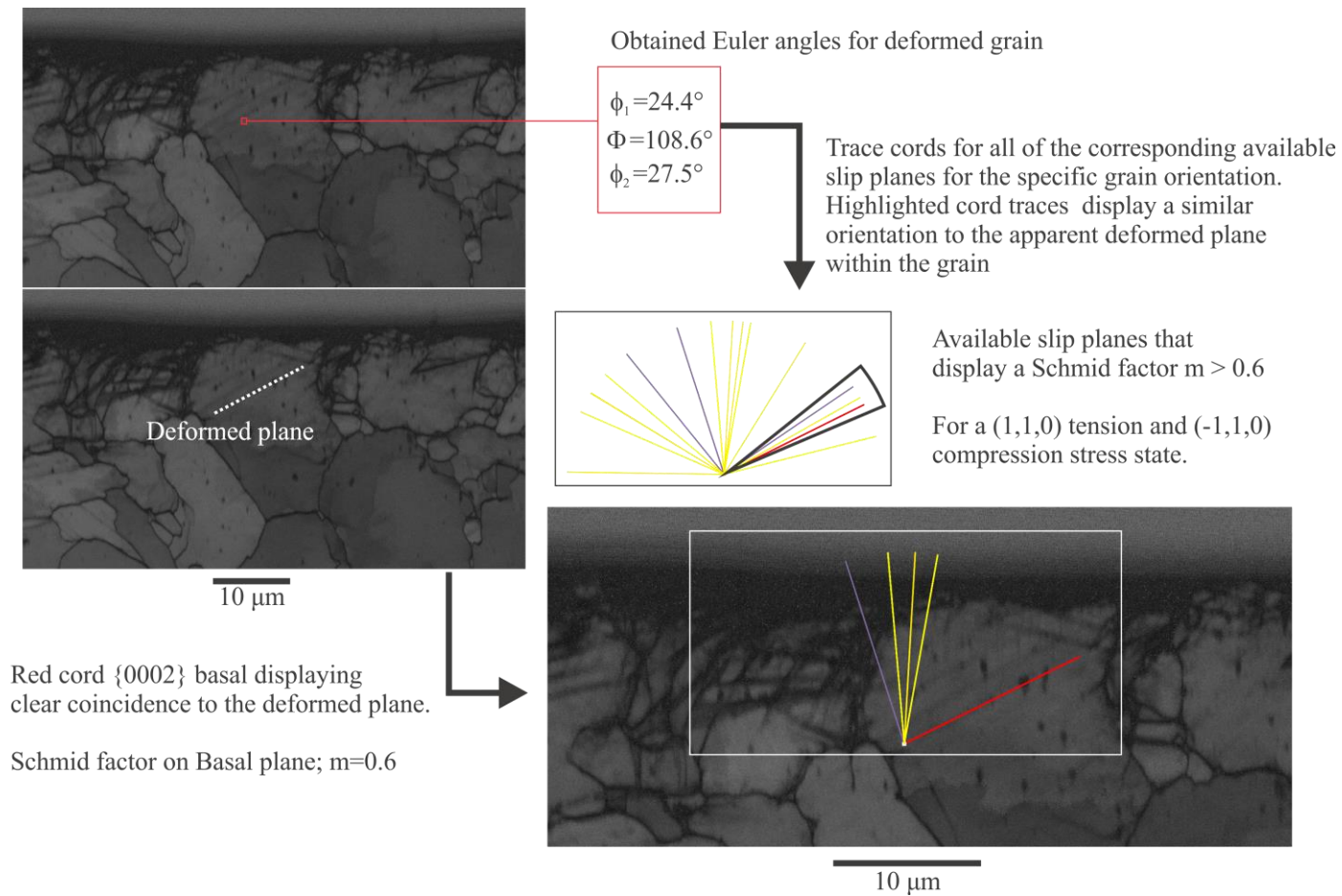


Figure 3.15 Application of the slip trace tool used to determine the available deformation planes for a specified region of material. After a Schmid factor filter of $m = 0.6$ is applied this allows the user to more easily identify the coincidence of the deformed plane, which for this example can be aligned to fit the {0002} basal plane.

3.7.5 Determining the K_1

For an individual twinning mode such as $\{10\bar{1}2\}$, there are 8 possible twinning orientations that can be activated. After a twin is created the parent grain and the twin share one of these planes and is referred to as the K_1 plane. When illustrated on a pole figure the plotted shared location will appear normal to the orientation of the twin. This method was used as a validation tool to confirm the identity of the delineated twin features highlighted using the special boundaries function in the OIM software. The Euler angles of both the parent and twin were collected. Using the Euler angles, the orientation of all of the twin planes and the angular difference between the parent and twin pole locations were calculated. The orientation of the K_1 plane corresponds to the location of the parent and twin pair that possesses the smallest angular difference, referred to as being a nearest neighbour. Figure 3.16 demonstrates the predicted location of a K_1 plane for the obtained parent and the twin Euler angles. The location of the K_1 plane displays clear coincidence to the normal orientation of the twin boundary trace.

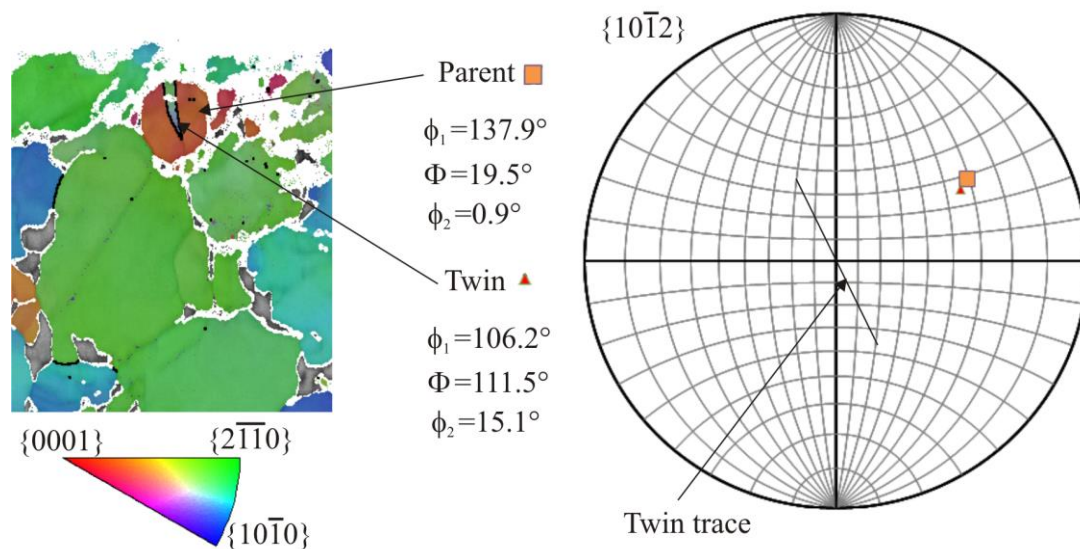


Figure 3.16 Inverse pole figure orientation image map after a noise reduction and twin delineation. Using the deformed grains average Euler angles for the parent and the twin material the corresponding location of their nearest neighbours are shown on the $\{10\bar{1}2\}$ pole figure. Here the location of the determined K_1 plane displays clear coincidence to the normal orientation of the twin trace.

3.8 Summary

This chapter outlines the common experimental procedures and operating principles used during the research project detailing; the methods used during metallographic specimen preparation, a best practice guide for imaging both optically and using an SEM, an overview of EBSD covering the fundamental principles, operational guidelines and methods used for data representation, the mathematical methodology used during crystallographic orientation analysis for slip trace analysis and Schmid factor calculations. The following chapters make use of these analysis techniques when investigating the presence of mechanically induced deformation generated during machining.

Chapter 4 - Subsurface microstructure deformation during precision turning of Ti-834

4.1 Introduction

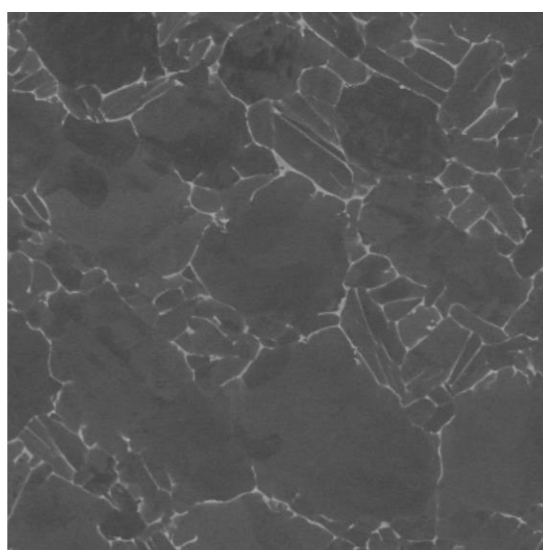
This chapter addresses the potential deleterious effects of machining at elevated cutting speeds during precision turning operations on the important titanium alloy, Timetal® 834 (Ti-834). Ti-834 was developed in the UK in the 1950's by Imperial Metal Industries (IMI), which is now currently operated by TIMET UK. Ti-834 is currently used for blades, rings and discs in the intermediate pressure compressor stage of an aero-engine due to its good mechanical properties at high temperatures. Critical components such as discs are precision turned and inspected using standard surface integrity techniques. Here a conventional approach to analysing the severity of the deformation imparted during the machining has been adopted that covers tool wear characteristics, and surface roughness analysis, with subsurface microstructure analysis undertaken via microhardness and beta distortion measurements. These results have been further supplemented with quantitative crystallographic analysis via EBSD. As Ti-834 is exposed to temperatures around 600°C in-service, an assessment of the thermal stability of the machined surfaces was conducted in order to evaluate the thermal stability of the modified surface.

4.2 Experimental methods

For the work covered in this chapter the following experimental methods were followed, these are in addition to the material analysis procedures outlined in §3.2.

4.2.1 As received material

The material used in this study was supplied by TIMET UK Ltd. For this study, the near-alpha titanium alloy Timetal® 834 (Ti-834) was supplied from cross section of a billet with an outer diameter of 250 mm. The material was supplied in the as-forged condition whereby the billet has been allowed to cool slowly following hot working low in the ($\alpha+\beta$) phase field. Following this cool the material has not been subjected to any further thermomechanical processing or heat treatment, the resulting microstructure can be seen in Figure 4.1. The as-forged material was chosen for this investigation due to its coarse-grained α microstructure, which provided a model microstructure for ease of analysis compared to the in-service Ti-834 microstructure, which has a finer bimodal morphology.



50 μm

Figure 4.1 Backscatter electron micrograph of the as-forged Ti-834 microstructure.

Compositional analysis of the as-received billet material was provided by TIMET UK. The chemical composition measurements are taken at the centre and the edge of each billet. The average composition of the material is given in Table 4.1.

Table 4.1 Billet composition of the near-alpha titanium alloy Ti-834 (wt. %).

Al	Sn	Zr	Nb	Mo	Si	Fe	O	N	C	Ti
5.8	4.0	3.5	0.7	0.5	0.335	0.006	0.1028	0.0025	0.06	Balance

4.2.2 Machining trials

Turning was undertaken using a Mori Seiki NT5400 lathe with Sandvik CNMG 120408-23 H13A uncoated carbide cutting inserts mounted in a Sandvik C5-DCLNL-35060-12 tool holder providing a clearance angle of 6° and a rake angle of 7° . Water based coolant Hocut 795B at 4-7% concentration was ‘flood’ delivered at 13 litres per minute. For each pass, a fresh cutting edge on the insert was used. Force feedback measurements were not recorded during this trial.

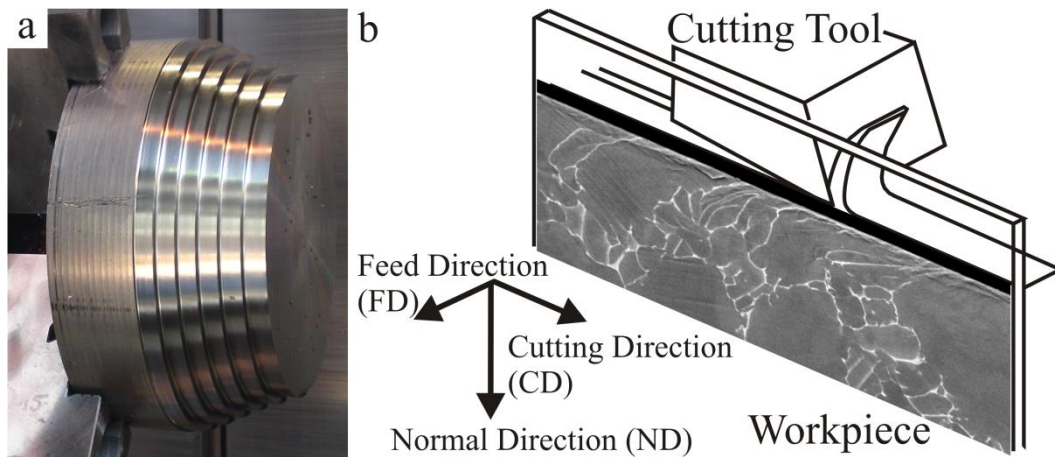


Figure 4.2(a) Photograph of the roughly turned stepped Ti-834 billet workpiece prior to the outer diameter precision turning trials; (b) Schematic illustrating the cutting process and typical subsurface microstructure deformation, sectioned parallel to the cutting direction.

Figure 4.2 shows the arrangement of the workpiece in the lathe prior to the experimental trials being carried out. Preparation of the billet required multiple roughing passes, carried out at a surface speed of $20 \text{ m}\cdot\text{min}^{-1}$, feed of $0.15 \text{ mm}\cdot\text{rev}^{-1}$, and a radial depth of cut of 1 mm. Outer-diameter precision turning trials were performed using a range of cutting surface speeds from $50 - 120 \text{ m}\cdot\text{min}^{-1}$, at a constant feed rate of $0.1 \text{ mm}\cdot\text{rev}^{-1}$ and a radial depth of cut of 1 mm. Each machining speed trial was allocated a stepped face on the workpiece, with the corresponding width of each cutting face adjusted to allow for a comparable spiral cut length for each speed,

(76 to 83 m). The machining parameters and corresponding workpiece geometries are given in Table 4.2.

Table 4.2 Machining parameters and workpiece geometry.

Machining surface speed	Feed rate	Depth of cut (radial)	Starting workpiece diameter	Cutting face width	Spiral cut length	Cutting time
(m.min ⁻¹)	(mm.rev ⁻¹)	(mm)	(mm)	(mm)	(m)	(s)
50	0.1	1.0	200.0	13.0	81	96
70	0.1	1.0	210.0	12.0	79	66
80	0.1	1.0	220.0	11.0	76	54
95	0.1	1.0	230.0	10.5	76	48
105	0.1	1.0	240.0	11.0	83	48
120	0.1	1.0	250.0	10.0	78	42

4.2.3 Tool wear

During outer diameter turning as a result of the tools position relative to the workpiece the tool is subjected to non-uniform contact around its exterior, as illustrated in the schematic shown in Figure 4.3(a). Figure 4.3(b) shows how the tool can be divided into two sections, these being; the leading edge and nose of the tool, with each having a corresponding rake and flank face. By virtue of the depth of cut being fixed for all trials, the length of tool wear occurring along the height of leading edge remains constant. At the nose of the tool, the uncut chip thickness (feed rate) dictates the size of the contact area of the tool with the workpiece. For the purpose of this investigation tool wear measurements were only obtained along the rake and the flank edges at the nose of the tool, since this region since the performance of the nose has a considerable impact on workpiece surface quality. A Carl Zeiss light microscope with AxioVision image acquisition software was used to measure the wear (VB) on the flank face and rake face at the nose of each used tool Figure 4.4(a-b). The micrographs shown in Figure 4.4(a-b) illustrate the change in appearance from an unworn to worn tool, with typical abrasive type wear occurring at the nose of a worn tool shown in Figure 4.4(b). For each set of wear measurement obtained from the cutting edges an average VB, and maximum VB_{max}, was determined. For industrial applications a VB and VB_{max} limit will be allocated relating to a surface

quality /dimensional tolerance criterion of the component. A common tool wear criterion as outlined by Sandvik defines a maximum acceptable tool wear limit for average flank wear at $VB= 0.25$ mm and maximum flank wear at $VB_{max}= 0.5$ mm. Examples of non-uniform wear include; notch, crater or severe rake face wear and chip adhesion [166].

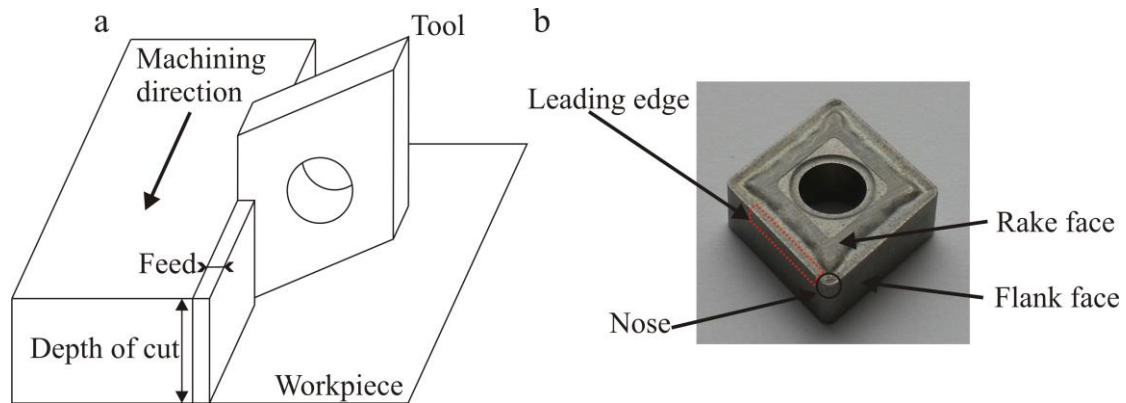


Figure 4.3 (a) Schematic diagram illustrating the tools orientation relative to the workpiece during precision turning. (b) Image of a Sandvik CNMG 120408-23 H13A cutting insert illustrating the location of the flank face, rake face, leading edge and nose.

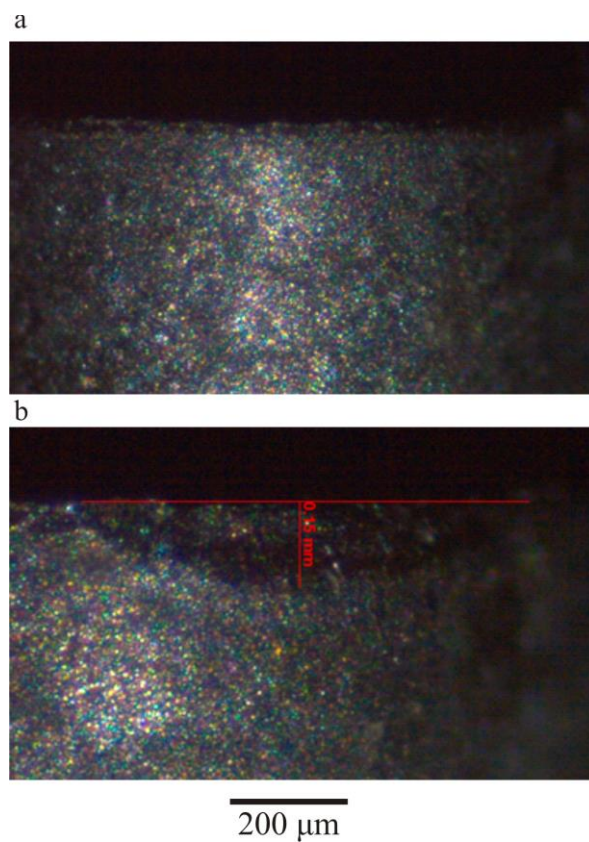


Figure 4.4 Light micrographs of the flank nose cutting edge for a Sandvik CNMG 120408-23 H13A cutting inserts (a) Unworn tool (b) worn tool.

4.2.4 Surface roughness

A Veeco Dektak 3ST surface profilometer was used to determine the surface roughness of machined workpiece material. The samples were positioned with the scan tracing perpendicular to the machined direction. On each machined surface 5 scans were carried out with each individual scan covering a length of 2 mm, the contact stylus had an applied load of 3.00 mg and a nose radius of 12.5 μm . A surface roughness average value (Ra) was acquired using a centre line average method where Ra is the arithmetic average of deviation for the surface valleys and peaks relative to a centre line in addition to a maximum roughness value (Rt).

4.2.5 Hardness profiling

Material hardness analysis was performed on the machined samples using a micro-Vickers indenter with a 2 kg load. To increase the resolution of the recorded data and to ensure each indent will not be influenced by a neighbouring test the measurements are taken in a series of offset diagonals as shown in Figure 4.5. Hardness values were obtained at 10 μm intervals from the surface to a depth of 110 μm beneath the surface. Each test was repeated four times on a new location on the sample.

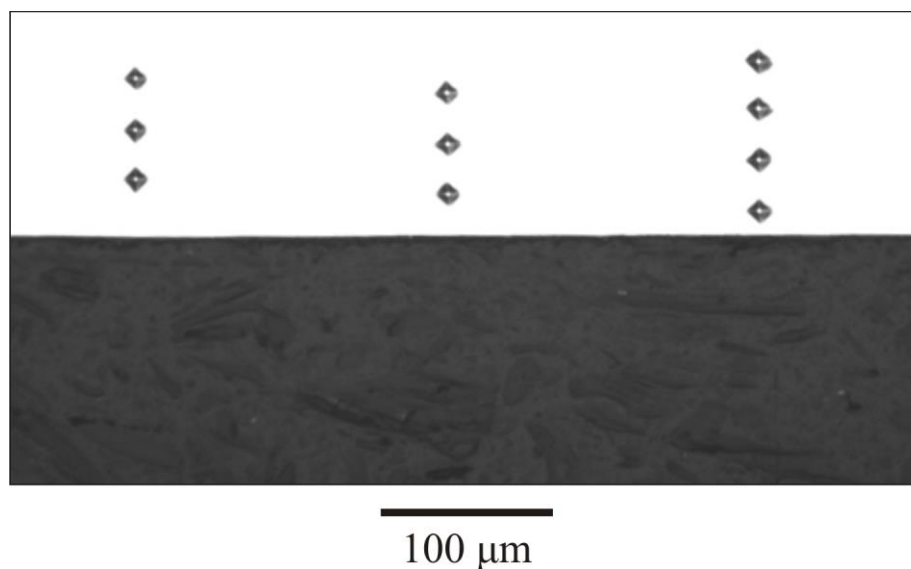


Figure 4.5 Hardness indent array at 10 μm intervals from the machined surface

4.2.6 Microstructure analysis

Following the precision turning trials, the workpiece was sectioned parallel to the normal-cutting direction (ND-CD) plane and prepared for metallographic analysis using the methods detailed in §3.3. Microstructure analysis of the machined material was carried out using an FEI Sirion field emission gun scanning electron microscope

and quantitative crystallographic orientation data was acquired using electron backscatter diffraction (EBSD) with a 20 kV accelerating voltage, a spot size of 3 and a step size of 0.06 μm . Automated indexing and post-processing of the electron diffraction data were performed using Oxford Instruments HKL Channel 5 software.

4.2.7 Heat treated samples

During operation an aerostructural component manufactured out of Ti-834 can be exposed to temperatures in excess of 600°C [191]. To ascertain the thermal stability of the machined surfaces at an elevated temperature; 10 mm wide 5 mm thick coupons were sectioned from each of the machined surface speed regions. The machined coupons were heat treated to a constant temperature of 750°C for 1600 hours followed by air cool. This time and temperature combination was selected in order to evaluate the thermal stability of the modified surface, rather than simulate specific in-service conditions.

4.3 Results and discussion

4.3.1 Tool Wear

The machining trials were undertaken such that each tool had a comparable spiral cut length (SCL) for each cutting speed. It is important to note that by virtue of the increasing machining speed and fixed SCL each tool remained in contact with the workpiece for a decreasing amount of time, as shown in Table 4.2. The observed wear mechanisms for all of the tools were abrasive, with the micrographs given in Figure 4.6 showing typical examples of the resulting wear with no evidence of crater wear, chipping, flaking, notching or fracture. In addition to the observed wear there was no evidence of any residual BUE formation ahead of the cutting edge after each cutting speed trial.

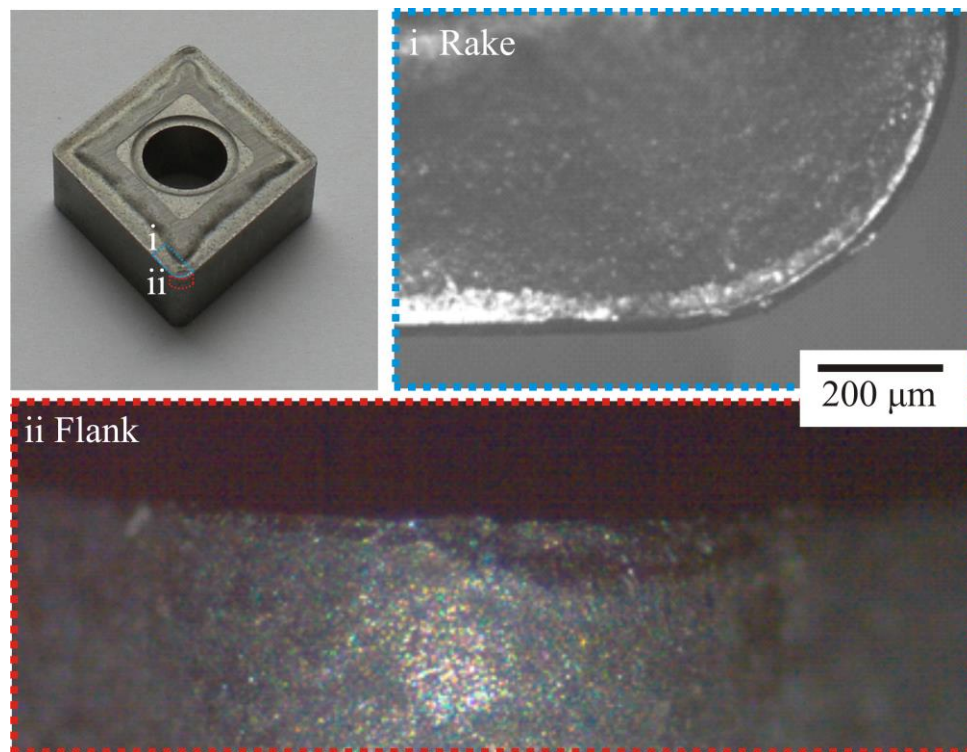


Figure 4.6 Image of a Sandvik CNMG 120408-23 H13A uncoated carbide cutting insert demonstrating the position of the (a) rake and (b) flank edges at the nose of the tool and the typical wear pattern appearance on each of the faces following 90 seconds of machining at $50 \text{ m}\cdot\text{min}^{-1}$.

Wear length measurements were obtained on the flank face and rake face at the nose of each worn tool, the plots given in Figure 4.7 show the distribution in maximum and average wear length for each respective cutting speed. Both the average and maximum wear values for the flank and rake faces of the tool show a similar distribution with the largest amount of wear ($VB \sim 0.07 \text{ mm}$ and $VB_{\text{max}} \sim 0.15 \text{ mm}$)

occurring during the slowest cut of 50 m.min⁻¹. As the cutting speed is increased the tool wear adopts the more gradual spalling type mechanism with rake face wear gradually decreasing to minimum VB ~0.03 mm and VB_{max} ~0.03 mm. For the flank face, which remains in sliding contact with the remaining workpiece, the amount of tool wear also rapidly decreases with the lowest amount of tool wear generated whilst cutting at a speed of 70 m.min⁻¹ (VB ~0.02 mm and VB_{max} ~0.02 mm). Following this minima wear point at 70 m.min⁻¹ as the speed is increased spalling wear dominates along the flank face of the tool, however is observed to marginally increase with a second peak in tool wear length occurring at 105 m.min⁻¹ (VB ~0.05 mm and VB_{max} ~0.05 mm). Prior to the investigation being undertaken the degree of tool wear sensitivity to spiral cut length (SCL) was unknown, therefore for the given prepared starting workpiece diameters for each surface speed trial an attempt was made to ensure the SCL were similar, with the SCL for the cutting trials ranging from 76 – 81 m. It is therefore important to note that the lowest measured wear length (VB_{max} =0.02 mm cut at 70 m.min⁻¹) also corresponds to the shortest SCL (76 m), thus implying that the amount of wear recorded at 70 m.min⁻¹ may have been significantly influenced by the reduced SCL. From literature there is a consensus amongst authors [59], [192] that cutting at faster surface speeds results in a larger amount of heat being generated at the tool chip interface, which is detrimental to tool wear performance. The results presented in Figure 4.7 conversely suggest that tool wear can be reduced with a progression towards faster cutting speeds, however the cutting times investigated here are significantly shorter than those experienced within industry, where expectations of a 15 minute minimum tool life are common [166]. In relation to the observed secondary peak in tool wear length at 105 m.min⁻¹, this result also corresponds to the longest SCL (81 m) and as such is unsurprising that it has resulted in an increased amount of tool wear.

This section of the trial has highlighted the need for further research to be undertaken to isolate the parameters which drive of tool wear. The author suggests the need to undertake trials that have an identical SCL for each cutting speed in addition a secondary trial investigating the wear mechanisms at each cutting speed following an identical total cutting time. Undertaking both trials would help isolate which is the most dominant influencing factor; cutting time or cutting distance.

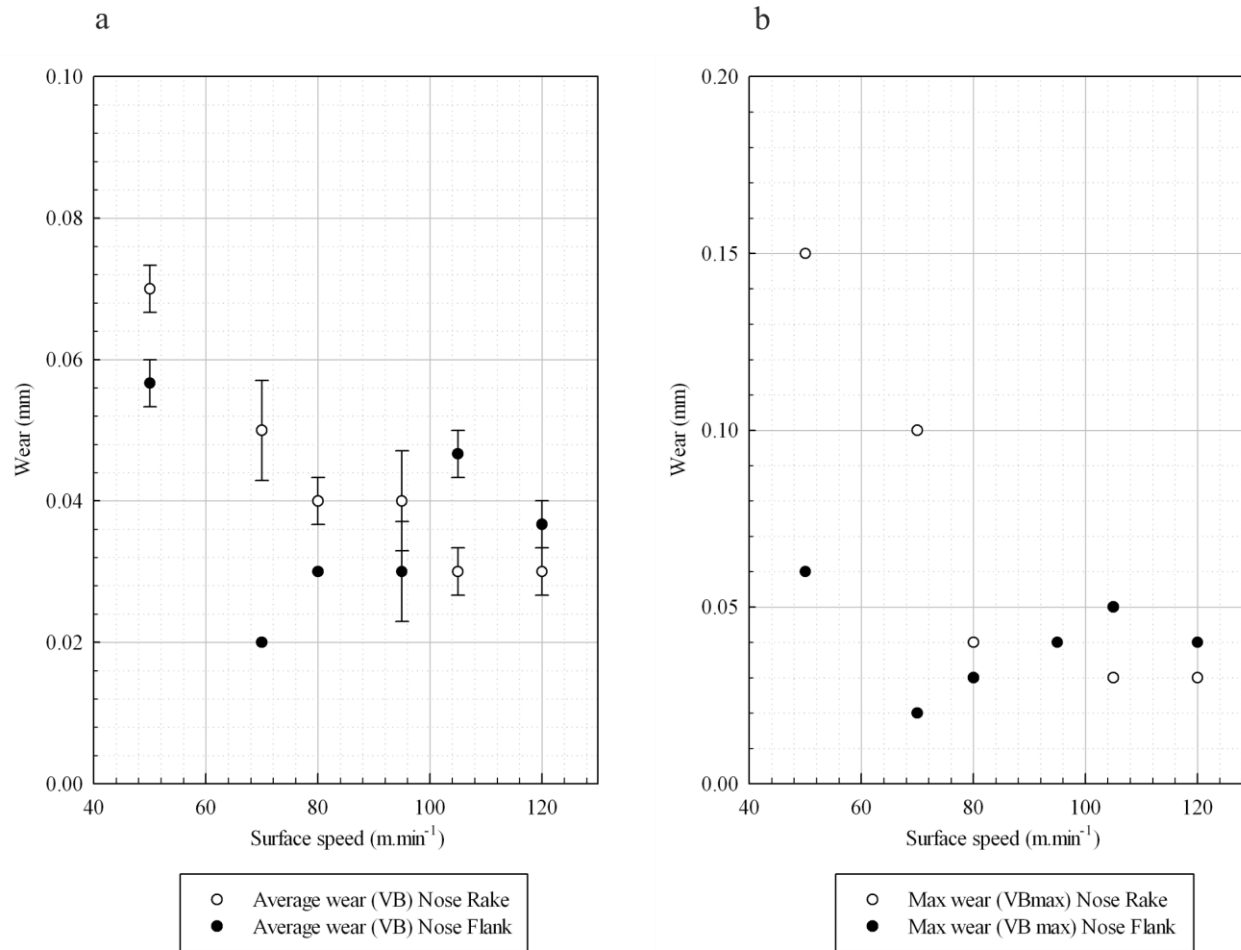


Figure 4.7 tool wear profiles for the (a) average (b) maximum tool wear, VB_{max} , for rake and flank wear at the nose of the tool as a function of machining speed. The error bars indicate the true spread in the recorded data.

4.3.2 Surface Roughness

The corresponding average (Ra) and maximum (Rt) surface roughness values of the workpiece are given in Figure 4.8. Both Ra and Rt follow the same relationship with the machining surface cutting speed, which incidentally is comparable to the relationship previously shown in Figure 4.7 for flank tool wear. The results presented in Figure 4.8 for each machining speed are the culmination of 5 independent scans and are representative of the entire machined surface, covering material that had been machined early and near the end of the cutting trial. Similarly to the behaviour shown for tool wear the workpiece surface roughness values start high (Ra \approx 0.55) at 50 $\text{m}\cdot\text{min}^{-1}$ and show a minima Ra value of \approx 0.45 at 70 $\text{m}\cdot\text{min}^{-1}$. As the machining speed is increased however, the surface roughness of the workpiece is observed to steadily increase to an Ra \approx 0.62 at 120 $\text{m}\cdot\text{min}^{-1}$, a behaviour which was not observed for tool wear which saw a reduction in wear at 120 $\text{m}\cdot\text{min}^{-1}$. In addition, the large surface roughness values observed at 50 $\text{m}\cdot\text{min}^{-1}$ were surpassed when the material was cut at speeds $>105 \text{ m}\cdot\text{min}^{-1}$, a behaviour that was not observed during the tool wear analysis that saw the maximum amount of tool wear occurring at 50 $\text{m}\cdot\text{min}^{-1}$ with further rises in tool wear with an increase in cutting speed remaining below this level.

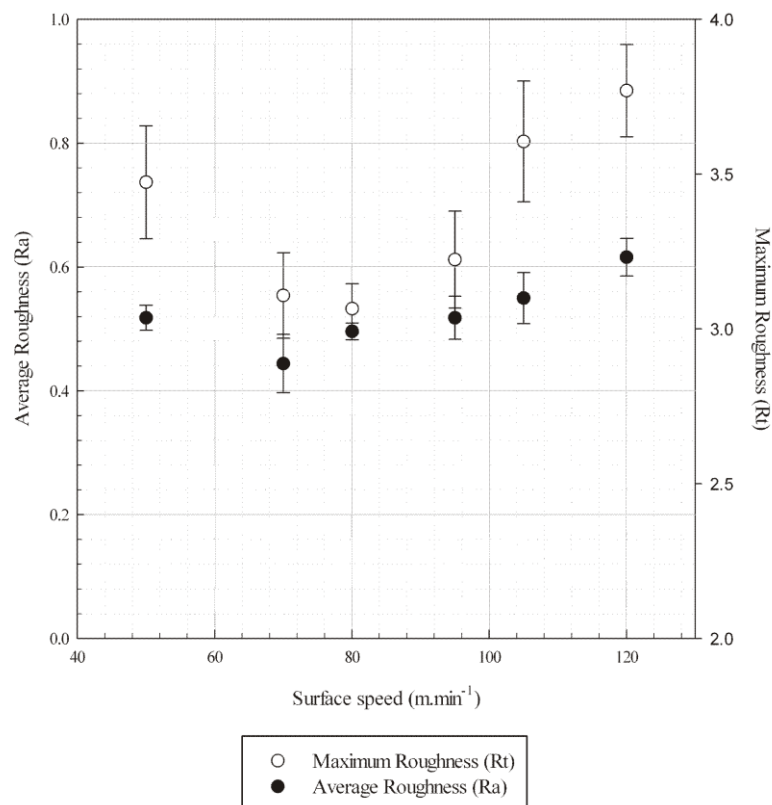


Figure 4.8 Roughness profiles of the workpiece material as a function of machining speed using, a centre Line Average approach, Ra. The included error bars indicate the true spread in the recorded data

Further quantitative analysis of the machined surface is required to ascertain if the modes of surface damage are changing as a function of surface speed and as such are venerable to the worn tools condition.

4.3.3 Hardness profiling

The following (Vickers) indentation hardness analysis was included as an opportunity to critique the methods and results obtained, since it is a common and almost default method of subsurface integrity evaluation and as shown in §2.4 the results can often seem to be inconsistent. Variation in hardness, as the result of machining induced microstructure changes can be influenced by localised grain refinement either through recrystallization or via mechanically induced; twinning, variation in localised phase volume fraction as a result of localised phase transformations, imparted residual stresses and induced crystallographic lattice rotation. Other influencing factors that are inherently present within the material and are not the result of the machining operation include; the localised starting phase volume fraction, grain shape and size and the underlying crystallographic texture of each grain.

The cross-sectional backscatter electron micrographs of turned Ti-834 with their corresponding indentation hardness profiles that representative of each of the machining speeds are given in Figure 4.9-4.11. Qualitative analysis of the micrographs indicates that the machining induced deformation can be observed to ~50 μm beneath the surface of the material, in the form of discernible distortion of the β phase and lattice rotation, such deformation characteristics will be discussed in greater detail in §4.3.4

Similarly to the profiles observed by Che-Haron *et al.* [112], the profiles given in Figure 4.9-4.11 showed a discernible increase in hardness within ~60 μm of the machined surface, however for speeds above 80 $\text{m}\cdot\text{min}^{-1}$ this increase in hardness becomes less evident. For material cut at 50 – 80 $\text{m}\cdot\text{min}^{-1}$ a reduction from the highest values of hardness can be observed within 10 μm of the surface. Though this phenomena has been attributed to being too close to the edge of the test specimen, resulting in the interaction volume of the indenter with the workpiece being reduced thus resulting in reduced values of hardness [65]. Beyond 60 μm from the machined surface the material can be considered to be representative of the bulk which has an average hardness of ~360 Hv, however as illustrated by the error bars for each data point, which indicate the true spread in the recorded data, there is a substantial amount of inherent scatter in localised hardness. Investigations that utilise hardness profiles rarely include the entire data set, thus illustrating the amount of spread in the data before producing an averaged value. Such variation in hardness values is common, as per the inherent material variables that can create regional variations.

Rugg *et al.* [66] also used hardness profiles to determine the amount of residual stress in a machined material. Interestingly, to overcome the effect of localised texture each analysed point was correlated with its parent grain crystallographic orientation, effectively normalising the data. This method was shown to reduce the amount of variation in the acquired hardness results; however such a method requires large scale orientation data the analysed areas prior to the hardness profiles being obtained. Without prior knowledge of the localised crystallographic orientation it is the author's opinion that hardness profiles are not a practical method for correlating residual stress of a machined surface.

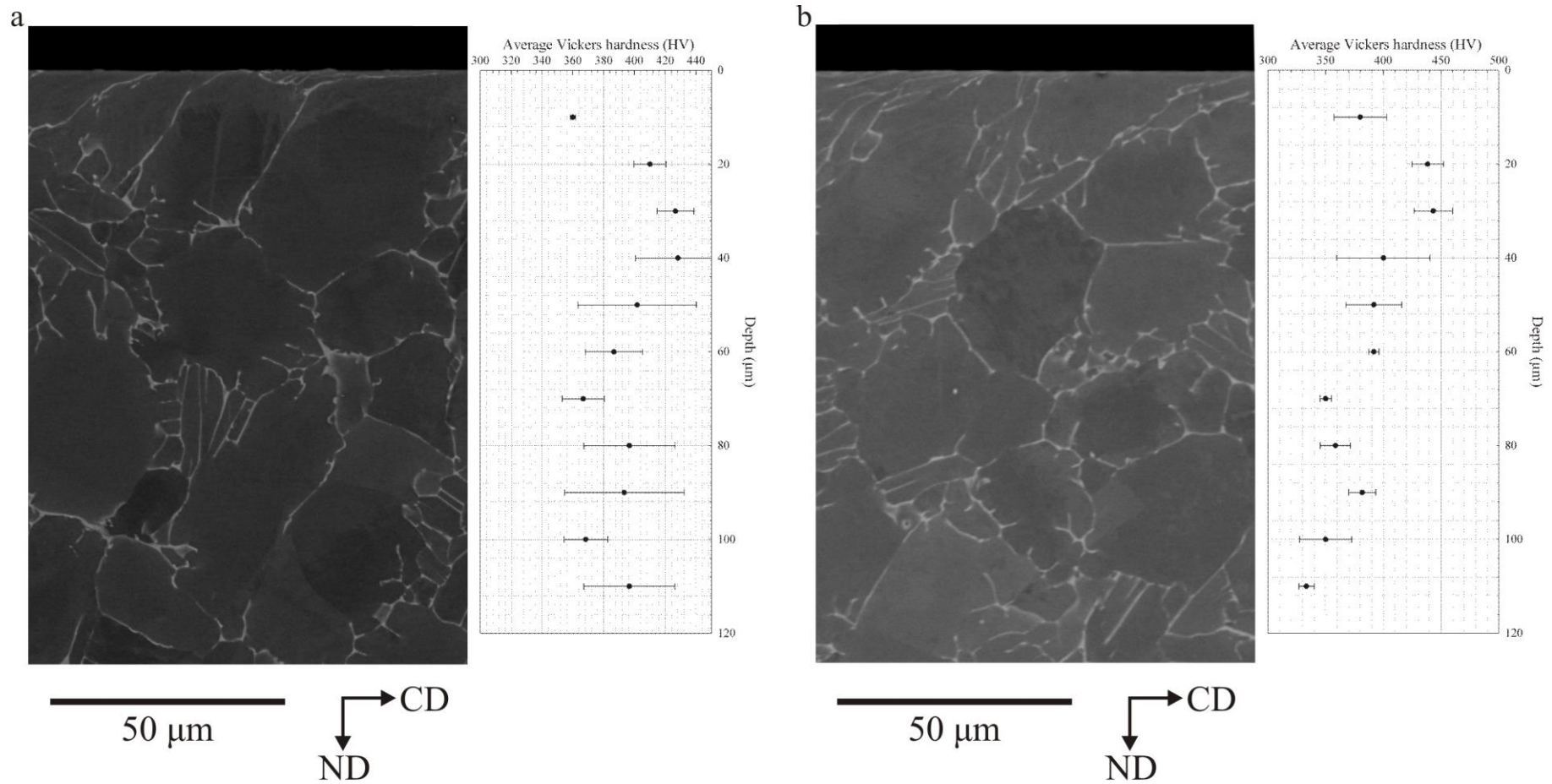


Figure 4.9 Cross-sectional backscatter electron micrograph of outer diameter turned Ti-834 and corresponding microhardness profile for (a) 50 m.min⁻¹ and (b) 70 m.min⁻¹. The error bars indicate the true spread in the recorded data.

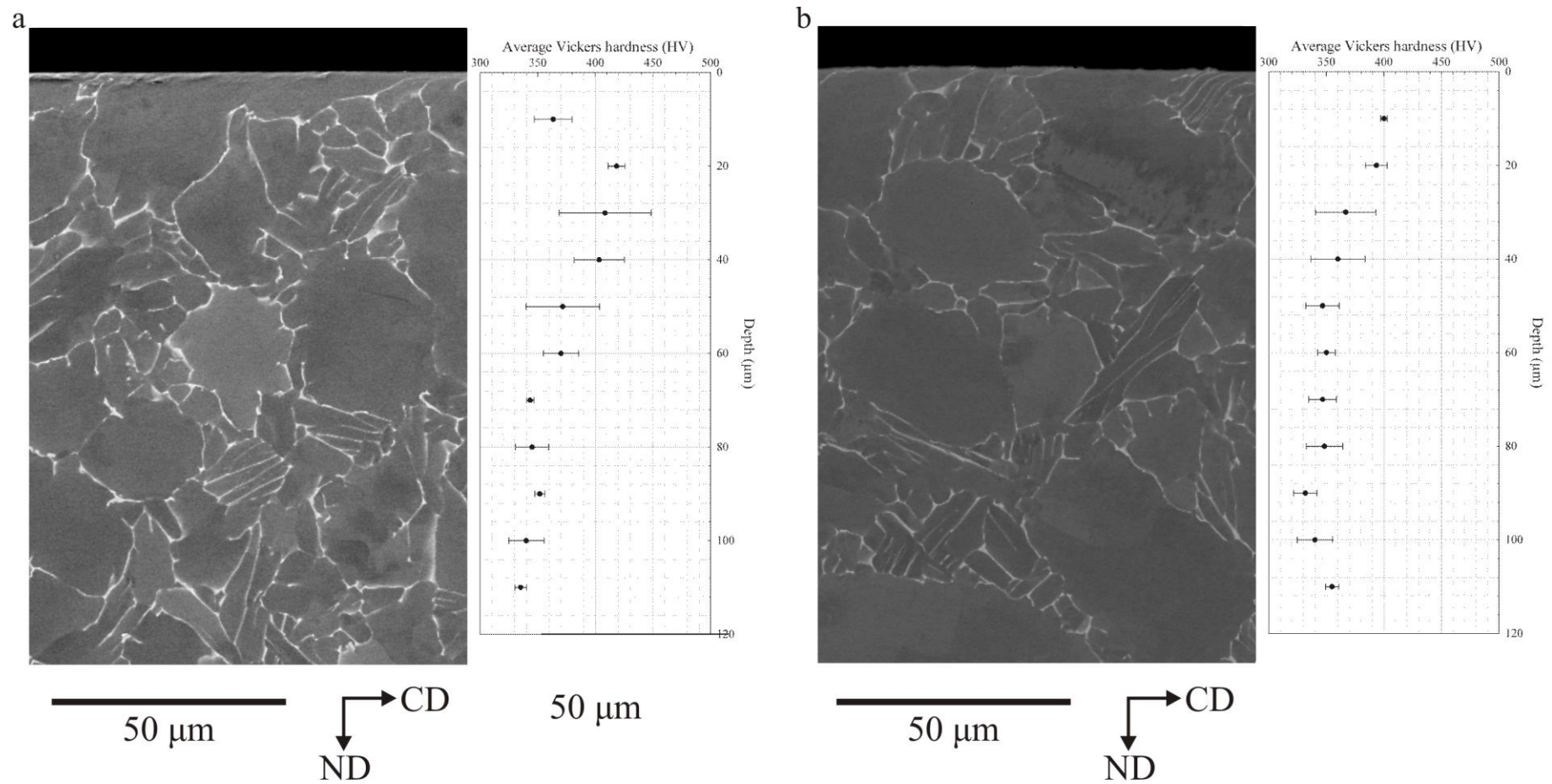


Figure 4.10 Cross-sectional backscatter electron micrograph of outer diameter turned Ti-834 and corresponding microhardness profile for (a) 80 m.min⁻¹ and (b) 95 m.min⁻¹. The error bars indicate the true spread in the recorded data.

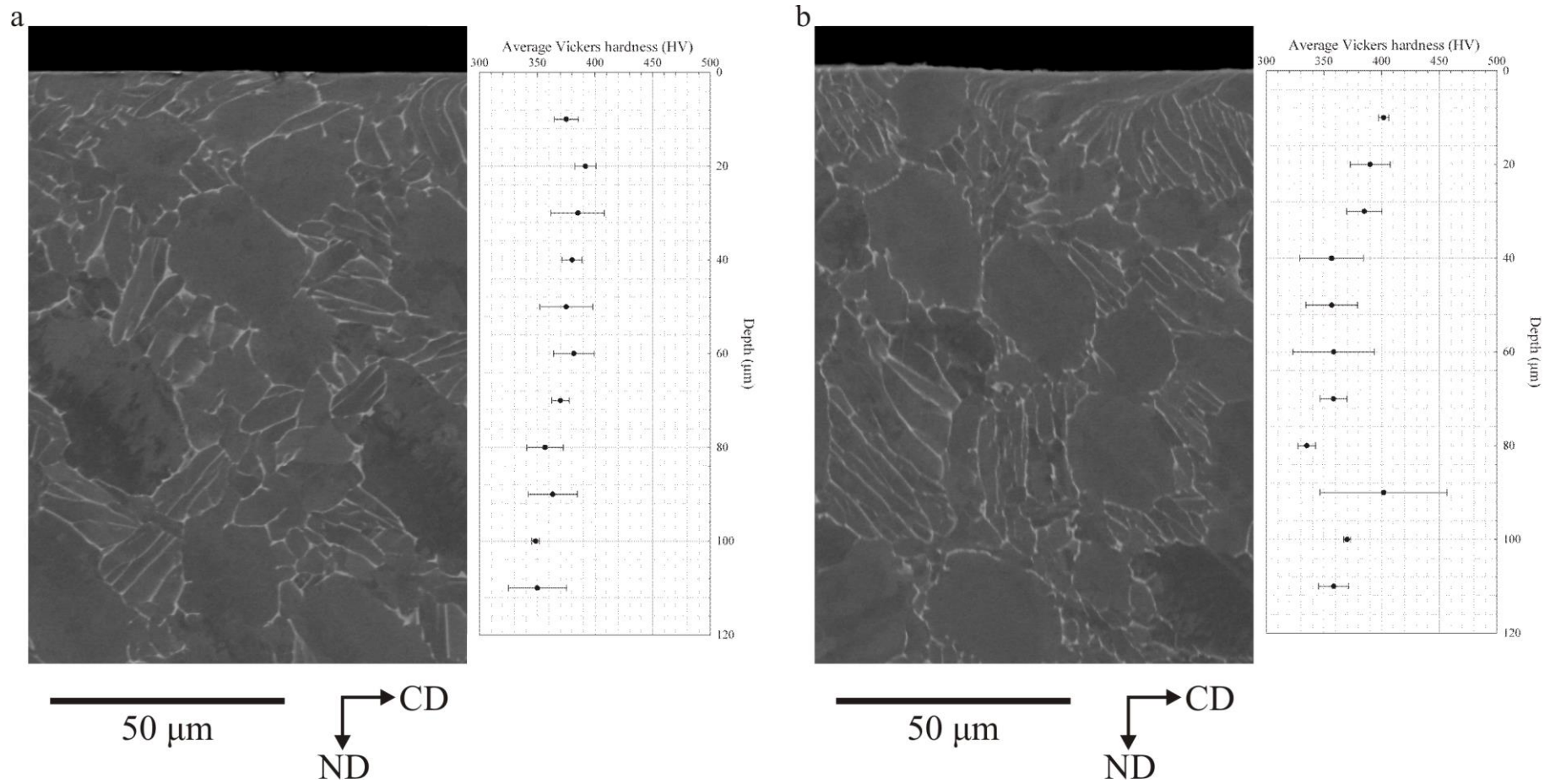


Figure 4.11 Cross-sectional backscatter electron micrograph of outer diameter turned Ti-834 and corresponding microhardness profile for (a) 105 m.min⁻¹ and (b) 120 m.min⁻¹. The error bars indicate the true spread in the recorded data.

4.3.4 Microstructure analysis

Distortion of the beta phase in the direction of cutting is observed for all cutting speeds, but the depth to which visible distortion can be observed decreases with increasing cutting velocity. Figure 4.12 shows that as the cutting speed is increased, the average depth of the induced plastic deformation, assessed using beta distortion, reduces from 10 μm at 50 $\text{m}\cdot\text{min}^{-1}$ to 3 μm at 120 $\text{m}\cdot\text{min}^{-1}$ where the observed deformation becomes part of the maximum shear zone. These observations are consistent with typical conventional surface integrity techniques that observe a similar decrease in the depth of imparted deformation as the machining speed is increased [59], [67], [108], [116]. The average deformation limits as shown in Figure 4.12 were assessed using the interface between the undeformed bulk material and the maximum perceived depth of deformation, examining beta distortion at 10 μm intervals across approximately 2000 μm of surface material. As the machining speed is increased the resulting microstructure response shows a reduction in the amount of imparted severe plastic deformation. As discussed as part of the literature review §2.6.1, both the thrust and cutting forces are expected to decrease to a minimum with increased cutting speed which, as shown in Figure 4.12, results in a reduction of total imparted strain to the machined microstructure.

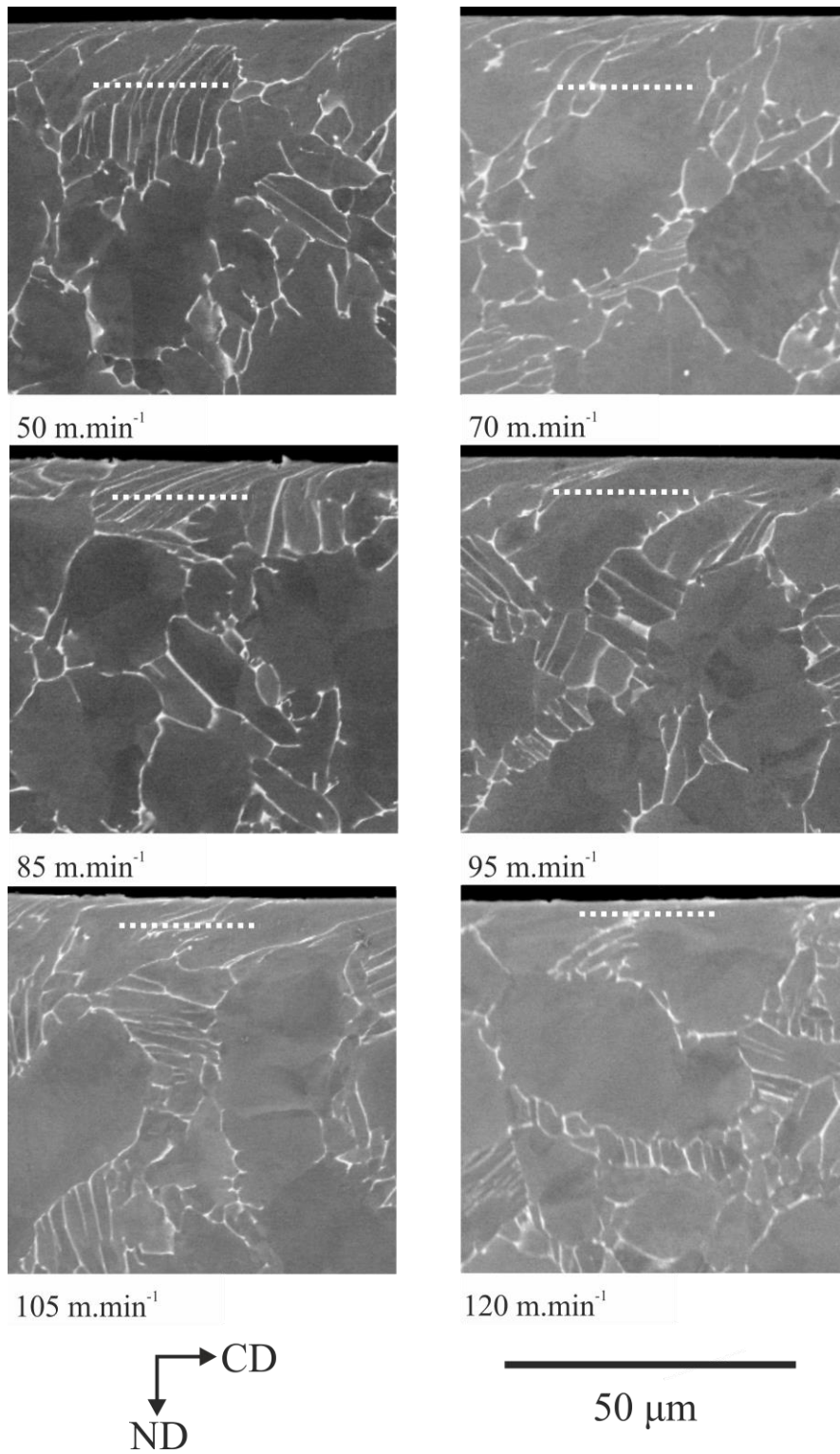


Figure 4.12 Electron backscatter images of the machined surface with increasing surface speed. The delineated line signifies the interface between the undeformed bulk material and the average depth of deformation assessed using beta distortion at 10 μm intervals across approximately 2000 μm of surface material.

The conventional analysis technique, as previously explained, would imply that titanium machining is not particularly sensitive to subsurface deformation which would in turn permit industry to progress towards increased machining speeds during manufacture. Since the imparted deformation appears to be reduced. However, when using a more metallurgical approach whilst analysing the machined material, greater subsurface deformation can be revealed. Examples of the microstructure response of Ti-834 to precision turning is shown in Figure 4.13(a, b and c) where low and high resolution electron backscatter images are given for 50m.min⁻¹, 80m.min⁻¹ and 105 m.min⁻¹ respectively.

As a result of electron channelling contrast within backscatter electron imaging regions containing twins and activated slip bands can be identified. In Figure 4.13(a ii) the needle-like features within the plastically deformed alpha grain are evidence of potential twins. With no distinct visible twin boundaries the changes in contrast within the grains in Figure 4.13(b ii) suggests that there has been the accommodation of plastic deformation through lattice rotation. The features observed in Figure 4.13(c ii) suggest that the underlying crystallographic orientation of parent grains have influenced the type of resulting deformation. The image shows neighbouring grains containing significant amounts of deformation although the orientation of this deformation is notably different. High resolution backscatter electron imaging offers insight into the activated mechanisms of deformation. However, these modes cannot be fully characterised without the use of further crystallographic analysis techniques such as electron backscattered diffraction (EBSD).

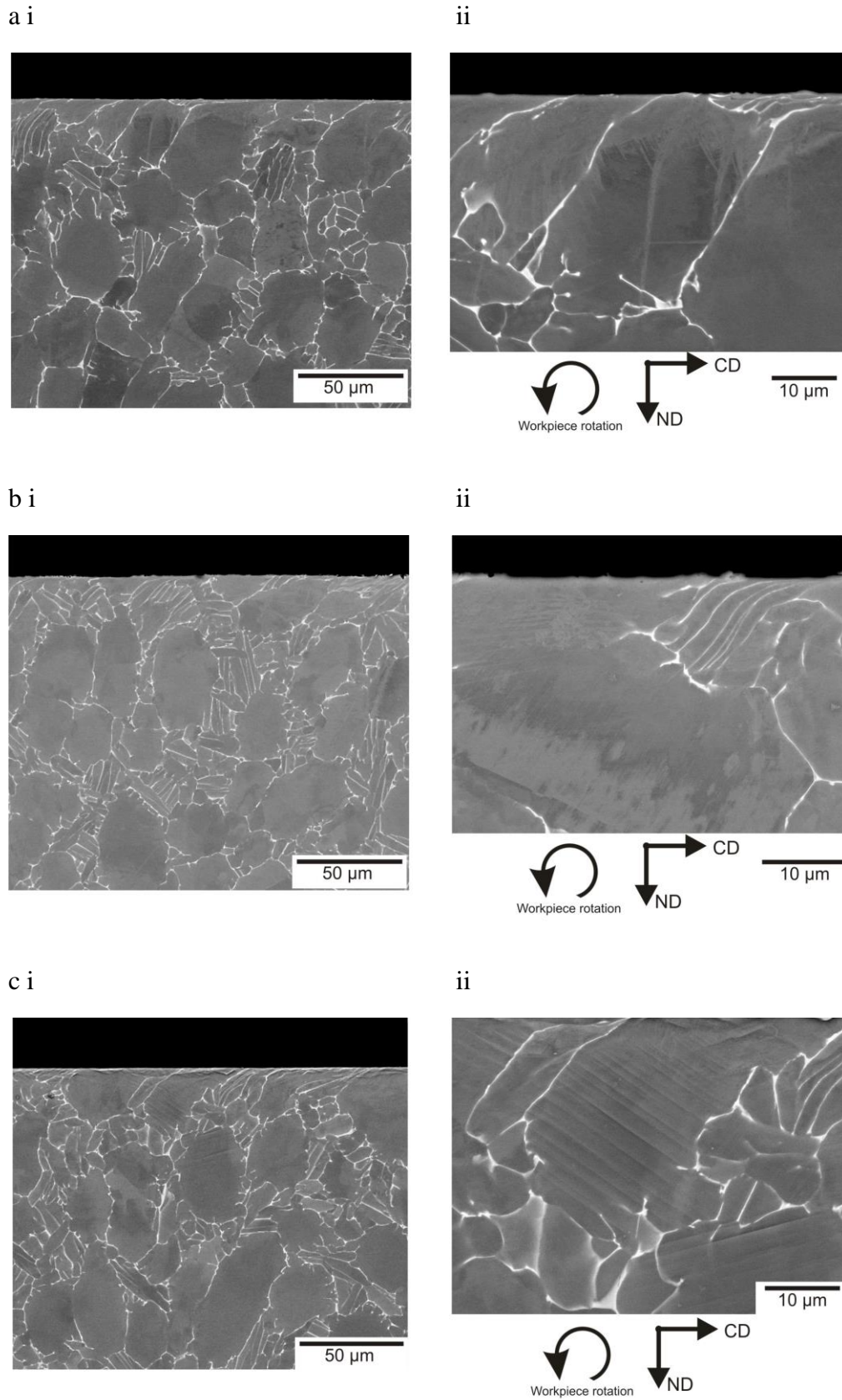


Figure 4.13 Cross-sectional backscattered electron micrographs of turned Ti-834 at surface speeds of (a) 50 m.min⁻¹, (b) 80 m.min⁻¹ and (c) 105 m.min⁻¹ with adjacent enlarged micrographs highlighting imparted deformation.

The material shown in Figure 4.12 was further analysed using EBSD. The orientation image maps (OIMs) obtained from the equivalent machined regions are displayed in Figure 4.14, where the delineated lines signifies the interface between the non-deformed bulk material and the maximum depth (white) and average depth (black) of damage observed within the surface layer for each machined surface speed sample. From the OIMs in Figure 4.14 it is possible to characterise the nature of the induced deformation, here the images show evidence that both slip and twinning occurs to much greater depths than can be easily defined using electron microscopy. The formation of twins caused by a machining process has never been reported in Ti-834. However, twin formation has been reported in shot peened Ti-834 [76]. During fatigue life cycle analysis, plastic deformation has been demonstrated to be accentuated at pre-existing twin interfaces. During load cycles, twins have been shown to be broken up into smaller irregular shaped twin fragments, incompatibility of slip deformation near such twin grain boundaries can allow fatigue cracks to nucleate preferentially within the twin boundary region. Permanent fatigue damage has been reported that has been associated with $\{10\bar{1}2\}$ and $\{11\bar{2}1\}$ tension type twins in alpha-titanium [45], [193]. The impingement of experimentally induced twins with pre-existing twins has also been shown to offer sites of crack initiation [46]. Therefore, for critical service applications, for the purpose of this investigation features such as mechanical twins and intense slip bands can be referred to as damage. The EBSD data displayed in Figure 4.14 shows heavily deformed layer of approximately 5 μm to be evident for all surface speeds, as identified by the region of unindexed data points. Beneath this heavily deformed layer, slip and twinning is evident within regions that have undergone a low amount of plastic strain, as illustrated by the grains showing zero distortion. Furthermore the OIM's illustrates how the maximum perceived depth to which twinning occurs, increases with speed. With an increase in surface speed it is inferred that the experienced effective strain rate also increases, qualitatively, the twins appear to form more frequently and the twin morphology progressively evolves from lenticular to needle-like, in agreement with Chichili *et al.* [45] and Sun *et al.* [46]. At slower surface speeds, intense slip bands appear to be more prevalent, for example at 70 $\text{m}\cdot\text{min}^{-1}$ in Figure 4.14, where slip has been indexed to have occurred along the prism $\{10\bar{1}0\}$ and first order pyramidal $\{10\bar{1}1\}$ planes.

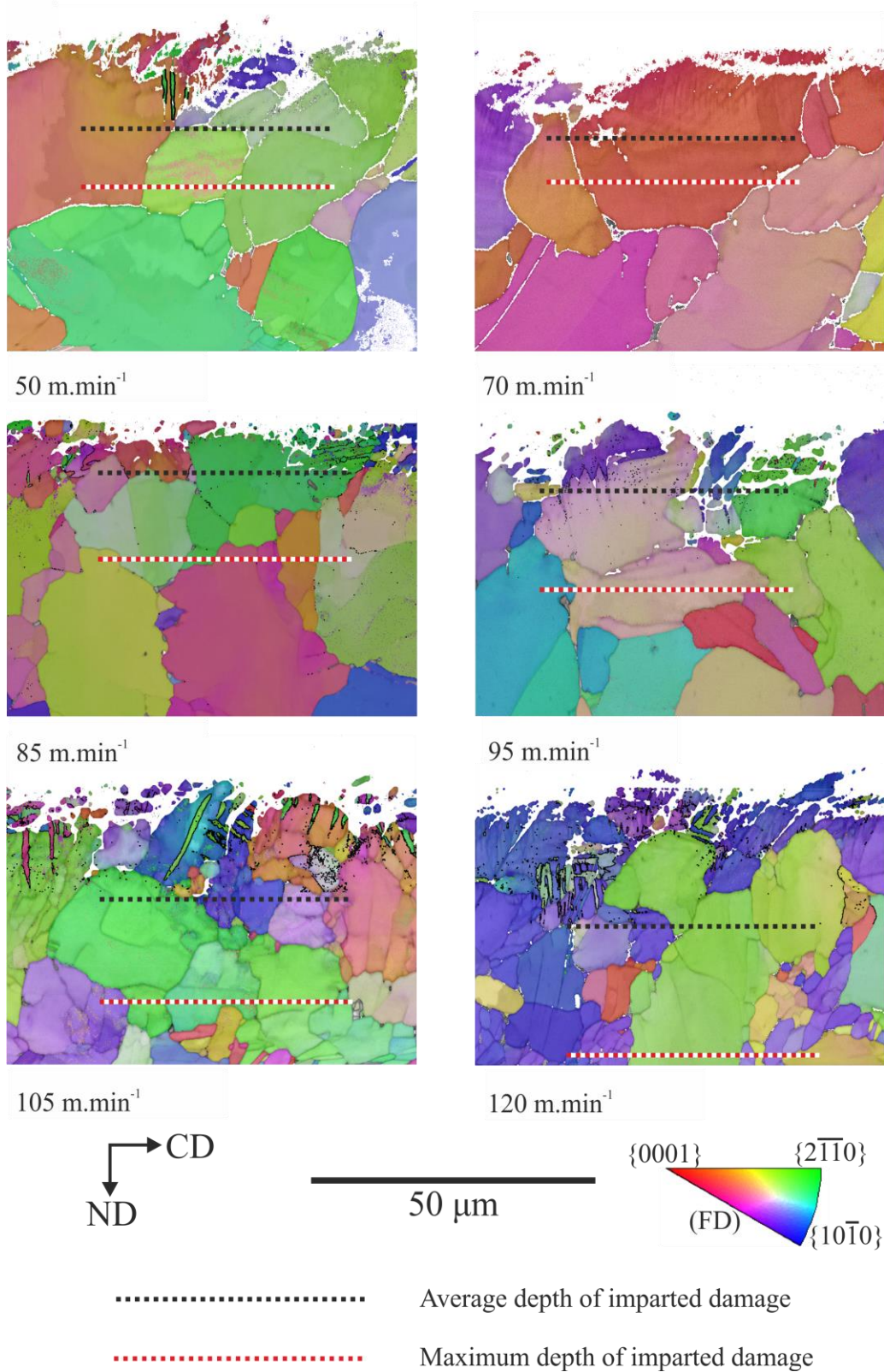


Figure 4.14 EBSD inverse pole figure (IPF) OIMs of the outer diameter turned Ti-834 surface material with increasing surface speed. The dashed black delineated line signifies the interface between the non-deformed bulk material and the average depth of damage. The dashed red delineated line signifies the interface between the non-deformed bulk material and the maximum depth of damage.

The conflicting results presented in Figure 4.15 show the comparative levels of plastic deformation assessed using both standard electron microscopy and EBSD. EBSD reveals evidence of damage within all grains beneath the SPD layer, and a consistently greater extent of damage to that observed under electron microscopy in as previously shown in Figure 4.12. Both the maximum and average depths of microstructure damage, as recorded using EBSD, follow a similar trend in agreement with Velásquez *et al.* [107] who also identified an increase in subsurface deformation with an increase in cutting speed for trials carried out to a maximum speed of 420 m.min⁻¹. Figure 4.15 illustrates that the depth of subsurface damage initially decreases from 50 m.min⁻¹ to a minimum value at approximately 70 m.min⁻¹, and then increases to the maximum recorded speed of 120 m.min⁻¹. Within the higher surface speed range (>70 m.min⁻¹), the increase in subsurface damage depth correlates with the increased strain rate on the material, the severity of the deformation also shows no evidence of reducing at speeds >120 m.min⁻¹. Therefore, author is reluctant to suggest how the material is expected to behave at elevated cutting speeds beyond those investigated here, without further experimental trials.

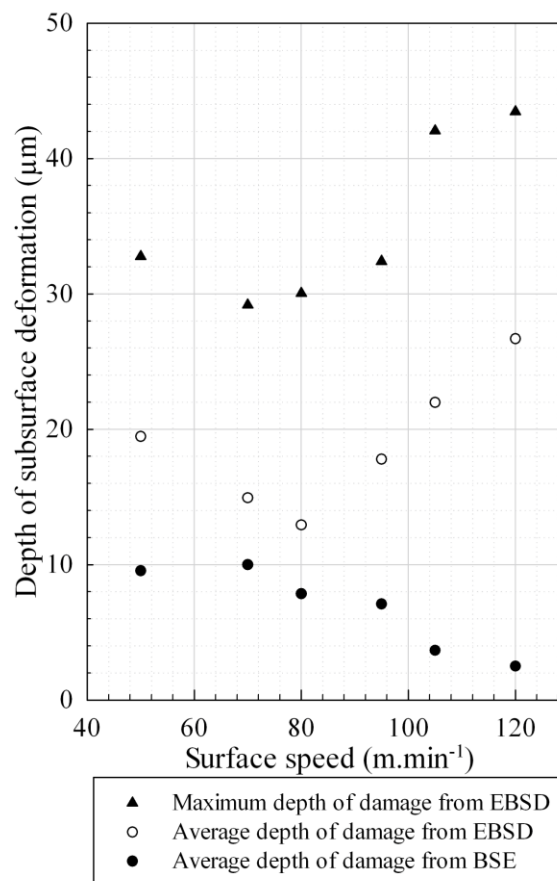


Figure 4.15 Graph illustrating the effect of surface speed on the depth of surface deformation assessed by measuring beta distortion using backscatter electron images and EBSD.

Finite element models for an orthogonal cut arrangement using a Ti-64 material data set have shown how the effective strain levels experienced by the workpiece evolve during machining [194]. The models produced by Thomas [194] showed how within the region immediately beneath the newly exposed surface the material has experienced an effective strain that approaches a maximum of 2, this strain level rapidly decays to zero at 40 μm beneath the surface. These findings correlate with the EBSD data shown in Figure 4.14 that illustrate the presence of twins within grains that display minimal further plastic deformation, suggesting that the twins have been formed under comparatively low strains. The grains that have deformed most severely have done so at the surface of the workpiece where the strain is at its greatest. The most highly deformed material has been disrupted to such an extent that the EBSD acquisition software has difficulty indexing the material due to the lattice being severely distorted. The plots in Figure 4.15 show an increase in subsurface deformation with increased cutting speeds beyond 70 $\text{m}\cdot\text{min}^{-1}$, which correlates with the previously observed increase in tool wear and surface roughness (observed in Figure 4.7 and Figure 4.8). The author has attributed the possible formation of a blunt unstable BUE, which resulted in a large wear scar on the cutting insert to the subsequent increased microstructure damage at 50 $\text{m}\cdot\text{min}^{-1}$. It is important to note that the increase in observed microstructure damage with increasing surface speed cannot exclusively be attributed to the expected increase in sustained strain rate, considering the tool is operating beyond its considered optimal service parameters of 70 $\text{m}\cdot\text{min}^{-1}$ for this material. Therefore, the mechanisms of wear and BUE formation will vary significantly between cuts and further influence the nature of the damage.

4.3.5 Thermal exposure to machined workpiece

After a prolonged thermal exposure, bright contrast precipitates under backscatter electron imaging are evident in the near surface region below the turned surface, as shown in Figure 4.16. The precise nature of the precipitates remains unresolved and further work using high resolution X-ray energy dispersive spectroscopy (X-EDS) and transmission electron microscopy (TEM) to accurately determine their composition and precise locations of origin is required. Thomas *et al.*[76] identified similar precipitates forming along twin boundaries within the near surface region of shot-peened Ti-834 samples that had been subjected to a thermal exposure of 700°C for 1800 hours. Similar to the precipitates identified by Thomas *et al.*[76] the precipitates shown in Figure 4.16, which appear bright under backscatter electron imaging, are rich in zirconium and are therefore inferred to be silicides of stoichiometry $(\text{Ti,Zr})_3\text{Si}_6$ commonly referred to as S_2 precipitates. S_2 precipitates are reported to readily form above 700°C in Ti-834 and other near- α titanium alloys based on the Ti-Al-Zr-Si system [195].

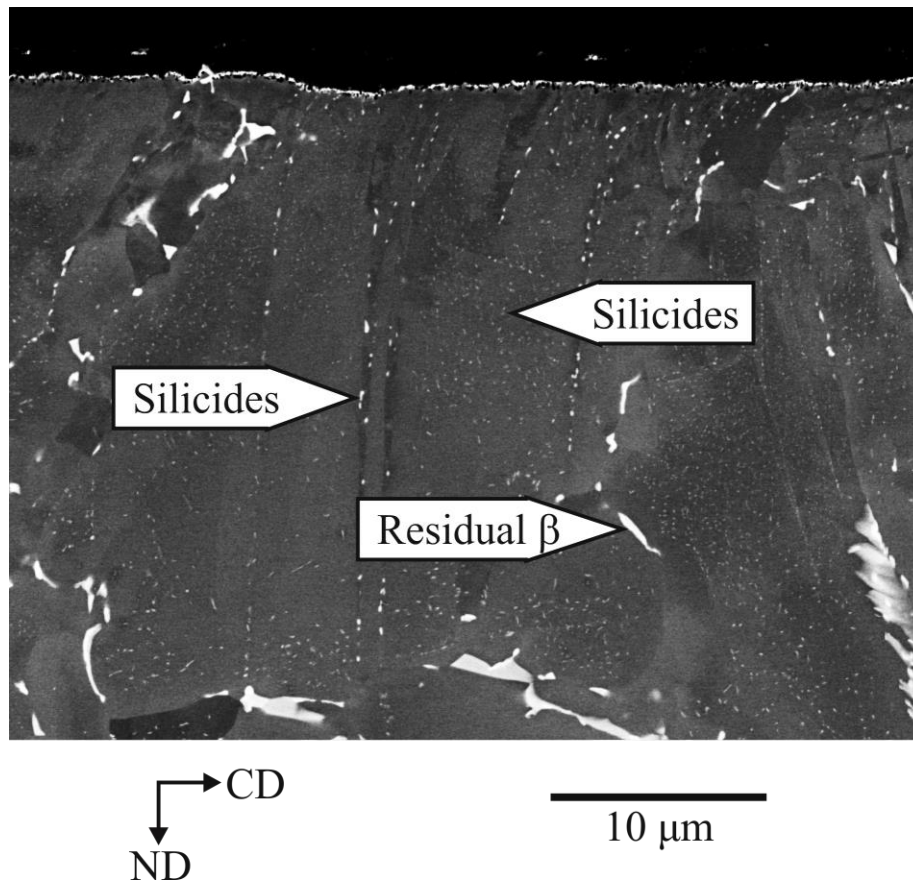


Figure 4.16 Cross-sectional backscatter electron micrograph of 80 m.min⁻¹ turned Ti-834, following a 1600 hour thermal exposure at 750°C. Silicide precipitates form in the vicinity of apparent twin boundaries and throughout a grains interior.

Close examination of backscattered micrographs, such as the one shown in Figure 4.16, reveal silicides apparently precipitating preferentially on or near to twin boundaries as well as on potential slip planes within alpha grains. Twins can be identified, though not formally characterised, using backscatter electron imaging as a result of electron channelling contrast. Slip bands and the surrounding material near twin boundaries are regions of significant dislocation density. The explanation for the formation of silicides within these dislocation rich regions can be drawn from various studies that have investigated their formation under various conditions. With the precise nature of silicide formation still being discussed their presence provides further evidence of machining induced plastic deformation. Since the precipitation is restricted to within the near surface plastically deformation region and is not observed within the bulk material, which has been subjected to the same thermal exposure temperatures and time. Figure 4.16 demonstrates further evidence of extensive silicide formation along apparent twin boundaries and within primary alpha grains. In addition, mechanical twins in Ti-834 have also been shown to enhance the kinetics for oxygen diffusion during high-temperature exposure [76], further promoting alpha-

case formation and subsequent surface embrittlement. The author feels it is important to reiterate that the time and temperature combination was selected in order to evaluate the thermal stability of the modified surface, rather than simulate specific in-service conditions.

Correlating EBSD data with the backscatter electron micrographs shown in Figure 4.17 has facilitated the identification of the modes of deformation that have promoted silicide growth. Using the EBSD data has shown that silicides have preferentially precipitated within regions of mechanically induced individual $\{10\bar{1}2\}$ twins and along in the vicinity of individual slip bands. Qualitative analysis has shown that the silicides appear to be coarser at twin boundaries compared to slipped regions, indicating a higher dislocation density at sites adjacent to the twin boundaries. The cumulative disorientation profile (Figure 4.17(b)) illustrates plastic deformation has been accommodated in the form of lattice rotation across the grain highlighted in Figure 4.17(a ii). Within this grain, through slip trace analysis, silicides have been identified to precipitate along individual $\{2\bar{1}\bar{1}2\}$ $\langle c + a \rangle$ type slip planes. The formation of silicides could lead to the localised loss of creep strength near the surface due to draining of silicon atoms from the surrounding alpha phase [196], [197]. In addition to the use of EBSD to assess the severity of the extensive plastic deformation, inspection of such silicides act as an indirect marker for the amount of residual plastic deformation imparted during the machining operation.

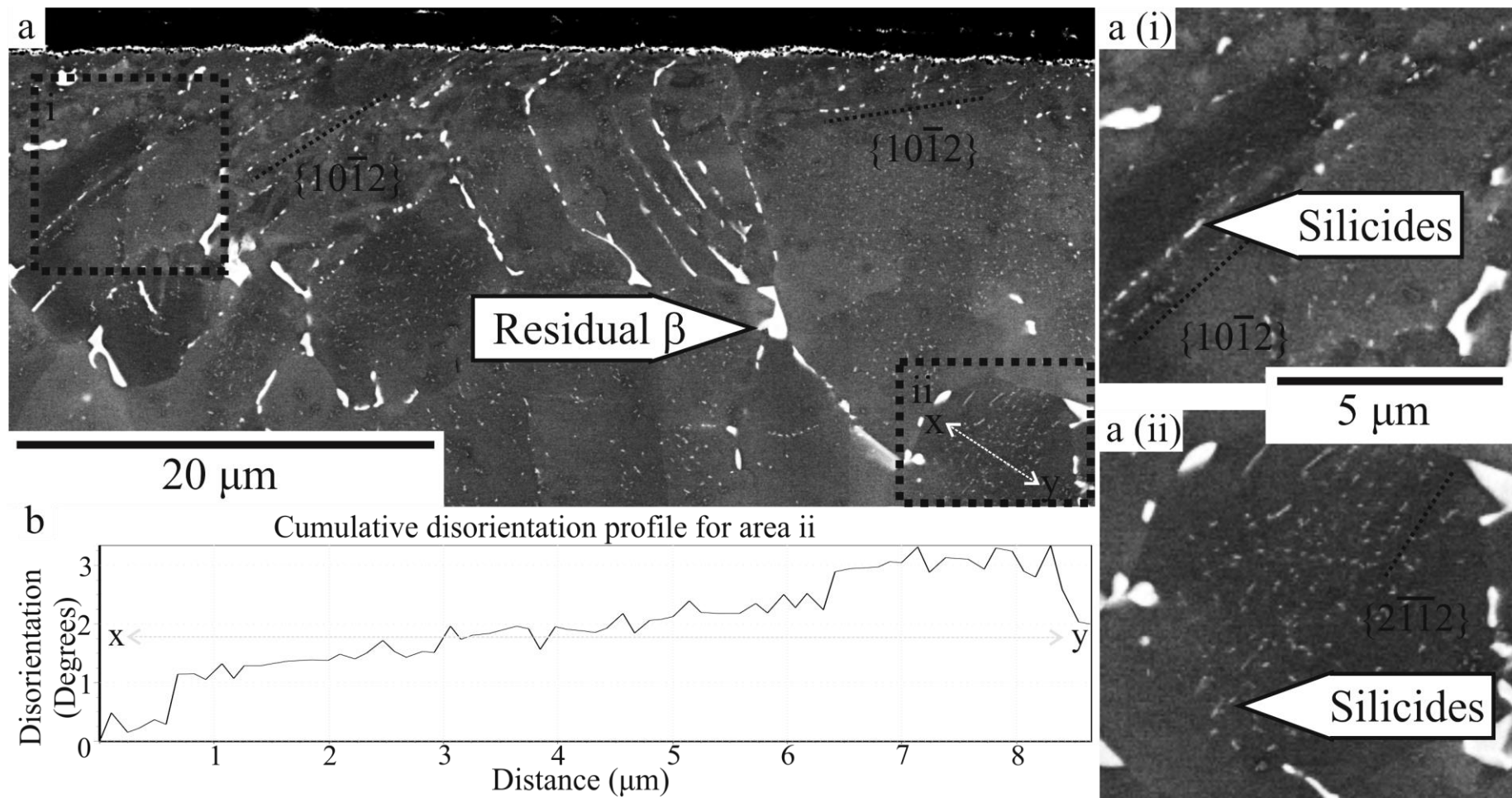


Figure 4.17 Cross-sectional backscatter electron micrographs of high speed turned Ti-834 ($95 \text{ m}\cdot\text{min}^{-1}$). a) Following thermal exposure at 750°C for 1600 hours mechanically induced deformation generated during the machining process promotes silicides to precipitate adjacent to; a (i) mechanical twin boundaries, a (ii) along slip planes. b) Cumulative disorientation profile illustrating lattice rotation across transect x to y.

4.4 Further Ti-834 billet characterisation identification of ‘i-type’ twin

The billet used for this investigation was received in the as-forged condition, consisting of large primary α grains, bulk OIM maps revealed the presence of a twin that did not satisfy any of the standard rational twin systems as suggested by Mironov [28].

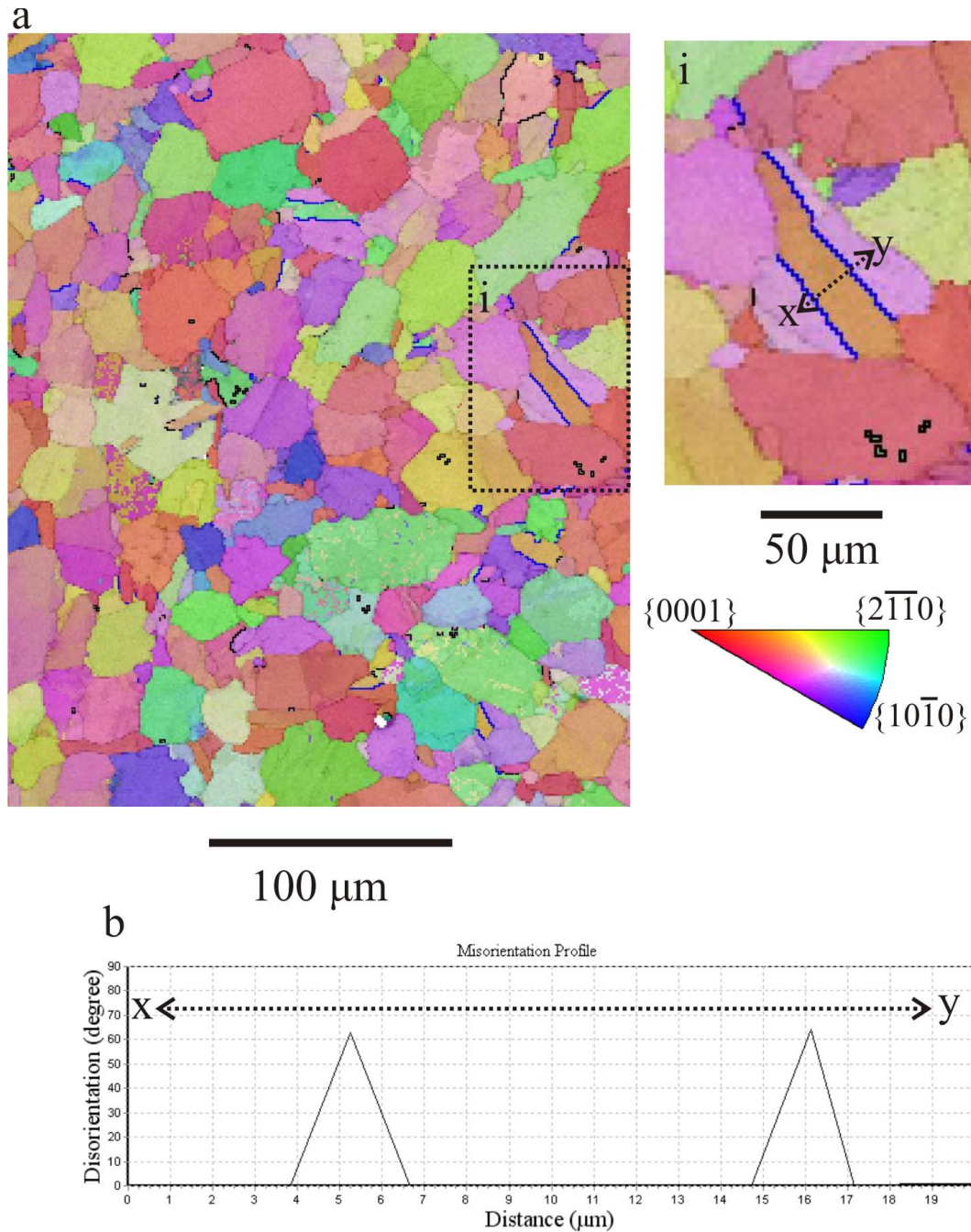


Figure 4.18(a) Representative EBSD inverse pole figure (IPF) OIMs of as-forged Ti-834 illustrating the presence of twin features distributed throughout the material, enlarged region (i) shows their appearance with a transect across the delineated boundaries. (b) The corresponding disorientation profile for the transect given in (i) shows the relative disorientation across the boundary displaying a regular 64° rotation, satisfying the features of the “i” twin.

The type of twinning shown in Figure 4.18 (having a disorientation angle of $\sim 60^\circ$) had also been previously reported during hot deformation simulations of Ti-834 by Thomas [31] and Davies [19]. During their investigations Thomas [31] and Davies [19] were unable to fully characterise this commonly occurring twin system. Therefore, an approximation was made to identify its plane, direction rotation axis and disorientation angle. More recently, an investigation by Diiorio *et al.* [29] identifying twinning modes in Ti-64 during monotonic loading under cryogenic conditions, found that under such conditions the irrational twinning “i” twin mode $\{5\bar{6}1\bar{3}\}$ could be identified and fully characterised using TEM. The blue delineated lines shown in Figure 4.18 identify the presence of the “i” twin and have been automatically applied using the special boundaries function within Channel 5. The special boundaries function uses the twinning relationship identified by Diiorio *et al.* [29] which was also given in Table 1.2.

During their investigation, Diiorio *et al.* [29] identified how the $\{5\bar{6}1\bar{3}\}$ twin plane could form microcracks and voids; this response occurred following the generation of further secondary twins within the interior of the “i” twin. These secondary twins were observed to be able to accommodate a further 10% of the applied strain. However, it was also observed that this accommodation in strain lead to further internal stresses which promoted the plane to become detached from the matrix. In light of such findings and considering the criticality of the application of Ti-834 in aerostructural components, the author feels that the occurrence of “i” twin within Ti-834 needs to be further investigated as a potential deleterious feature -but falls beyond the scope of the current investigation.

4.5 Summary

During outer diameter turning of Ti-834, it was observed that, for constant feed rate and depth of cut, increasing the cutting speed resulted in a decrease in tool wear and gross subsurface plastic deformation. Surface roughness however, increased with increasing cutting speed, in addition to an increase in induced microstructure damage, resolved via EBSD. Hardness analysis indicated an increase in hardness within the immediate near surface region, with the slowest speeds displaying the most significant increase in localised hardening with an increase of ~80 HV resulting in a maximum hardness of ~440 HV at 60 μm beneath the machined surface. This increase in hardness correlates with the observation of gross plastic deformation. Through the application of high resolution analysis techniques, such as backscatter electron microscopy and EBSD, the activation of multiple deformation modes were identified within Ti-834; these occurred as a result of the machining operation. Observed deformation features included; mechanically induced twins, the most common of which was characterised to be the $\{10\bar{1}2\}$ tension type twin. These occurred in addition to the activation of basal, prismatic and pyramidal slip. EBSD facilitated the identification and characterisation of the imparted deformation features, which were activated at depths $>50 \mu\text{m}$ beneath the machined surface. Deformation features that could be considered deleterious to a component's in-service properties, such as mechanical twins, were being activated within grains that show little/zero significant distortion and therefore appear to have undergone minimal/zero strain. This has demonstrated that traditional methods of machining microstructure analysis needs to be re-evaluated, since relying upon methods such as 'beta distortion' will not offer the user enough insight into the severity of the imparted deformation. Positively, the minimum depth of damage (maximum ~29 μm and average ~13 μm) was observed to occur at 70 $\text{m}\cdot\text{min}^{-1}$, which is the surface speed recommended by the tooling supplier [165] for optimum tool life. Deviation from the recommended cutting speed results in an increase in subsurface damage. Silicide precipitates were observed on the induced microstructure damage following prolonged thermal exposure at 750°C which could lead to a reduction in creep and fatigue performance. EBSD analysis of Ti-834 within the bulk regions of the material identified the presence of residual forging induced twins, these were characterised satisfying the irrational "i" twin mode $\{5\bar{6}1\bar{3}\}$.

The author does however wish to clarify that the findings outlined in the current chapter are not intended to scaremonger, considering Ti-834 is still currently widely used in structurally critical components. More importantly these results need to serve as a point of initiation for further investigations to be undertaken to gain a more complete understanding as to how detrimental such induced features may be to in-service properties and what impact this may have on the machining of other titanium alloys.

Chapter 5 - Identifying critical machining parameters for subsurface damage in high speed machined titanium

5.1 Introduction

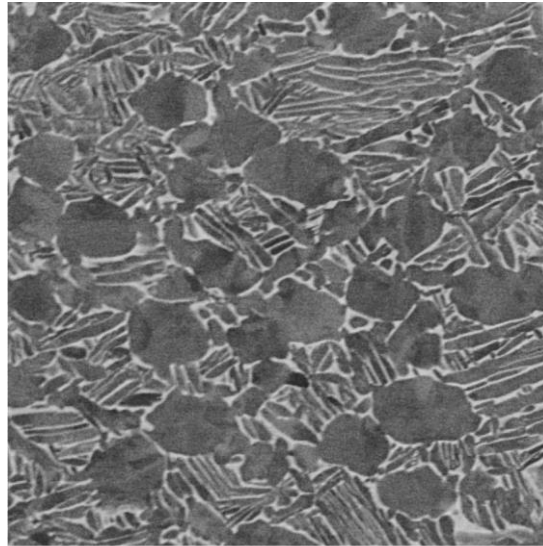
Traditionally, machinability is assessed by chip formation, cutting force, tool life and surface condition, but with no detailed examination or quantification of the subsurface microstructure. Following on from the findings discussed in Chapter 4 where it was shown that for Ti-834, conventional and emerging machining practices impart substantial subsurface microstructure damage, such as mechanical twinning. Surface and subsurface twins in structure critical components have the potential to reduce service life. The objective of this chapter is to begin to identify and determine the critical conditions required to generate them.

5.2 Experimental methods

For the work covered in this investigation the following experimental methods were followed, these are in addition to the material analysis procedures as outlined in §3.2.

5.2.1 As received material

The material used in this investigation was supplied by TIMET UK Ltd. For this study, the $\alpha+\beta$ titanium alloy Timetal® 54M (Ti-54M) was supplied from a cross section of a billet with an outer diameter of 240 mm, with an as forged microstructure. Prior to the machining trials the material was further heat treated with a mill anneal at a temperature of 700°C for 8 hours, this was followed by an air cool. The heat treatment schedule prevented excessive growth of the β phase. The $\alpha+\beta$ mill annealed morphology for Ti-54M as shown in Figure 5.1 displays an approximate ~0.7 volume fraction of the α phase. The mill anneal heat treatment has resulted in a microstructure that contains approximately 30% primary α grains which show no evidence of epitaxial growth. Each primary α grain is surrounded at the grain boundary by the residual β phase. The microstructure displays a typical α colony structure, which formed during the initial cool during forging within transformed prior β regions.




 50 μm

Figure 5.1 Backscatter electron micrograph of the Ti-54M mill annealed microstructures.

Compositional analysis of the received billet was provided by TIMET UK where measurements were taken from the bottom and top of each billet. The average composition of the material is given in Table 5.1.

Table 5.1 Billet composition of the $\alpha+\beta$ titanium alloy Ti-54M (wt. %).

Al	V	Mo	Fe	C	O	N	Ti
5.18	4.10	0.62	0.50	0.0006	0.16	0.003	Balance

5.2.2 Machining trials

Outer diameter (OD) Turning trials were performed using a MAG Cincinnati Hawk lathe. Sandvik CNMG 120408-23 H13A inserts were mounted in a Sandvik C5-DCLNL-35060-12 tool holder, providing a clearance angle of 6° and a rake angle of 7° . A constant feed rate of $0.1 \text{ mm}\cdot\text{rev}^{-1}$ and a 1 mm depth of cut was used (2 mm off the diameter). The water based coolant, Hocut 795B at 5% concentration was ‘flood’ delivered at ~ 13 litres per minute. Arrazola *et al.* [126] determined under similar machining parameters, that Ti-54M could be machined at a maximum speed of $95 \text{ m}\cdot\text{min}^{-1}$, whilst satisfying a Sandvik tool rejection criteria that specifies after 15 minutes cutting the used tool must have a VB_{average} no greater than 0.25 mm and a VB_{max} lower than 0.5mm.

Considering this, all Ti-54M machining trials used as part of this investigation were machined at this high machining speed of $95 \text{ m}\cdot\text{min}^{-1}$.

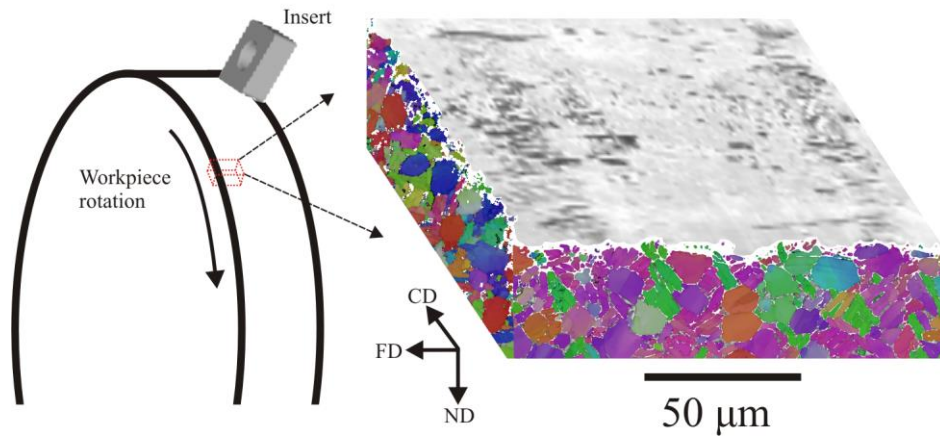


Figure 5.2 Schematic diagram of the outer diameter turning process to illustrate the sample coordinates; Normal direction (ND); Feed direction (FD) and Cutting direction (CD), and a schematic arrangement of the obtained EBSD data orientated parallel and perpendicular to the cutting direction.

Specimen coordinates and a schematic arrangement of the turning operation are given in Figure 5.2. Following the trials and in reference to Figure 5.2, turned test pieces were sectioned parallel and perpendicular to the cutting direction (CD) plane and prepared using the standard methods for microscopic analysis.

5.2.3 Microstructure Analysis

Secondary and backscatter electron imaging was performed using an FEI Inspect F (FEG SEM). Quantitative crystallographic EBSD data was acquired using a FEI Sirion (FEG SEM) with a 20 keV accelerating voltage, with a spot size of 3 and a step size of 0.1 μm . Automated indexing and “post processing” of the diffraction data were performed using Oxford Instruments HKL Channel 5 software using the methods outlined in §3.5.

5.3 Results and discussion

5.3.1 Material response of Ti-54M after high speed machining.

The secondary and backscatter electron composite micrographs shown in Figure 5.3 highlight the typical surface defects imparted during the machining process, which are as follows;

- Scratches
 - Shallow scratches potentially caused by poor handling of the workpiece after machining
- Channelling
 - Regular height undulations caused by the tool as it progresses over the workpiece forming a groove, the width of which corresponds to the $0.1\text{mm}\cdot\text{rev}^{-1}$ feed.
- Deposited debris
 - During the cutting process worn tool fragments and swarf can re-adhere to the workpiece.
- Cavitation
 - Can be caused by either grain pull or gouging from the tool when a built up edge become detached.

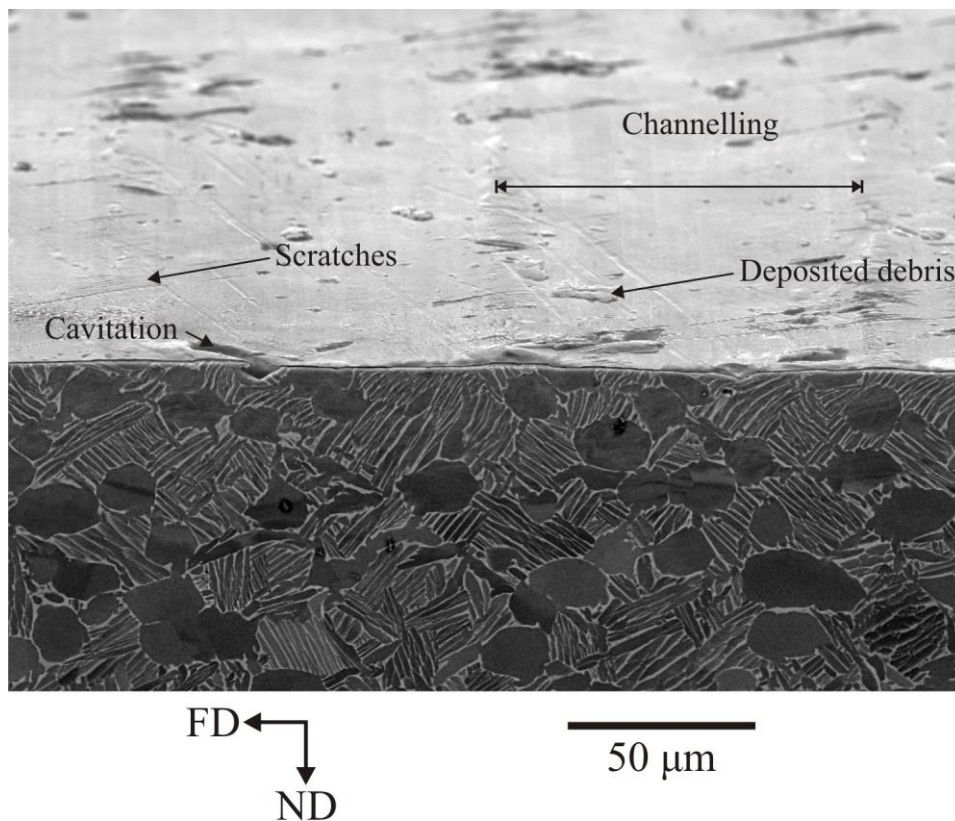


Figure 5.3 Composite image of the outer diameter turned material using a secondary electron detector for the surface combined with a backscatter electron detector for the subsurface.

The composite image in Figure 5.3 shows the nature of common surface defects, with example highlighted; scratches; channelling; deposited debris and cavitation. Note: the cutting direction lies perpendicular to the cross section of the image.

5.3.2 Backscatter electron image analysis of machined Ti-54M

Through the use of high resolution imaging of Ti-54M following outer diameter turning, the subsurface material shows a high propensity for deformation. Typical features such as those shown within the primary α grains in Figure 5.4 and Figure 5.5 are characteristic of channelling contrast, the mechanisms of which have been detailed in §3.4.2.

The cross sectional backscatter electron micrographs of turned Ti-54M were prepared both perpendicular and parallel to the cutting direction, as shown in Figure 5.4 and Figure 5.5 respectively. Each image illustrates the high level of plastic strain that is being accommodated by the subsurface microstructure following a turning operation. Regions of mechanically induced deformation are evident within the first 50 μm of material from the turned surface. The swept morphology of the microstructure typically associated with the passing of the tool parallel to the cutting direction can also be identified in Figure 5.4 (a-b) with the swept features aligning with the feed direction (FD) of the tool. The parallel features within the central primary α grain shown in Figure 5.4(a) are indicative of deformation via slip, whereas the high contrast features shown within the α grain in Figure 5.4(b) are typical for the presence of mechanically induced twins. Characterisation of the activated modes of deformation via electron backscatter diffraction (EBSD) has been completed and described in detail further within this chapter, §5.3.3.

Typical examples of mechanically induced severe lattice rotation are shown in Figure 5.5, here the material has been sectioned parallel to the cutting direction. The uppermost region of material exhibits the typical swept type microstructure that penetrates to approximately 20 μm beneath the machined surface. This region of displaced material gives the reader a clear visual representation of the amount of imparted plastic strain. It would appear from these observations that the colony structure is able to accommodate the swept type induced plastic deformation more readily, with the local increase in volume fraction of residual β appearing to aid the grain boundary movement. Whereas individual primary α grains, appear to offer some resistance to adopting the swept type microstructure suggesting their deformation characteristics are more closely dictated by the underlying crystallographic orientation of individual α grains. This can be observed in Figure 5.5(b) that shows neighbouring α grains, under what can be assumed a similar stress state, displaying different modes of deformation.

It is important to note that following machining the majority of α grains within 50 μm of the surface display evidence of induced deformation regardless of the grains size. Contradicting the observations made by Armstrong *et al.* [38] who identified a size effect relationship

between the dimension of the parent grain and the propensity for deformation to occur. However qualitative analysis has shown that primary α grains, appear to more readily deform via the activation of slip or twinning as shown by the distinct bands within the grains interior show in the micrographs in Figure 5.5. The observed variance of the deformation type between regions of colony α and primary α grains has been attributed to a partitioning effect of the induced strain, with the residual beta matrix appearing to offer a cushioning effect to the induced strain for the colony α grains.

The backscatter electron micrographs shown in Figure 5.6 highlight further examples of imparted plastic deformation beneath the machined surface. This comprises of extensive colony α and primary α grain distortion plus a significant amount of twinning within primary α grains. A noteworthy feature of the enlarged micrograph in Figure 5.6(i) show twins appearing to progress unimpeded across the residual beta. This feature also corresponds to an apparent surface defect directly above it. The author suggests that there could potentially be a correlation between these two features considering their close proximity. The presence of the surface defect may have significantly altered the associated surrounding stress state further inducing the formation of the twins.

The author appreciates that the obtained micrographs can only offer a limited insight into the activated deformation mechanisms, since the images capture a cross sectional representation of what is occurring within the entire volume of machined material. However, qualitative observations show that the twins largely propagate from α grain boundaries at the α - β phase boundary interface. The twin morphology often correlates to features at the grain boundary such as the near vertical twins shown in Figure 5.6(i), these appear to emanate from a β phase feature protruding into the deformed primary α grain. Twins largely lie either parallel or perpendicular to the machined surface and often appear to adopt a fine needle like appearance that can be attributed to a high strain rate environment [45], [46]. Figure 5.6(i) also illustrates the presence of twins that have appeared to have grown spanning the whole length of α alpha grains and transferred unimpeded into a neighbouring α grain across the residual β rich zone at the α grain boundaries. As detailed as part of the literature review, the Meyer constitutive model [41] for the transfer of strain across a grain boundary can be similarly attributed to these machining induced deformation features. However, these models have been generated considering a single-phase material. Therefore, the precise role the residual beta is playing falls within a key knowledge gap that details the role microstructure has in dictating the deformation behaviour in a multi-phase system.

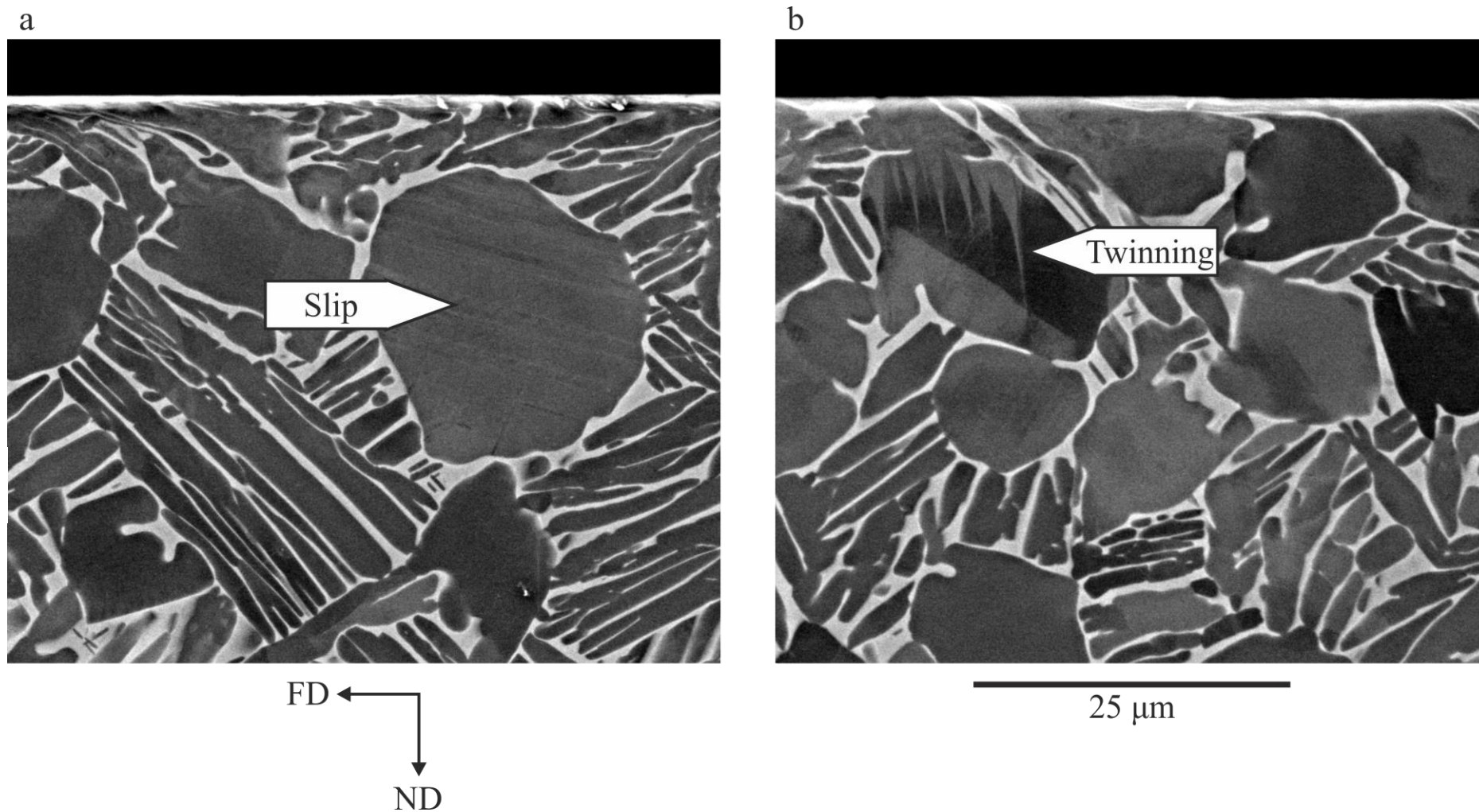


Figure 5.4 Cross sectional backscatter electron micrograph of outer diameter turned Ti-54M sectioned perpendicular to the cutting direction, the image illustrates the presence of mechanically induced subsurface deformation in the form of (a) slip and (b) twinning. Where (FD) and (ND) represent the feed direction and normal direction respectively

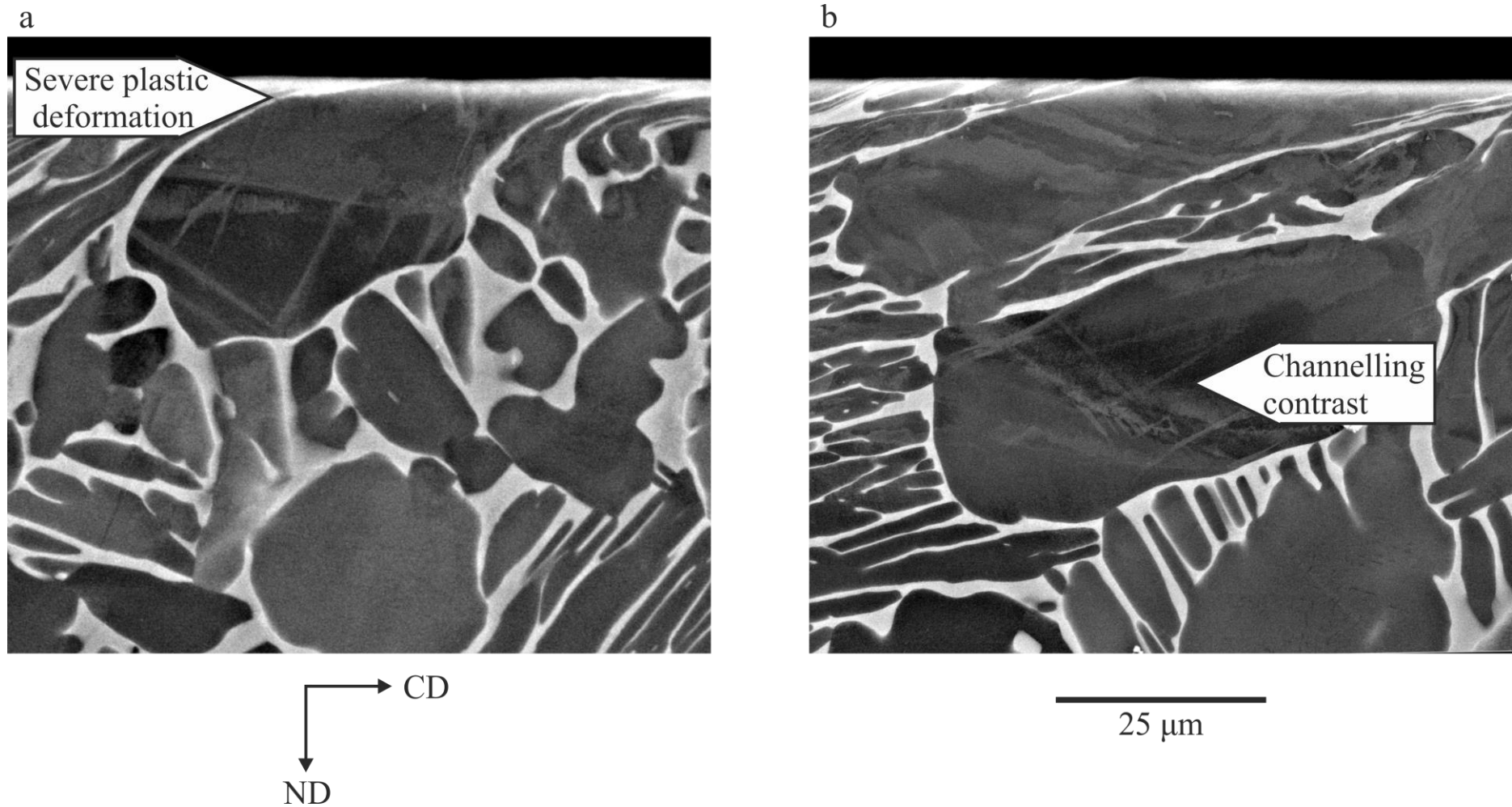


Figure 5.5 Cross sectional backscatter electron micrograph of outer diameter turned Ti-54M sectioned parallel to the cutting direction, the image illustrates evidence of mechanically induced subsurface deformation within primary α grains, manifesting in a substantial channelling contrast image effect. (a) Uppermost deformed primary α grain surrounded by colony α , (b) Deformed neighbouring primary α grains. Where (CD) and (ND) represent the cutting direction and normal direction respectively

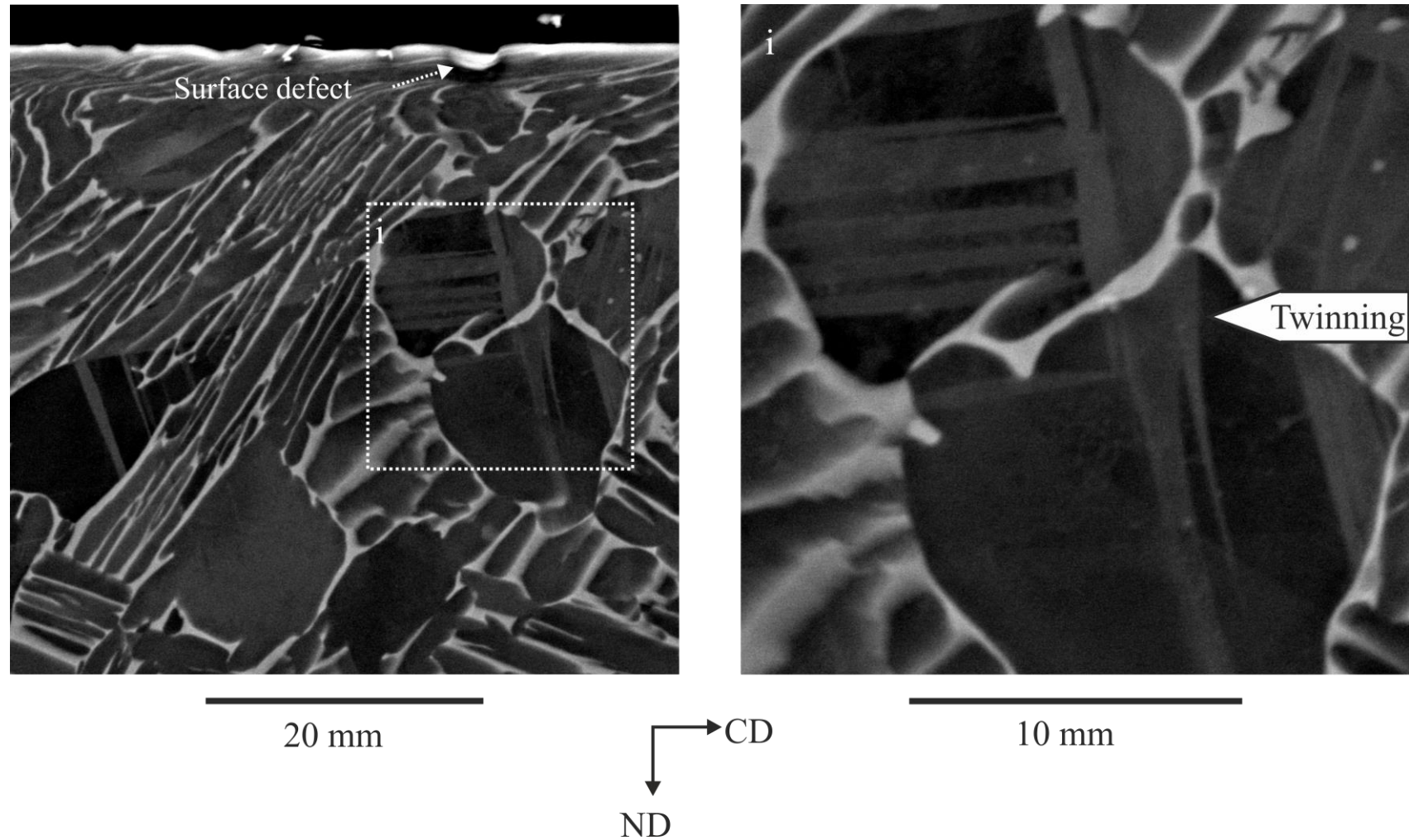


Figure 5.6 Cross sectional backscatter electron micrograph of turned Ti-54M with a machining induced surface defect identified. High magnification micrograph of subsection (i) shown in inset image. Where (CD) and (ND) represent the cutting direction and normal direction respectively

5.3.3 Electron backscattered diffraction analysis of machined Ti-54M

Using backscatter electron imaging it has been observed that following a high speed machining operation Ti-54M deforms severely through a large number of deformation modes. These deformation modes have been identified through the implementation of electron backscattered diffraction (EBSD) and the subsequent analysis of the data. When presented in the form of orientation image maps (OIM) the most predominant and easy to identify mode of deformation is that of $\{10\bar{1}2\}$ tensile mechanical twinning. The boundaries of $\{10\bar{1}2\}$ type twins are characterized by a misorientation of 86.5° about the $\langle 1\bar{2}10 \rangle$ axis and has a shear direction of $\langle \bar{1}011 \rangle$. Careful analysis of the entire data set has revealed that some grains occasionally twin by the $\{11\bar{2}1\}$ tension type twin that has been characterized by a misorientation of 35° about the $\langle \bar{1}010 \rangle$ axis and has a shear direction of $\langle \bar{1}\bar{1}26 \rangle$. Multiple slip systems are activated following the turning operation; most commonly prismatic slip $\{10\bar{1}0\}[11\bar{2}0]$, pyramidal slip $\{10\bar{1}1\}[10\bar{2}0]$ and $\langle c+a \rangle$ slip $\{11\bar{2}2\}[11\bar{2}3]$ has been identified with variation in slip intensity, including slip band spacing, between neighbouring grains. The localised elevated temperatures associated with the cutting processes caused by adiabatic heating have been attributed to the activation of the $\langle c+a \rangle$ slip mode. It has previously been recorded that at temperatures above 400 K there is a significant reduction in the critically resolved shear stress for the along higher order deformation planes [198].

The EBSD data shown in Figure 5.7 has been extracted from a larger data set; each enlarged region area represents the typical regions that display slip and twinning. These modes of deformation have been indexed using the methods outlined in §3.7. Using a combination of pattern quality coloured, IPF and band contrast OIMs, the user can characterise the induced plastic deformation. The extent of the twinning typically extends to a depth of 40 μm , with localised regions experiencing deformation to a depth of up to approximately 60 μm . The plastic deformation imparted directly beneath the cutting tool leads to either; (i) the generation of a large amount of needle-like twins that refine the near surface microstructure or (ii) severe lattice rotation within grains. This results in a near surface region, 5 -10 μm from the surface, that cannot be indexed and is recorded as a 'zero' solution in the IPF OIM. The extent of this region is more easily identifiable using the pattern quality map (Figure 5.7(b)). From the EBSD data shown in Figure 5.7 it is possible to identify two macrozones, these are depicted by the average colour variation within the IPF OIM the regions A and B have been presented on a pole figure with a contour plot. The influence of these regions of similarly orientated grain on the resulting deformation will be discussed in detail in §5.3.3. In brief, the creation of a macrozone stems from the primary forging stages, where the material is worked and held above the β transus (950°C). When the material is raised and held above the β transus the structure comprises of large β grains. During forging, every attempt is made to reduce the size of the β grains since on cooling, the orientation of the transformed α

grains is governed by a Burgers relationship. Therefore, the size of the resulting macrozone after transformation correlates to the size of the materials' prior beta grains [19].

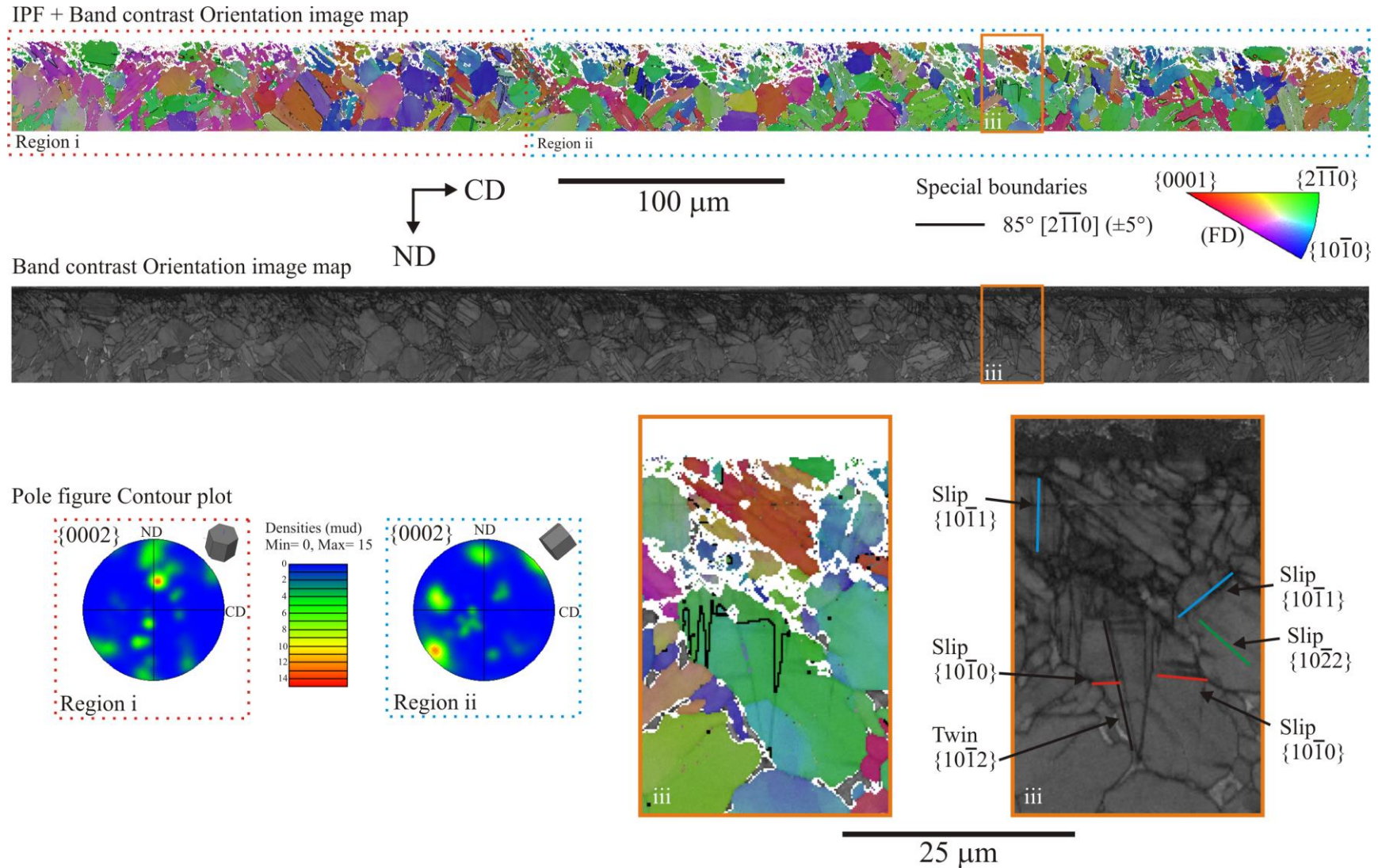


Figure 5.7 Cross sectional EBSD OIMs of outer diameter turned Ti-54M (a) IPF coloured OIM with corresponding (b) pattern quality OIM, delineated region i and ii in (a) indicate two macrozone regions with the corresponding pole figures for both regions presented in (c). Region iii has been enlarged in (d) and (e) with $\{10\bar{1}2\}$ twin boundary delineation and slip trace analysis.

By pooling EBSD data sets from analysed areas around the circumference of a machined mill annealed Ti-54m billet analysis was performed in order to identify whether a relationship exists between the cutting process and orientation of the grains in which $\{10\bar{1}2\}$ mechanical twins are observed. Following the method detailed in §3.7 the orientation of both the parent and the twin were analysed and the orientation of the activated twinning plane (K_1) was identified and presented on the pole figure shown in Figure 5.8.

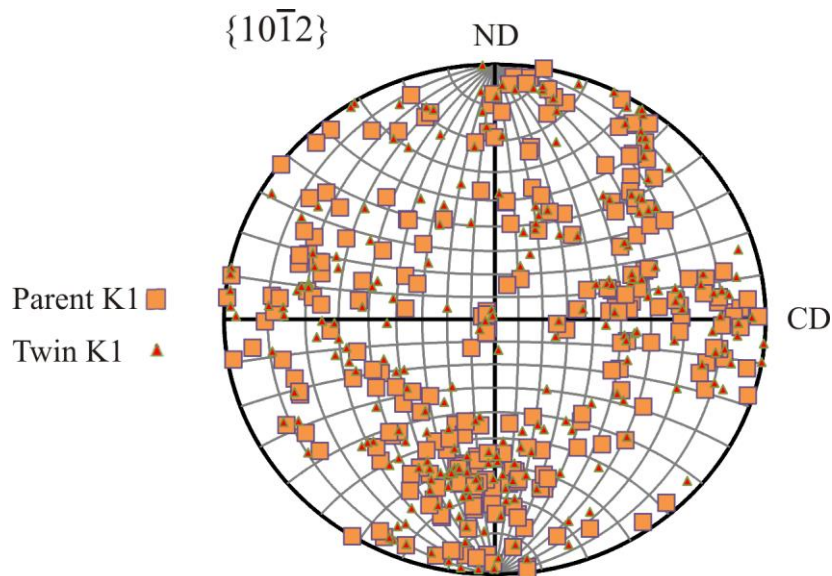


Figure 5.8 Resulting $\{10\bar{1}2\}$ pole figure projection for the activated twins illustrating the position of the assumed activated K_1 plane for each parent twin pair. Note further lattice rotation between parent and twin has caused some deviation of both planes.

It has been shown that the formation of a twin is governed by the texture of its parent grain. Song *et al.* [42] found whilst studying the stress-strain response of zirconium over a range of strain rates that the nucleation of a twin always starts within a grain having a K_1 plane close to the maximum local stress plane. Using this principle, the data obtained via EBSD was analysed further to see whether or not there is a similar correlation of the K_1 plane for the twins that have occurred in Ti-54M. The orientation of the basal plane of the parent grains which exhibit $\{10\bar{1}2\}$ tensile twins have been plotted in the pole figure shown in Figure 5.9. The diagram illustrates a preferential orientation for the grains that have twinned; this is indicated by the clustering of points on the basal projection that are similarly angled ($\pm 45^\circ$) above and below the cutting direction. The position of the corresponding K_1 planes are largely orientated either parallel or perpendicular to the cutting direction, matching the morphology of the $\{10\bar{1}2\}$ twins shown in Figure 5.7. This suggests that the stress state

during the machining operation may allow for specific twinning modes to activate preferentially to others.

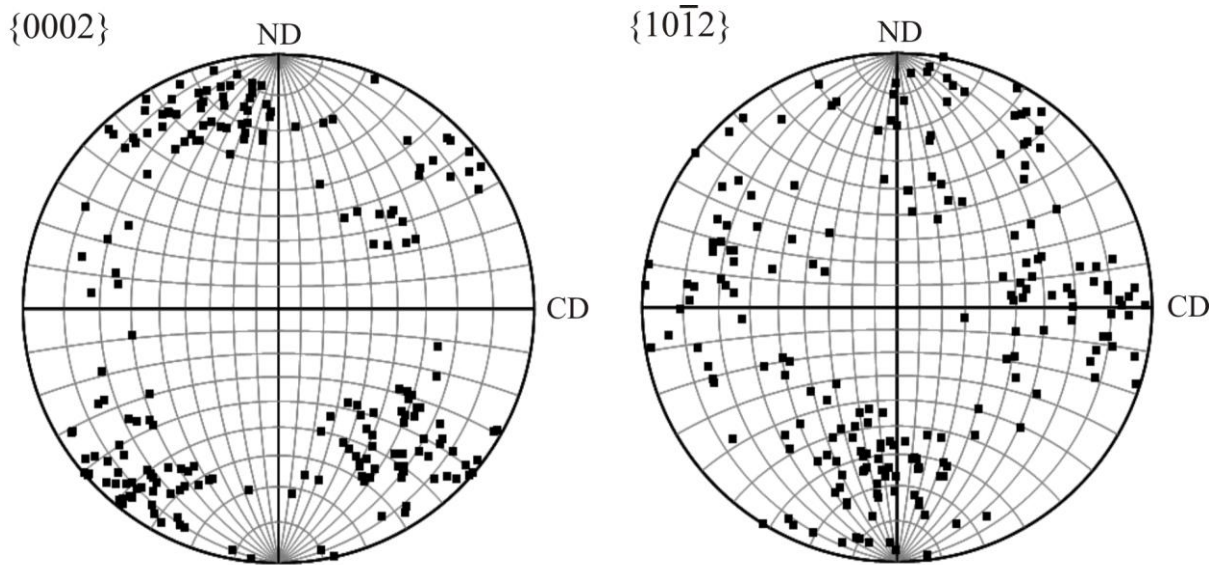


Figure 5.9 Pole figure projections of the $\{0002\}$ and $\{10\bar{1}2\}$ for the parent material for each grain displaying evidence of twinning, following filtering to remove rogue twined grain orientations.

The location of the basal plane for each of the parent grains that have twinned can be divided into two discrete groups of similar orientations, as shown in Figure 5.10 and highlighted in yellow and green. A filter has been applied grouping the orientations of the basal planes for the grains that have displayed evidence of twinning, as well as removing the presence of some of the spurious data points.

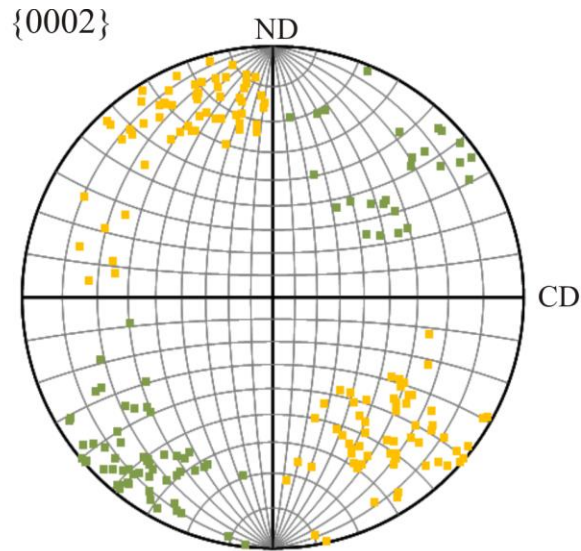


Figure 5.10 Pole figure projections of the $\{0002\}$ for the parent material for each grain displaying evidence of twinning, the data presented has been filtering to remove rogue orientations and divided into two discrete opposing groups as labelled.

To facilitate a $\{10\bar{1}2\}$ tension type twin an elongation along the c-axis is required. Considering both of the discrete orientation groups that are highlighted in Figure 5.10 are opposing, the associated stress states that would permit their activation must operate independently. Therefore, it can be determined that for these two groups of twinned parent grains to independently activate, a forward and reverse mechanism of shear must occur. This has been attributed to a reversal in the local macroscopic stress state as the tool progresses over the workpiece. The schematic shown in Figure 5.11(a) illustrates the position of the two independent shear stress conditions and how they permit the activation of a tension type twin. The associated stress state that would allow for this shape change to occur within a grain orientated with their c-axis at $\pm 45^\circ$ to CD would be plane simple shear parallel to CD. As previously highlighted by Song *et al.* [42], for a K_1 plane to activate it must preferentially align with the plane of maximum shear. The schematics shown in Figure 5.11(b) illustrate how the application of a simple two dimensional shear stress model interacts with a HCP. The ideal orientations that allow the K_1 to be aligned with the planes of maximum shear are 38° and 52° for the vertical and horizontal components respectively. This correlates with the observed data that shows an average orientation near 45° off the cutting direction. For the forward component of the cutting process, Figure 5.11(b) illustrates the application of a plane simple shear model and its interaction with the HCP lattice.

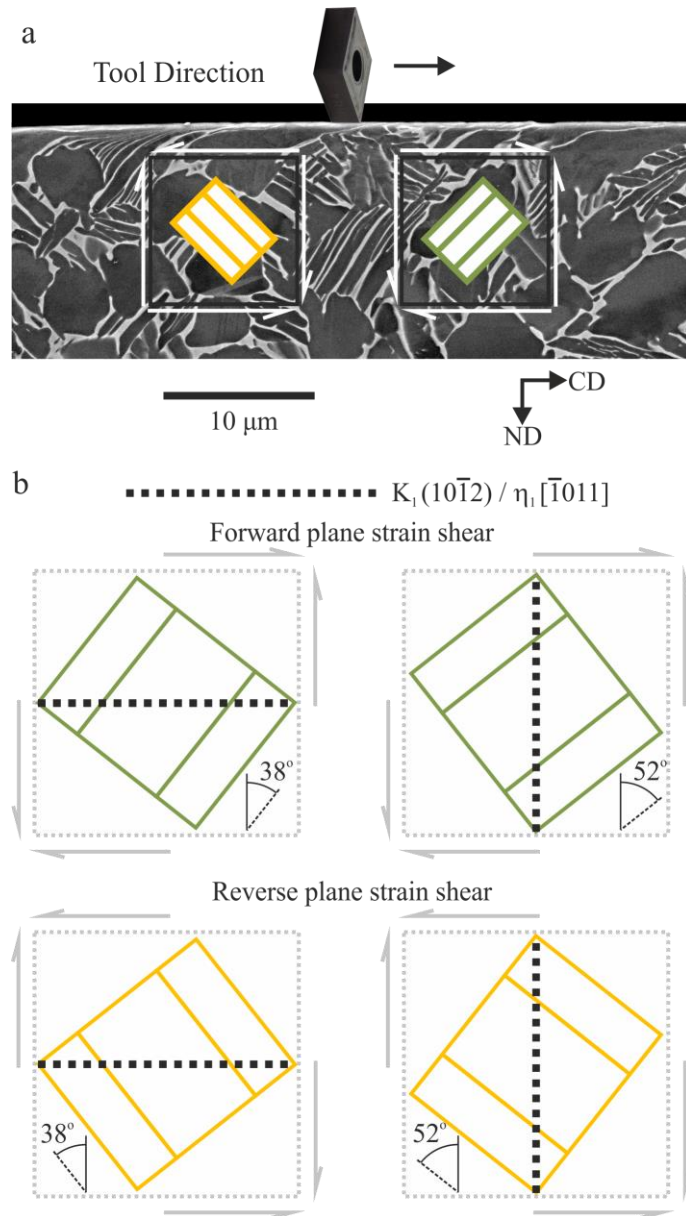


Figure 5.11(a) Composite backscatter electron image illustrating the forward and reverse simple shear components ahead and behind the tool with the corresponding inclined HCP crystal, (b) The application of the plane simple shear model and its interaction with the HCP crystal; $\pm 38^\circ$ and $\pm 52^\circ$ correspond to the optimal orientation of the HCP crystal for both the forward and reverse condition.

For each activated twin that has been identified the corresponding individual K_1 plane has been determined and displayed on the $\{10\bar{1}2\}$ pole figure (Figure 5.12). Using the position of the activated K_1 plane it is possible to indirectly determine the orientation of the plane of maximum shear that was active during deformation, since their orientations are assumed to be the same.

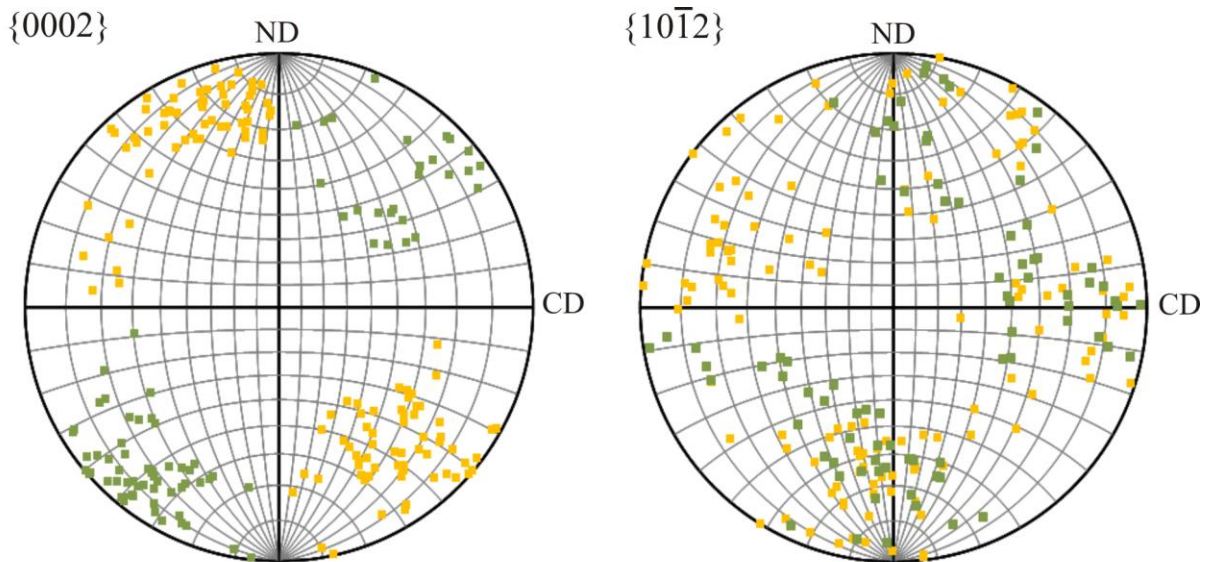


Figure 5.12 Pole figure projections of the $\{0002\}$ and $\{10\bar{1}2\}$ for the parent material for each grain displaying evidence of twinning, following filtering and dividing into discrete groups.

Bearing in mind the processes of metal removal involves applying a considerable amount of force along the cutting direction; the reader would be excused to assume that the plane of maximum shear would appear parallel to the cut surface. However, using the data shown in the Figure 5.12 it is possible to deduce that this is only part of the complete deformation environment. The locations of the corresponding K_1 planes are shown in Figure 5.12, here the distribution demonstrates zero bias for either of the grouped parent orientations. This would suggest that the magnitude of the vertical and horizontal planes of maximum shear must be roughly equal. Considering the apparent likely hood of a vertical or horizontal K_1 plane being generated appears the same for either of the opposing orientation groups. Therefore, a balanced simple plane shear stress model can be applied when approximating the induced stress state, since if the environment were imbalanced a preference would be highlighted by a shift in the deformation data.

It is important when evaluating the acquired data for both the parent and twin, to be able to confidently determine which part is the parent material and which is the twin. For this study the orientation of the twin variant within a twinned grain is manually identified as being the one with the smallest area fraction. This can easily lead to confusion when analysing small grains or ones that have been severely distorted. As such, some poles in the $\{0002\}$ pole figure may have been wrongly divided into twin and parent variants and have been subsequently attributed to being activated during the opposite deformation region (forward rather than reverse shear or the other way around). Tirry *et al.*[199] previously highlighted this potential error whilst determining the difference between parent and twin orientations when investigating the shearing behaviour of Ti-6Al-4V. During their investigation the

material was subjected to single simple forward shear deformation process and the subsequent deformation was analysed. The formation of the twins were observed to have been generated in a similar manner to those highlighted in this present study, with the majority of the K_1 planes aligning parallel to the shear direction and the subsequent orientation of the grains basal plane being $\pm 45^\circ$ to the shear direction. Ambiguity during the identification of the twin and parent variants was attributed to the number of sporadic data points that did not conform to the general overall observed trend. However as Tirry *et al.* [199] correctly explains this cannot be concluded for sure since the macroscopic stress state has only been considered. If the local stress states were also taken into consideration it may strongly differ from the macroscopic one and could explain why some of the identified poles are clearly different from the general trend of distribution.

The following typical examples, given in Figure 5.13, show regions of deformed material that support the hypothesis of a forward and reverse shear mechanism that is generated as the tool progresses over the workpiece. The twin examples shown illustrate the presence of two distinct grains whose parent and twin variants can be easily identified and both satisfy the alignment of the two opposing grain orientation groups. The grains identified in the OIM in Figure 5.13(a-b) have been attributed to forward and reverse shear respectively. The OIMs shown in Figure 5.13 further support the assumption that the induced stress state follow a simple planar shear stress model with equal vertical and horizontal planes of maximum shear, with the individual highlighted grains displaying evidence of twins that have propagated both vertically and horizontally.

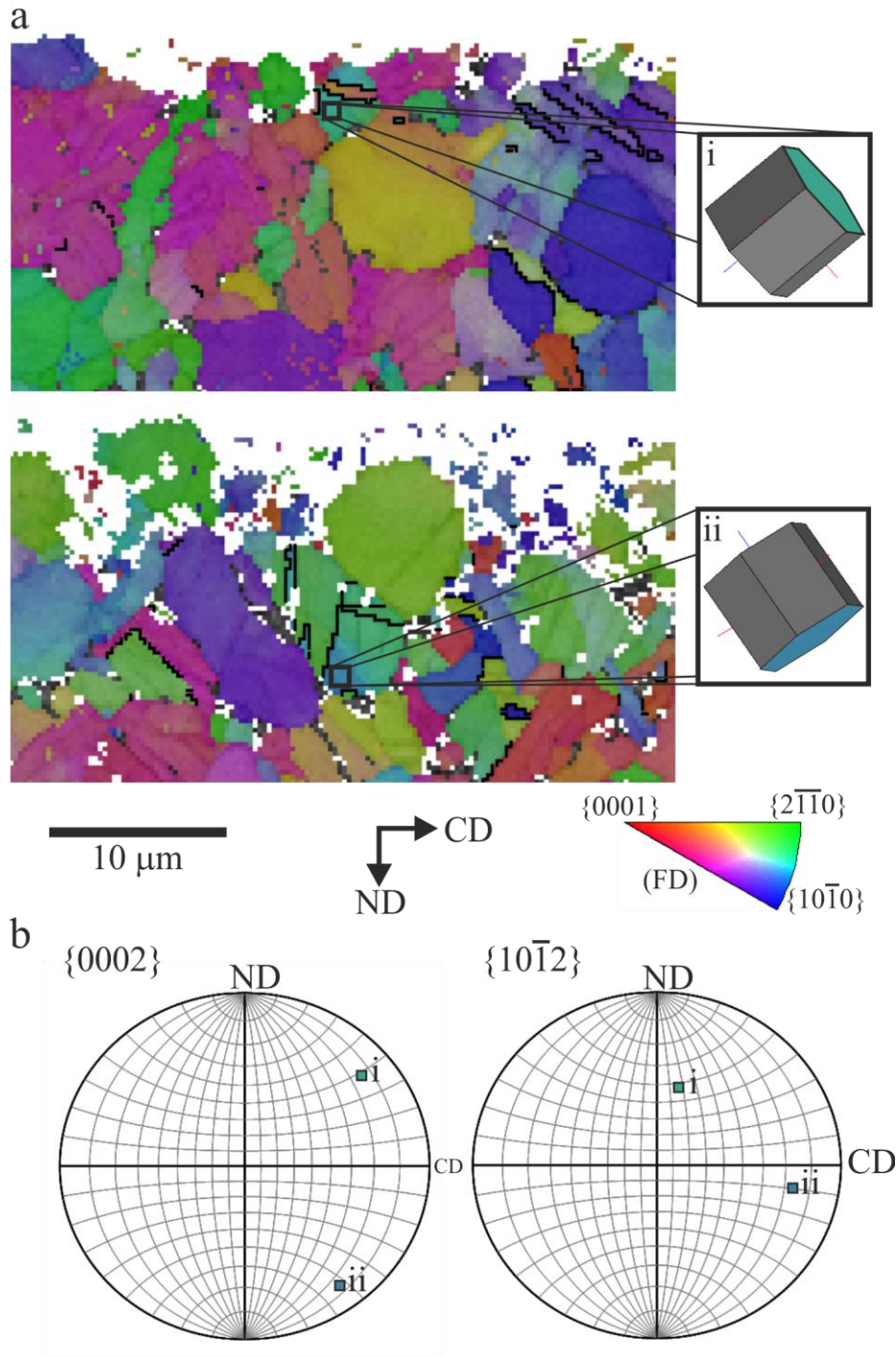


Figure 5.13(a) IPF coloured, with respect to FD, OIM of outer diameter turned Ti-54M illustrating the orientation of the parent grains that contain $\{10\bar{1}2\}$ twins via (i) forward and (ii) reverse simple shear. (b) Corresponding $\{0002\}$ and $\{10\bar{1}2\}$ stereographic pole figure projections.

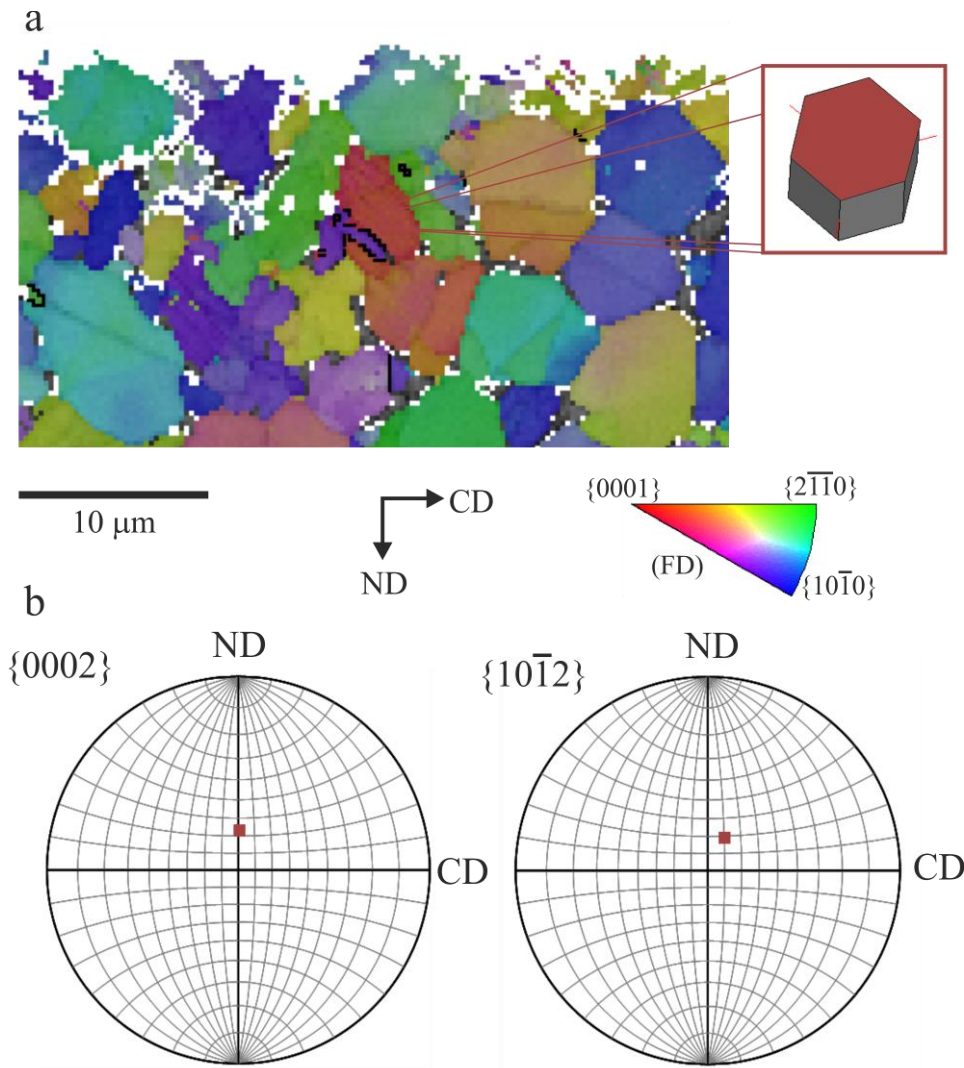


Figure 5.14(a) IPF coloured, with respect to FD, OIM of outer diameter turned Ti-54M illustrating the orientation of abnormally orientated parent grain that contain $\{10\bar{1}2\}$ twins (b) Corresponding $\{0002\}$ and $\{10\bar{1}2\}$ stereographic pole figure projections.

Amongst the acquired data the presence of $\{10\bar{1}2\}$ type twins whose occurrence could be considered ‘abnormal’ have not been ignored. Twins such as the example shown in Figure 5.14 display a low Schmid factor value (< 0.2) for $\{10\bar{1}2\}$ type twins calculated using the assumed simple plane shear stress model. Their formation could be result of the interaction of a critical combination of neighbouring grain orientations that in turn cause a localised stress concentration, which may induce twinning. As discussed in §1.3.5, investigating the role neighbouring grains play in promoting specific modes of deformation is an area of ongoing research; with slip induced twins and twin-twin combinations being well documented. Never the less the author feels it is of great importance to further investigate the role of neighbouring grain combinations have under more realistic conditions seen during machining (high strain and high strain rate etc.). Since if the following model that is being proposed can account for the majority of twins that are being generated, it is of further interest/importance

to understand what is activating the remaining ‘abnormal’ twins. Through the application of the simple shear stress model the relative Schmid factor for $\{10\bar{1}2\}$ type twinning has been calculated using the methods outlined in §3.7. The Histogram shown in Figure 5.15 compares the relative frequency of the calculated Schmid factor for each grain that has twinned to the Schmid factor of all of the grains within 100 μm of the surface.

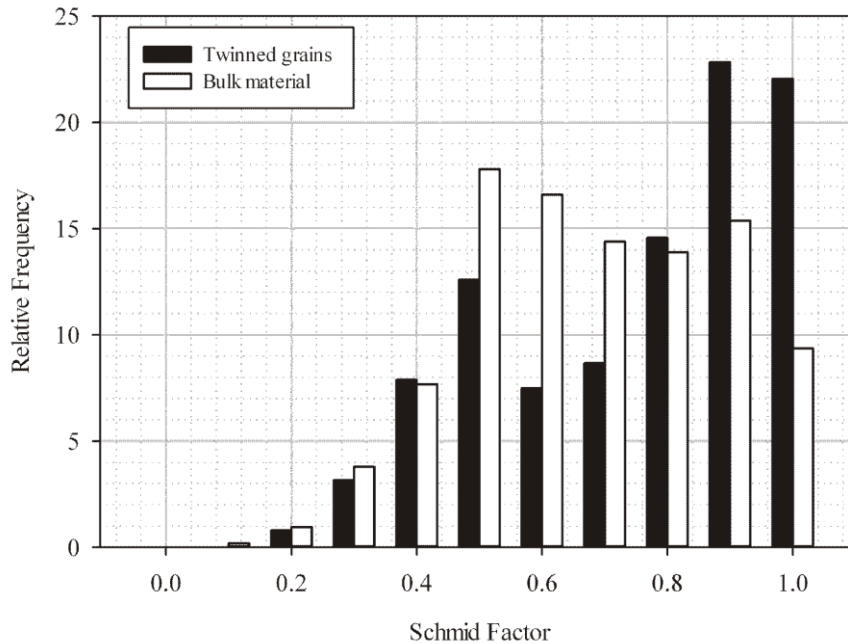


Figure 5.15 Histogram comparing the distribution of the relative frequency of the calculated Schmid factor for $\{10\bar{1}2\}$ twinning for each that has twinned to that of all of the grains within 100 μm of the surface. Schmid factor calculated assuming plane simple shear.

The histogram displayed in Figure 5.15 shows that unsurprisingly for the majority of grains that display evidence of $\{10\bar{1}2\}$ type twinning, the grains have a Schmid factor approaching 1 on the activated K_1 plane. For all the $\{10\bar{1}2\}$ type twinned grains analysed the activated K_1 plane displayed the highest Schmid factor out of all of the planes within the $\{10\bar{1}2\}$ family. This Schmid factor distribution profile follows a similar trend to that seen under more controlled loading environments - such as the work carried out by Beyerlein *et al.* [44] who investigated the twinning behaviour in magnesium using compression loading. Similarly to the work presented here, Beyerlein *et al.* [44] found that grains are able to twin even when their respective Schmid factor values are comparatively low. It is important to note that the Schmid factor distribution displayed by the twinned grains does not match that of the bulk material. Confirming that the resulting deformation is governed by the specific orientation of the underlying grains and that the twinning is not a random occurrence.

The stress state surrounding a tool during a machining operation is complex. However, as a first order approximation for calculating Schmid factor, it would appear that the system can be simplified to a simple plane shear stress model. When using Schmid factor as a tool to analyse bulk data one should note that only the most favourable orientations for a specific mode of deformation is quantified. The actual operation of the deformation modes also depends on the specific shear strain required for activation. Nevertheless, Schmid factor values serve as a good starting point for assessing a material's propensity for deformation under a specified load.

The simple shear model and the Schmid factor analysis technique has been applied as an analytical tool to ascertain the theoretical alignment of grains that are most favourably orientated for twinning. These favourably aligned grains have been identified using the following assumptions; for twinning to occur the grain must be theoretically 'hard' for $\langle a \rangle$ type slip to occur, therefore their $\langle a \rangle$ type Schmid factor must be below 0.6, in addition to this the grains displayed are 'soft' for $\{10\bar{1}2\}$ type twinning and have a schmid factor above 0.7. The pole figures in Figure 5.16, display colour contour plots for the bulk material, twinned grains and the theoretical preferentially orientated twinning grains. The observed data does show a slight shift away from the theoretical orientations which could be attributed to other machining parameters - and may affect the true nature of the local stress state. For example, the downward force on the tool would alter the orientations of the principle stresses. However, as a first order approximation for calculating the Schmid factor for $\{10\bar{1}2\}$ type twinning in each individual grain, it would appear that the system is operating under plane simple shear.

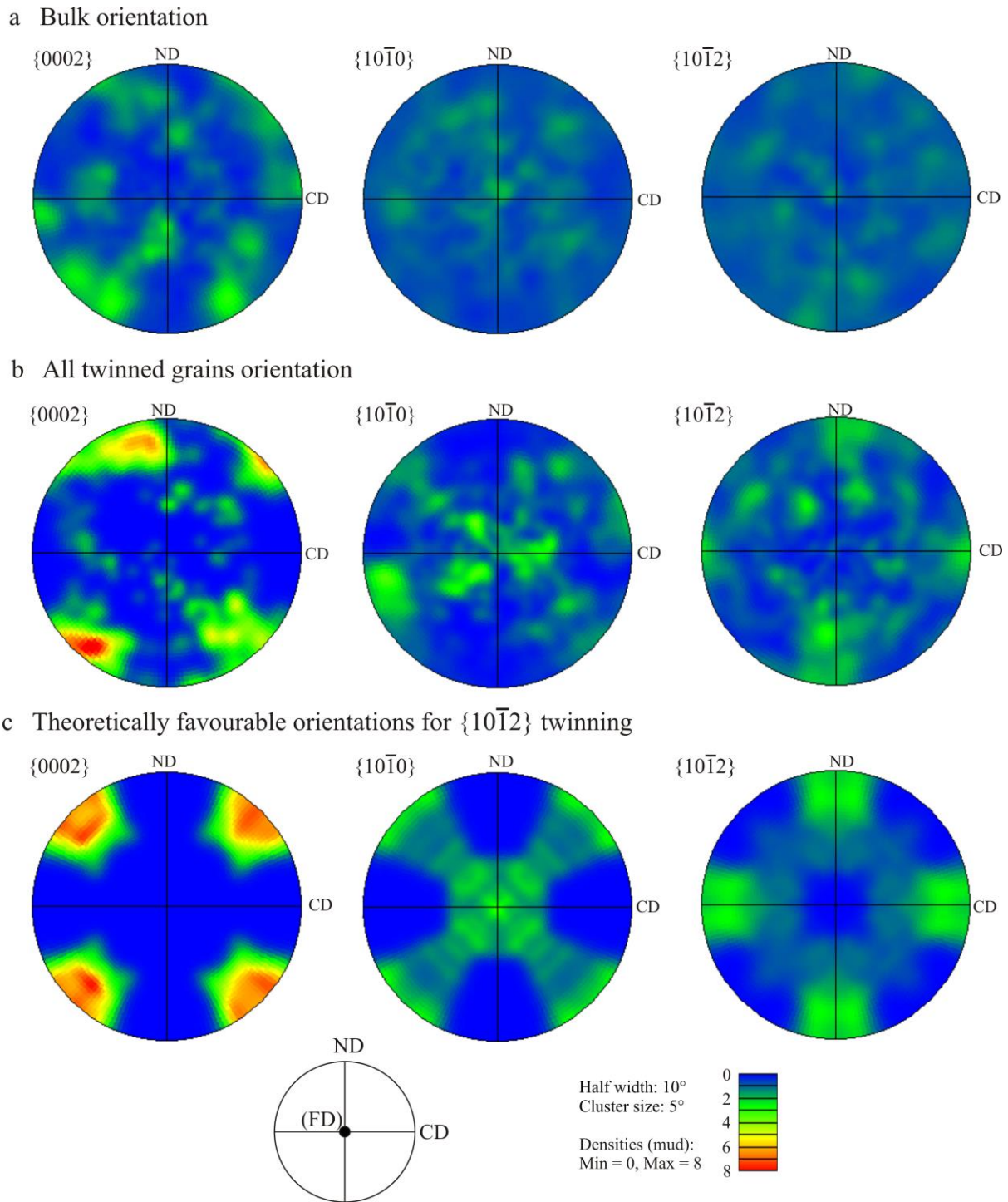


Figure 5.16 bulk material surface, orientation of parent grains which have twinned, theoretical orientation Figure 5 (a) The crystallographic texture of all material within 100 μm of the surface, (b) orientation of the parent grains that have deformed via {10 $\bar{1}$ 2} twinning, (c) theoretical orientation of grains that are most favourably orientated for {10 $\bar{1}$ 2} twinning assuming plane simple shear.

5.4 Microstructure analysis of material following a machining dwell.

Machining guidelines warn titanium machinists against allowing the tool feed rate to drop significantly, thus preventing the tool from dwelling whilst it is in moving contact with the workpiece. As quoted in the Titanium ASM handbook [15]; *Allowing a tool to dwell when it is in moving contact with titanium causes work hardening and promotes smearing, galling and seizing* [on the workpiece]. *This can lead to total tool breakdown* [15].

The secondary electron micrograph of the machined surface, shown in Figure 5.17, covers an area that has been subjected to an abnormal cutting regime. During this cutting cycle the tool feed was intentionally reduced so that the tool could be removed for wear inspection after which it was later reinstated such that the cut could resume. During this process the workpiece material was subjected to both a dwell when the tool was removed and a ‘secondary hit’ as the tool was brought back in contact with the workpiece at a feed rate of $0.1 \text{ mm}\cdot\text{rev}^{-1}$. The material that has been delineated between the two marked lines signifies the region of material that was subjected to this multi-step cut. Here the material displays no obvious excessive topographical deformation, with the surface imperfections appearing uniform across the whole workpiece surface. The offset in diameters either side of the dwell zone has been attributed to the insert not returning to its original position within the tool holder after wear inspection.

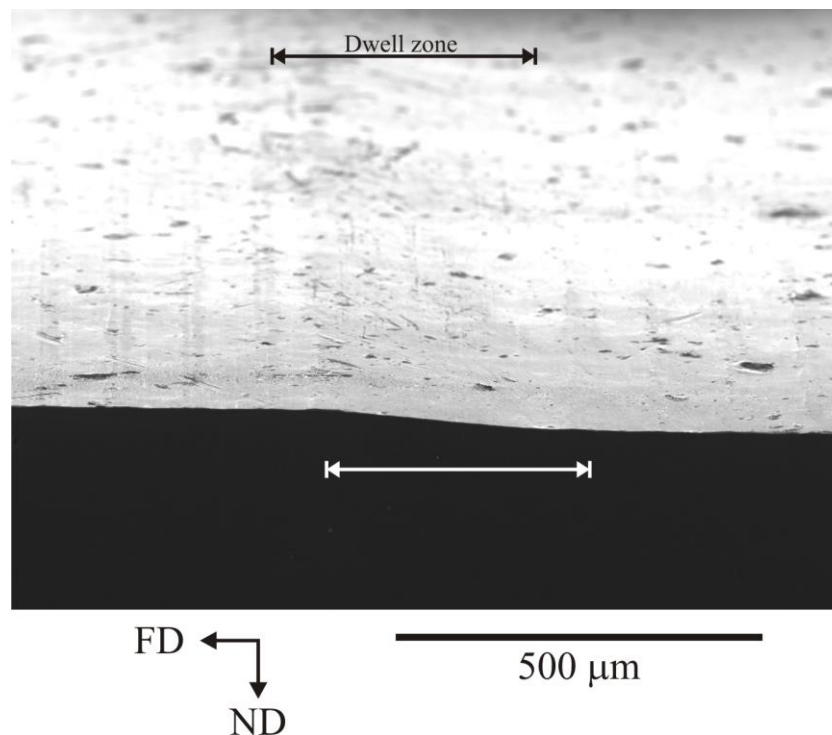


Figure 5.17 Secondary electron micrograph of an inclined machined Ti-54M surface following a machining tool dwell. The shoulder highlighted within the area between the two delineated lines locates the dwell zone.

However, subsurface analysis demonstrates that the experienced stress state beneath the dwell zone has been significantly altered in comparison to areas outside of this region. When machining a structurally critical component manufacturers wish that a tool will survive the full duration of a cutting cycle, eliminating the risk of needing to replace a worn out tool mid-way through a cut. This is not only due to the possibility of excessive workpiece damage, caused by the use of an excessively worn tool but also the impact of drawing out a tool and feeding back in. The following example has been included to illustrate how vulnerable Ti-54M is to severe subsurface deformation if machined in such an undesirable manner. The backscatter electron micrographs shown in Figure 5.18 and Figure 5.19 have been sectioned parallel and perpendicular to the machining direction, respectively. These images show typical subsurface material from within the dwell zone, which appears to be confined to a (relatively shallow) 20 μm layer beneath the machined surface, rather than to within the first 50 μm , as observed elsewhere in this work. Qualitative analysis of the surrounding grains indicates that substantially less lattice rotation has occurred within the α grains interior. However, as can be identified clearly, this confined region has been subject to catastrophic microstructure deformation manifesting in the form of severe micro-cracking; this is indicative of extensive work hardening.

The deformation induced micro-cracks have been generated within both colony and primary α grains, with their regular morphology and frequency suggesting a dependency on the underlying crystallographic orientation of the α grains. The majority of the micro-cracks span the width of the parent α grains, with many appearing to propagate into neighbouring α grains through the residual β phase. The backscatter electron micrograph shown in Figure 5.18(a) illustrates how the deformation behaviour can vary dramatically between regions that are comparatively close together. The large individual primary α grain, near the machined surface, appears to have resisted deforming as severely as its neighbours. This example demonstrates how the texture of the individual primary α grain may also not be as favourably orientated to permit deformation to occur, thus resulting in a partitioning of the induced strain to the “weaker” regions. The identified deformation also illustrates the “cushioning” effect the residual β offers to the colony α regions, whereby the residual β permits the α grains to rearrange more easily. On preparation for microstructure analysis the deformed subsurface layer has generated a topographical relief, whereby the deformed region protrudes above the planar prepared surface, as can be seen in Figure 5.18(b). The displayed topographical relief is indicative of material that had been under significant residual stress, through the accumulation of strain, which has resulted in the observed spontaneous plastic yielding upon sample preparation. Beneath the heavily deformed region, in Figure 5.18(b), twins can be observed. However, as previously stated, the amount of induced lattice rotation within the surrounding grains does not appear to be as extensive as that observed away from the dwell region.

The presence of a machining-induced white layer has been extensively documented for the most common manufacturing metallic materials. However, its precise role during machining, the conditions required to generate a white layer plus even its composition and morphology is still under debate [116], [200], [201]. Therefore the author feels it is out of the scope of this investigation to discuss in detail the presence of the obvious white layer that can be identified in Figure 5.19, bearing in mind that it is widely accepted that the presence of a white layer is undesirable, often associated with conditions of rapid tool wear [112]. The enlarged area in Figure 5.19(i) is positioned close to a machined surface defect. Similarly to the feature highlighted in Figure 5.6 the defect appears to have influenced the associated stress state at the surface of the material. Since this feature is already positioned within the dwell region it is therefore difficult to ascertain the initiation point for the induced microcracks. However, it is possible to identify microcracks that have progressed from an α grain unimpeded into the surrounding residual beta matrix where they appear to have either terminated at a α grain interface or progressed into a further α grain.

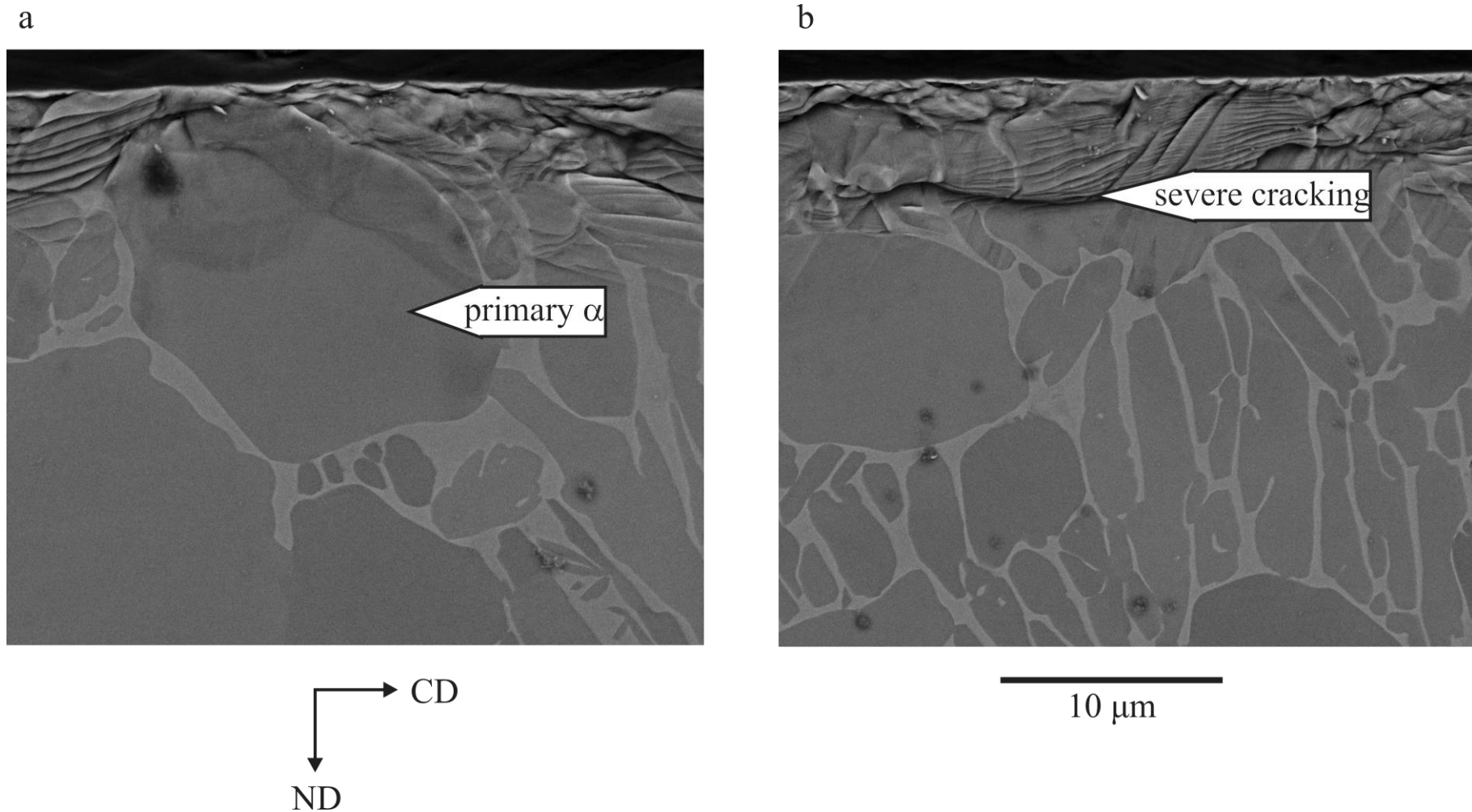


Figure 5.18 Cross sectional backscatter electron micrographs of outer diameter turned Ti-54M, sectioned parallel to the cutting direction from within the dwell region. The images illustrate the typical gross mechanically induced subsurface deformation, manifesting in twins and intense slip that have developed into severe cracking. (a) Has captured a primary α grain that has appeared to resist deformation, (b) severe cracking progressing unimpeded through neighbouring primary α grains and through grain boundary β .

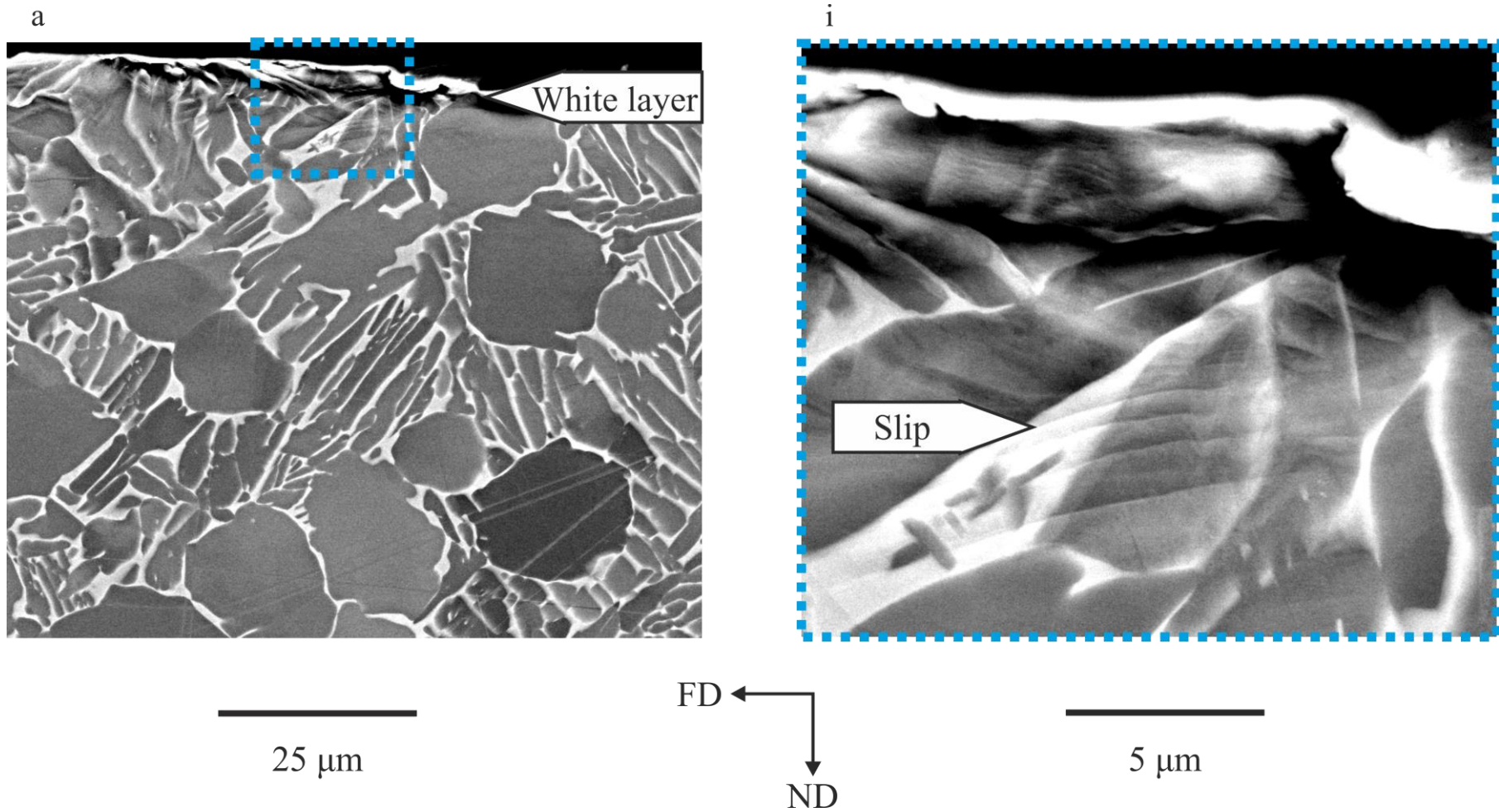


Figure 5.19 Cross sectional backscatter electron micrograph of outer diameter turned Ti-54M sectioned parallel to the feed direction within the dwell region, the images illustrate the occurrence of a residual white layer at the surface interface, the enlarged micrograph (i) shows evidence of slip progressing unimpeded through the residual grain boundary β .

EBSD data acquired from within the dwell zone (Figure 5.17) reveals how the induced stress state varies considerably to that of the surrounding regions, with the high resolution IPF coloured OIM (step size of 0.06 μm) demonstrating how the induced stress state within the dwell zone can be considered abnormal. Due to the small area size that has been analysed it would be irresponsible to draw broad conclusions as to the mechanisms that are occurring throughout the whole dwell region. However, the data shown in the Figure 5.20(a) has highlighted features that have not been observed elsewhere in the substructure and are specific to this region. Within the dwell region the abnormal stress state has permitted excessive deformation in the form of $\{10\bar{1}2\}$ mechanical twins. However, the twins appear to have propagated within regions of colony α , a condition that has not previously been commonly observed within the bulk of the machined material. The orientations of the twinned α grains also do not comply with the standard condition that has been outlined as part of the simple shear stress model. Whereby, all of the grains that display evidence of twinning are orientated such that their c-axis is positioned perpendicular to the cutting direction. The bulk orientation contour pole figure, shown in Figure 5.20(b), highlights a corresponding location at the centre of the plot which corresponds to the parent α grains that display $\{10\bar{1}2\}$ twins.

a

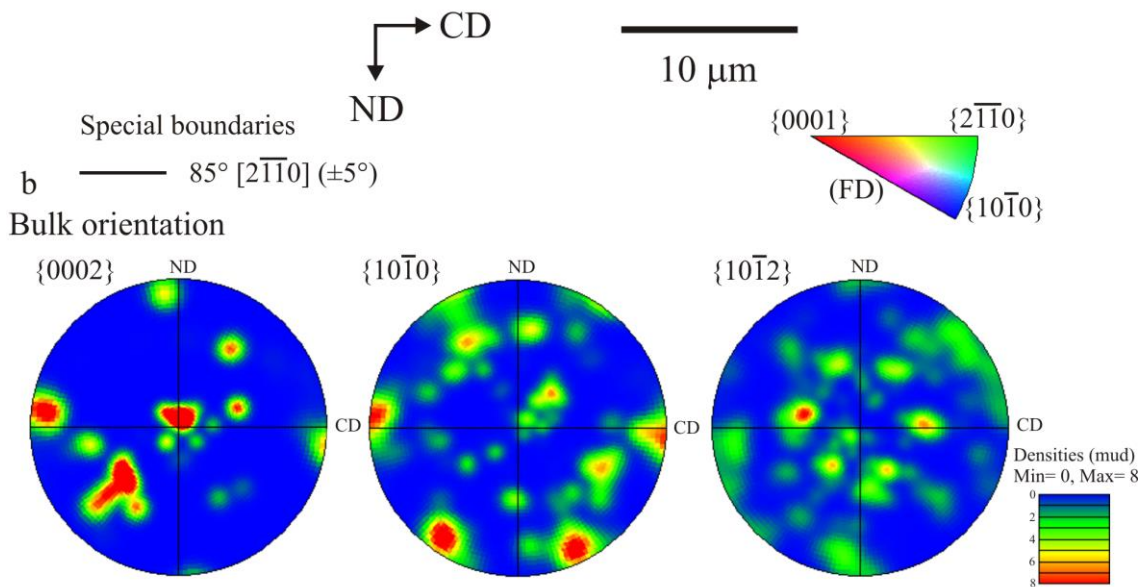
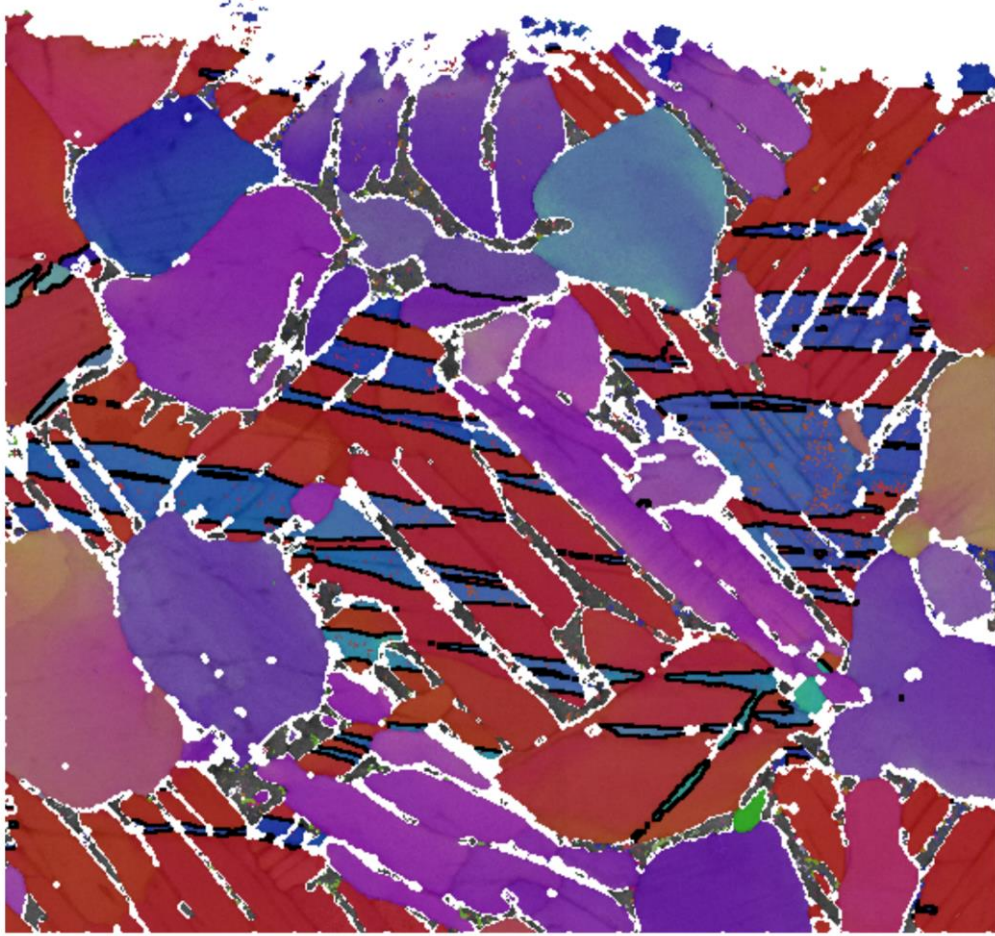


Figure 5.20 (a) IPF coloured, with respect to FD, OIM of outer diameter turned Ti-54M illustrating the occurrence of mechanically induced $\{10\bar{1}2\}$ tension type twins within the dwell zone (b) Corresponding $\{0002\}$, $\{10\bar{1}0\}$ and $\{10\bar{1}2\}$ stereographic pole figure projections of the bulk region indicating strong alignment of the basal plane along CD and FD.

5.5 Summary

Through the application of high resolution analysis techniques, such as backscatter electron microscopy and EBSD the activation of multiple deformation modes were identified within Ti-54M, these occurred as a result of the machining operation. These deformation features included; mechanically induced twins, the most common of which was characterised to be the $\{10\bar{1}2\}$ tension type twin, these occurred in addition to the activation of basal, prismatic and pyramidal slip. Turning trials were performed on Ti-54M to determine the conditions required for the formation of subsurface $\{10\bar{1}2\}$ twins in the workpiece. Twins were mostly observed in two orientation clusters at approximately $\pm 45^\circ$ to CD, which is attributed to a plane simple shear state that operates in a forward mode ahead of the tool and in reverse behind the tool. This means that upstream metallurgical processing to develop specific crystallographic texture components, could have a direct impact on the level of subsurface damage caused by machining. The possibility therefore exists to develop upstream processing routes that could minimise damage - leading to enhanced performance in-service.

Chapter 6 - Quantifying the cutting forces as a function of material chemistry and billet forging route

6.1 Introduction

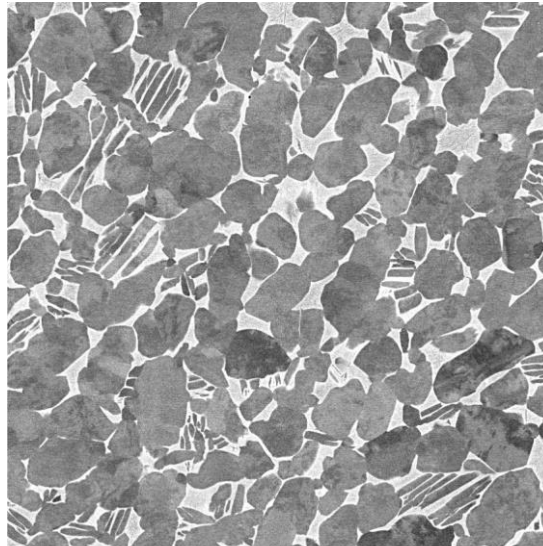
This chapter investigates the material aspects that influence the machining process during variable parameter orthogonal cutting trials, through the analysis of the resulting cutting forces. As a result of the non-uniform strain distribution generated during the multiple step forging route, once the billet undergoes machining the machine tool will see significant variations in microstructure and likewise crystallographic texture variations over the whole billet cross section. Further machining trials will be undertaken to investigate the influence of the forging process on the machining behaviour within different areas of the billet.

6.2 Experimental methods

For the work covered in this investigation the following experimental methods were followed, these are in addition to the material analysis procedures outlined in §3.2.

6.2.1 As received material

For this study, the $\alpha+\beta$ titanium alloy Timetal® 54M (Ti-54M) 255 mm diameter was supplied by TIMET UK Ltd in the as-forged condition. Billets of this size are considered to be chemically homogeneous but, due to the complex non-linear deformation history experienced during cogging, the microstructure can vary significantly. The typical as-forged microstructure for Ti-54M is shown in Figure 6.1, which displays an approximate 0.7 volume fraction of α phase - of which approximately 60% is primary α grains and 40% colony α . Residual β is observed between the primary α and colony α structures. The microstructure displays isolated regions of typical colony α structure, which formed during the initial cool during forging within transformed prior β regions.



50 μm

Figure 6.1 Backscatter electron micrograph of Ti-54M, with an as-forged microstructure.

Compositional analysis of the received billet was provided by TIMET UK, composition measurements were taken from the bottom and top of the billet. The average composition of the material is given in Table 6.1

Table 6.1 Billet composition of the $\alpha+\beta$ titanium alloy Ti-54M (wt. %).

Al	V	Mo	Fe	C	O	N	Ti
5.18	3.99	0.78	0.45	0.0006	0.16	0.003	Balance

6.2.2 Microstructure analysis

The four cardinal points (north, east, south and west) as shown in Figure 6.2(a) were scribed onto the billet cross section, prior to orthogonal cutting trials. The orientations of these points were applied arbitrarily onto the billet, since information regarding the specific orientation of the billet relative to prior forging steps was unknown at this stage. These orientations were logged throughout the investigation and served as reference markers when coupling the force feedback data with the billet microstructure.

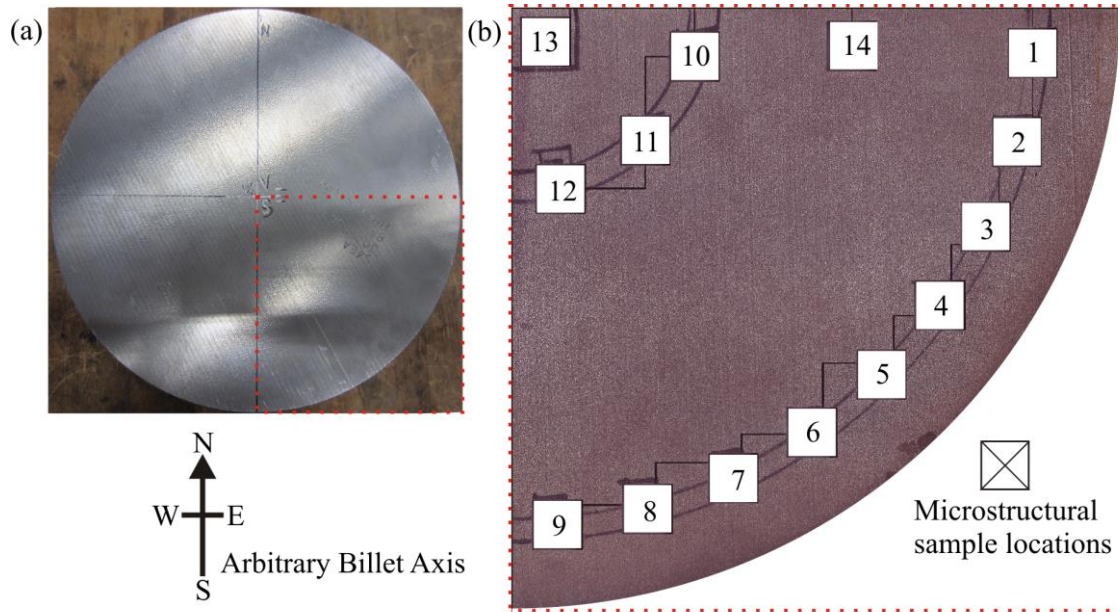


Figure 6.2 (a) Photograph showing the orientation of the arbitrary Ti-54M billet axis with the cardinal points scribed onto the billet cross section (b) location and orientation of the sectioned microstructure analysed samples.

A 5 mm thick transverse slice was obtained from the 255 mm diameter Ti-54M billet of which a quarter (from east to south) was analysed using scanning electron microscopy and electron backscatter diffraction (EBSD). The location of the samples analysed correspond to the position of two concentric rings of diameter ~ 223 mm and ~ 83 mm as indicated in Figure 6.2(b). Specimens were sectioned via electron discharge machining (EDM) with dimensions 9.98 x 9.98 x 5 mm. The macroscopic coordinate system used for this analysis is also shown in Figure 6.2 and the specimens were prepared for metallography using the standard methods detailed in Chapter 3. Microstructure imaging analysis of the billet material was carried out using an FEI Inspect F (FEG-SEM). Quantitative EBSD crystallographic orientation data was acquired using a FEI Sirion (FEG-SEM) with a 20 keV accelerating voltage, a spot size of 3 and a step size of 5 μm . Automated indexing and post-processing of the electron diffraction data were performed using Oxford Instruments HKL Channel 5 software.

6.2.3 Machining trials

Orthogonal cutting trials were undertaken on the as-forged Ti-54M billet. Firstly, the workpiece required a series of preparation steps in order to construct the desired test piece geometry, which comprised of a ring with a 4 mm wall thickness and 17 mm axial length, as seen in Figure 6.3.



Figure 6.3 Ti-54M billet position held in a MAG Cincinnati Hawk lathe prepared for an orthogonal cutting trial.

All aspects of the current investigation, preparation and orthogonal cutting trials, were performed using a MAG Cincinnati Hawk lathe. Table 6.2 details the tools used during the workpiece preparation stage and force measurement investigation and corresponding uncoated carbide cutting inserts.

Table 6.2 Tooling required for orthogonal cutting force trials.

Operation	Insert	Tool Holder
Groove preparation	N123 H2 0400 0002 GF H13A	C5-570-32-RG
General preparation	CNMG 12 04 08 – 23 H13A	C5-DCLNL-35060-12
Force measurement	TCMT 16 T3 08 KM H13A	STGCL-2020K-16
For all operations; water based coolant, Hocut 795B, 5% delivered at 13 l.min ⁻¹		

Sandvik triangular TCMT 16T308KM H13A uncoated carbide inserts were mounted in a SANDVIK TCMT 16 T3 08 KM tool holder that provided a clearance angle of 6° and a rake angle of 7°, this cutting geometry being the same as the investigations followed in Chapter 5

The force feedback response was recorded using a Kistler acquisition system; this comprised of a Kistler 9121 dynamometer that held the tool holder, as shown in Figure 6.4. The output

signals were processed through a Kistler 5070 8 channel amplifier and the data was recorded using the Kistler DynoWare software at an acquisition rate of 20 kHz.

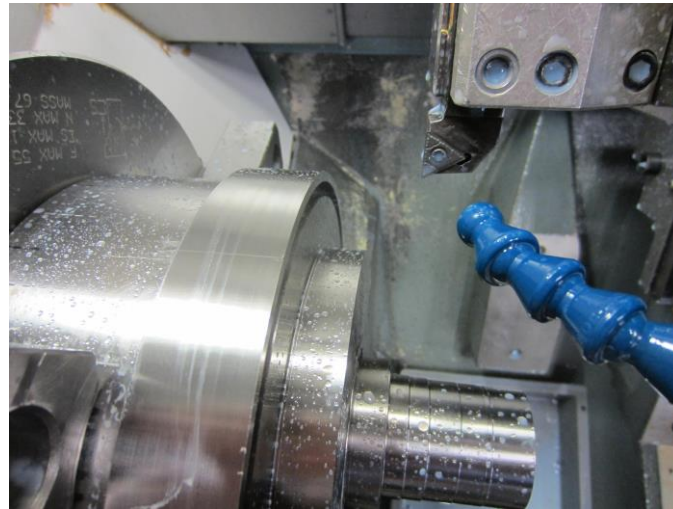


Figure 6.4 Ti-54M Workpiece and tool arrangement following an orthogonal cutting trial.

Force readings were recorded along the three Cartesian planes (x, y, z), where the Normal direction (x) normal force (radial) is equal to F_x , the feed direction (y) thrust force is equal to F_y as and the cutting direction (z) cutting force is equal to F_z shown in Figure 6.5. However, since this was an orthogonal arrangement, there was no movement along the x plane, thus F_x remains constant.

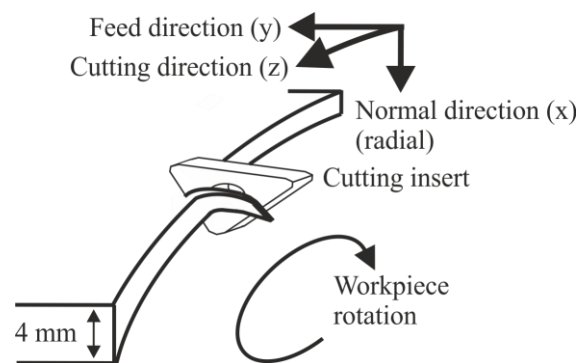


Figure 6.5 Schematic diagram illustrating the orientation of the Cartesian planes used when recording the force feedback data.

As part of this study, the turning trials were all undertaken using a Cincinnati Hawk lathe whilst using a water based coolant, Hocut 795B at 4-7% concentration, ‘flood’ delivered at 13 litres per minute to act as a lubricant and to avoid the tool from overheating.

6.2.4 Parametric orthogonal cutting trials

Feed rate variable orthogonal cutting trials were performed using a feed rate range of 0.025 – 0.25 mm.rev⁻¹ at a constant speed of 40 m.min⁻¹ and at a fixed ring diameter of 223 mm. The depth of cut for both the speed and feed variable trials was maintained by virtue of the ring wall thickness of 4 mm. The machining parameters and corresponding workpiece geometries are given in Table 6.3. Speed variable orthogonal cutting trials were conducted on the as-forged Ti-54M billet, using a cutting speed range of 6 – 160 m.min⁻¹ at a constant feed of 0.1 mm.rev⁻¹. In order to achieve the lowest speeds and to overcome the minimum rotational velocity threshold limiter on the lathe, reduced speed trials were undertaken on rings that were prepared with a reduced diameter. Throughout the investigation a fresh insert edge was used for each cut with each trial being repeated a minimum of two times, with some receiving >3 repeats. Following each cutting trial the chip was dried and collected for follow up analysis though the present study has not included a thorough review of the acquired chip.

Offline data handling of the acquired data was managed using Kistler DynoWear, SignalLab SIGVIEW spectrum analyser and Microsoft Excel.

Table 6.3 Machining parameters for feed variable orthogonal cutting trials and workpiece geometries.

Trial	Speed (m.min ⁻¹)	Feed rate (mm.rev ⁻¹)	Ring diameter			RPM	No. Revs	Material removed (mm)
			Outer (mm)	Inner (mm)	Average (mm)			
Feed trials	40.0	0.25	223.00	215.00	219.00	58	15	3.8
	40.0	0.2	223.00	215.00	219.00	58	15	3.0
	40.0	0.15	223.00	215.00	219.00	58	15	2.3
	40.0	0.1	223.00	215.00	219.00	58	15	1.5
	40.0	0.05	223.00	215.00	219.00	58	20	1.0
	40.0	0.025	223.00	215.00	219.00	58	15	0.4
	40.0	0.01	223.00	215.00	219.00	58	15	0.2

Table 6.4 Machining parameters for speed variable orthogonal cutting trials and workpiece geometries.

Trial	Speed (m.min ⁻¹)	Feed rate (mm.rev ⁻¹)	Ring diameter			RPM	No. Revs	Material removed (mm)
			Outer (mm)	Inner (mm)	Average (mm)			
Speed trials	6.0	0.1	98.00	90.00	94.00	20	7	0.7
	9.0	0.1	98.00	90.00	94.00	30	7	0.7
	10.5	0.1	98.00	90.00	94.00	36	7	0.7
	12.0	0.1	98.00	90.00	94.00	41	7	0.7
	15.0	0.1	98.00	90.00	94.00	51	7	0.7
	18.0	0.1	98.00	90.00	94.00	30	7	0.7
	18.0	0.1	198.00	190.00	194.00	61	7	0.7
	30.0	0.1	198.00	190.00	194.00	49	7	0.7
	40.0	0.1	223.00	215.00	219.00	58	15	1.5
	50.0	0.1	223.00	215.00	219.00	73	20	2.0
	60.0	0.1	198.00	190.00	194.00	98	7	0.7
	70.0	0.1	223.00	215.00	219.00	102	20	2.0
	80.0	0.1	223.00	215.00	219.00	116	20	2.0
	95.0	0.1	223.00	215.00	219.00	138	20	2.0
	105.0	0.1	223.00	215.00	219.00	153	20	2.0
	120.0	0.1	198.00	190.00	194.00	197	10	1.0
	120.0	0.1	223.00	215.00	219.00	174	20	2.0
	160.0	0.1	198.00	190.00	194.00	263	10	1.0

6.2.5 The mechanics of machining

The methods used to resolve the dynamics of the cutting system followed the Albrecht [143] adapted Merchant [51] empirical machining formulae.

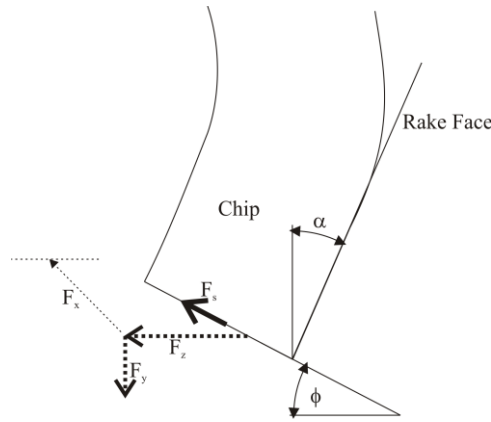


Figure 6.6 Schematic diagram of a simple two-dimensional orthogonal steady state cutting operation illustrating the resulting stress components acting within the arrangement.

The schematic in Figure 6.6 illustrates the resulting stress components acting within a simplified orthogonal cutting arrangement. During this investigation the tooling employed a rake angle (α) = 6° and the shear angle (ϕ) has been assumed to remain constant throughout at 45° . Using the resolved forces, (F_y) and (F_z), the effective coefficient of friction (μ) for the cutting environment (Equation 6.1), the resultant shear plane force (F_s) (Equation 6.4) and the average shear stress (τ) of the material acting on the shear plane (Equation 6.5) have been calculated.

The coefficient of friction, μ ;

$$\mu = \frac{F_y + F_z \tan \alpha}{F_z - F_y \tan \alpha} \quad \text{Equation 6.1}$$

The specific cutting energy for thrust and cutting, F'_y , F'_z respectively, where t_1 represents the uncut chip thickness which equates to the feed rate and ω is represents to the depth of cut (DOC) which is equal to the thickness of the prepared ring, 4 mm.

$$F'_y = \frac{F_y}{\omega \cdot t_1} \quad \text{Equation 6.2}$$

$$F'_z = \frac{F_z}{\omega \cdot t_1} \quad \text{Equation 6.3}$$

The resultant force occurring parallel to the shear plane, F_s , may be resolved as such;

$$F_s = F_z \cos \phi - F_y \sin \phi \quad \text{Equation 6.4}$$

Using the resultant shear plane force F'_s the average shear stress of the material, τ ;

$$\tau = \frac{F'_s + \sin \phi}{\omega t_1} \quad \text{Equation 6.5}$$

The Merchant empirical formulae [51] however, as previously discussed §2.7, does not account for the ploughing effect, which has been shown not to contribute to the chip removal process and therefore is required to be separated from the total resulting force [143]. The corresponding cutting and thrust ploughing forces, P_1 and P_2 respectively, are determined by extrapolating the feed rate vs force linear relationship back to the y-intercept. Taking into account the ploughing forces, Albrecht [88] adapted the Merchant empirical formulae such that the total resulting cutting force F_z (Equation 6.6) can be written in terms of the ploughing force (P_1) and the component of force in the direction of the tool motion (Q_1).

$$F_z = P_1 + Q_1 \quad \text{Equation 6.6}$$

Similarly the total resulting thrust force F_y (Equation 6.7) can be written in terms of the ploughing force (P_2) and the component of force perpendicular to the direction of the tool motion (Q_2)

$$F_y = P_2 + Q_2 \quad \text{Equation 6.7}$$

Therefore the effective friction coefficient (μ_Q) (Equation 6.8) for the cutting process can be determined by substituting the ploughing forces from the cutting and thrust forces.

$$\mu_Q = \frac{(F_y - P_2) + (F_z - P_1) \tan \alpha}{(F_z - P_1) - (F_y - P_2) \tan \alpha} \quad \text{Equation 6.8}$$

Furthermore the resultant force occurring parallel to the shear plane, F'_s (Equation 6.9), may be resolved as such after removing the ploughing force components P_1 and P_2 ;

$$F'_s = (F_z - P_2) \cos \phi - (F_y - P_1) \sin \phi \quad \text{Equation 6.9}$$

Therefore to determine the shear strength of the material τ_Q (Equation 6.10) the equation remains the same, noting that the ploughing forces have previously been removed when calculating F'_s .

$$\tau_Q = \frac{F'_s + \sin \phi}{\omega \cdot t_1} \quad \text{Equation 6.10}$$

6.2.6 Orthogonal cutting trails for microstructure correlation.

A shallow notch was grooved into the face of ring of the Ti-54M billet (Figure 6.7), this served as a reference marker to enable the acquired force feedback data to be accurately correlated to the billet microstructure. The notch was grooved with a precision file and its location corresponded to North on the arbitrary billet axis. The shallow and tapered geometry of the notch ensured it would be removed within 3-5 revolutions whilst minimizing unwanted shock loading that may accelerate wear on the tool. The machining parameters and corresponding workpiece geometry are detailed in Table 6.5.

Table 6.5 Machining parameters for orthogonal cutting trials and workpiece geometries for microstructure correlation.

Speed ($\text{m}\cdot\text{min}^{-1}$)	Feed rate ($\text{mm}\cdot\text{rev}^{-1}$)	Ring diameter			RPM	No. Revs	Material removed (mm)
		Outer (mm)	Inner (mm)	Average (mm)			
95.0	0.1	223.00	215.00	219.00	138	20	2.0

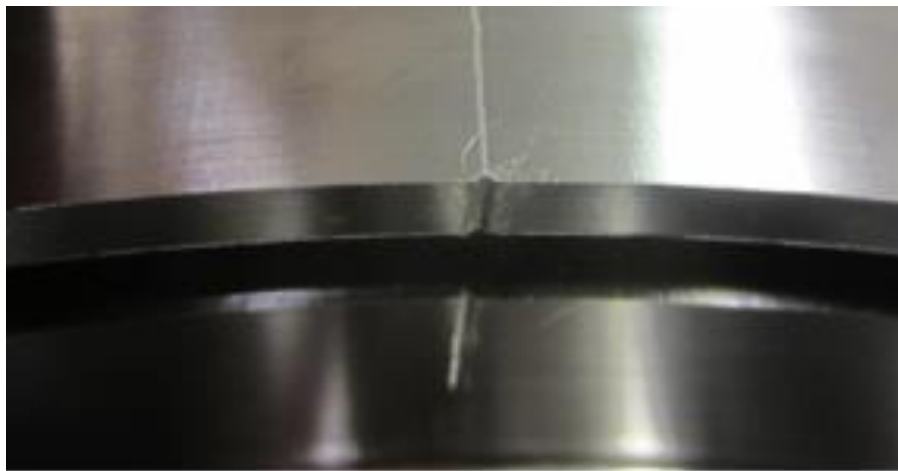


Figure 6.7 Shallow notch grooved onto the orthogonal cutting surface of Ti-54M.

6.2.7 Ultrasound analysis

Further evaluation of the regions analysed through EBSD were undertaken using ultrasound to measure the elasticity of the material. In order to determine Young's modulus (E) the longitudinal and shear wave sound velocity of the test piece was measured using an Olympus OmniScan iX UT. To calculate the sound wave velocity (Equation 6.11) the round-trip transit time, through an area of known thickness with both longitudinal and shear wave transducers is recorded [202].

$$\text{sound wave velocity} = \frac{\text{Sample thickness}}{\text{Round trip transit time}/2} \quad \text{Equation 6.11}$$

Using the shear and longitudinal velocities (centimetres per second) the Young's modulus equation can be calculated by firstly determining the Poisson's ratio using Equation 6.12 and subsequently Equation 6.13.

$$v = \frac{1 - 2(V_T/V_L)^2}{2 - 2(V_T/V_L)^2} \quad \text{Equation 6.12}$$

Where

v = sound wave velocity; V_T = Shear (transverse) velocity; V_L = Longitudinal velocity

$$E = \frac{V_L^2 \rho (1 + v)(1 - 2v)}{1 - v} \quad \text{Equation 6.13}$$

Where

E = Young's modulus; V_L = Longitudinal velocity; ρ = Density; v = Poisson's ratio

6.3 Results and discussion

6.3.1 Characterisation of Ti-54M Billet

The material throughout this investigation was forged through a multi-step cogging operation. The strain contour plot, presented in Figure 6.8, was simulated using Deform-3D finite element software and supplied by TIMET UK in order to predict the final strain distribution and is representative of the Ti-54M billet. The prediction shows the typical non-uniform strain distribution with circumferential and radial variation corresponding to the regions that have experienced the greatest levels of total strain, occurring at approximately every 90°.

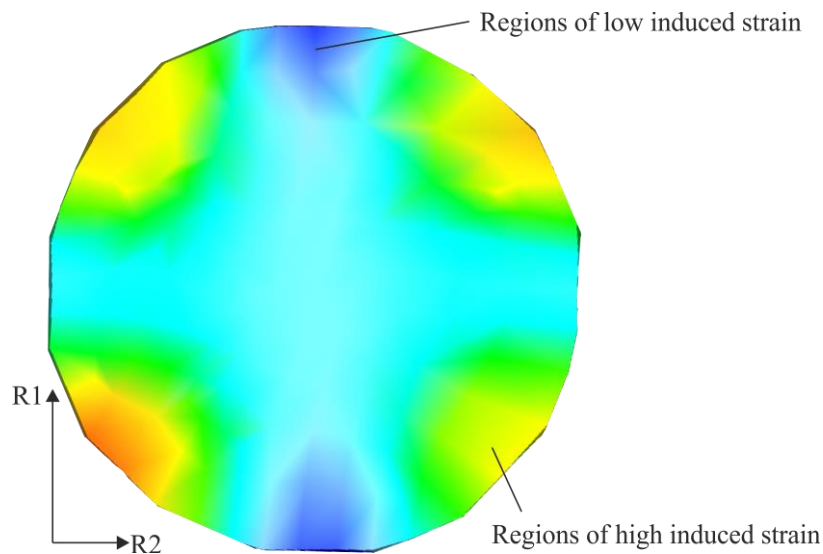


Figure 6.8 DEFORM-3D finite element software simulation identifying the total strain distribution within a Ti-54M billet, following a typical multi-stage cogging process performed by TIMET. Data supplied courtesy of TIMET UK, note scale bar not included with colour distribution to be used only as a guide for relative strain variance.

Microstructure analysis of the cross section taken from the Ti-54M billet was characterised using EBSD to ascertain orientation data and scanning electron microscopy for metallographic imaging. Significant differences in the microstructure were observed from the edge to the centre of the billet.

6.3.2 EBSD analysis

Low resolution EBSD data was gathered to ascertain the global texture of the Ti-54M billet, the composite image shown in Figure 6.9 illustrates the textural variation across the billet cross section. Around the billet the average texture orientation for each region can be determined using the position of the 'hot spots' on each of the given pole figures, which correspond to the location of the $\{0002\}$ plane. During forging, due to the anisotropy of the HCP crystal, the induced deformation results in the c-axis re-orientating itself, such that, it lies perpendicular to the maximum applied load, allowing further deformation to occur more

easily. Hence without prior knowledge of the precise strain path history, the global crystallographic texture map offers the reader insight into the how the billet has been processed.

The pole figures given in Figure 6.9 are considered to be representative of each region, with the EBSD data for region being acquired after scanning a significantly large area (8 mm x 4 mm) whilst using a 5 micron step size. The obtained EBSD data saw a minimal zero solutions resulting in a hit rate average ranging from 74-81% for each region. As shown by the pole figures around the billet, the average texture for each region is affected by the non-uniform strain distribution. It is however important to note the scale bar used to depict the average texture for each region, since across the whole billet each region shows orientation dominance with a maximum Multiples of Uniform Density (MUD) value of only 3, where MUD values of 0 would indicate a completely random texture. Regions possessing low mud values indicate how a significant proportion of the material contains grains that have maintained a random orientation. Around the billet perimeter, the global texture can be observed to shift and its relative intensity also varies, with the regions that align to the cardinal points SE and S displaying the weakest average texture. Caution is however required when comparing the relative intensities of the mud values from one region to another, since this data can be notably affected by the acquisition hit rate, which had remained approximately constant across the billet however was not exactly the same. As a result of the varying hit rates, the data can only be used qualitatively to determine the average orientation of each region.

During the multi-step cogging operation for billet cross sectional area reduction, Ti-54M adopts an extruded core and compressive mandrel type morphology. This is evident using the pole figures given in Figure 6.9 and in the schematics given in Figure 6.10 and Figure 6.11, where it can be observed that as the centre of the billet is approached, the analysed regions evolve from possessing a single dominant average orientation, towards one that shows a balanced orthorhombic symmetry. Such textural variation is similar to that observed in other forged $\alpha + \beta$ alloys, such as Ti-6246 [22] and Ti-64 [23]. This similarity in forged properties has been attributed to their significant amount of residual β that receives a partition of the applied load and allows the α grains to more easily flow and rearrange when strained. This core and mandrel structure is not observed in the near α alloy Ti-834 that shows a plain strain type orientation throughout the billet interior [19].

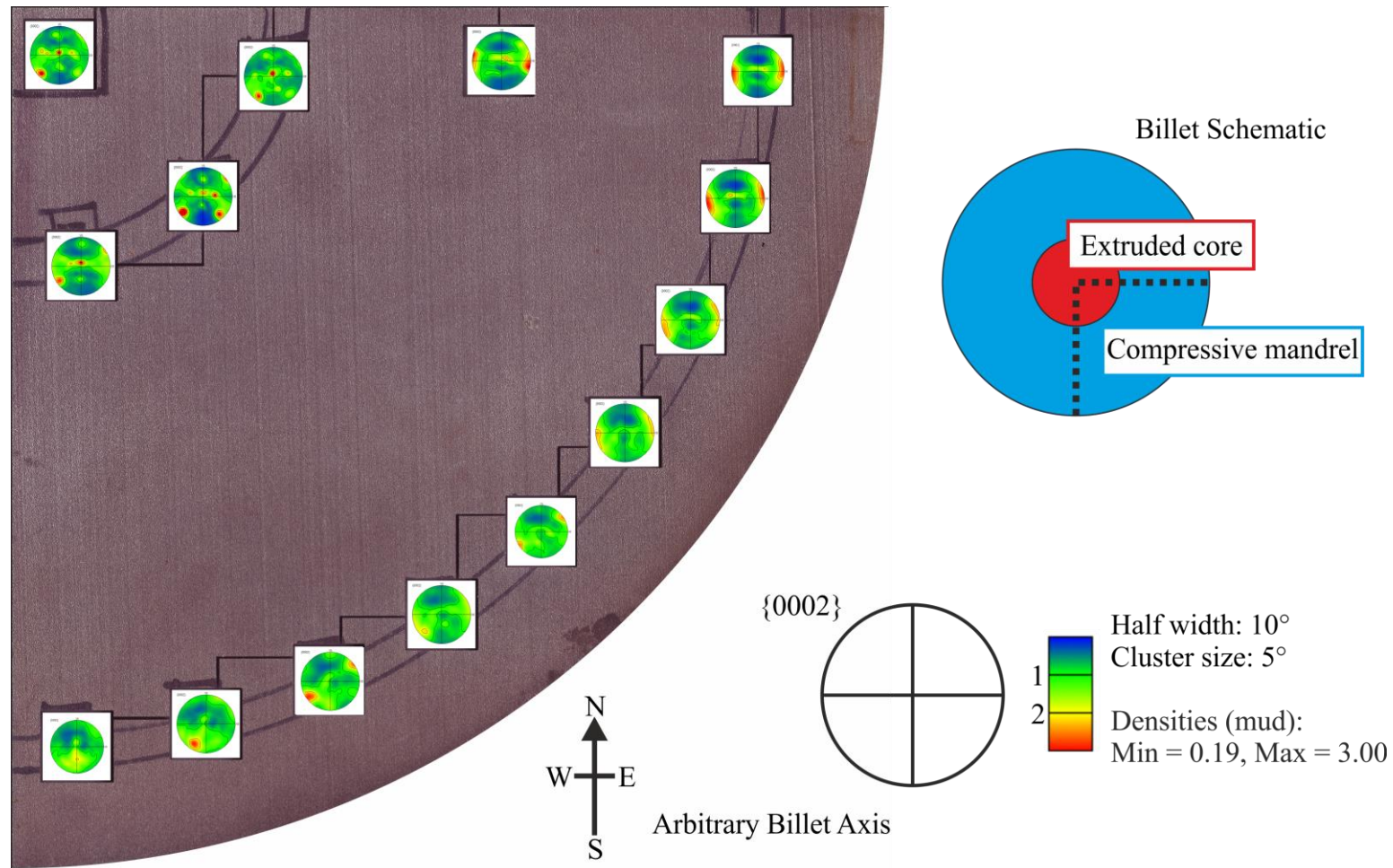


Figure 6.9 Composite image comprising of a quarter cross section taken of the Ti-54M billet, positioned between East and south on the arbitrary billet axis. Representative basal stereographic pole figure projections, each presented as a contour plot illustrating the average bulk texture for each region. The location of the samples analysed correspond to the position of two concentric rings of diameter ~ 223 mm and ~ 83 mm with two additional samples taken from the centre and midpoint of R2. Billet schematic illustrates the global texture of the billet

The composite orientation data for the Ti-54M cross section has been reproduced in Figure 6.10(a), where a chord has been included to demonstrate how the strong textural alignment shifts its orientation around the billet. The orientation of the maximum load for each region occurs perpendicular to each of the given chords. The plot given in Figure 6.10(b) illustrates how the inclination of the maximum load varies throughout the billet cross section, with material around the outer perimeter displaying the largest rotation, such that the outer material at 95° and 175° is aligned to be approximately 5° and 85° from the arbitrary billet axis, respectively. Towards the centre, the material approaches an average orientation inclination angle of 45° from the arbitrary billet axis. The alignment of the orientation chord is governed by the non-equal strains imposed around the billet axis during the forging process. For illustrative purposes the pole figures given in Figure 6.10(a) that surround the composite cross section orientation map have each been normalised with respect to their experienced orientation of maximum load, by having their inclination angle removed. Following this transformation the datasets can be more easily analysed. The inset schematic given in Figure 6.10(c) after Lütjering [4], illustrates the resulting rolled textures for $\alpha+\beta$ titanium alloys and their sensitivity to rolling at different temperatures. Comparing the resulting pole figures in Figure 6.10(a) to the examples given in Figure 6.10(c), the material around the outer and middle radii can be seen to have adopted a characteristic plane strain transverse morphology. This is commonly observed in rolled material processed below the β transus, but above $\sim 930^\circ\text{C}$, as depicted in Figure 6.10(c iii). Towards the centre of the billet, for the inner and centre radii material shows a characteristic symmetrical texture indicative of a rolled type structure deformed above the β transus, as demonstrated by the example given in Figure 6.10(c iv).

Davies [19] was able to hypothesise using the alignment of the material throughout a Ti-834 billet, how it was processed and how it had been originally orientated with respect to the initial rectangular cross section of the as-cast ingot, prior to the primary breakdown stages during the multi-step cogging processes. Using the strength and orientation of the two regions on the middle and outer radii that are positioned parallel to R2, these orientations have been attributed to being positioned perpendicular to the prior long axis reduction of the ingot. Using this alignment, the orientation of the initial rectangular cross section relative to the billet has been estimated, as shown in Figure 6.11. The variation in macrostructural alignment corresponds around the outer radii to the large dimensional reductions that were associated with location of the historical corners of the ingot. Using this method, the long axis of the prior rectangle was determined to have a $\sim 90^\circ$ rotation in relation to the initial arbitrary billet axis, thus the billet axis R1 has a $\sim 90^\circ$ rotation from N on the arbitrary billet axis.

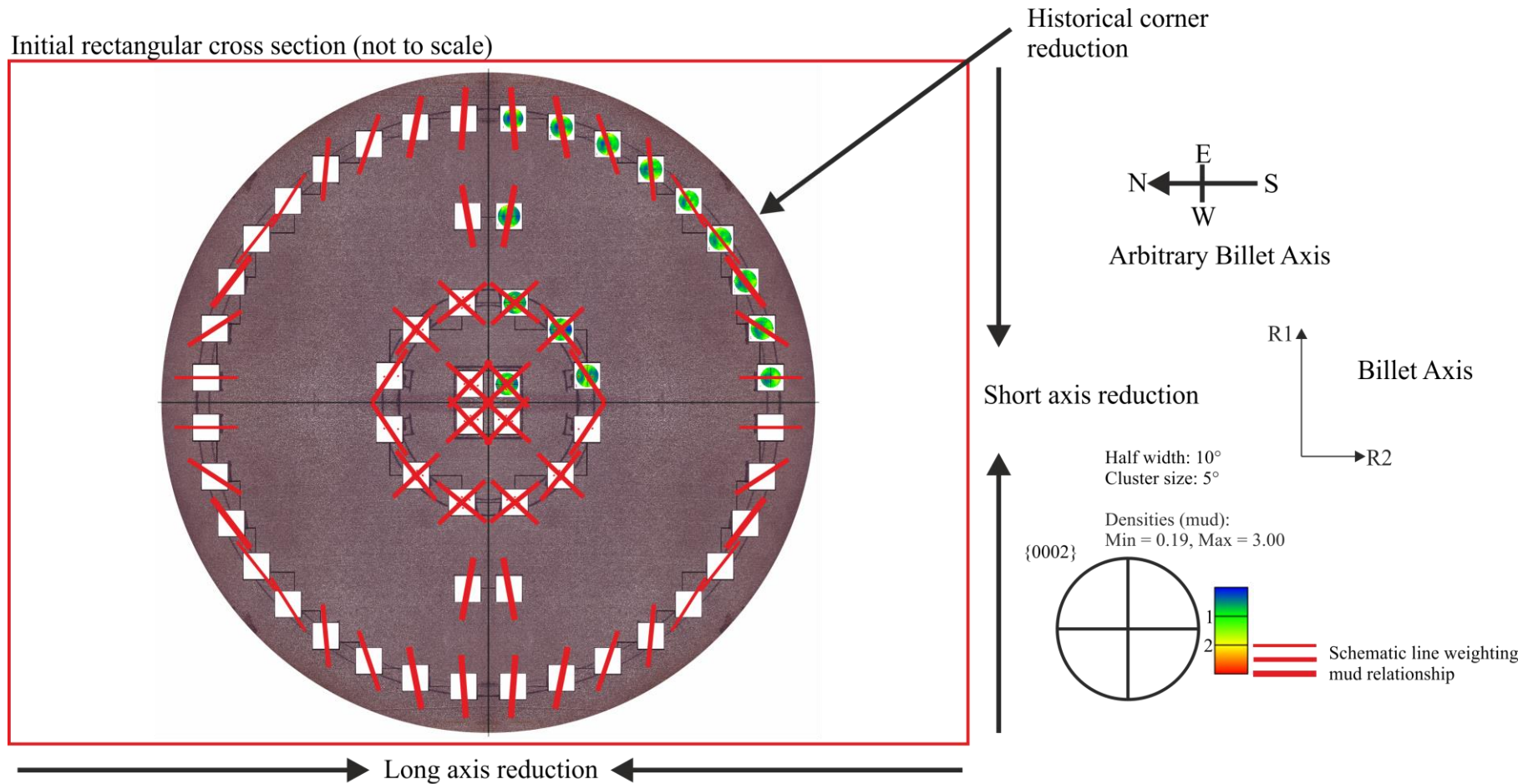


Figure 6.11 Proposed orientation of the initial rectangular cross-section of the intermediate billet with respect to the arbitrary coordinates, the weighted lines indicate the average microstructure alignment of the bulk material in the transverse plane.

6.3.3 Microstructure analysis

The composite image shown in the Figure 6.12 illustrates the relative location of the acquired backscatter electron micrographs and the associated regional average crystallographic orientation. The microstructure consists of ~70% primary α (~20 μm \O) with residual β and a small amount of secondary α . There were, however, some variations in microstructure throughout the cross-section; the percentage of secondary α increased slightly closer to the surface and the shape of the primary α and their aspect ratio alignment varies throughout the cross-section. The shape and alignment variation suggests that principal strain directions vary throughout, with the maximum principal strain direction in the high strain region at 45° to R1 and approximately parallel to R1 near the centre of the billet. The increased level of secondary α near the surface (Figure 6.12(a-e)) suggests slightly faster cooling rates in this region following the final forging pass. Further representative backscatter electron micrographs from the centre to the edge of the billet in the transverse plane are shown in Figure 6.14. The centre of the forged billet contains a high volume fraction of blocky primary α grains with angular grain boundaries. The primary α morphology is also indicative of the extruded nature since at the centre (Figure 6.13(a)) the material has experienced largely balanced compressive forces, whilst the billet cross section was being reduced. During the forging process, the primary α grains realign themselves crystallographically and morphologically such that they are orientated perpendicular to the forging direction; Figure 6.13(b-c) displays a significant proportion of parallel lenticular shaped primary α grains. At the edge of the billet in Figure 6.13(d) the alignment of the primary α grains has been disrupted by the growth of regions of lamellar secondary α colonies. Additionally, around the outer radii in Figure 6.14(a-c), the lenticular morphology of the primary α grains can be seen to complement their structure relative to the underlying texture, as the grains appear to be aligned parallel to R2, at 45° to R2 and parallel to R1, respectively. The given micrographs for each of the analysed regions (Figure 6.12 -Figure 6.14) are considered to be representative of the material. However within isolated regions microstructure features were observed that suggest chemical inhomogeneity, with Figure 6.15(a-b). Figure 6.15(a) showing an isolated large secondary α lamellar colony with Figure 6.15(b) displaying the occurrence potential α'' precipitates forming along distinct apparent crystallographic planes within a primary α grain as depicted by the dark plate like features. The occurrence of the α'' precipitate require further analysis to verify their composition, since this morphology is not supported within the literature, which commonly reports α'' precipitates occurring at a much smaller scale (on the nano-scale) to the features shown in Figure 6.15(a). Their morphology is however characteristic of a precipitate, which similarly to the large secondary α lamellar colony is symptomatic of variations in the chemistry around the billet. The regions analysed in Figure 6.15(a-b) are both considered to have experienced a comparable total strain, both being positioned adjacent to the assumed location of the prior rectangular ingot corner. In order to

ensure the billet composition is homogenous, the forging processes drives diffusion of the alloying additions throughout the material via the high amount of total strain. The route by which the strain is applied, the strain path, dictates the final texture. As such, the features shown in Figure 6.15(a-b) suggest that isolated regions are receiving an inadequate amount of total strain to drive chemical homogeneity, which is the purpose of primary processing. However, it is important to consider the production route used for Ti-54M billets, which are produced via an electric beam (EB) single melt route, which utilise a high scrap feedstock. EB melt ingots can be considered to be comparatively small, compared to conventional vacuum arc re-melting (VAR) ingots. Therefore the total strain penetration in an EB melt ingot will be inherently less during cogging and breakdown.

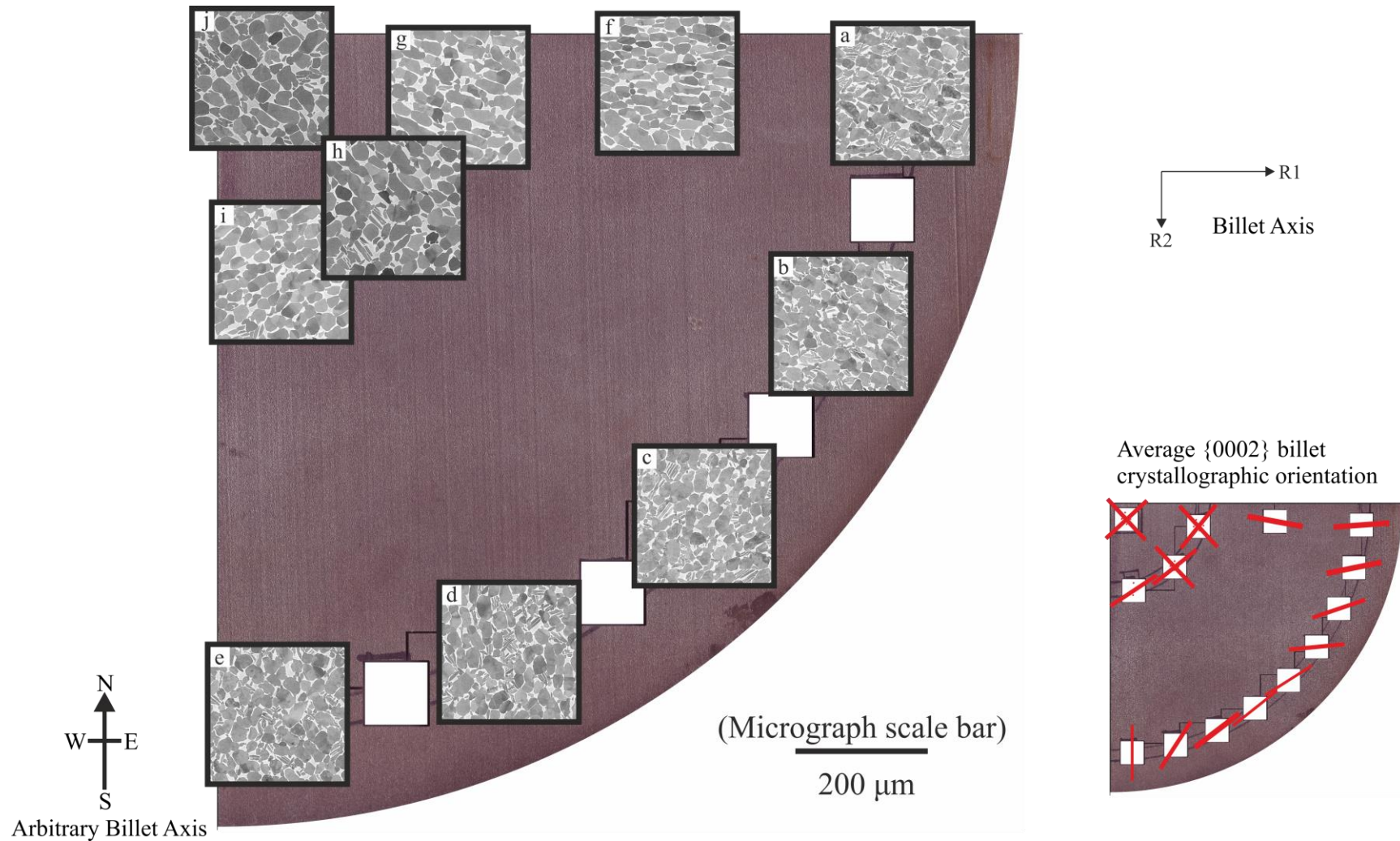


Figure 6.12 Representative backscatter electron micrographs illustrating the microstructure variation across a quarter cross section of a 250 mm \varnothing Ti-54M billet in the as-forged condition. (a-e) illustrate the circumferential microstructure variation taken at 223 mm \varnothing , (f) corresponds to a midpoint parallel to R1 at 150 mm \varnothing , Micrographs (g-i) taken at 75 mm \varnothing , (j) centre. Inset average {0002} crystallographic orientation image to be used as a reference when analysing the microstructure.

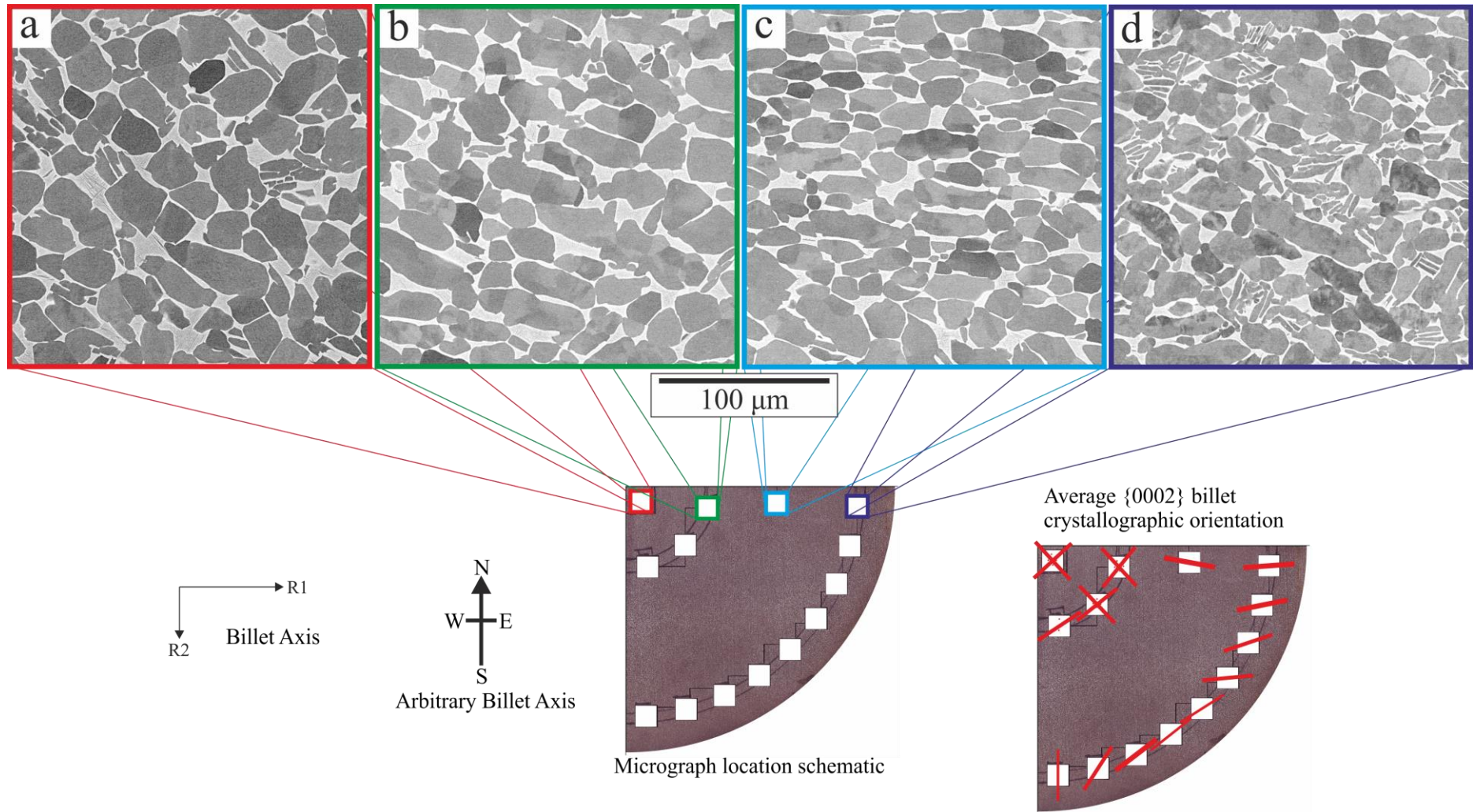


Figure 6.13 Representative backscatter electron micrographs illustrating the microstructure variation within a 250 mm Ø Ti-54M billet in the as-forged condition across the R2 axis.

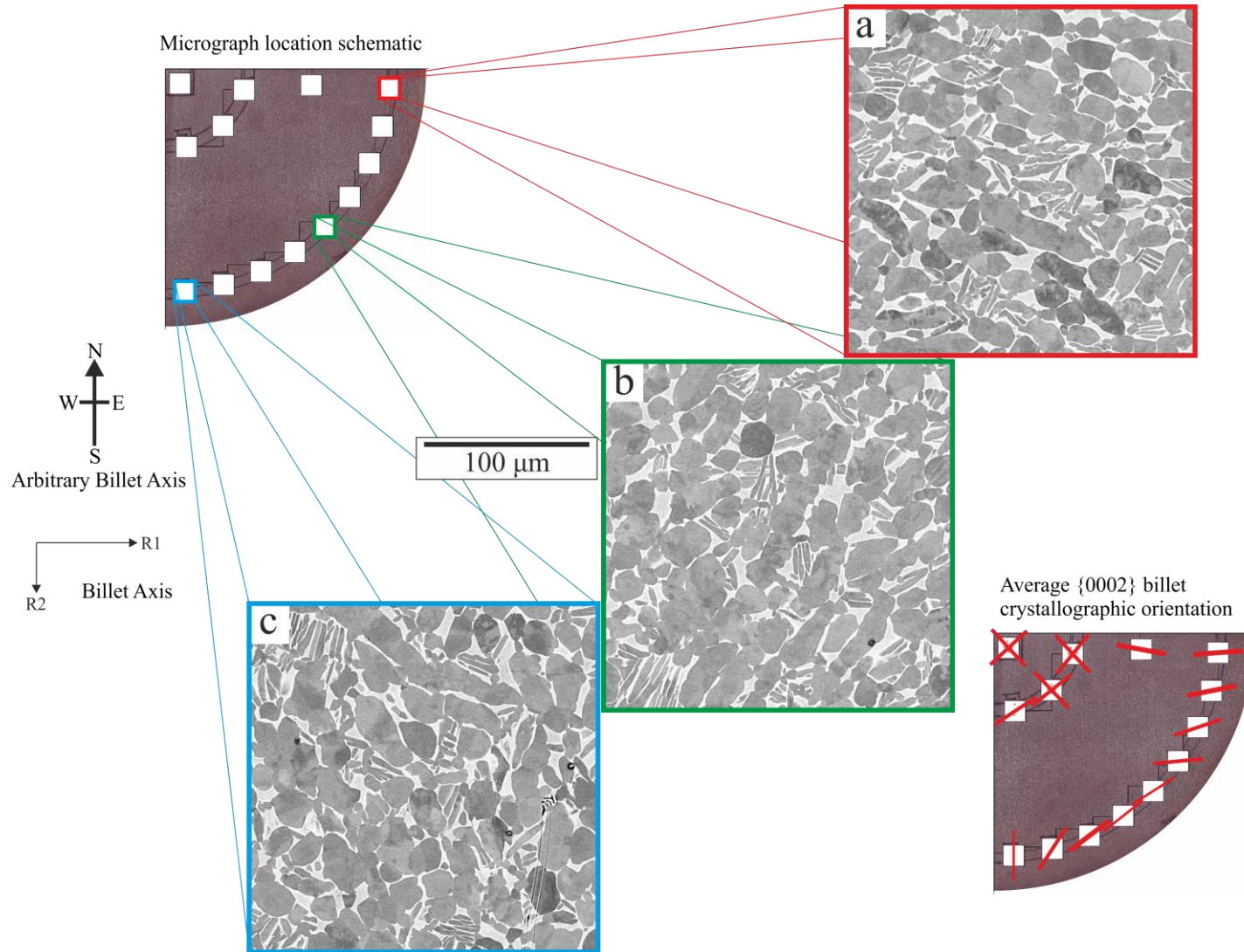


Figure 6.14 Representative backscatter electron micrographs illustrating the microstructure variation within a 250 mm \varnothing Ti-54M billet in the as-forged condition taken; (a) parallel to the R2 axis, (b) at 45° and (c) parallel to the R1 axis.

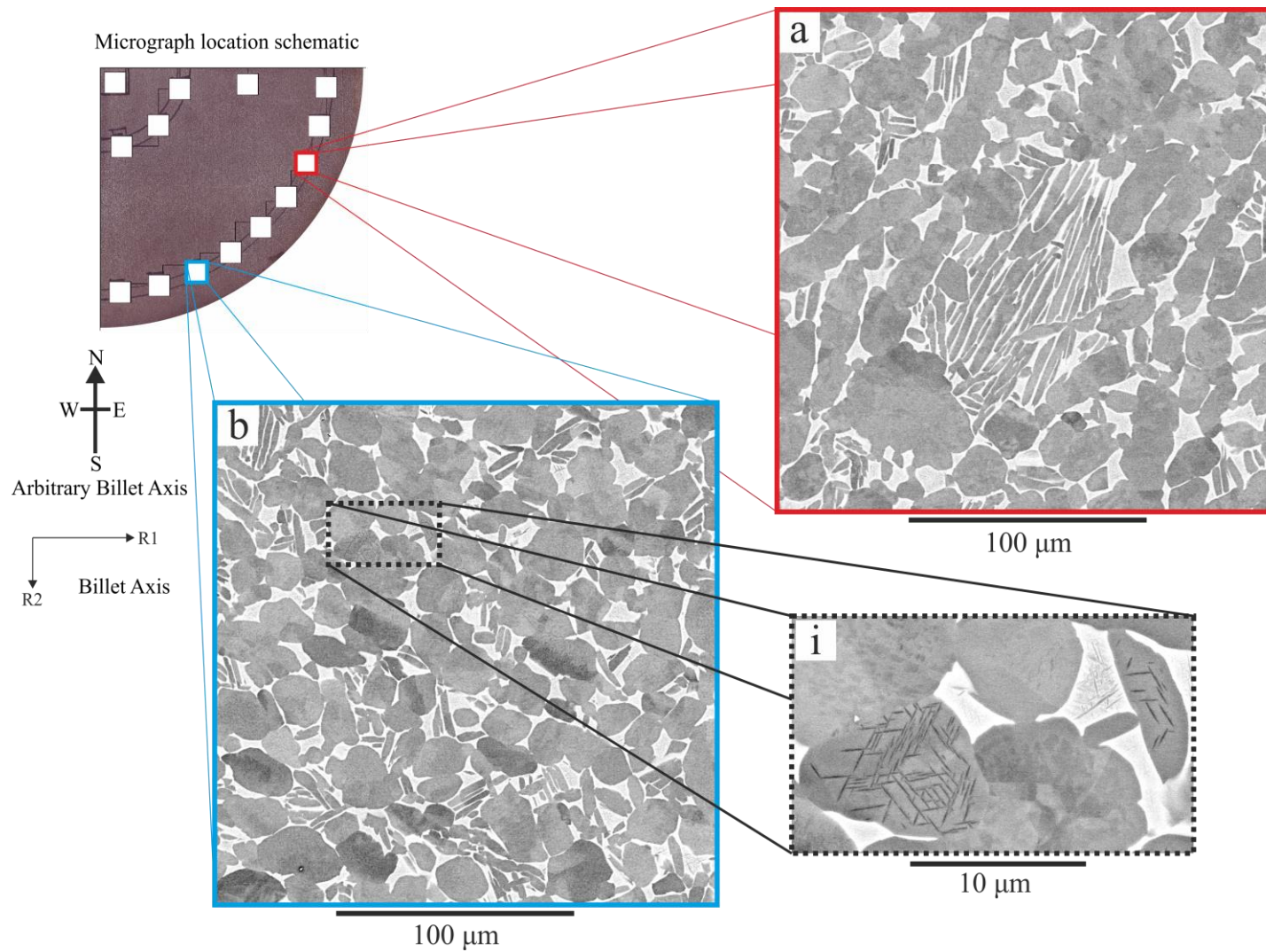


Figure 6.15 Representative backscatter electron micrographs illustrating the microstructure variation within a 250 mm Ø Ti-54M billet in the as-forged condition taken; (a) at 22.5° to the R2 axis and (b) at 67.5° to the R2 axis. With enlarged region (i) illustrating the presence of potential α' precipitates.

6.4 Data handling of orthogonal cutting trials.

The normal, thrust and cutting force feedback signal data (x, y, z respectively) were acquired at 20 kHz. The force feedback response during a typical orthogonal cutting trial is shown in Figure 6.16. During the trials the data output corresponding to force along the x force data was monitored for stability to verify that an orthogonal arrangement was being maintained, since throughout the investigation the x force remained constant it has not been included in any further figure. Data acquisition for raw y and z force data was set to ensure the whole cut is captured, typically within a 20 second period. Using the plotted data shown in Figure 6.16 it is possible to identify the following regions within the cutting cycle;

1. **Start**, zero cut, once data acquisition begins an artefact within the hardware is generated this creates an offset that is usually ± 50 N. This value was logged for each trial and applied to each data set during offline data processing.
2. **Contact**, during the early stages of contact the y force data is observed to rise faster than the z force data, this is a result of an imbalance between the size of contact area ahead of the tool in both the y and z directions respectively. As the tool becomes in contact with the workpiece the increase in y force demonstrates how efficiently the insert is embedding into the workpiece, with the increase in the z forces illustrating the progression from sliding contact to being fully engaged and therefore cutting.
3. **Steady state**, following contact the forces begin to rise to a level corresponding to the cutting process reaching a point of steady state after 2-5 initial revolutions. During this period the forces are susceptible to change as a result of changes in the tool edge geometry, either through wear or the formation of a built up edge.
4. **Finish**, once the tool is retracted from the workpiece force returns to zero.

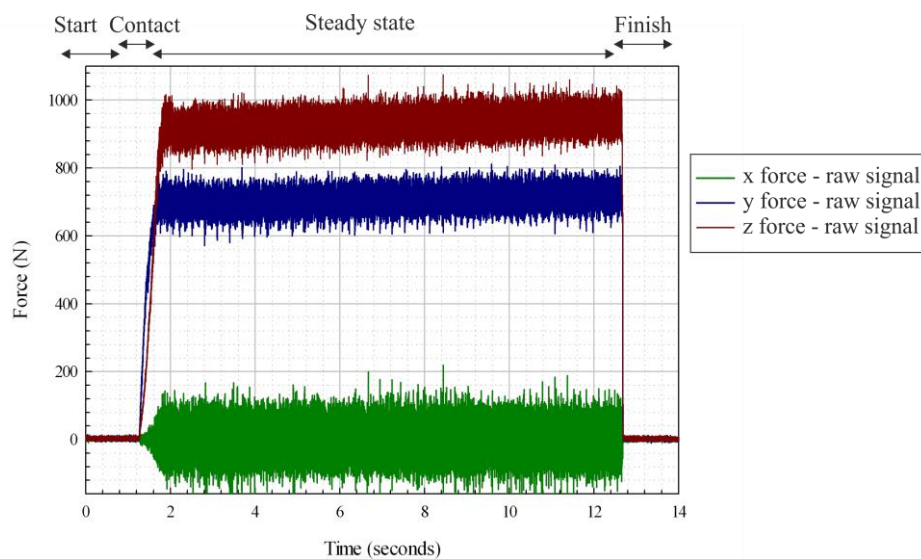


Figure 6.16 Resulting cutting force data along the x, y and z planes, the acquired data monitors a complete cutting cycle with the corresponding cutting regions identified; start, contact, steady state and finish.

6.4.1 Machining force response during variable feed orthogonal cutting trials

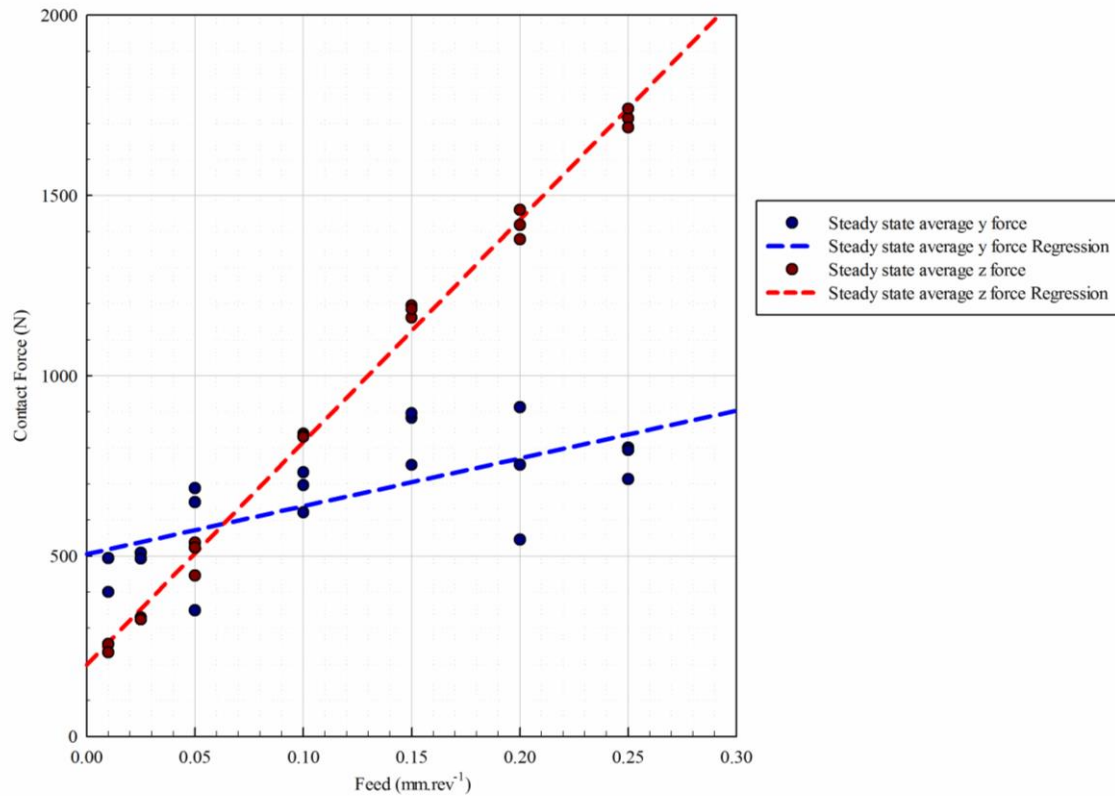


Figure 6.17 Compiled steady state thrust (y) and cutting (z) force data for each feed rate analysed, with additional regression line for each dataset.

The relationship between the resultant forces and the machining feed rate have been commonly used as a measure of a material's machining performance, with researchers adopting the Oxley model, which can be used to gain cutting force coefficients (CFCs) by isolating the gradient and the y-intercept value of each plot. Orthogonal feed rate variable cutting trials were undertaken on the Ti-54M as-forged billet. The data points presented in Figure 6.17 show each result from a series of three repeat trials for each individual feed rate, with the recorded data captured along the feed direction (y) and the cutting direction (z) the corresponding force data was obtained during the steady state region of each trial. When machining, the most significant factor in governing how much force is required to generate a chip, and thus remove material, is the amount of force required to create a shear band. The plots shown illustrate the typical force relationship with increasing feed rate that is commonly reported in the literature [126], whereby as the feed rate is increased, the resulting y and z forces increase proportionally. When machining at low feed rates, by virtue of the small interaction volume of material with the tool the resultant forces remain low, with the z cutting force values remaining lower than that of the y thrust forces. As the feed rate increases, the volume of material ahead of the tool also increases, resulting in a rapid rise in z cutting force

values, with the resulting gradient of the z cutting forces being closely related to the materials shear strength [125]. At low feed rates, the initial y thrust force is higher than that of the z cutting force, but as the feed rate is increased, the proportional increase of force rises at a steadier rate. Each trial was undertaken using a new cutting edge with all parameters (except for feed rate) remaining constant. However as illustrated in Figure 6.17, the resulting average y thrust force data displays significantly more variability than the z cutting force data. As will be discussed in greater detail throughout the remainder of this chapter, the cutting force data shows significant sensitivities to changes in localised microstructure and cutting edge preparation, with y thrust force data displaying a higher sensitivity than that of the z cutting force data.

6.4.2 The size effect

The series of plots presented in Figure 6.18 were calculated using the standard Merchant empirical machining formulae (Equations 6.1- 6.5) and show the relationship between the feed rate (t_1) and the following material properties; the effective coefficient of friction (μ) (Figure 6.18(a)), the thrust and cutting specific cutting energy (F'_y, F'_z) (Figure 6.18(b)) and the shear stress of the material (τ) (Figure 6.18(c)). Due to the induced feed and cutting forces having high initial values when machining at small feeds, as illustrated in Figure 6.17, when applying the Merchant empirical machining formulae this results in a non-linear relationship of μ, F'_y, F'_z and τ . This phenomenon has been commonly reported [130] and as discussed in the literature review §2.7 authors refer to this paradox simply as being a size effect, whereby at small interaction volumes the material properties appear to change significantly. Figure 6.18(a) demonstrates that as t_1 is increased the effective friction reduces, with significant losses with each increment of uncut chip thickness. Such observations have been attributed to an increase in thermal softening of the workpiece material with increased feed rates. The plots presented in Figure 6.18(b) are commonly used to support the claim that a reduced uncut chip thickness results in a claimed reduction in the number of potential failure initiation sites. Thus for small interaction volumes one sees an effective increase in the material's apparent strength [130]. As a result of the induced thrust force has a significantly higher initial value than that of the cutting forces, when calculating the effective shear stress of the material (τ) the material appears to undergo a severe amount of softening, which as shown in Figure 6.18(c) results in a calculated negative shear strength at small feed rates. The data presented in Figure 6.18(c) demonstrates how the size effect must be a gross misinterpretation of the resulting force data, since a negative shear strength of such magnitude cannot be explained rationally. As a result of other machining trials that have been undertaken in the literature commonly using feed rates $> 0.1 \text{ mm.rev}^{-1}$, the author has not noted such a behaviour being previously reported.

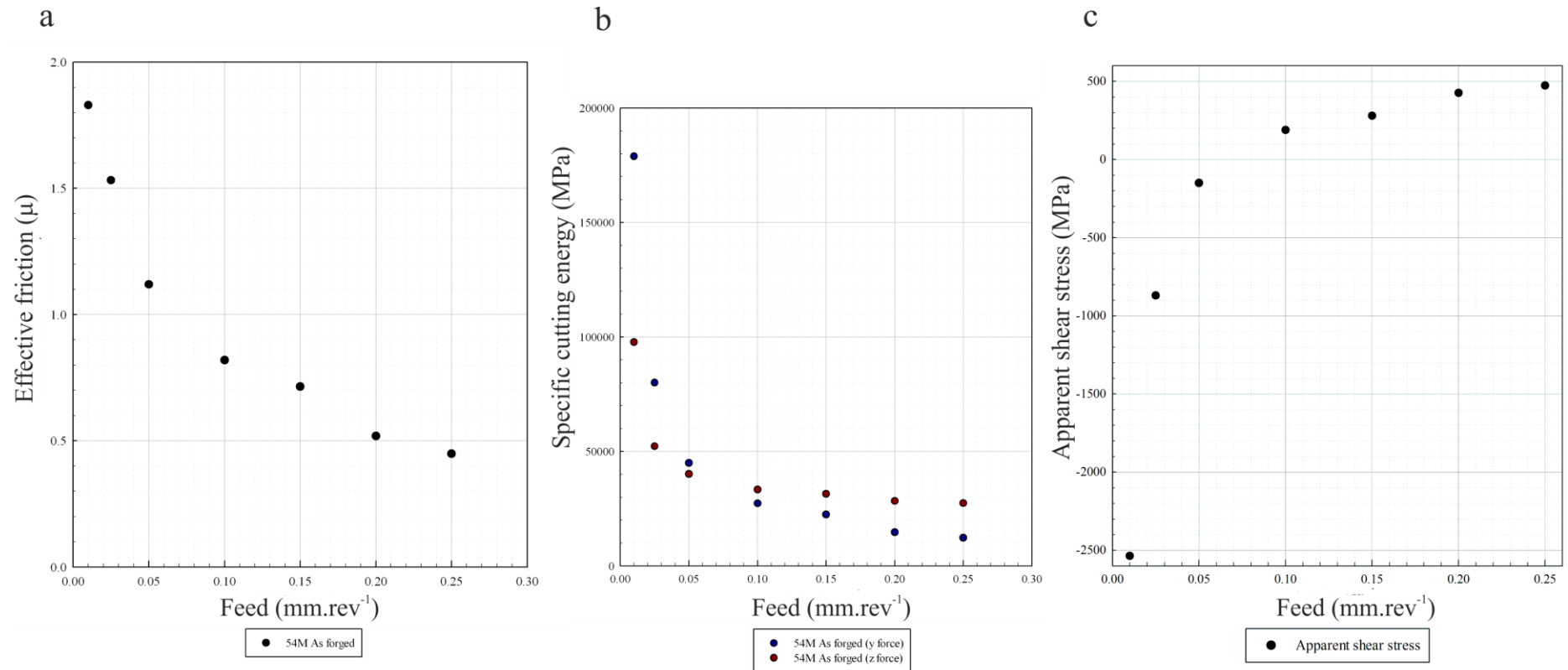


Figure 6.18 A series of plots demonstrating the typical ‘size effect’ for the (a) coefficient of friction (μ), (b) specific cutting energy (F'_y , F'_z) and (c) apparent shear stress of the material (τ) in relation to the applied feed rate

6.4.3 Cutting force analysis and tool engagement behaviour

Prior to each trial being undertaken the workpiece was refaced, thus ensuring each trial started under comparable conditions. The facing operation created in a planar finish to the prepared ring. As a result of this, once the tool had become in contact and progressed into the workpiece, the forces experienced by the tool are analogous to orthogonal cutting with an increasing feed, as illustrated in Figure 6.19. For example, if the tool has a feed rate of $0.25 \text{ mm}\cdot\text{rev}^{-1}$ after half a revolution, the effective feed of the tool will be $0.125 \text{ mm}\cdot\text{rev}^{-1}$ and the resulting forces at that point will be representative of such a feed rate.

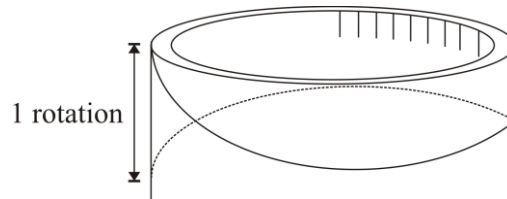


Figure 6.19 Schematic illustrating the resulting tool path into the workpiece during a single rotation, assuming the billet has been faced prior to machining resulting in a planar finish.

In order to reveal a smooth signal trace, as shown in Figure 6.20, a 15Hz Fourier transform low band pass filter was applied to each data set. It was determined through a series of preliminary trials that the 15Hz Fourier transform low band pass filter removed all high frequency noise without effecting the underlying signal trace, which will be discussed in §6.5 and is caused by localised variation in the billets elastic modulus.

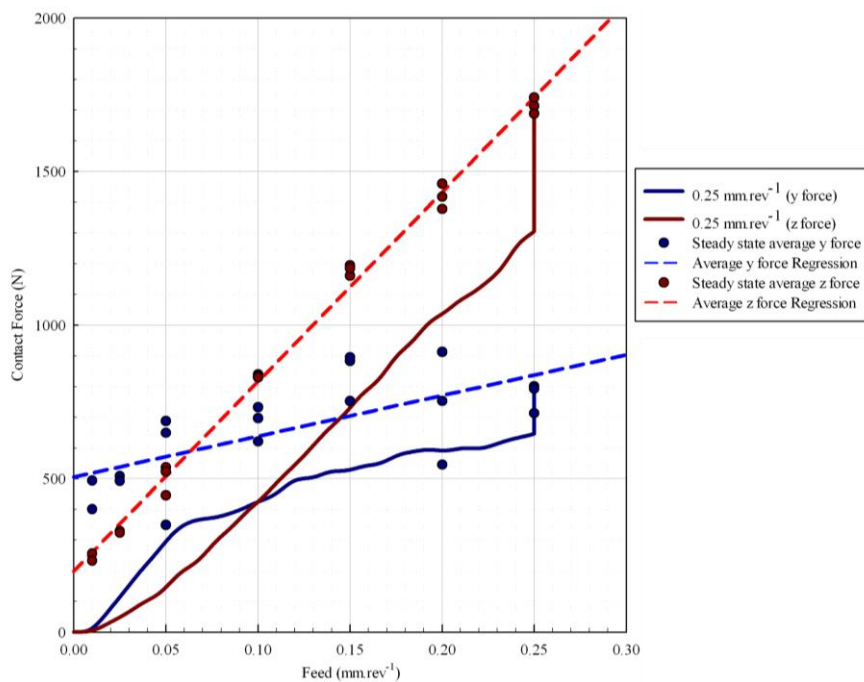


Figure 6.20 Compiled steady state thrust (y) and cutting (z) force data for each feed rate analysed, with additional regression line for each dataset. Superimposed onto the plot, the $0.25 \text{ mm}\cdot\text{rev}^{-1}$ initial contact data with its position and thus effective feed equalling the tools corresponding displacement.

The non-linear size effect relationships as previously shown in Figure 6.18(a-c) are the result of a common assumption that there is no transitional period between the tool being brought into contact with the workpiece and it becoming fully embedded when cutting within a steady state condition. The signal data presented in Figure 6.21 illustrates this transitional period, with the forces steadily rising to a point, after which the cutting dynamics change and the forces rise proportionally with the effective feed rate. To investigate the nature of this transitional point, the data obtained during the variable feed rate trials was analysed further; the plots presented in Figure 6.21 illustrate the amount of feed displacement required to achieve a steady state cut for each feed rate investigated. For feed rates $> 0.05 \text{ mm.rev}^{-1}$ both the y and z force plots follow approximately the same path with the initial gradient change at $\sim 0.06 \text{ mm}$, relative to the point at which the forces began to rise, followed by the steeper rise in force to the point where the cut reaches a steady state condition. For the feed rates $< 0.05 \text{ mm.rev}^{-1}$ the inflection point cannot be observed, this is the result of material being removed via smearing which slows the tool becoming fully embedded into the workpiece.

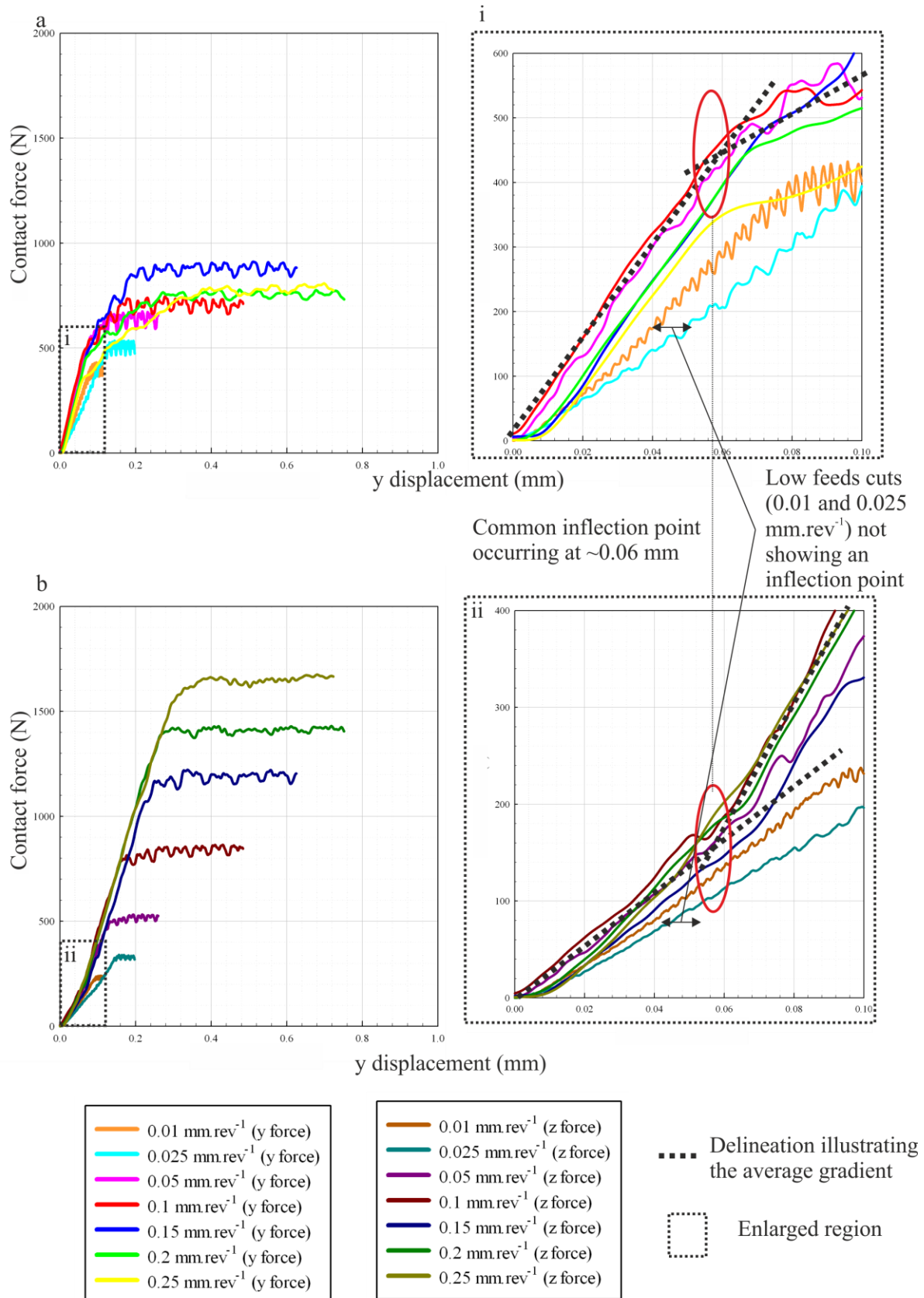


Figure 6.21 Compiled initial contact data for each machining trial with the resulting forces plotted in relation to the total displacement of the tool into the workpiece. (a) Thrust forces and (b) cutting forces, Enlarged regions (i) and (ii) illustrate the common inflection point occurring at ~0.06 mm.

After offsetting the filtered signal data by 0.06 mm and continuing the calculated effective feed from the point of inflection, the plots shown in Figure 6.22 show how the signal data can be brought into alignment with the compiled average values with an undisputable resemblance. With the corresponding total force at the inflection point being attributed to the amount of force that is required to fully embed the tool total and is referred to as the ploughing force contribution of both the y and z components of force. The z force signal data lines traces are comparable to that of the regression line, with a small amount of drift near the end of the cut. The y data does however show a larger initial y-intercept offset in comparison to the compiled average data regression line, but does have a comparable gradient.

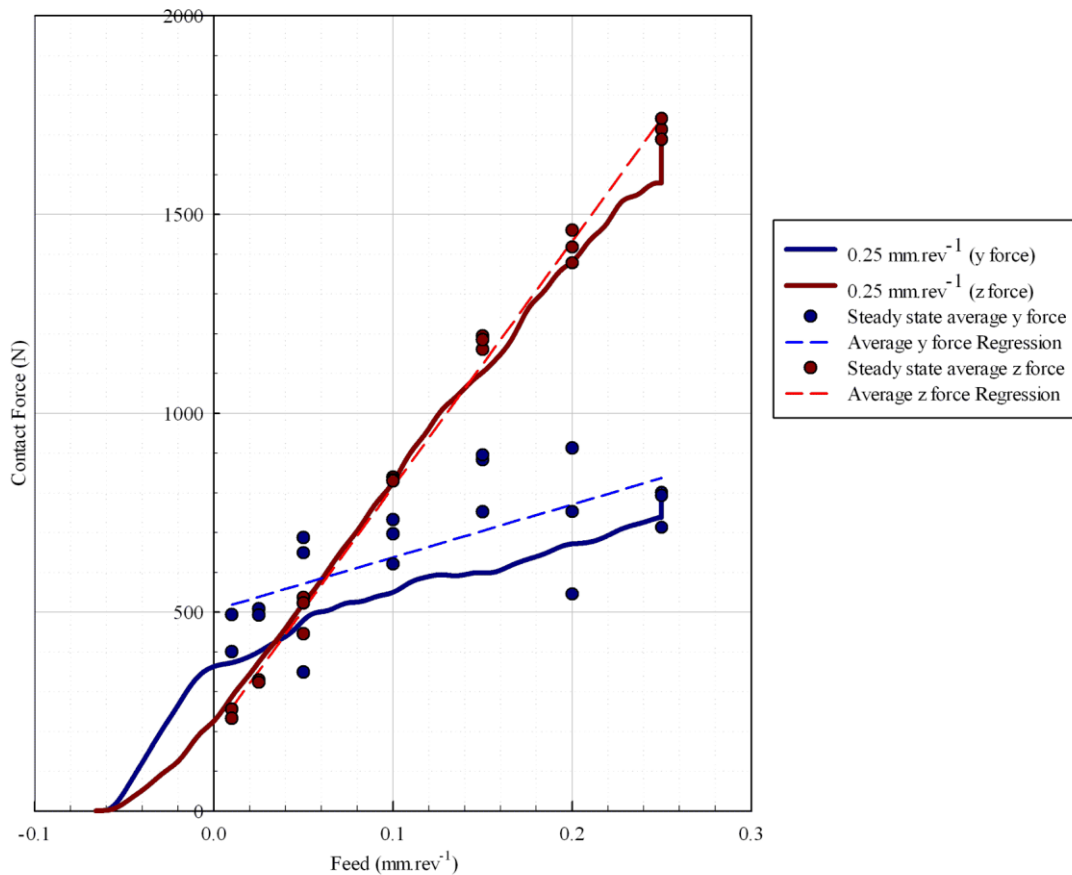


Figure 6.22 Compiled steady state thrust (y) and cutting (z) force data for each feed rate analysed, with additional regression line for each dataset. Superimposed onto the plot, the 0.25 mm.rev⁻¹ initial contact data with its position taking into account the initial offset of ~0.06 mm, following this offset the effective feed equals that of the tools corresponding displacement.

The author has attributed the total offset of ~0.06 mm to the following two main contributing factors that are illustrated in Figure 6.23. Every attempt was made to ensure the tool approaches the prepared workpiece parallel, thus ensuring the cut remains representative of an orthogonal cut throughout. However during the trials, the swarf showed evidence of the

tool not approaching the workpiece in a parallel manner, with the initial portions of removed material showing a thick to thin morphology; indicative of the tool approaching the workpiece at an angle, as illustrated in the schematic shown in Figure 6.23(b). This initial tool offset has been attributed to account for $\sim 40 \mu\text{m}$ of the total amount of tool displacement required before the tool has fully engaged. In addition to this initial offset as a result of the cutting edge not being infinitely sharp the size of the edge radius has to also be considered. For the cutting inserts used throughout this investigation, the edge radius can be within the range of $20 - 30 \mu\text{m}$. Before the tool has become fully embedded during the initial contact period the effective uncut chip thickness is less than that of the edge radius, which as discussed in §2.7, the tool adopts an affective negative rake angle resulting in the material being smeared across the workpiece's surface. It is therefore necessary to overcome the edge radius by progressing the tool into workpiece a further $20 - 30 \mu\text{m}$. The culmination of these two factors results in a tool contact transitional period. It is important to note that during this period material will still be being removed, thus at the inflection point which is brought into alignment as being an effective zero for the orthogonal cutting arrangement, this is the point at which tool has now become fully engaged.

Commonality is observed for the feed rate data presented in Figure 6.24, with each feed rate plot tracing similar paths when the signal data sets have been offset by 0.06 mm . The z cutting force data shows the most consistency with the y thrust force data showing a larger amount of most scatter. Analysis of the y force signals show how the scatter appears to be generated by the initial y intercept value, since following the inflection point the plots follow comparable gradients. The author suggests that the intercept values, which correspond to the ploughing force contribution of the cut, are dictated by machining influences such as tool sharpness. The total ploughing force can therefore be considered to be a measure of how efficiently the tool has become embedded into the workpiece, with blunt tools requiring a significantly larger force to be applied. In addition, Arsecularatne [133] highlighted how the ploughing force can be almost eliminated when cutting with a tool that has an edge radius less than that of the uncut chip thickness. The gradient however for both the y and z forces have been attributed to be more directly related to the material shear strength and therefore independent of variable machining and tooling parameters (for speeds $>40 \text{ m}\cdot\text{min}^{-1}$ as will be discussed in §6.4.4).

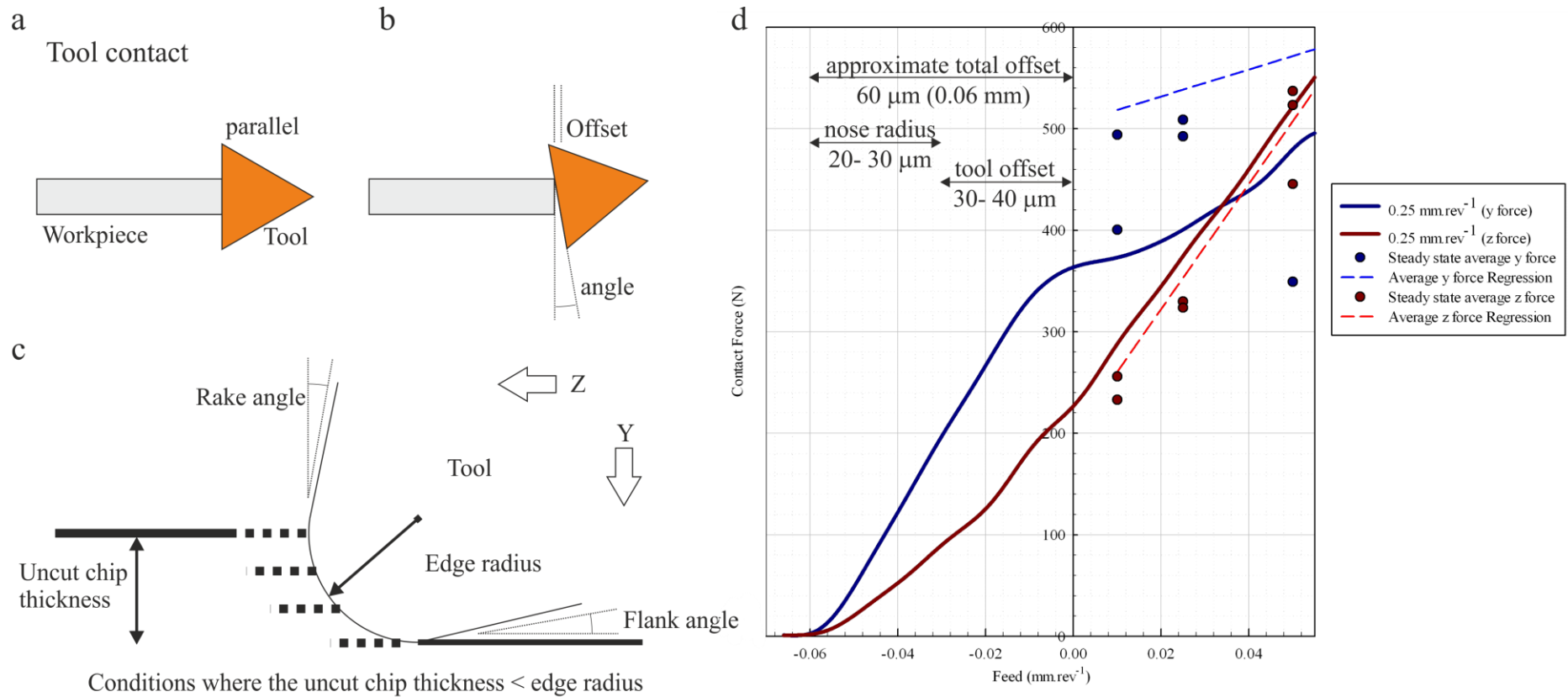


Figure 6.23 Composite images illustrating the proposed root causes of the data offset. (a) Assumed ideal contact scenario with the tool approaching the workpiece in parallel, (b) non parallel contact, thus resulting in an offset. (c) Role of edge radius of the cutting edge in relation to the uncut chip thickness (equal to feed rate during orthogonal cutting) (d) force data plot illustrating how the culmination of the edge radius and the tool approaching the workpiece at an angle results in a total offset of ~0.06 mm.

The plots in Figure 6.24 show the y and z signal data obtained during the 0.2 mm.rev⁻¹ trial closely replicating their corresponding compiled average regression lines; as a result of this the 0.2 mm.rev⁻¹ filtered signal data will be used for all proceeding calculations.

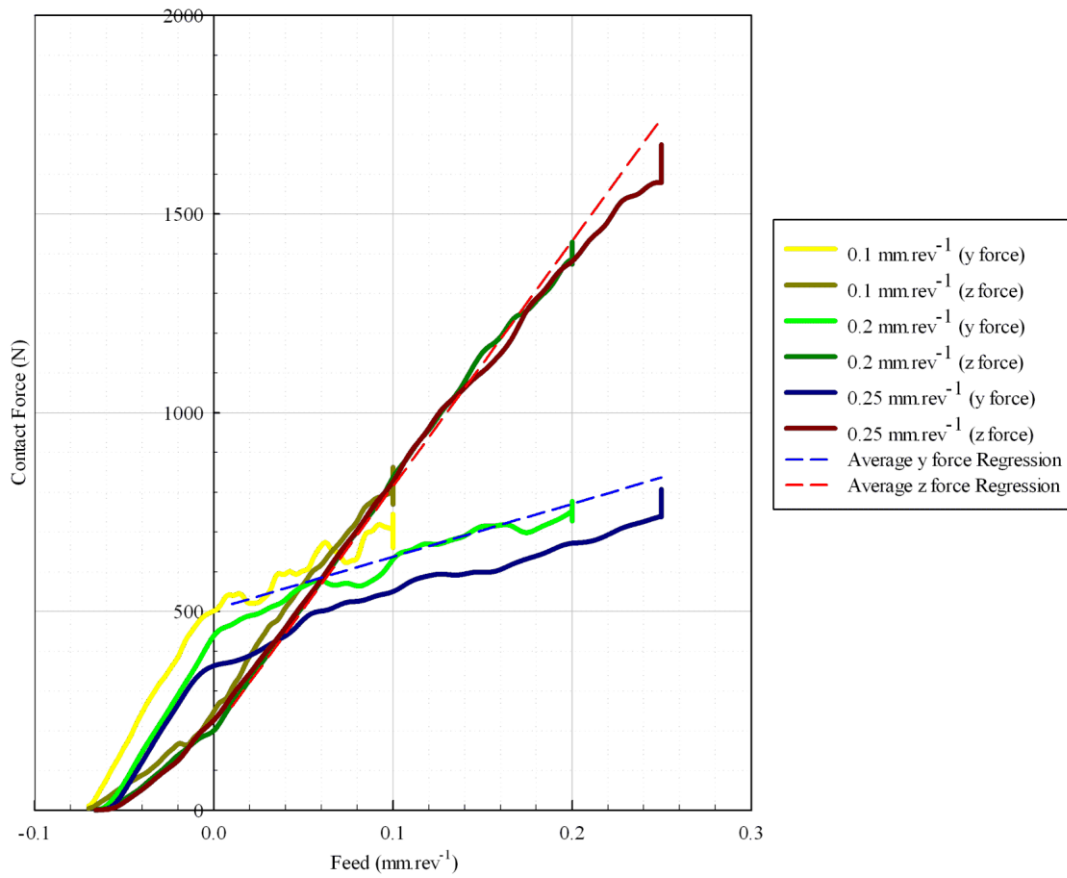


Figure 6.24 Compiled initial contact data for each machining trial with the resulting forces plotted following the removal of the initial offset, the thrust and cutting data plots have been determined using an effective feed rate calculated in relation to the tools displacement into the workpiece. The calculated regression line acquired during the steady state trials has also been included as a reference.

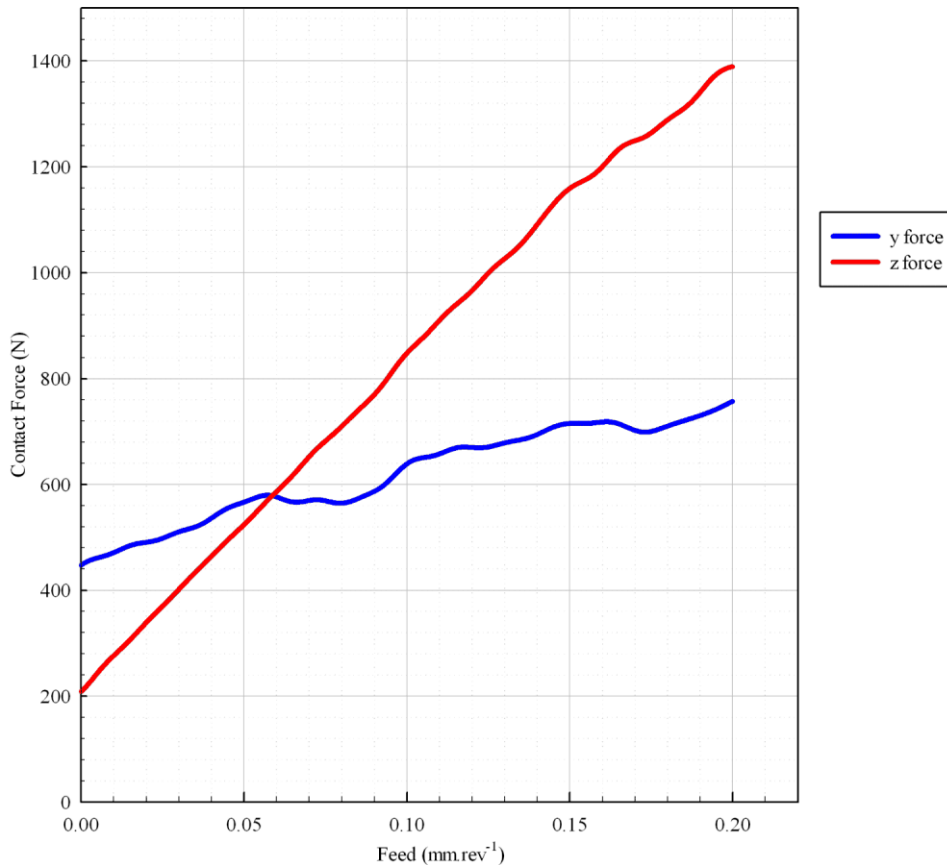


Figure 6.25 Typical resulting thrust (y) and cutting (z) force relationship with respect to feed rate acquired using a non-compiled individual 0.2 mm.rev^{-1} initial data following the removal of the offset data.

The plot shown in Figure 6.25 uses the isolated 0.2 mm.rev^{-1} 15 Hz Fourier transform filtered signal data that has been obtained following a single machining trial. To correlate the signal data with its effective feed rate, the inflection point was determined and brought into line with the y-axis, thus determining the y-intercept values as the thrust and cutting ploughing contribution to the total force. Considering the data used has been acquired during a brief contact period, the tool condition can be considered to remain consistent throughout, therefore the author proposes the adoption of such a method to acquire the cutting force response rather than by compiling average steady state data, which is susceptible to signal drift as a result of tool wear. Such a methodology would substantially reduce the total number of trials required to gain the necessary cutting force data and by reducing the potential effects of tool wear this proposed method could be used to compare different material types more effectively and efficiently.

In order to calculate the effective friction, the specific cutting energy and the apparent shear stress of the material, it is necessary to remove the ploughing force from the total cutting force as per the adapted [143] Merchant empirical machining formulae (Equations 6.6- 6.10). Figure 6.26 illustrates the size of the corresponding ploughing force that is required to fully embed the tool into the workpiece and offers no further contribution to the chip removal process. Here it has been calculated for this trial to be ~420 N and ~200 N for the thrust (y) and cutting (z) cutting forces respectively.

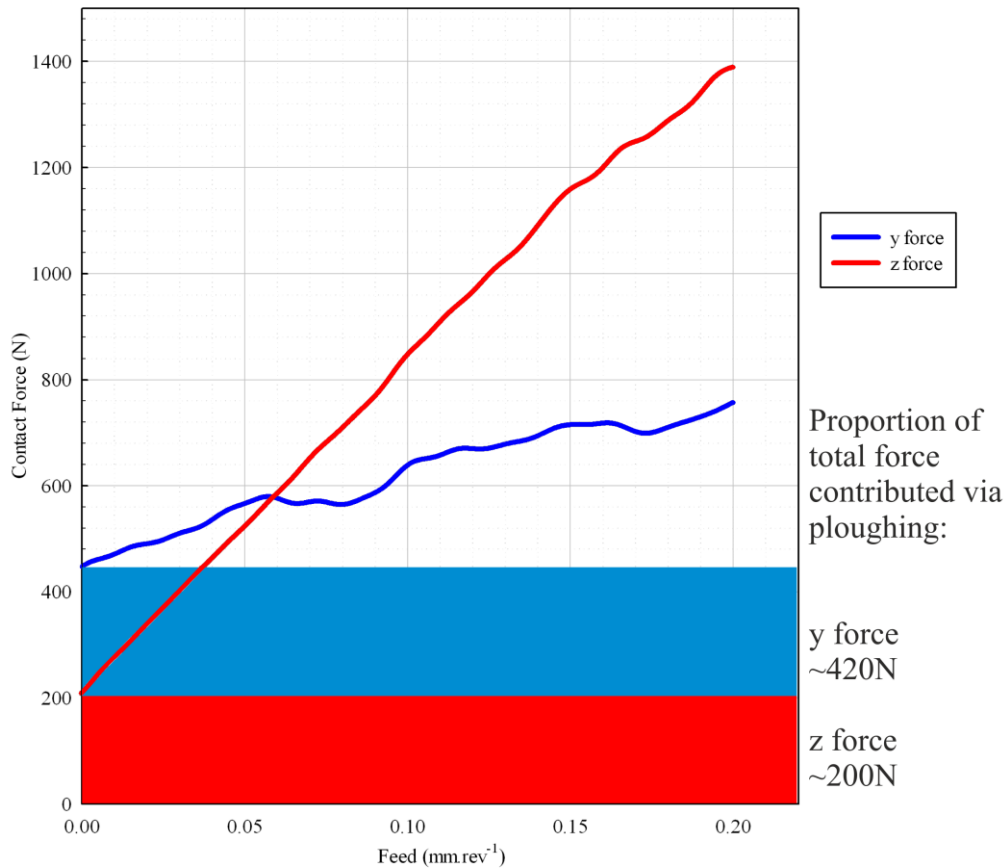


Figure 6.26 Illustrates the proportion of the total force for both the thrust (y) and cutting (z) that is accounted for by the initial ploughing forces, which remain constant throughout and offer no further contribution to the chip removal process.

Following the removal of the ploughing forces from the y and z signal, the resulting data has been re-plot in Figure 6.27, such that both signals intersect approximately at the origin (note there is a ± 0.05 N accuracy when removing the ploughing force).

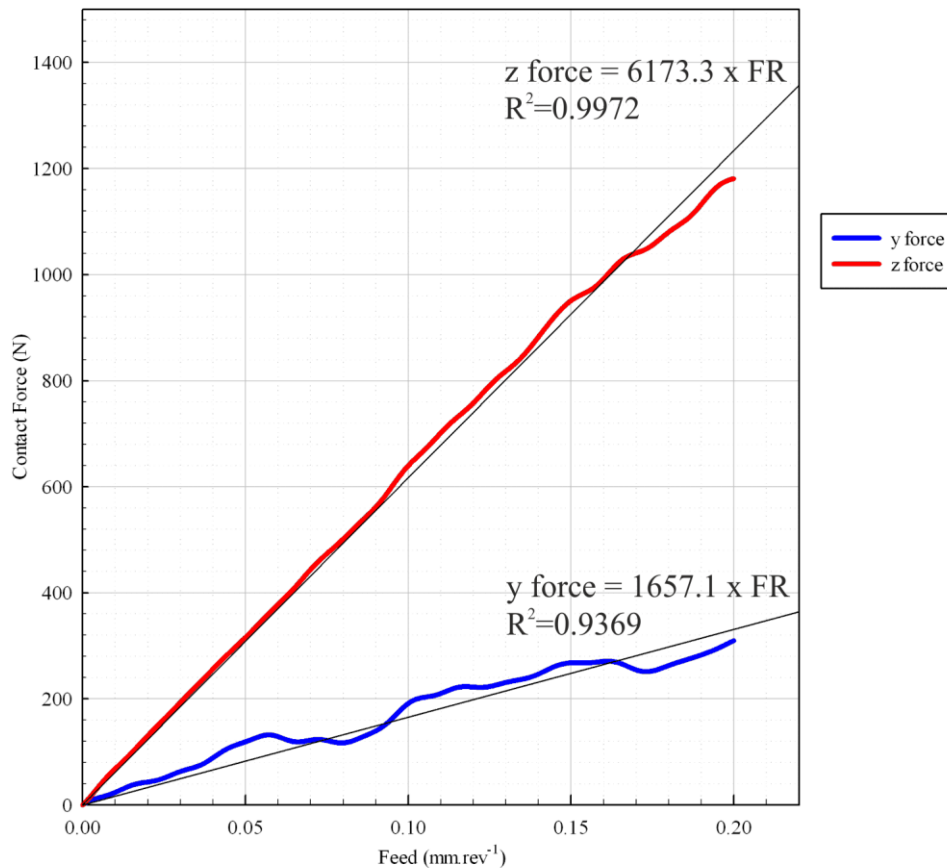


Figure 6.27 Resulting thrust (y) and cutting (z) force relationship with respect to feed rate acquired using a non-compiled individual $0.2 \text{ mm}\cdot\text{rev}^{-1}$ cutting trial following the removal of the ploughing forces each dataset pass through the origin. The gradient has been determined using a linear fit regression relationship for both the thrust and cutting forces, with the corresponding R^2 value.

After the removal of the ploughing forces, for the resulting plots given in Figure 6.27 the gradient of both of the signals of both the y and z data remains proportional with the feed rate. Through the application of a regression, the gradient of both the thrust (y) and cutting (z) data was determined, as given in Equation 6.14 and Equation 6.15 respectively (where FR = feed rate). The coefficient of determination (R^2) for each dataset illustrates the minimal amount of spread amongst the filtered signal data relative to the regression line, with given values of 0.9369 and 0.9972 for the y and z force respectively (where $R^2 = 1$ would represent a perfect match).

Thrust force $y \text{ force} = 1657.1 \times \text{FR}$ Equation 6.14

Cutting force $z \text{ force} = 6173.3 \times \text{FR}$ Equation 6.15

The plots presented in (Figure 6.28 -Figure 6.30 show how following the identification and subsequent removal of the ploughing forces from the acquired data, size effect phenomena can be eliminated when calculating the effective friction, specific cutting energy (SPE) and apparent shear stress of the material. For the filtered signal data presented, as a result of the dataset not initially intersecting precisely through the origin (Figure 6.27), for feed rates $< 0.01 \text{ mm.rev}^{-1}$ the rapid increase/ decrease in the should not be considered. However after the effective feed rate is increased $> 0.01 \text{ mm.rev}^{-1}$ the calculated data becomes representative. Further fluctuations within the filtered signal data are generated as the result of microstructure variation around the circumference of the billet and illustrate the dependency of the cutting performance on the underlying material, as will be discussed in greater detail in §6.5. Alongside the filtered signal data a signal average line has been included that has been compiled using the whole of signal dataset as well as a regression line average that has been calculated using the relationship given in Figure 6.27. In each case the data presented for the effective friction, SPE and apparent shear stress of the material show equivalent results using either the filtered signal data, signal average or regression average approaches.

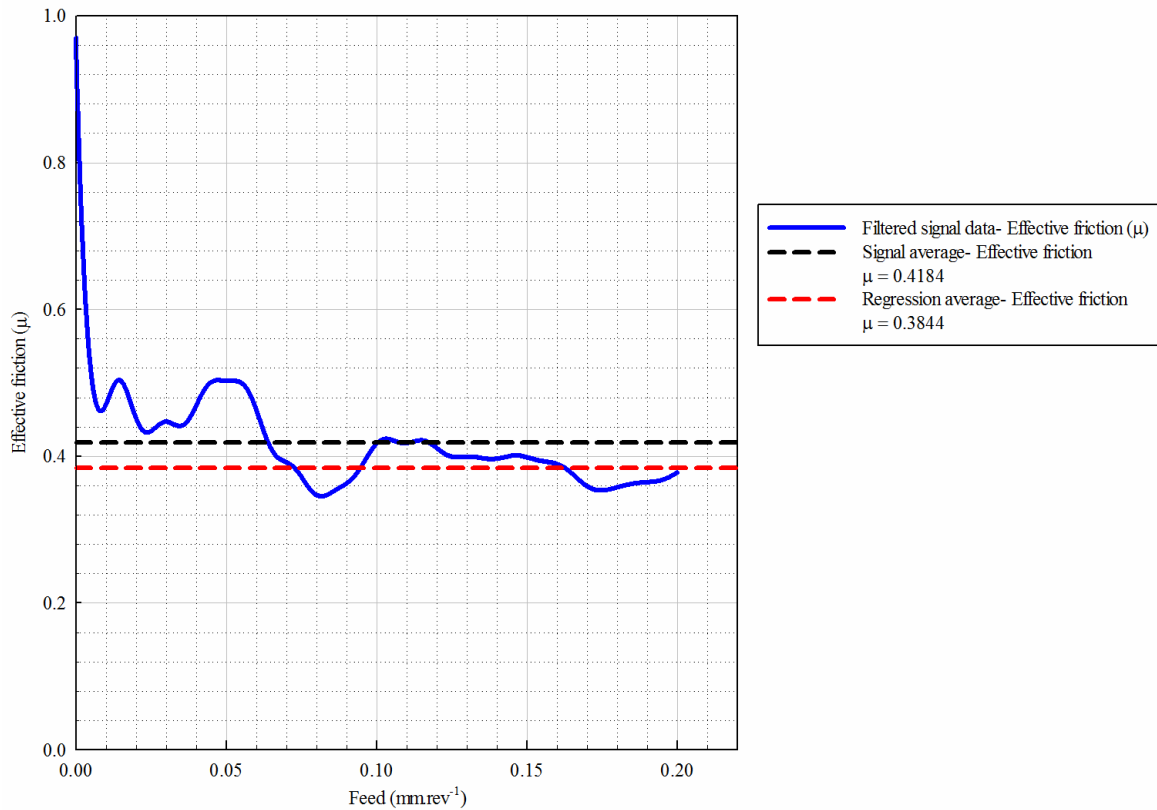


Figure 6.28 Resulting effective friction of the cutting environment as determined using the single cut initial contact filtered 15 Hz signal data (solid line), black dashed line denoting the filtered signal compiled average and the red dashed line representing resulting effective friction as calculated using the linear fit regression relationship.

The data presented in Figure 6.28 show the calculated effective coefficient of friction (μ), across the range of effective feed rates. The signal average has been calculated to be $\mu = 0.4184$ and the regression average is $\mu = 0.3844$. Such values are indicative of titanium during sliding contact as demonstrated by Budinski [203] during a series of abrasion resistance trials for Ti-64 and CP titanium. Budinski [203] showed that for $\mu = 0.35 - 0.53$ sliding contact was observed however material transfer and galling was also recorded. It is therefore expected that under the machining conditions used during this study if machining were to be carried out over a prolonged period of time, tool wear would be expected to become an influencing factor. After the removal of the ploughing forces it has been shown that the coefficient of friction is independent of feed rate, however as demonstrated by the fluctuations in the signal data the coefficient of friction shows a considerable sensitivity to the underlying microstructure.

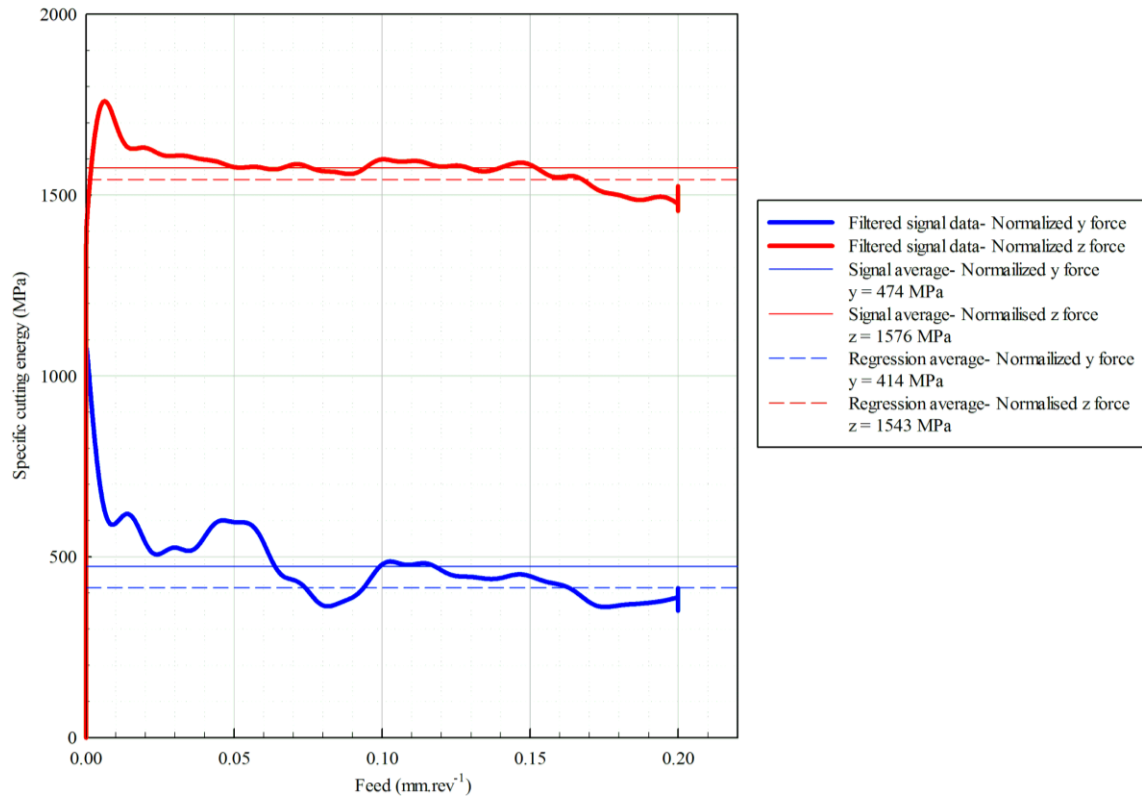


Figure 6.29 The resulting specific cutting energy of the cutting environment for thrust force (y) in blue and the cutting force (z) in red. As determined using the single cut initial contact filtered 15 Hz signal data (thick solid line), thin solid line denoting the filtered signal compiled average and the dashed line representing resulting specific cutting energy as calculated using the linear fit regression relationship.

The SPE relationship shown in Figure 6.29 represents the amount of force applied along the thrust (y) and cutting (z) directions and is calculated by normalising the acquired cutting forces with respect to the tools contact area, thus are representative of machining a chip area of 1 mm^2 of a thickness of 1 mm (k_{c1}). Following the removal of the ploughing forces the relationship given in Figure 6.29 illustrate how the SPE is independent to feed rate and has no size effect dependency. The magnitude of the calculated y and z specific cutting energies are governed by the nature of the system (materials, tooling geometry, cutting parameters etc.); which for this particular cutting arrangement has been shown to have a y thrust force signal average of 474 MPa and a regression average of 414 MPa; the z cutting force signal average of 1576 MPa and a regression average of 1543 MPa. The data presented in Figure 6.29 illustrates how each analysis strategy; signal data, signal average and regression average each show comparable results, with the signal average data showing a slight reduction due to it incorporating the $< 0.01 \text{ mm.rev}^{-1}$ signal data. The filtered y and z signal data demonstrates the sensitivity of the applied loads to the circumferential variation in microstructure. The magnitude of such SPE values are in agreement with the user guidelines detailed by tooling supplier Sandvik that groups all titanium based alloys having a SPE $k_{c1} = 1400 \text{ MPa}$. Note

that this value has only been recalled as a benchmark to compare the magnitude of the SPE, since the method used by Sandvik in determining SPE incorporates the ploughing force contribution [204].

Through the application of the calculated specific cutting energies the average shear strength of the material has been further calculated using the adapted Merchant formulae, here it was assumed that the shear band angle remained constant throughout at 45° , as observed by Gente *et al.*[117] during high speed machining trials of Ti-64. The plots presented in Figure 6.30 show a signal average of 553 MPa and a regression average of 564.5 MPa, with the filtered signal data remaining comparatively stable across the experimental range. The signal variability caused by the circumferential microstructure variation appears less sensitive for the calculated material shear strength due to the calculation incorporating both the y and z components of force, with the highest amount of signal variability observed along the thrust y component.

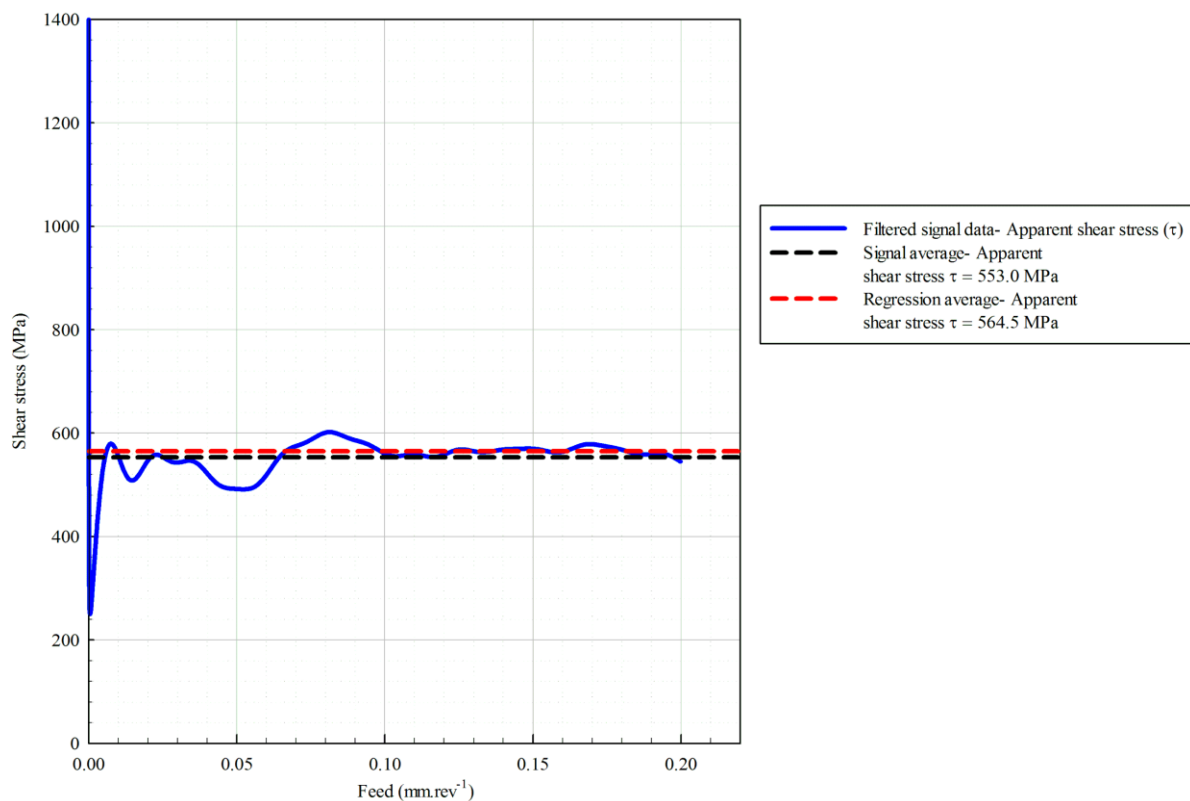


Figure 6.30 Resulting apparent shear stress of the cutting environment as determined using the single cut initial contact filtered 15 Hz signal data (solid blue line), black dashed line denoting the filtered signal compiled average and the red dashed line representing resulting apparent shear stress as calculated using the linear fit regression relationship.

As a first order approximation, the von Mises yield criterion [25] can be used to determine the shear strength of a material using the relationship given in Equation 6.16. The following

methodology has been used as a first order approximation to validate the calculated results present in Figure 6.30 that were obtained using machining acquired data.

$$k = \frac{\sigma_y}{\sqrt{3}} \quad \text{Equation 6.16}$$

The material specification given for the Ti-54M billet as used throughout this investigation had a nominal ultimate tensile strength (UTS) of $\sigma_y = 964$ MPa, therefore the resulting von Mises theoretical shear strength equals $k = 556.6$ MPa. This result falls between those calculated using the signal average and regression average. These findings illustrate how as a method of material characterisation, such a technique that incorporates a lathe can be adopted to benchmark material performance within a machining environment. Such a methodology could also be used to capture material sensitivities when subjected to high strain rates, which is an environment that is inherently very difficult to capture experimentally.

6.4.4 Machining force response during variable speed orthogonal cutting trials

Orthogonal speed variable cutting trials were undertaken on the Ti-54M as-forged billet.

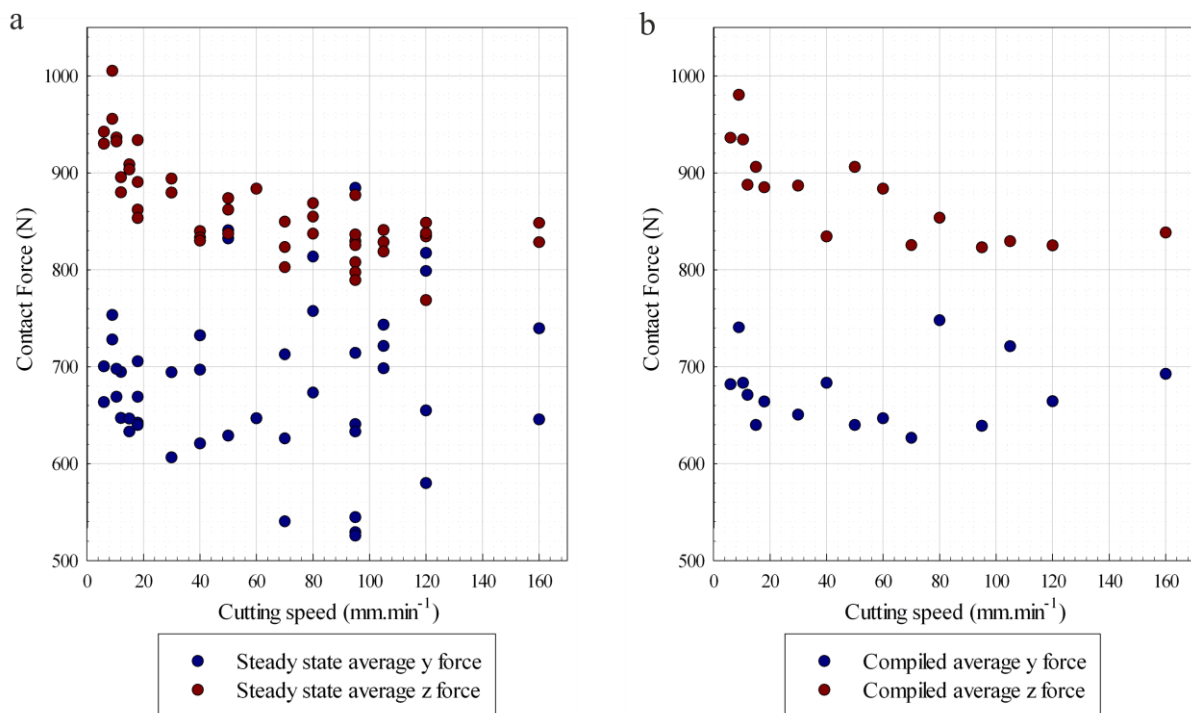


Figure 6.31 Resulting thrust (y) and cutting (z) force relationship with respect to cutting speed obtained during orthogonal cutting trials (a) individual run raw data (b) compiled average data for each individual speed.

The data points presented in Figure 6.31(a) represent the average cutting force recorded along the y and z data channels during the steady state region for each cut. Figure 6.31(b) shows a compiled average for each individual cutting speed. The plots in Figure 6.31 illustrate the typical force relationship with cutting speed that is commonly reported within the literature

[120], [205], whereby as a result of the increase in cutting speed there is a decrease in cutting forces, which reduces to a plateau at speeds above $40 \text{ m}\cdot\text{min}^{-1}$. This reducing force behaviour, which has been attributed to an increase in the shear angle ahead of the tool, can be observed in Figure 6.31(b) through the z force data; that displays a maximum average load that approaches $\sim 1000 \text{ N}$ at $8 \text{ m}\cdot\text{min}^{-1}$ and reduces to an asymptote value of $\sim 820 \text{ N}$ for speeds $>95 \text{ m}\cdot\text{min}^{-1}$. The z force data shows a moderate level of variability, with the greatest amount of scatter, in the order of $\sim 100 \text{ N}$, occurring at $95 \text{ m}\cdot\text{min}^{-1}$. However the occurrence of such scatter does not severely disrupt the easily identifiable reducing trend of applied force with increasing speed. The y force data however demonstrates a significant amount of scatter across all machining speeds. Throughout the speed variable investigation each machining trial was completed using a new cutting edge with all machining parameters remaining constant (with exception of speed). The recorded data was obtained within the steady state region and no other further incidents occurred that could be attributed to the variability in the y force data. As shown previously in Figure 6.26, the y component of ploughing force was determined to be $\sim 420 \text{ N}$ (machined at $40 \text{ m}\cdot\text{min}^{-1}$), which for the compiled average data shown in Figure 6.31(b) accounts for $\sim 63\%$ of the total y force that has an average for all of the speeds of $\sim 670 \text{ N}$. The ploughing force accounts for a threshold of force that is required to be overcome to ensure the tool has become fully embedded into the workpiece. Therefore the size of the ploughing force can be seen to be a measure of how efficiently the tool has initiated machining. Once the tool has become embedded, the ploughing force has been shown not to contribute to the chip removal process; therefore potential variables that could affect how the tool is embedding itself will have a profound effect on the resulting total force. First and foremost, it has been shown that the absolute sharpness of the cutting edge, or edge roundness, has the most influence on the size of the ploughing effect. Arsecularatne *et al.* [133] showed how when cutting with a tool that has an edge radius less than that of the uncut chip thickness, the ploughing force diminishes. The tools used throughout this investigation are pressed and sintered with their cutting edges prepared such that the tolerances used during manufacture result in a potential variation in edge roundness of $10\text{-}40 \mu\text{m}$ [165]. The author is not aware of the relative distribution within the tolerance range nor which radius is the most frequent. Therefore it would be necessary to conduct profile scans of each tool prior to machining in order to confidently track its potential influence. Even though the embedding process is completed over a very short period of time, and the wear and built up edge mechanisms could be considered to be negligible, it would be irresponsible to negate their potential effect since any variation in the tool edge preparation could have a significant influence. Machining at higher speeds is inherently more aggressive on the tool and the raw data presented Figure 6.31(a) suggests that at higher speeds ($>40 \text{ m}\cdot\text{min}^{-1}$) there appears to be more spread. However, the amount of spread does not seem to be proportional to the machining speed. As a result of the multistage cogging process used during the forging of the

billet, the non-linear strain path leads to regional variations in microstructure and crystallographic texture, which have a significant impact on the subsequent cutting forces. The author suggests that at the point at which the tool becomes embedded, the nature of the crystallographic texture within that region could have a further defining impact on the total forces; with ‘softer’ regions of material allowing the tool to become fully embedded with lower total forces. For the purpose of this investigation, it is assumed that there is minimal variation down the axis of the billet, however, during the cogging process the billet undergoes a series of overlapping impacts from the die presses, resulting in slight variations in the underlying microstructure down the axis of the billet [23].

6.5 Orthogonal cutting trials and microstructure correlation

The enlarged signal plots presented in Figure 6.32 show the typical force feedback response of the material as the tool progresses circumferentially around the workpiece. Through the application of a 15 Hz Fourier transform, low band pass filter, the channel data can be “cleaned” to reveal an in-phase repeating cycle within both of the y and z force datasets. The filtered signal plot, given in Figure 6.32, illustrates the presence of a repeating ‘M’ signal pattern within the z force data. Relating the constant time intervals of the repeating signal with the time of the fixed rotational speed of the billet has shown that a pair of ‘M’ signal patterns corresponds to a single revolution of the billet.

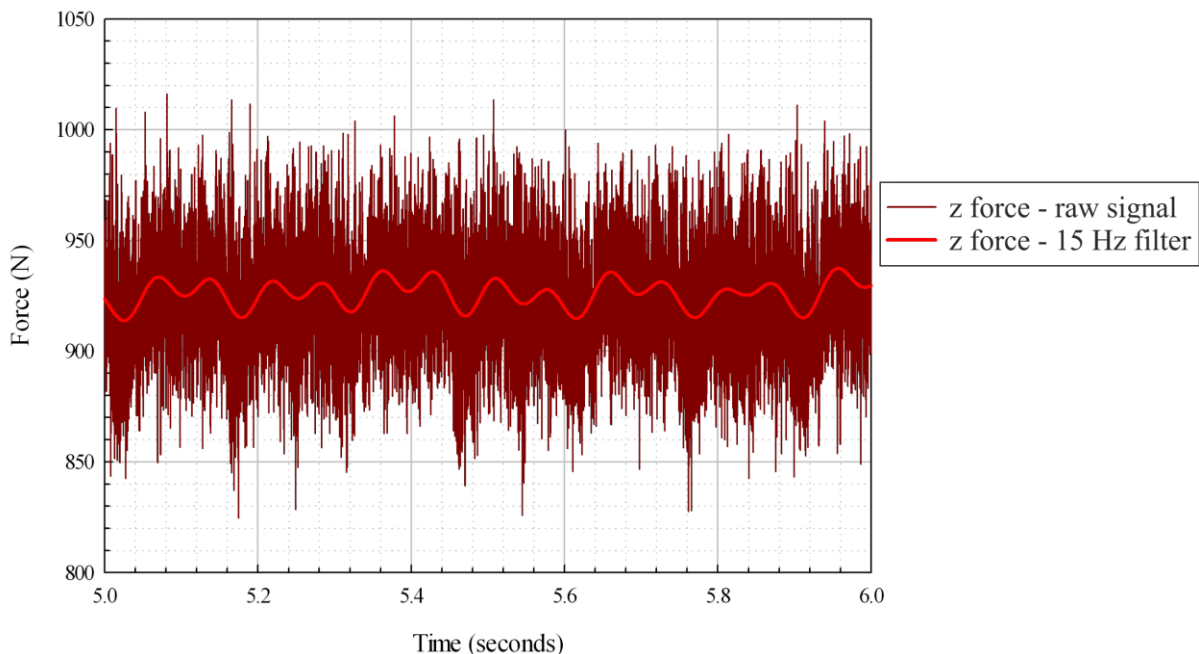


Figure 6.32 Resulting signal cutting (z) force, showing both the raw and 15 Hz Fourier transformed low band pass filtered data.

As demonstrated by Wilson *et al.* [20], the multistage cogging procedure produces strain as high as 2 near the surface decreasing to about 1 in the centre, which has a direct impact on the fraction of globurised α and localised crystallographic texture throughout the cross-section. As a result of this, during a machining operation the machine tool will see significant variation in microstructure over the whole cross section but over local regions of $\sim 10 \text{ mm}^2$ can be considered to have a comparatively homogeneous microstructure. This gives confidence to the fact that any systematic variation in force feedback seen is due to the underlying microstructure and not individual one-off events. The repeating signal shown in Figure 6.32 has been attributed to the microstructure variation around the billet imparted during the forging process. The circumferential variation in the morphology of the billet microstructure has influenced the cutting process, with regions of high and low relative stiffness being identified within the peaks and troughs of the repeating 'M' signal. It is worth noting that under the cutting parameters used throughout this investigation, the sampling rate of 20 kHz is still too low to be able to accurately resolve fluctuations in the force that can be attributed to chip segmentation. To resolve chip segmentation, it is necessary to use lower cutting speeds at larger depth of cuts than have been used during this investigation.

6.5.1 Force data processing

In order to analyse to what extent the underlying microstructure influences the cutting dynamics, prior to the facing operation a radial groove was engraved onto the surface of the workpiece this was in order to provide a reference mark for each revolution. This marker groove manifested itself as a significant spike in the raw recorded force data. The time at which each mark occurred was further recorded in order to isolate the force feedback data for each rotation, thus enabling the correlation of the data with its location on the billet face. The raw data plots shown in Figure 6.33(a-c) demonstrates the result of the tool passing over the notch manifesting itself as a sharp spike on the plot (Figure 6.33(i)). Inevitably the size of the spike reduces with each rotation as the material is removed. However, only one spike is required to serve as a reference marker since the billet's rotational velocity is maintained throughout the test. It is worth noting that throughout the trial the notch spike always appeared at the same point on the curve, providing further evidence that the signal trace is a result of material variation.

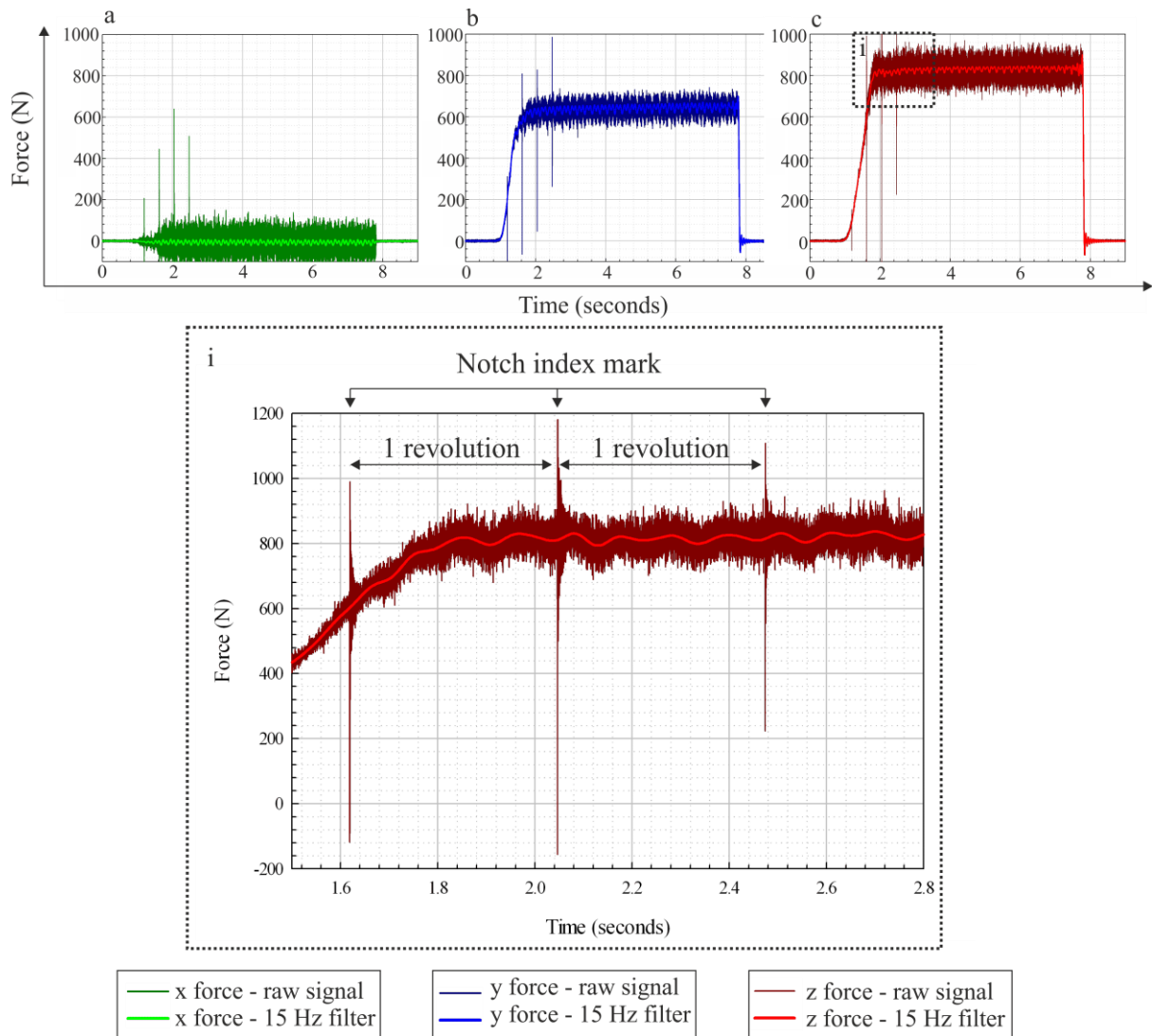


Figure 6.33 Identification of a single rotation using reference notch index mark manifesting as a spike in the resulting fixed (x) thrust (y) cutting (z) force data, a, b and c respectively, included for each forces both the raw and 15 Hz Fourier transformed low band pass filtered data. The enlarged plot i for the z force data illustrates the nature of the index mark.

The signal plots shown in Figure 6.34(a-b) use the 15 Hz Fourier transformed low band pass filtered data from both y and z forces respectively, which have been transposed onto a circle plot. Relating the profile plots to the simulated non-uniform strain distribution (Figure 6.8), the average orientation data (Figure 6.9) and the cross sectional microstructure variation (Figure 6.12) the billet force profile plot can be seen to display a similar appearance with comparable circumferential variation within both the y and z forces. The vertical regions of the billet, parallel to R1, that were shown to have experienced the lowest total strain values have in turn undergone the lowest cutting forces. With the diagonal regions $\pm 45^\circ$ to R1, that have withstood the highest levels of residual strain, display the highest values of cutting force. From the signal plots data shown in Figure 6.33(b-c) and (i), the amplitude between the

peaks and troughs of the 'M' signal remain largely constant at ~80 N for y force and ~ 50 N for z force.

The composite images in Figure 6.34(a-b) show the aligned filtered y and z data circle plots that have been transposed onto the corresponding cross sectional quadrant of the billet with the related basal pole figures included. By superimposing these data fields together, an effective map of the material's modulus during the machining has been created. This allows the user to correlate resultant cutting forces to individual regions across the billet cross section. The regions of highest stiffness, i.e. regions 5 and 6, have an average orientated such that HCP crystal is positioned approximately parallel to the cutting direction. The regions of least stiffness correspond to areas 1, 2, 3 and 9, where the orientation of the HCP crystal is aligned perpendicular to the plane of the cutting direction. The regions displaying a nominal stiffness are areas 4 and 8, which have an average orientation where the corresponding basal plane is positioned at approximately 45° relative to the cutting direction. This material property dependency shares commonality to the observations made by Lütjering *et al.* [4] who showed how the elastic modulus of fully equiaxed Ti-64 samples exhibited significant property variation as a direct result of the test direction in relation to the material's orientation.

As a method of billet analysis, if the billet force profiles were applied alongside supplementary microstructure analysis techniques such as spatially resolved acoustic spectroscopy (SRAS) [206] or electron backscatter diffraction (EBSD) this could lead to a greater understanding of how upstream processing steps are influencing a materials performance during machining.

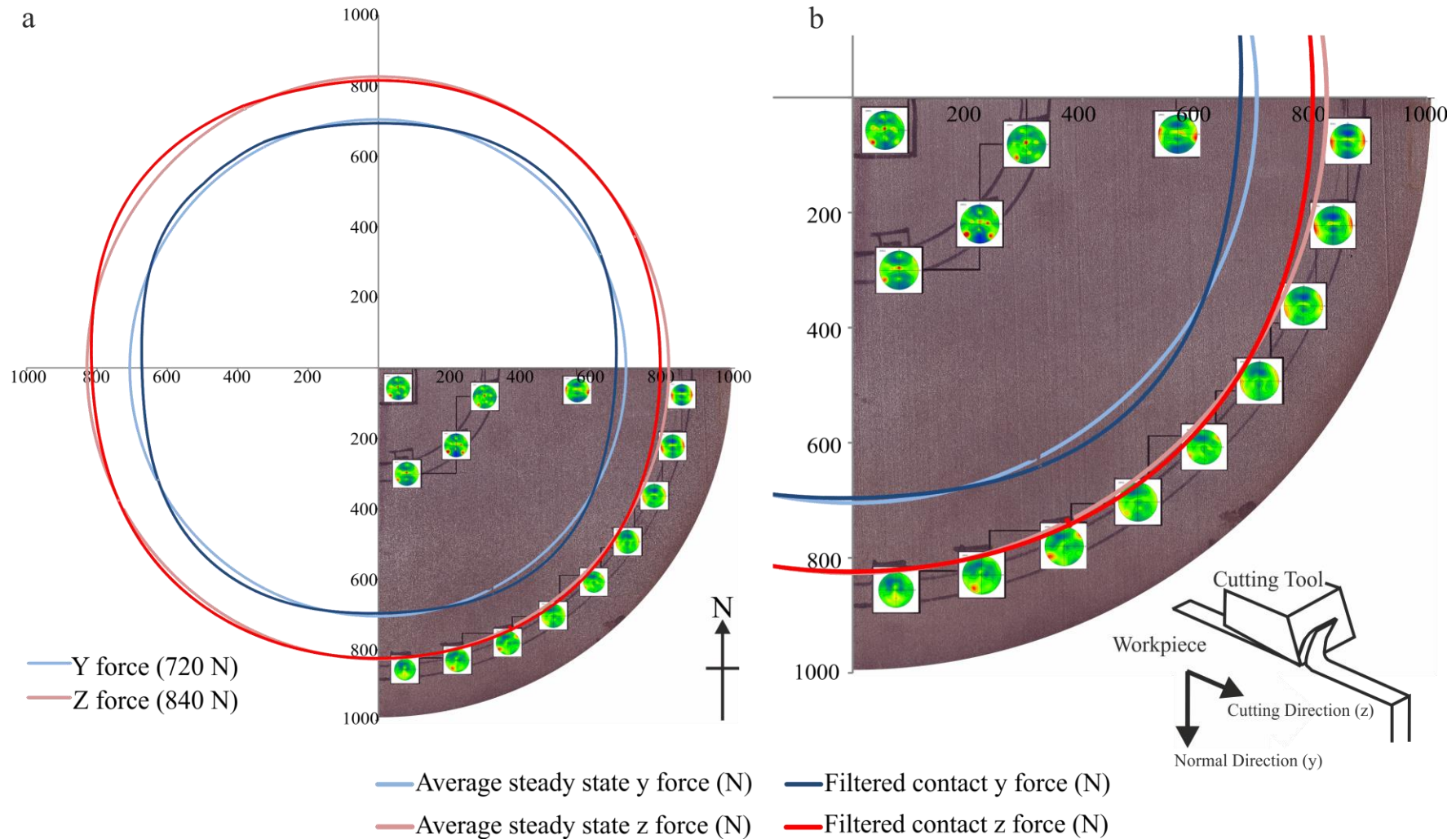


Figure 6.34 Aligned filtered thrust (y) and cutting (z) force data transposed on to circle plots aligning with the corresponding cross sectional quadrant of the billet with the related basal pole figures for each region.

6.5.2 Ultrasound analysis

Ultrasound is a commonly used method of non-destructive analysis and during the production of titanium forged billet material will undergo a series of ultrasound scans in order to ensure the material has undergone adequate forging. Bescond *et al.* [24] revealed using ultrasonic imaging of a forge billet two high noise bands separated by 90°, the location of these features corresponded to the location of the prior corners of the initial rectangular bar stock which resulted in microstructure variation around the billet. Using ultrasound analysis it is possible to determine the elastic modulus via a method that incorporates the time of flight of induced shear or longitudinal waves that interact with the bulk structure. Using Equations 6.11- 6.13 the bulk elastic modulus was determined for the regions analysed via EBSD. The ultrasound data presented in Figure 6.35 have been superimposed onto the raw and 15 Hz Fourier transformed filtered y force data. The results show a similarity, with the peak in elastic modulus, occurring at approximately the same location as the peak in resultant force. This result illustrates that the precise nature of the force feedback response is being dictated by the local microstructure, which is determined by the forging route.

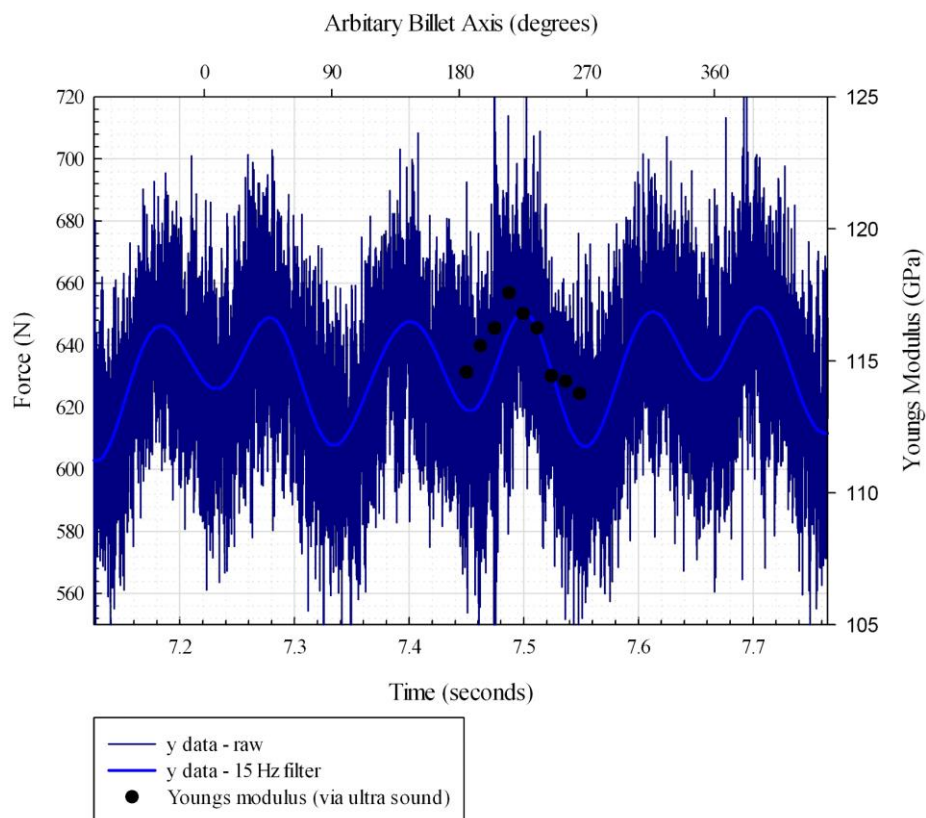


Figure 6.35 Composite signal plot illustrating the repeating “M” within the thrust (y) force using the raw and filtered data. Superimposed onto the plot is the corresponding Young’s modulus as determined via ultrasound analysis, its position determined using the arbitrary billet axis and the prior notch index mark.

Further analysis is required to ascertain what role the underlying texture is having on the resulting forces. This investigation has shown evidence to suggest that the observed circumferential variations in cutting forces around the billet are the result of changes in macroscopic material properties. However, what still remains unclear is what the main influencing factors are. As a result of the multi-stage cogging processes, the imparted non-linear strain distribution results in regional variations in; localised phase morphology, volume fraction of phases, potential inhomogeneities in alloying additions and changes in crystallographic orientation structure, which will affect the inherent bulk properties of the material through variations in elastic modulus and machining deformation characteristics. The resulting sensitivities of the force response to the material will however most likely be the culmination of a proportion of all of the above factors.

6.6 Application of the plane simple shear stress state model and the role of forging route on the resulting induced machining damage.

The following case study applies some of the key findings that were made during the course of the PhD study by investigating how forging, which dictates the material's microstructure and crystallographic texture, can influence the deformation behaviour of the material during machining.

Throughout this investigation the predominant type of mechanically induced twin that was identified was the $\{10\bar{1}2\}$ tension type twin, of which its activation during machining was shown in §5.3.1 to operate within a stress state that could be approximated to a simple shear model. Ti-54M was also shown in §6.3.1 to adopt a highly textured microstructure as a result of the multi-stage cogging process used during forging, which has been shown to have a profound influence on the experienced cutting forces. What has remained unclear however is what effect the regional variations in material properties and subsequent resulting forces are having upon the substructure. For this study, the $\alpha+\beta$ titanium alloy Timetal® 54M (Ti-54M) was supplied as a 181 mm \varnothing billet in a mill annealed condition. Ti-54M is a development alloy purporting lower supply costs and an improvement in machinability over conventional alloys such as Ti-6Al-4V (Ti-64) [128].

The mill annealed morphology for Ti-54M, as previously shown in Figure 5.1, has an approximate 0.7 volume of α phase, of which ~30% are primary α grains with the remainder adopting a transformed colony type structure. Outer diameter (OD) turning trials were performed using a MAG Cincinnati Hawk lathe. At a constant cutting velocity of 95 m.min⁻¹, feed rate of 0.1 mm.rev⁻¹ and a 1 mm radial depth of cut (2 mm off the diameter). Sandvik CNMG 120408-23 H13A uncoated carbide inserts

were mounted in a Sandvik C5-DCLNL-35060-12 tool holder, providing a clearance angle of 6° and a rake angle of 7° . The water based coolant, Hocut 795B at 4-7% concentration was ‘flood’ delivered at ~ 13 litres per minute. Following the turning operation, the workpiece was sectioned parallel to the plane of the normal direction–cutting direction, with two coupon samples (regions A and B) obtained from areas positioned with a 45° separation relative to the billet axis (Figure 6.36).

Samples A and B were removed in such a manner as to ensure their average texture showed dissimilar properties and as result had different inherent propensities for deformation. Following sectioning the metallographic samples were prepared for metallography using standard methods. The average bulk crystallographic orientation of each region data (Figure 6.36) was acquired using electron backscatter diffraction (EBSD) with a 20 kV accelerating voltage, a 10 nA probe current and a step size of $5 \mu\text{m}$ over an area of $\sim 8 \times 8 \text{ mm}$. Automated indexing and post-processing of the electron diffraction data were performed using Oxford Instruments HKL Channel 5 software. Microstructure analysis of the deformed subsurface layer was undertaken optically using a Nikon Eclipse LV150 with cross-polarising lenses, images were obtained of the immediate subsurface layer covering $\sim 8 \text{ mm}$. Quantitative analysis of the optical images were undertaken using a linear intercept method whereby each individual grain was counted and a further assessment was made discerning whether the grain had also deformed via twinning (Figure 6.37).

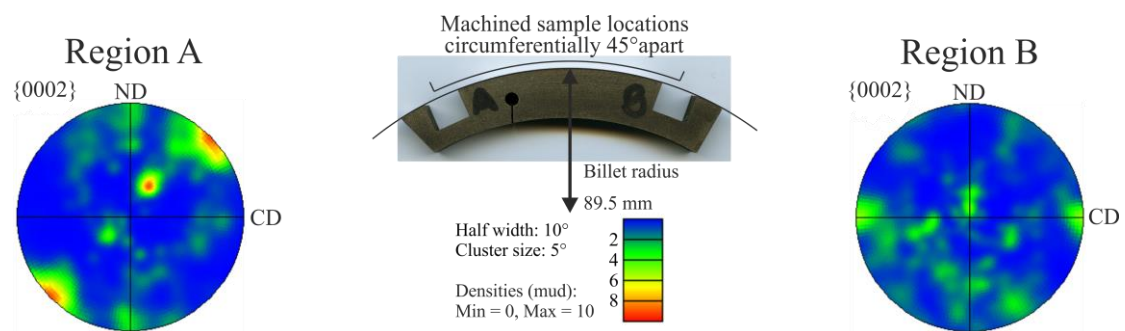


Figure 6.36 (left and right) Representative stereographic contoured $\{0002\}$ pole figures for region A and region B respectively. (Centre) corresponding photograph illustrating the location of region A and region B.

The representative pole figures that illustrate the average bulk orientation of regions A and B are presented in Figure 6.36. As a result of the forging processes, region A has become highly textured, note that the scale used has a maximum MUD value of 10 rather than 3 as seen in §6.3.2, suggesting further sensitivities of the billet to its precise strain history and that the amount of imparted strain appears to vary axially down the billet. The average textures of regions A and B indicate a 45° rotation, with

region A positioned at 45° to the cutting direction (CD) and region B aligning parallel to CD. A linear intercept method was used at a depth of 30 and 60 μm across an 8 mm transect beneath the machined surface and was conducted on both regions as shown in Figure 6.37. The enlarged region shown in Figure 6.37(i) illustrates the high density of twins that have been imparted into the materials substructure.

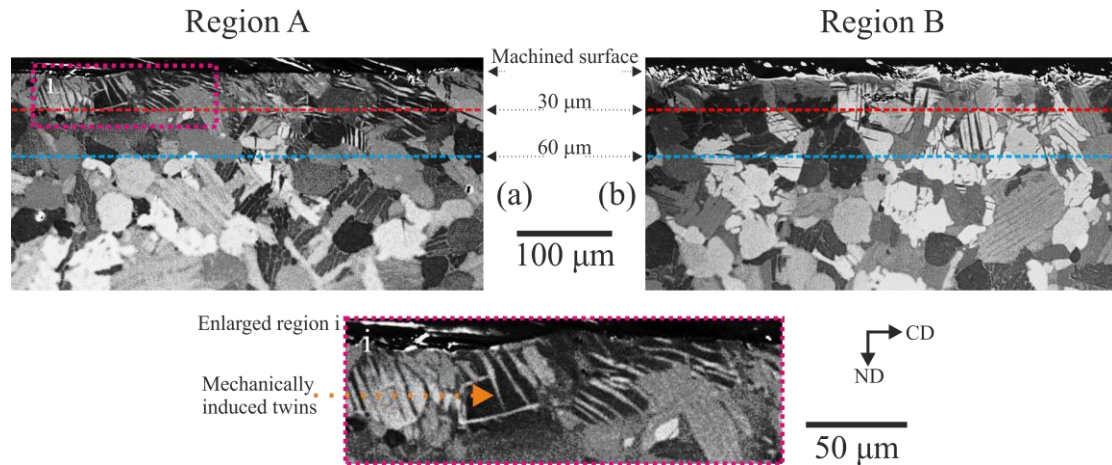


Figure 6.37 Representative polarised light micrographs at the machined surface of region A and region B, illustrating the occurrence of mechanically induced twins beneath the machined surface. The delineated lines represent transects used when calculating the frequency of the induced twins at a depth of 30 and 60 μm beneath the machined surface. The enlarged region (i) show the high density of induced twins that can be found within region A.

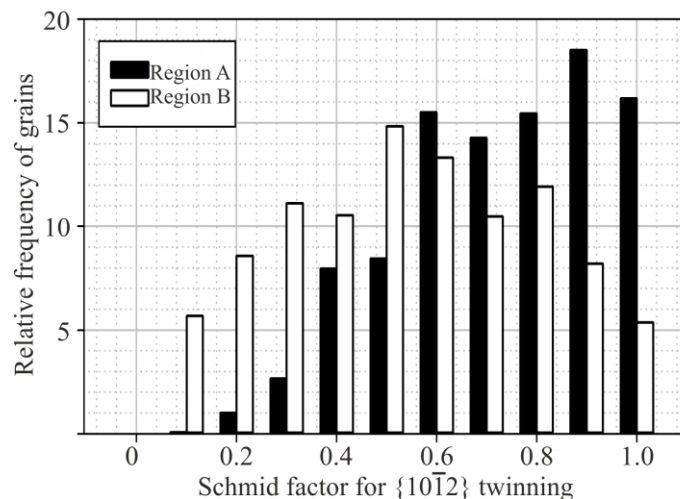


Figure 6.38 Histogram comparing the distribution of the relative frequency of the calculated Schmid factor for $\{10\bar{1}2\}$ twinning for region A and region B. Schmid factor calculated assuming plane simple shear.

The histogram presented in Figure 6.38 shows the relative Schmid factor distribution for $\{10\bar{1}2\}$ type twins for regions A and B and are representative of the whole bulk

material, as calculated using the simple shear model approach. The histogram illustrates how Region A displays the highest propensity for twinning to occur, with significantly more grains that orientated favourably (Schmid factor > 0.8).

The histogram given in Figure 6.39 shows the frequency of grains counted that intersected the 30 and 60 μm transects for both region A and B. The microstructures of both region A and B show similar characteristics with ~ 1100 grains intersecting both transects in region A and ~ 1200 intersecting both transects in region B. The proportion of grains that show evidence of twinning however varied significantly; with $\sim 28\%$ of grains at 30 μm and $\sim 13\%$ at 60 μm depth for region A and $\sim 9\%$ of grains at 30 μm and $\sim 5\%$ at 60 μm depth for region B. The author appreciates that by virtue of the method used, significantly large grains may have been counted twice, however the results illustrate how a region's average texture can have a significant influence on the severity of the imparted deformation

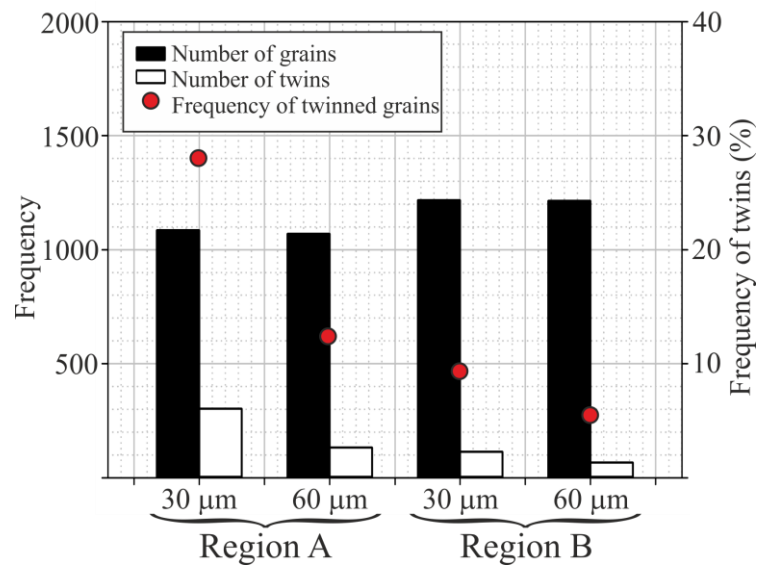


Figure 6.39 Histogram comparing the distribution, within region A and region B, of the absolute number of grains to that of the number of grains that have twinned using a transect method at a depth of 30 and 60 μm beneath the machined surface. The overlaid points signify the frequency of the twins within each region at each specified depth.

6.7 Summary

Variable parameter orthogonal cutting trials were undertaken on Ti-54M in the as-forged condition in order to investigate the material aspects that influence the machining process. Through the analysis of the cutting force data the relationship between cutting forces with variable feed rates and cutting speeds was studied. Analysis of the resulting cutting forces, used to monitor the mechanisms involved during the initial engagement period of the tool into the workpiece, offered further insight into the paradox of the machining size effect, with the mechanisms that control the ploughing / edge effects also being explored. Following the acquisition of cutting force data, key material property features such as the effective shear strength and apparent inherent friction was determined. This required firstly the identification and subsequent removal of the ploughing force, which has been shown not to contribute to the chip removal process. A novel approach for acquiring cutting force coefficients and cutting force material data was also detailed and could be considered to be analogous to using the lathe as an effective high strain rate material test. An improved method of obtaining cutting force coefficients was proposed, offering the user significant gains in acquisition time and data reliability. It has also been demonstrated that microstructure variations across a billet's cross-section, which occur as a result of multiple cogging procedures, have a profound impact on the material's performance during machining. It has been shown that by capturing the resulting force feedback response of a tool during a simple facing operation, the microstructure variations can be transformed into an effective map of the billet. The resulting billet cutting force profile plots closely replicate the observations made during the total strain distribution simulations.

This investigation has also shown how the forging process can have a significant influence on the material's performance during machining with regions that show a higher propensity to imparted subsurface deformation. Following a significant number of further investigations future industrial machining operations could be designed to mitigate the amount of residual deformation, through altered machining parameters such as rake angle, speed or feed rate -tailored to the specific region that is being machined. The imparted damage may also be managed for structural components that possess critical load bearing surfaces, by effectively orientating the component within the billet such that the critical regions align with areas that have a lower propensity for deformation. This investigation has also illustrated the importance of knowing the nature of a material's crystallographic orientation when assessing the amount of imparted deformation. If for example, the amount of imparted damage were to be used to compare two differing machining operations and the

metallographic samples analysed showed significantly different results, it would be important to know whether or not the two samples had comparable average textures, since the results may be being influenced by the underlying texture more than by the machining operation itself.

Conclusions

The following outline the key findings made during this PhD research project,

- Through the application of backscattered electron microscopy and EBSD, the activation of multiple deformation modes were identified within Ti-834; these occurred as a result of the machining operation. The observed deformation features included mechanically induced twins, the most common of which was characterised to be the $\{10\bar{1}2\}$ tension type twin. These occurred in addition to the activation of basal, prismatic and pyramidal slip.
- During outer diameter turning of Ti-834, it was observed that, for a constant feed rate and depth of cut, increasing the cutting speed resulted an increase in induced microstructure damage.
- EBSD facilitated the identification and characterisation of the imparted deformation features, which were activated at depths $>50\ \mu\text{m}$ beneath the machined surface. This study demonstrated that traditional methods of subsurface microstructure analysis need to be re-evaluated, since relying upon methods such as ‘beta distortion’ does not offer enough insight into the severity of the imparted deformation.
- Silicide precipitates were observed on the induced microstructure damage following prolonged thermal exposure at 750°C , which could lead to a reduction in creep and fatigue performance.
- EBSD analysis of Ti-834 within the bulk regions of the material identified the presence of residual forging induced twins, these were characterised as satisfying the irrational “i” twin mode $\{5\bar{6}1\bar{3}\}$.
- Turning trials were performed on Ti-54M to determine the conditions required for the formation of subsurface $\{10\bar{1}2\}$ twins in the workpiece. Twins were mostly observed in two orientation clusters at approximately $\pm 45^\circ$ to CD, which has been attributed to a plane simple shear state operating in a forward mode ahead of the tool and in reverse behind the tool.
- Variable parameter orthogonal cutting trials were undertaken on Ti-54M in the as-forged condition. Analysis of the resulting cutting forces offered further insight into the cutting process, allowing the paradox of the machining size effect to be explored (and later rebutted).

- An improved method of obtaining cutting force coefficients has been proposed, which could be considered to be analogous to using the lathe as an effective high strain rate test, allowing key material property features such as the effective shear strength and effective friction to be determined.
- This investigation has demonstrated that microstructure variations that occur as a result of a material's processing history have a profound impact on the performance during machining, with isolated regions showing a higher propensity to suffer imparted subsurface deformation.
- It has also been shown that by capturing the resulting force feedback response of a tool during a simple facing operation can be transformed into an effective microstructure map of the billet. The resulting billet cutting force profile plots closely replicate the observations made during the total strain distribution simulations.

Recommendations for further work

The mechanical and material processes which take place during machining and more specifically during the machining of titanium are understandably complicated with many interesting subject facets available for research. The following will detail some of the important avenues of research that have spawned as potential topics of further work.

- A full and comprehensive review of the mechanism of tool wear fell beyond the scope of this investigation, therefore the author suggest that further work is required covering the fundamental aspects of tool wear by isolating its governing mechanisms. During the speed variable cutting trials tool wear was observed to decrease with increasing cutting speed, however this result may be significantly influenced by the short contact time of the tool with the workpiece as each trial had comparable spiral cut lengths. Therefore to capture the effect of surface speed on tool wear it would be necessary to undertake a repeat trial with each cut completing comparable total cutting times.
- Previous studies undertaken by Kramer *et al.* [171] have shown that a significant limiting factor that can determine the rate of tool wear is the stability of the built up edge; the built up edge can form a stable barrier between the tool and the aggressive sliding contact of the workpiece. If a built up edge does not form the tool will undergo rapid abrasive wear; if however a large built up edge forms it may be prone to breaking leading to crater wear of both the tool and the workpiece. Therefore the author recommends a simplified chemical reactivity investigation, studying the relative chemical

reactivity of a desired workpiece with the cutting inserts. In brief this proposed investigation will require cutting inserts being positioned in direct contact with workpiece test specimens and subjected to a thermal exposure within a vacuum environment. Such an investigation will demonstrate whether or not each insert-workpiece material combination has a significant propensity for chemical interactions.

- It was identified during the literature review that a significant knowledge gap remains in regard to the positive role a BUE can have during cutting and how it could be exploited during the production of high value components. It is feasible to develop a method that allows a tool to undergo a pre-cut that conditions the tool, in order to ultimately improve its tool wear characteristics. A detailed investigation will be required, studying the formation characteristics of BUEs and their stability.
- Following the identification of machining induced deformation further investigations are required in order to specifically measure and quantify the precise impact they may have on in-service performance. This applies not only for titanium or HCP materials but all metallic systems. Considering work other than that presented on beryllium (see §2.8) there has been no other notable work that discusses the specific role (and the detrimental impact) that machining induced damage has on a component's life.
- The parameters used during the outer diameter turning trials were comparable to parameters used during the manufacture of components, however in industry, following machining, many components will undergo further surface treatments such as etching or shot peening. It is therefore important to analyse the effect of the machining damage following such normal industrial surface treatment techniques, which in the case of chemical etching, used to remove the uppermost machined smeared layer, subsurface induced damage may become exposed which may promote diffusion or act as sites for crack initiation. It is also important to consider the environment that a component may be exposed to during operation, machining induced microstructure damage may have further deleterious effects for a component if the material is introduced into a corrosive environment for example gas may be more easily absorbed as a result of enhancing the kinetics for diffusion.
- During the speed variable machining trials, surface roughness analysis on the as machined material indicated that there was an increase in surface roughness with increasing surface speed. It was proposed that this may have been a result of the variable size of the BUE that may have formed ahead of the tool. However, no visual evidence of residual BUE material remained on either the tool or as

chips on the workpiece. A complete investigation into the mechanisms that were driving surface roughness fell beyond the scope of this investigation. Considering there was also an observed increase in microstructure deformation, the author feels it is pertinent to investigate the potential link between the surface roughness and condition of the subsurface material. Such an investigation could be used to develop non-destructive analysis techniques that could be used to help assess a component following machining, using surface analysis techniques to infer the severity of residual subsurface deformation.

- As a result of the reported sensitivities of subsurface microstructure damage to an increase in cutting speed. A natural progression for subsequent investigations would include further parametric studies studying the amount of induced sub surface damage as a function of other machining parameters, such as; feed rate, tool type, tool geometry and tool holder positions (variable rake and relief angles). Also parametric studies could be performed, investigating the role of the workpiece in controlling the amount of imparted subsurface deformation either as a function of alloying chemistry, grain morphology or crystallographic orientation.
- For the purpose of this investigation each machining trial was undertaken using a fresh cutting edge, tool wear was qualitatively monitored throughout but no further correlation was made between tool wear and the induced microstructure damage. Since it was assumed tool wear was minimal throughout with each cut lasting no longer than 3 minutes. In industry however, when manufacturing a component the parameters used have a 15 minute expected tool life as to ensure the cutting insert's integrity is maintained throughout. During prolonged cuts the cutting edge undergoes further developments that can influence the way it interacts with the workpiece; with the formation of interfacial layers, a built up edge (BUE) and towards the end of the tool's life, rapid tool wear. From a surface integrity and metallurgical standpoint it would be appropriate to carry out a series of progressive machining trials, which assess the resulting microstructure damage sustained during machining operations and the function of tool edge integrity. Thus completing a series of interrupted cutting trials that can be used to monitor microstructure damage as a function of the development of features such as a BUE and subsequent tool wear. Interrupted cutting trials also offer the opportunity to monitor the wear characteristics and the workpiece interaction with cutting inserts of differing substrate and coatings chemistry.

- During the orthogonal cutting trials there were observed discrepancies in tool/workpiece performance when comparing cuts that were using repeating machining parameters and fresh cutting inserts. Such variables include significant differences in the experienced cutting forces, which have so far been attributed to variations in the tool's starting condition, such as variations in edge roundness. It should therefore be considered that detailed surface profiling of the cutting edges should be characterised prior to each operation during experimental machining trials as a further supplement to the acquired data.
- The most predominantly observed twinning mode was the $\{10\bar{1}2\}$ tension type twin, the activation of which was attributed to a simple shear mechanism. In order to capture how this shear mechanism interacts with the workpiece a quick stop interrupted cutting trial would allow the material to be analysed via EBSD thus capturing how the deformation dynamics change around the tool within the material.
- On occasions twins were observed to activate within grains that were unfavourably orientated, as assessed using the simple shear model. It is therefore recommended that a further investigation would study the driving factors of twin initiation within these unfavourable grains, thus ascertaining whether or not they have been activated as a result of a more complex macroscopic stress state or through more localised stress variations generated by interactions between neighbouring grains.
- During variable speed machining trials as the speed is increased, from slow ($<40 \text{ m.min}^{-1}$) cutting speeds, the resulting cutting forces initially decrease towards a plateau commonly occurring at speeds $>40 \text{ m.min}^{-1}$. What still remains unclear however, are the reasons why there is an observed increase in subsurface with increased cutting speed even though as reported the cutting forces reduce/ remain constant. The author has attributed this phenomenon to changes in the material's behaviour as a result of its strain rate sensitivity. At higher cutting speeds there was a reduction in the amount of gross plastic distortion occurring within the grains, however there was an increase in the depth of activated deformation features such as intense slip or twins. These activated features occurred within grains that exhibited little/ zero plastic distortion, thus indicating the region had undergone minimal levels of total strain. These results have shown that the material displays further sensitivities to the machining operation as a result of altering the associated stress state. A combination of controlled compression tests and experimental machining trials, in conjunction with finite element simulations to ascertain the

experienced stress state, can be used to replicate the deformation environment in order to study how the stress state evolves when the cutting speed is increased and how the material is expected to react.

- Following a prolonged heat treatment, machined Ti-834 displayed evidence of precipitation occurring within regions that had undergone plastic deformation. The precipitates were assumed to be S2 silicides rich in zirconium and of stoichiometry $(\text{Ti,Zr})_3\text{Si}_6$. Following analysis of regions that had undergone a heat treatment with EBSD showed how the silicides were encouraged to form in the vicinity of twin boundaries and on intense slip planes. The relative density of silicide precipitation was shown to diminish away from the machined surface indicating that the imparted strain from the machining process could be attributed to their formation. The depth to which the silicides formed was significantly deeper than the maximum depth of induced deformation recorded prior to heat treatment. Silicides were shown to be encouraged to form as a result of minimal levels of plastic deformation, with evidence of silicide precipitation within grains showing minimal lattice rotation. It is therefore proposed that further studies could exploit the formation of silicides in Ti-834, thus using it as a model alloy in which the precipitates act as a marker illustrating the total amount of induced plastic deformation. Such an approach could be used for further variable parametric investigations using the formation of the silicides to demonstrate the severity of the plastic deformation and also as a method to validate simulated trials that predict the amount of imparted strain.
- The obtained force feedback data has shown that microstructure variation across the face of a billet has a pronounced effect on the cutting forces and can be captured using a simple facing operation. Following this observation the author proposes the development of a machining technique that can measure these fluctuations in elastic modulus and therefore generate an effective microstructure map that captures the processing history of the billet. Applying the billet force profiles alongside supplementary microstructure analysis techniques such as electron backscatter diffraction (EBSD) could lead to a greater understanding of how upstream processing steps are influencing a material's performance during machining. This investigation has gone some way to advancing the developing subject of metallurgy of machining. However, there still remains a significant knowledge gap concerning how the metallurgy of the workpiece dictates the development of features such as; subsurface damage, white layers and residual stresses -as well as the

metallurgical influence on general operational performance such as tool wear and cutting forces.

- This investigation has demonstrated how the severity of machining induced subsurface microstructure damage is sensitive to both variations in localised microstructure and changes in cutting speed. The author feels it is of critical importance for further parametric trials to be undertaken in order to help identify specific critical machining conditions that component manufacturers can apply to control the development of deformation features. Following a series of machining trials a summary correlation diagram could be constructed that would offer an overview for key process variables such as; cutting speed, feed rate, depth of cut and workpiece alloy heat treatment path. This diagram would illustrate the respective impact of changes to the cutting environment on deformation features such as surface roughness, grain distortion, twinning and slip.
- Further development of the force mapping technique may progress towards using a custom roller bearing attachment in place of the tooling, allowing the process to be non-destructive. These processes could be used prior to machining and would offer the operator an insight into how the material can be expected to behave. Once the techniques have been optimised, the technique could be used to examine the role of chemistry and microstructure through the analysis of alloys of varying chemical composition and material samples that have been subjected to a range of heat treatments.

References

- [1] Roskill, “Titanium: Market Outlook to 2018,” 2013. [Online]. Available: http://www.roskill.com/downloads/Tim_Prepub_2013.pdf. [Accessed: 07-Feb-2014].
- [2] “Global Market Forecast 2013-2032 | Airbus, a leading aircraft manufacturer.” [Online]. Available: <http://www.airbus.com/company/market/forecast/>. [Accessed: 07-Feb-2014].
- [3] “High Value Manufacturing,” *Technology Strategy Board*,. [Online]. Available: <https://www.innovateuk.org/documents/1524978/2139688/High+Value+Manufacturing+Strategy+2012-15/9b7e55f0-ed9a-4efe-89e5-59d13b2e47f7>. [Accessed: 07-Feb-2014].
- [4] G. Lütjering and J. C. Williams, *Titanium*. Springer, 2007, p. 454.
- [5] S. Seong, O. Younossi, B. W. Goldsmith, T. Lang, and M. J. Neumann, *Titanium*. RAND Corporation, 2009, p. 154.
- [6] C. Leyens and P. Manfred, *Titanium and Titanium Alloys: Fundamentals and Applications*. John Wiley & Sons, 2006, p. 532.
- [7] P. Bania, “Beta titanium alloys and their role in the titanium industry,” *JOM*, vol. 46, no. 7, pp. 16–19, 1994.
- [8] G. Welsch, R. Boyer, and E. W. Collings, *Materials Properties Handbook: Titanium Alloys*. ASM International, 1993, p. 1176.
- [9] S. Banerjee and P. Mukhopadhyay, *Phase Transformations: Examples from Titanium and Zirconium Alloys*. Elsevier, 2010, p. 840.
- [10] G. Lutjering and J. C. Williams, “*Fundamental Aspects*” in *Titanium*, 2nd ed. springer, 2007, pp. 13–50.
- [11] H. M. Flower, “Microstructural development in relation to hot working of titanium alloys,” *Mater. Sci. Technol.*, vol. 6, no. 11, pp. 1082–1092, 1990.
- [12] E. O. Hall, “The Deformation and Ageing of Mild Steel: III Discussion of Results,” *Proc. Phys. Soc. Sect. B*, vol. 64, no. 9, pp. 747–753, Sep. 1951.
- [13] R. Goosey, “Development in Titanium Alloys for Aerospace,” *Met. Mater.*, vol. 5, no. 8, pp. 451–455, 1989.
- [14] J. I. Qazi, H. J. Rack, and B. Marquardt, “High-strength metastable beta-titanium alloys for biomedical applications,” *Jom*, vol. 56, no. 11, pp. 49–51, Nov. 2004.

- [15] M. J. Donachie, *Titanium: A Technical Guide*. ASM International, 2000, p. 381.
- [16] I. Weiss, “Thermomechanical processing of alpha titanium alloys—an overview,” *Mater. Sci. Eng. A*, vol. 263, no. 2, pp. 243–256, May 1999.
- [17] N. Gey and M. Humbert, “Characterization of the variant selection occurring during the $\alpha \rightarrow \beta \rightarrow \alpha$ phase transformations of a cold rolled titanium sheet,” *Acta Mater.*, vol. 50, no. 2, pp. 277–287, 2002.
- [18] J. Sieniawski, R. Filip, and W. Ziaja, “The effect of microstructure on the mechanical properties of two-phase titanium alloys,” *Mater. Des.*, vol. 18, no. 4–6, pp. 361–363, Dec. 1997.
- [19] P. S. Davies, “An Investigation of Microstructure and Texture Evolution in the Near- α Titanium Alloy Timetal® 834,” PhD Thesis, The University of Sheffield, 2009.
- [20] A. F. Wilson, V. Venkatesh, R. Pather, J. W. Brooks, and S. P. Fox, “The Prediction of Microstructural Development During TIMETAL® 6-4 Billet Manufacture,” in *Ti-2003 Science and Technology: Proceedings of the 10th World Conference on Titanium, Hamburg, Germany, 13-18 July, 2003*, p. 677.
- [21] P. Davies, W. Kockelmann, B. Wynne, R. Eccleston, B. Hutchinson, and W. M. Rainforth, “Validation of neutron texture data on GEM at ISIS using electron backscattered diffraction,” *Meas. Sci. Technol.*, vol. 19, no. 3, p. 034002, Mar. 2008.
- [22] N. Nasser, “Microstructure and texture evolution of titanium 6-2-4-6,” PhD Thesis, The University of Sheffield, 2009.
- [23] B. Wynne and M. Thomas, “Private communication between University of Sheffield and Timet UK,” 2010.
- [24] C. Bescond, D. Lévesque, J. B. Guénette, and J. P. Monchalain, “Synthetic focusing for imaging the ultrasonic backscattered noise in dual phase titanium forged pieces,” in *Proceedings of the 16th World Conference on Non Destructive Testing (16 WCNDT)*, 2004, p. 678.
- [25] R. V. Mises, “Mechanik der plastischen Formänderung von Kristallen,” *ZAMM - Zeitschrift für Angew. Math. und Mech.*, vol. 8, no. 3, pp. 161–185, 1928.
- [26] E. O. Hall, *Twinning and diffusionless transformations in metals*. Butterworths Scientific Publications, 1954, p. 181.
- [27] Y. Hu and V. Randle, “An electron backscatter diffraction analysis of misorientation distributions in titanium alloys,” *Scr. Mater.*, vol. 56, no. 12, pp. 1051–1054, Jun. 2007.

- [28] S. Mironov, G. Salishchev, M. Myshlyaev, and R. Pippan, "Evolution of misorientation distribution during warm 'abc' forging of commercial-purity titanium," *Mater. Sci. Eng. A*, vol. 418, no. 1–2, pp. 257–267, Feb. 2006.
- [29] S. Diiorio, L. Briottet, E. Rauch, and D. Guichard, "Plastic deformation, damage and rupture of PM Ti–6Al–4V at 20K under monotonic loading," *Acta Mater.*, vol. 55, no. 1, pp. 105–118, Jan. 2007.
- [30] A. G. Crocker, R. I. Jaffee, N. E. Promisel, and M. Bevis, "The crystallography of deformation twinning in titanium," in *The Science, Technology and Application of Titanium*, 1970, pp. 453–458.
- [31] M. J. Thomas, "The Effect of Thermomechanical Process Parameters on the Microstructure and Crystallographic Texture Evolution of Near- α Aerospace Alloy Timetal 834," The University of Sheffield, UK, 2007.
- [32] J. Christian and S. Mahajan, "Deformation Twinning," *J. Mater. Sci.*, vol. 240, no. 7, pp. 229–648, Jul. 1995.
- [33] R. J. McCabe, E. K. Cerreta, A. Misra, G. C. Kaschner, and C. N. Tomé, "Effects of texture, temperature and strain on the deformation modes of zirconium," *Philos. Mag.*, vol. 86, no. 23, pp. 3595–3611, Aug. 2006.
- [34] E. Cerreta and G. T. Gray, "The influence of texture, strain rate, temperature, and chemistry on the mechanical behavior of hafnium," *Metall. Mater. Trans. A*, vol. 35, no. 7, pp. 1999–2011, Jul. 2004.
- [35] M. A. Meyers, O. Vöhringer, and V. A. Lubarda, "The onset of twinning in metals: a constitutive description," *Acta Mater.*, vol. 49, no. 19, pp. 4025–4039, Nov. 2001.
- [36] M. D. Sangid, H. J. Maier, and H. Sehitoglu, "The role of grain boundaries on fatigue crack initiation – An energy approach," *Int. J. Plast.*, vol. 27, no. 5, pp. 801–821, May 2011.
- [37] A. Ghaderi and M. R. Barnett, "Sensitivity of deformation twinning to grain size in titanium and magnesium," *Acta Mater.*, vol. 59, no. 20, pp. 7824–7839, Dec. 2011.
- [38] R. W. Armstrong and P. J. Worthington, "A Constitutive Relation for Deformation Twinning in Body Centered Cubic Metals," in *Metallurgical Effects at High Strain Rates*, R. W. Rohde, B. M. Butcher, J. R. Holland, and C. H. Karnes, Eds. Springer US, 1973, pp. 401–414.
- [39] L. Capolungo, P. E. Marshall, R. J. McCabe, I. J. Beyerlein, and C. N. Tomé, "Nucleation and growth of twins in Zr: A statistical study," *Acta Mater.*, vol. 57, no. 20, pp. 6047–6056, Dec. 2009.
- [40] F. J. Zerilli and R. W. Armstrong, "Dislocation mechanics based constitutive equation incorporating dynamic recovery and applied to thermomechanical

- shear instability,” in *AIP Conference Proceedings*, 1998, vol. 429, no. 1, pp. 215–218.
- [41] H. W. Meyer, “A Modified Zerilli-Armstrong Constitutive Model Describing the Strength and Localizing Behavior of Ti-6Al-4V,” 2006.
- [42] S. G. Song, “Influence of temperature and strain rate on slip and twinning behavior of zr,” *Metall. Mater. Trans. A*, vol. 41, no. 10, pp. 2611–2675, Oct. 1995.
- [43] E. Schmid and W. Boas, *Plasticity of crystals: with special reference to metals*. Chapman & Hall, 1968, p. 353.
- [44] I. J. Beyerlein, R. J. McCabe, and C. N. Tomé, “Effect of microstructure on the nucleation of deformation twins in polycrystalline high-purity magnesium: A multi-scale modeling study,” *J. Mech. Phys. Solids*, vol. 59, no. 5, pp. 988–1003, May 2011.
- [45] D. Chichili, K. Ramesh, and K. Hemker, “The high-strain-rate response of alpha-titanium: experiments, deformation mechanisms and modeling,” *Acta Mater.*, vol. 46, no. 3, pp. 1025–1043, 1998.
- [46] J. L. Sun and J. T. Wang, “Microstructures and Mechanical Properties of Pure Titanium by Dynamic Plastic Deformation,” *Mater. Sci. Forum*, vol. 667–669, pp. 337–342, Dec. 2010.
- [47] L. Wang, Y. Yang, P. Eisenlohr, T. R. Bieler, M. A. Crimp, and D. E. Mason, “Twin Nucleation by Slip Transfer across Grain Boundaries in Commercial Purity Titanium,” *Metall. Mater. Trans. A*, vol. 41, no. 2, pp. 421–430, Nov. 2009.
- [48] L. Wang, P. Eisenlohr, Y. Yang, T. R. Bieler, and M. a. Crimp, “Nucleation of paired twins at grain boundaries in titanium,” *Scr. Mater.*, vol. 63, no. 8, pp. 827–830, Oct. 2010.
- [49] G. E. Dieter, *Mechanical Metallurgy, SI edition*. McGraw-Hill Higher Education, 1989, p. 776.
- [50] M. E. Merchant, “Mechanics of the metal cutting process. I. Orthogonal Cutting and a type 2 chip,” *J. Appl. Phys.*, vol. 16, no. 5, pp. 267–275, 1945.
- [51] M. E. Merchant, “Basic mechanics of the metal cutting process,” *J. Appl. Mech.*, pp. 168–175, 1944.
- [52] H. Ernst and M. E. Merchant, *Chip formation friction and finish*. Cincinnati milling machine Company, 1940, p. 48.
- [53] J. R. Sims and R. E. Feigel, “The Use of Risk-Based Approaches in Post-Construction Standards,” *J. Press. Vessel Technol.*, vol. 122, no. 3, p. 247, Aug. 2000.

- [54] L. Wagner, "Mechanical surface treatments on titanium, aluminum and magnesium alloys," *Mater. Sci. Eng. A*, vol. 263, no. 2, pp. 210–216, May 1999.
- [55] M. Bayoumi and A. Abdellatif, "Effect of surface finish on fatigue strength," *Eng. Fract. Mech.*, vol. 51, no. 5, pp. 861–870, 1995.
- [56] J. I. Hughes, K. Ridgway, and A. R. C. Sharman, "The effect of cutting tool material and edge geometry on tool life and workpiece surface integrity," *Proc. Inst. Mech. Eng.*, vol. 220, pp. 1–15, 2006.
- [57] C. Che-Haron and A. Jawaid, "The effect of machining on surface integrity of titanium alloy Ti–6% Al–4% V," *J. Mater. Process. Technol.*, vol. 166, no. 2, pp. 188–192, Aug. 2005.
- [58] R. Pawar and R. Pawade, "Surface Integrity Analysis in Dry High Speed Turning of Titanium Alloy Ti-6Al-4V," 2012.
- [59] A. Ginting and M. Nouari, "Surface integrity of dry machined titanium alloys," *Int. J. Mach. Tools Manuf.*, vol. 49, no. 3–4, pp. 325–332, 2009.
- [60] J. L. Cantero, M. M. Tardío, J. a. Canteli, M. Marcos, and M. H. Miguélez, "Dry drilling of alloy Ti–6Al–4V," *Int. J. Mach. Tools Manuf.*, vol. 45, no. 11, pp. 1246–1255, Sep. 2005.
- [61] N. F. M. Aris and K. Cheng, "Characterization of the surface functionality on precision machined engineering surfaces," *Int. J. Adv. Manuf. Technol.*, vol. 38, no. 3–4, pp. 402–409, Jan. 2008.
- [62] P. Partridge, "Effect of cyclic stresses on the microstructures of hexagonal close packed metals," *Czechoslov. J. Phys.*, vol. 19, no. 3, pp. 323–332, 1969.
- [63] M. Jackson, "Superplastic forming and diffusion bonding of titanium alloys," in *Superplastic forming of advanced metallic materials: Methods and applications*, G. Giuliano, Ed. Woodhead Publishing Ltd., Cambridge, UK, 2011, pp. 225–245.
- [64] J. Puerta Velasquez, B. Bolle, P. Chevrier, G. Geandier, and A. Tidu, "Metallurgical study on chips obtained by high speed machining of a Ti–6wt.% Al–4wt.% V alloy," *Mater. Sci. Eng. A*, vol. 452, pp. 469–474, 2007.
- [65] A. Warren and Y. Guo, "Surface Hardening: Hard Turning or Grinding?," *Gear Solut.*, pp. 45–56, 2007.
- [66] D. Rugg, T. B. Britton, J. Gong, a. J. Wilkinson, and P. a. J. Bagot, "In-service materials support for safety critical applications – a case study of a high strength Ti-alloy using advanced experimental and modelling techniques," *Mater. Sci. Eng. A*, Jan. 2014.

- [67] N. Narutaki, "Study on Machining of Titanium Alloys," *CIRP Ann. - Manuf. Technol.*, vol. 32, no. 1, pp. 65–69, 1983.
- [68] J. Wyatt and J. Berry, "A new technique for the determination of superficial residual stresses associated with machining and other manufacturing processes," *J. Mater. Process. Technol.*, vol. 171, no. 1, pp. 132–140, Jan. 2006.
- [69] T. Özel and D. Ulutan, "Prediction of machining induced residual stresses in turning of titanium and nickel based alloys with experiments and finite element simulations," *CIRP Ann. - Manuf. Technol.*, vol. 61, no. 1, pp. 547–550, Jan. 2012.
- [70] E. Abboud, B. Shi, H. Attia, V. Thomson, and Y. Mebrahtu, "Finite Element-based Modeling of Machining-induced Residual Stresses in Ti-6Al-4V under Finish Turning Conditions," *Procedia CIRP*, vol. 8, pp. 63–68, Jan. 2013.
- [71] V. Schulze, P. Arrazola, F. Zanger, and J. Osterried, "Simulation of Distortion Due to Machining of Thin-walled Components," *Procedia CIRP*, vol. 8, pp. 45–50, Jan. 2013.
- [72] D. Novovic, "The effect of machined topography and integrity on fatigue life," *Int. J. Mach. Tools Manuf.*, vol. 44, no. 2–3, pp. 125–134, Feb. 2004.
- [73] P. Dahlman, "The influence of rake angle, cutting feed and cutting depth on residual stresses in hard turning," *J. Mater. Process. Technol.*, vol. 147, pp. 181–184, Mar. 2004.
- [74] J. Sun and Y. B. Guo, "A comprehensive experimental study on surface integrity by end milling Ti-6Al-4V," *J. Mater. Process. Technol.*, vol. 209, no. 8, pp. 4036–4042, Apr. 2009.
- [75] A. Javidi, U. Rieger, and W. Eichseder, "The effect of machining on the surface integrity and fatigue life," *Int. J. Fatigue*, vol. 30, no. 10–11, pp. 2050–2055, Oct. 2008.
- [76] M. Thomas, T. Lindley, and M. Jackson, "The microstructural response of a peened near-alpha titanium alloy to thermal exposure," *Scr. Mater.*, vol. 60, pp. 108–111, 2009.
- [77] M. Imran, P. T. Mativenga, A. Gholinia, and P. J. Withers, "Evaluation of surface integrity in micro drilling process for nickel-based superalloy," *Int. J. Adv. Manuf. Technol.*, vol. 55, no. 5–8, pp. 465–476, Dec. 2010.
- [78] Y. Guo, R. M'Saoubi, and S. Chandrasekar, "Control of deformation levels on machined surfaces," *CIRP Ann. - Manuf. Technol.*, vol. 60, no. 1, pp. 137–140, Jan. 2011.

- [79] Y. Guo, C. Saldana, W. Dale Compton, and S. Chandrasekar, "Controlling deformation and microstructure on machined surfaces," *Acta Mater.*, vol. 59, no. 11, pp. 4538–4547, Jun. 2011.
- [80] Y. Guo, C. Saldana, J. B. Mann, R. M'Saoubi, and S. Chandrasekar, "Deformation and Microstructure in Machining," *Adv. Mater. Res.*, vol. 223, pp. 325–331, Apr. 2011.
- [81] R. W. Evans, R. J. Hull, and B. Wilshire, "The effects of alpha-case formation on the creep fracture properties of the high-temperature titanium alloy IMI834," *J. Mater. Process. Technol.*, vol. 56, no. 1, pp. 492–501, 1996.
- [82] D. Umbrello, "Finite element simulation of conventional and high speed machining of Ti6Al4V alloy," *J. Mater. Process. Tech.*, vol. 196, no. 1–3, pp. 79–87, 2008.
- [83] T. Hryniewicz, P. Konarski, R. Rokicki, and J. Valicek, "SIMS studies of titanium biomaterial hydrogenation after magnetoelectropolishing," *Surf. Coatings Technol.*, vol. 206, no. 19, pp. 4027–4031, 2012.
- [84] R. C. Dawes and D. K. Aspinwall, "Processing Technology Materials A review of ultra high speed milling of hardened steels," *J. Mater. Process. Technol.*, vol. 69, 1997.
- [85] B. Lauwers, "Surface Integrity in Hybrid Machining Processes," *Procedia Eng.*, vol. 19, pp. 241–251, Jan. 2011.
- [86] P. Chevrier, "Investigation of surface integrity in high speed end milling of a low alloyed steel," *Int. J. Mach. Tools Manuf.*, vol. 43, no. 11, pp. 1135–1142, Sep. 2003.
- [87] M. Calamaz, D. Coupard, and F. Girot, "A new material model for 2D numerical simulation of serrated chip formation when machining titanium alloy Ti–6Al–4V," *Int. J. Mach. Tools Manuf.*, vol. 48, no. 3–4, pp. 275–288, Mar. 2008.
- [88] T. Özel and E. Zeren, "Determination of work material flow stress and friction for FEA of machining using orthogonal cutting tests," *J. Mater. Process. Technol.*, vol. 153–154, pp. 1019–1025, Nov. 2004.
- [89] H. Bil, "A comparison of orthogonal cutting data from experiments with three different finite element models," *Int. J. Mach. Tools Manuf.*, vol. 44, no. 9, pp. 933–944, Jul. 2004.
- [90] M. Cotterell and G. Byrne, "Characterisation of chip formation during orthogonal cutting of titanium alloy Ti–6Al–4V," *CIRP J. Manuf. Sci. Technol.*, vol. 1, no. 2, pp. 81–85, 2008.

- [91] Y. B. Guo and D. W. Yen, "A FEM study on mechanisms of discontinuous chip formation in hard machining," *J. Mater. Process. Technol.*, vol. 155–156, pp. 1350–1356, Nov. 2004.
- [92] J. Hua and R. Shivpuri, "Prediction of chip morphology and segmentation during the machining of titanium alloys," *J. Mater. Process. Tech.*, vol. 150, no. 1–2, pp. 124–133, 2004.
- [93] R. Shivpuri, J. Hua, P. Mittal, a Srivastava, and G. Lahoti, "Microstructure-Mechanics Interactions in Modeling Chip Segmentation during Titanium Machining," *CIRP Ann. - Manuf. Technol.*, vol. 51, no. 1, pp. 71–74, 2002.
- [94] M. Sima and T. Özel, "Modified material constitutive models for serrated chip formation simulations and experimental validation in machining of titanium alloy Ti–6Al–4V," *Int. J. Mach. Tools Manuf.*, vol. 50, no. 11, pp. 943–960, Nov. 2010.
- [95] Y. Zhang, T. Mabrouki, D. Nelias, and Y. Gong, "Chip formation in orthogonal cutting considering interface limiting shear stress and damage evolution based on fracture energy approach," *Finite Elem. Anal. ...*, pp. 1–14, 2011.
- [96] M. Calamaz, J. Limido, M. Nouari, C. Espinosa, D. Coupard, M. Salaün, F. Girot, and R. Chieragatti, "Toward a better understanding of tool wear effect through a comparison between experiments and SPH numerical modelling of machining hard materials," *Int. J. Refract. Met. Hard Mater.*, vol. 27, no. 3, pp. 595–604, May 2009.
- [97] M. Dirikolu, T. Childs, and K. Maekawa, "Finite element simulation of chip flow in metal machining," *Int. J. Mech. Sci.*, vol. 43, pp. 2699–2713, 2001.
- [98] Wilde-Analysis, "Discrete multi-phase material modeling for micromachining simulations DEFORM news winter 2013." [Online]. Available: <http://wildeanalysis.co.uk/news/2013/discrete-multi-phase-material-modeling-for-micro-machining-simulations>. [Accessed: 27-Sep-2013].
- [99] S. Jeelani and K. Ramakrishnan, "Subsurface plastic deformation in machining annealed red brass," *Wear*, vol. 82, pp. 67 – 79, 1982.
- [100] D. Turley, E. Doyle, and S. Ramalingam, "Calculation of shear strains in chip formation in titanium," *Mater. Sci. Eng.*, vol. 55, no. 1, pp. 45–48, Aug. 1982.
- [101] E. Doyle, "Machining of Light Metals: Challenges for Surface Engineering," *Mater. Sci. Forum*, pp. 117–126, 2009.
- [102] M. Shankar, B. Rao, S. Lee, S. Chandrasekar, a King, and W. Compton, "Severe plastic deformation (SPD) of titanium at near-ambient temperature," *Acta Mater.*, vol. 54, no. 14, pp. 3691–3700, Aug. 2006.

- [103] C. Huang, T. G. Murthy, M. R. Shankar, R. M'Saoubi, and S. Chandrasekar, "Temperature rise in severe plastic deformation of titanium at small strain-rates," *Scr. Mater.*, vol. 58, no. 8, pp. 663–666, Apr. 2008.
- [104] G. Sutter, L. Faure, A. Molinari, N. Ranc, and V. Pina, "An experimental technique for the measurement of temperature fields for the orthogonal cutting in high speed machining," *Int. J. Mach. Tools Manuf.*, vol. 43, no. 7, pp. 671–678, May 2003.
- [105] M. Thomas, S. Turner, and M. Jackson, "Microstructural damage during high-speed milling of titanium alloys," *Scr. Mater.*, vol. 62, no. 5, pp. 250–253, Mar. 2010.
- [106] D. Rugg, M. Dixon, and F. P. E. Dunne, "Effective structural unit size in titanium alloys," *J. Strain Anal. Eng. Des.*, vol. 42, no. 4, pp. 269–279, 2007.
- [107] J. D. P. Velásquez, a. Tidu, B. Bolle, P. Chevrier, and J.-J. Fundenberger, "Sub-surface and surface analysis of high speed machined Ti6Al4V alloy," *Mater. Sci. Eng. A*, vol. 527, no. 10–11, pp. 2572–2578, 2010.
- [108] J. I. Hughes, K. Ridgway, and A. R. C. Sharman, "The effect of tool edge preparation on tool life and workpiece surface integrity," *Proc. Inst. Mech. Eng.*, vol. 218, pp. 1113–1123, 2004.
- [109] S. Jeelani and K. Ramakrishnan, "Subsurface plastic deformation in machining annealed 18% ni maraging steel," *Wear*, vol. 81, no. 2, pp. 263–273, Oct. 1982.
- [110] I. S. Jawahir, E. Brinksmeier, R. M'Saoubi, D. K. Aspinwall, J. C. Outeiro, D. Meyer, D. Umbrello, and a. D. Jayal, "Surface integrity in material removal processes: Recent advances," *CIRP Ann. - Manuf. Technol.*, vol. 60, no. 2, pp. 603–626, Jul. 2011.
- [111] Z. Pu, O. W. Dillon, I. S. Jawahir, and D. A. Puleo, "Microstructural Changes of AZ31 Magnesium Alloys Induced by Cryogenic Machining and Its Influence on Corrosion Resistance in Simulated Body Fluid for Biomedical Applications," in *ASME 2010 International Manufacturing Science and Engineering Conference, Volume 1*, 2010, pp. 271–277.
- [112] C. Che-Haron, "Tool life and surface integrity in turning titanium alloy," *J. Mater. Process. Technol.*, vol. 118, no. 1–3, pp. 231–237, Dec. 2001.
- [113] M. S. Dargusch, M.-X. Zhang, S. Palanisamy, A. J. M. Buddery, and D. H. StJohn, "Subsurface Deformation After Dry Machining of Grade 2 Titanium," *Adv. Eng. Mater.*, vol. 10, no. 1–2, pp. 85–88, Feb. 2008.
- [114] S. Jeelani and K. Ramakrishnan, "Surface damage in machining titanium 6Al-2Sn-4Zr-2Mo alloy," *J. Mater. Sci.*, vol. 20, pp. 3245–3252, 1985.
- [115] S. Jeelani, "Subsurface plastic deformation in machining 6Al-2Sn-4Zr-2Mo titanium alloy," *Wear*, vol. 85, pp. 121–130, 1983.

- [116] D. Jin and Z. Liu, "Damage of the machined surface and subsurface in orthogonal milling of FGH95 superalloy," *Int. J. Adv. Manuf. Technol.*, pp. 1573–1581, Apr. 2013.
- [117] A. Gente, H. Hoffmeister, and C. Evans, "Chip Formation in Machining Ti6Al4V at Extremely High Cutting Speeds," *CIRP Ann. - Manuf. Technol.*, vol. 50, no. 1, pp. 49–52, 2001.
- [118] W. S. Lee and C. F. Lin, "High-temperature deformation behaviour of Ti6Al4V alloy evaluated by high strain-rate compression tests," *J. Mater. Process. Technol.*, vol. 75, no. 1–3, pp. 127–136, Mar. 1998.
- [119] M. Hokka, D. Gomon, a. Shrot, T. Leemet, M. Bäker, and V.-T. Kuokkala, "Dynamic Behavior and High Speed Machining of Ti-6246 and Alloy 625 Superalloys: Experimental and Modeling Approaches," *Exp. Mech.*, Aug. 2013.
- [120] D. G. Flom, "High-Speed Machining of Metals," *Annu. Rev. Mater. Res.*, vol. 14, no. 1, pp. 231–278, Jan. 1984.
- [121] I. Dagiloke, A. Kaldos, S. Douglas, and B. Mills, "High-speed machining: an approach to process analysis," *J. Mater. Process. Technol.*, vol. 54, no. 1–4, pp. 82–87, 1995.
- [122] T. Childs and K. Maekawa, *Metal machining: theory and applications*. Arnold, 2000, p. 408.
- [123] G. Sutter, "Chip geometries during high-speed machining for orthogonal cutting conditions," *Int. J. Mach. Tools Manuf.*, vol. 45, no. 6, pp. 719–726, May 2005.
- [124] A. Ugarte, R. M'Saoubi, A. Garay, and P. Arrazola, "Machining Behaviour of Ti-6Al-4V and Ti-5553 Alloys in Interrupted Cutting with PVD Coated Cemented carbide," *Procedia CIRP*, vol. 1, pp. 208–213, 2012.
- [125] P. L. B. Oxley and M. C. Shaw, "Mechanics of Machining: An Analytical Approach to Assessing Machinability," *J. Appl. Mech.*, vol. 57, no. 1, p. 253, 1990.
- [126] M. Armendia, P. Osborne, a. Garay, J. Belloso, S. Turner, and P.-J. Arrazola, "Influence of Heat Treatment on the Machinability of Titanium Alloys," *Mater. Manuf. Process.*, vol. 27, no. 4, pp. 457–461, Apr. 2012.
- [127] Y. Kosaka and S. P. Fox, "Influences of alloy chemistry and microstructure on the machinability of titanium alloys," in *Cost Affordable Titanium, TMS Conference*, 2004, pp. 169–176.
- [128] Y. Kosaka, J. C. Fanning, and S. P. Fox, "Development of low cost high strength alpha/beta alloy with superior machinability," in *Proceedings of the 10th World Conference on Titanium*, 2004, pp. 3028–3034.

- [129] K. Liu and S. N. Melkote, "Material Strengthening Mechanisms and Their Contribution to Size Effect in Micro-Cutting," *J. Manuf. Sci. Eng.*, vol. 128, no. 3, p. 730, 2006.
- [130] M. C. Shaw, "The size effect in metal cutting," *Sadhana*, vol. 28, no. 5, pp. 875–896, Oct. 2003.
- [131] W. Backer, E. Marshall, and M. Shaw, "The size effect in metal cutting," *Trans. Asme*, vol. 74, no. 61, 1952.
- [132] J. H. Ko, W.-S. Yun, D.-W. Cho, and K. F. Ehmann, "Development of a virtual machining system, part 1: approximation of the size effect for cutting force prediction," *Int. J. Mach. Tools Manuf.*, vol. 42, no. 15, pp. 1595–1605, Dec. 2002.
- [133] J. Arsecularatne, "On tool-chip interface stress distributions, ploughing force and size effect in machining," *Int. J. Mach. tools Manuf.*, vol. 37, no. 7, pp. 885–899, 1997.
- [134] A. Aramcharoen and P. T. Mativenga, "Size effect and tool geometry in micromilling of tool steel," *Precis. Eng.*, vol. 33, no. 4, pp. 402–407, Oct. 2009.
- [135] A. Mian, "Size effect in micromachining," PhD Thesis, The Univeristy of Manchester, 2011.
- [136] A. J. Mian, N. Driver, and P. T. Mativenga, "Identification of factors that dominate size effect in micro-machining," *Int. J. Mach. Tools Manuf.*, vol. 51, no. 5, pp. 383–394, May 2011.
- [137] C. K. Ng, S. N. Melkote, M. Rahman, and a. Senthil Kumar, "Experimental study of micro- and nano-scale cutting of aluminum 7075-T6," *Int. J. Mach. Tools Manuf.*, vol. 46, no. 9, pp. 929–936, Jul. 2006.
- [138] M. Armendia, A. Garay, L.-M. Iriarte, and P. J. Arrazola, "Comparison of the machinabilities of Ti6Al4V and TIMETAL® 54M using uncoated WC–Co tools," *J. Mater. Process. Technol.*, vol. 210, no. 2, pp. 197–203, Jan. 2010.
- [139] D. Waldorf, "An evaluation of ploughing models for orthogonal machining," *J. ...*, vol. 121, no. November, 1999.
- [140] S. Ranganath, A. B. Campbell, and D. W. Gorkiewicz, "A model to calibrate and predict forces in machining with honed cutting tools or inserts," *Int. J. Mach. Tools Manuf.*, vol. 47, no. 5, pp. 820–840, Apr. 2007.
- [141] W. Hintze, H. Frömming, and a. Dethlefs, "Influence of machining with defined cutting edge on the subsurface microstructure of WC–Co parts," *Int. J. Refract. Met. Hard Mater.*, vol. 28, no. 2, pp. 274–279, Mar. 2010.

- [142] M. Masuko, "Fundamental research on the metal cutting- first report a new analysis of cutting force," *Trans. Soc. Mech. Eng.*, vol. 19, p. pp 32–39, 1953.
- [143] P. Albrecht, "New Developments in the Theory of the Metal-Cutting Process: Part I. The Ploughing Process in Metal Cutting," *J. Eng. Ind.*, vol. 82, no. 4, p. 557, Nov. 1960.
- [144] M. C. Shaw and N. P. Suh, "Discussion: 'New Developments in the Theory of the Metal-Cutting Process: Part I. The Ploughing Process in Metal Cutting' (Albrecht, P., 1960, ASME J. Eng. Ind., 82, pp. 348–357)," *J. Eng. Ind.*, vol. 82, no. 4, p. 357, Nov. 1960.
- [145] E. Tenckhoff, *Deformation Mechanisms, Texture, and Anisotropy in Zirconium and Zircaloy*. ASTM International, 1988, p. 77.
- [146] A. Goldberg, *Beryllium Manufacturing Processes*. United States. Department of Energy, 2006.
- [147] H. Moreen, "Fractographic evidence of machining damage in beryllium," *Metallography*, vol. 484, no. 1977, pp. 481–484, 1977.
- [148] E. H. Rennhack, "Influence of machining temperature on the surface damage, residual stress, and texture of hot-pressed beryllium," *Metall. Trans.*, vol. 5, no. 5, pp. 1095–1101, May 1974.
- [149] R. E. R. Snider and J. J. F. Kahles, "Machining Data for Beryllium Metal," *Airforce Mach. Data Cent.*, p. 29, 1966.
- [150] M. Field, J. Kahles, and J. Cammett, "A Review of Measuring Methods for Surface Integrity," *Ann. CIRP*, vol. 21, no. 2, pp. 219–230, 1972.
- [151] W. Taylor and J. S. White, "Grinding induced machining damage in beryllium," *J. Mater. Sci.*, vol. 9, no. 4, pp. 569–575, Apr. 1974.
- [152] S. W. Porembka and H. D. Hanes, "Surface damage in machined beryllium," *Battelle Meml. Inst. Columbus Ohio Def. Mater. Inf. Cent.*, p. 16, Jan. 1965.
- [153] R. J. Runck, E. W. Cawthron, G. W. Cunningham, S. W. Porambka, R. J. Lund, and A. Levy, "Report of beryllium committee," 1975.
- [154] J. Hanafee, "Effect of machining on properties of impact-ground beryllium," *Lawrence Livermore Lab.*, no. V, 1977.
- [155] N. Kota and O. B. Ozdoganlar, "Orthogonal machining of single-crystal and coarse-grained aluminum," *J. Manuf. Process.*, vol. 14, no. 2, pp. 126–134, Apr. 2012.
- [156] N. Kota, "Mechanical Micromachining-Effect of Crystallographic Anisotropy on Machining Forces," Carnegie Mellon University, 2011.

- [157] W. Lee, "Effect of crystallographic orientation in diamond turning of copper single crystals," *Scr. Mater.*, vol. 42, no. 10, pp. 937–945, Apr. 2000.
- [158] W. Lee, "A theoretical analysis of the effect of crystallographic orientation on chip formation in micromachining," *Int. J. Mach. Tools*, vol. 33, no. 3, pp. 439–447, 1993.
- [159] E. Demir, "A method to include plastic anisotropy to orthogonal micromachining of fcc single crystals," *Int. J. Adv. Manuf. Technol.*, vol. 43, no. 5–6, pp. 474–481, Sep. 2008.
- [160] Z. Yuan, "Effect of Crystallographic Orientation on Cutting Forces and Surface Quality in Diamond Cutting of Single Crystal," *CIRP Ann. - Manuf. Technol.*, vol. 43, no. 1, pp. 39–42, 1994.
- [161] M. Sato, K. Kato, K. Tuchiya, K. Yosio, and T. Kazuhrio, "Effects of material anisotropy upon the cutting mechanism," *Trans. JIM*, 1978.
- [162] K. Ueda, "Chip Formation Mechanism in Single Crystal Cutting of β -Brass," *CIRP Ann. - Manuf. Technol.*, vol. 29, no. 1, pp. 41–46, 1980.
- [163] A. Bowen, "The influence of crystallographic orientation on tensile behaviour in strongly textured Ti 6Al 4V," *Mater. Sci. Eng.*, vol. 40, no. 1, pp. 31–47, 1979.
- [164] D. Tromans, "Elastic anisotropy of HCP metal crystals and polycrystals," *J. Res. Rev. Appl. Sci.*, vol. 6, no. 4, pp. 462–483, 2011.
- [165] Sandvik-Coromant, *Metalcutting Technical Guide: Turning, Milling, Drilling, Boring, Toolholding; Handbook from Sandvik Coromant*. Sandvik Coromant, 2005, p. 617.
- [166] Sandvik, *Modern Metal Cutting- A Practical Handbook*. Sandvik Coromant, 1994.
- [167] V. Marinov, *Manufacturing Processes for Metal Products*. Kendall Hunt Pub Co, 2010, p. 298.
- [168] Z. M. Wang, M. Rahman, and Y. Wong, "Tool wear characteristics of binderless CBN tools used in high-speed milling of titanium alloys," *Wear*, vol. 258, no. 5–6, pp. 752–758, Feb. 2005.
- [169] W. Heginbotham and S. Gogia, "Metal cutting and the built-up nose," *Proc. Inst.*, no. 18, 1961.
- [170] D. Thakur, B. Ramamoorthy, and L. Vijayaraghavan, "Effect of high speed cutting parameters on the surface characteristics of superalloy Inconel 718," *practice*, vol. 3, 2010.

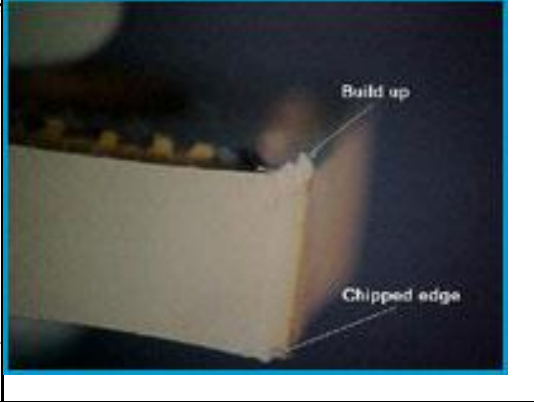
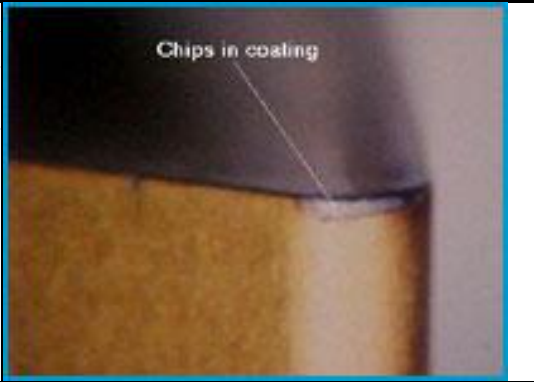
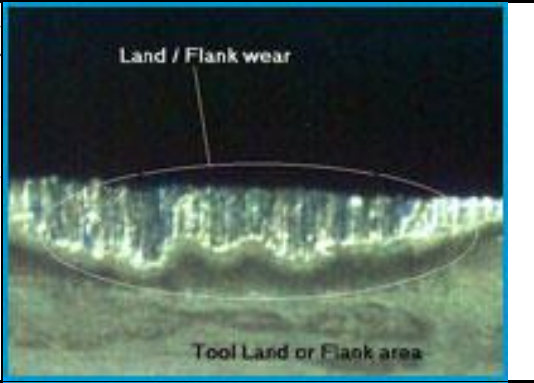
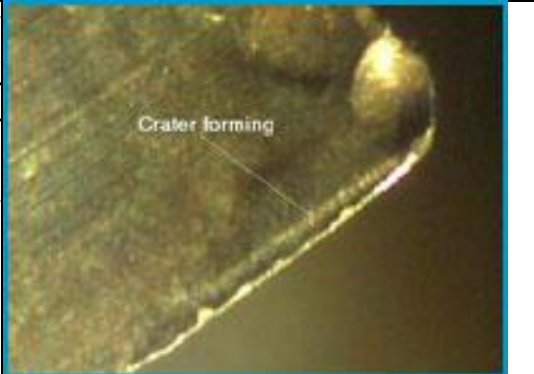
- [171] B. M. Kramer and B. Von Turkovich, "A Comprehensive Tool Wear Model," *CIRP Ann. - Manuf. Technol.*, vol. 35, no. 1, pp. 67–70, 1986.
- [172] P. Hartung, B. Kramer, and B. Von Turkovich, "Tool wear in titanium machining," *CIRP Ann. Technol.*, vol. 31, no. 1, pp. 75–80, 1982.
- [173] N. Muthukrishnan and P. Davim, "Influence of Coolant in Machinability of Titanium Alloy (Ti-6Al-4V)," *J. Surf. Eng. Mater. Adv. Technol.*, vol. 01, no. 01, pp. 9–14, Mar. 2011.
- [174] K. Dass and S. R. Chauhan, "Machinability Study of Titanium (Grade-5) Alloy Using Design of Experiment Technique," *Engineering*, vol. 03, no. 06, pp. 609–621, Jun. 2011.
- [175] F. Nabhani, "Machining of aerospace titanium alloys," *Robot. Comput. Integr. Manuf.*, vol. 17, no. 1–2, pp. 99–106, Feb. 2001.
- [176] J. Taylor, "The tool wear-time relationship in metal cutting," *Int. J. Mach. Tool Des. Res.*, vol. 2, no. 2, pp. 119–152, 1962.
- [177] S. I. Jaffery and P. T. Mativenga, "Assessment of the machinability of Ti-6Al-4V alloy using the wear map approach," *Int. J. Adv. Manuf. Technol.*, vol. 40, no. 7–8, pp. 687–696, Feb. 2008.
- [178] C. Y. H. Lim, S. C. Lim, and K. S. Lee, "Wear of TiC-coated carbide tools in dry turning," *Wear*, vol. 225–229, pp. 354–367, Apr. 1999.
- [179] S. C. Lim, S. H. Lee, Y. B. Liu, and K. H. W. Seah, "Wear maps for uncoated high-speed steel cutting tools," *Wear*, vol. 170, no. 1, pp. 137–144, Nov. 1993.
- [180] G. Kappmeyer, C. Hubig, M. Hardy, M. Witty, and M. Busch, "Modern machining of advanced aerospace alloys-Enabler for quality and performance," *Procedia CIRP*, vol. 1, pp. 28–43, 2012.
- [181] Z. Wang, "High-speed milling of titanium alloys using binderless CBN tools," *Int. J. Mach. Tools Manuf.*, vol. 45, no. 1, pp. 105–114, Jan. 2005.
- [182] G. Schuh, R. Neugebauer, and E. Uhlmann, *Future Trends in Production Engineering: Proceedings of the First Conference of the German Academic Society for Production Engineering (WGP), Berlin, Germany, 8th-9th June 2011*. Springer Science & Business Media, 2012, p. 414.
- [183] C. J. C. Rodríguez, *Cutting Edge Preparation of Precision Cutting Tools by Applying Micro-abrasive Jet Machining and Brushing*. kassel university press GmbH, 2009, p. 189.
- [184] E. A. Rahim, S. Sharif, Z. A. Ahmad, A. S. Mohrni, and I. A. Syed, "Machinability Investigation when Drilling Titanium Alloys," pp. 3–7, 2005.

- [185] P. J. Arrazola, A. Garay, L. M. Iriarte, M. Armendia, and S. Marya, “Machinability of titanium alloys (Ti6Al4V and Ti555.3),” *J. Mater. Process. Tech.*, vol. 209, no. 5, pp. 2223–2230, 2009.
- [186] “Electron Backscattered Diffraction Explained, Oxford Instruments Technical Briefing (PDF),” 2004. [Online]. Available: http://www.metallography.com/experts/EBSD_explained_by_OxfordInstruments.pdf. [Accessed: 12-Dec-2012].
- [187] A. J. Wilkinson and P. B. Hirsch, “Electron diffraction based techniques in scanning electron microscopy of bulk materials,” *Micron*, vol. 28, no. 4, pp. 279–308, Aug. 1997.
- [188] U. F. Kocks, C. N. Tomé, and H.-R. Wenk, *Texture and Anisotropy: Preferred Orientations in Polycrystals and their Effect on Materials Properties*. Cambridge University Press, 2000, p. 692.
- [189] M. Niewczas, “Lattice correspondence during twinning in hexagonal close-packed crystals,” *Acta Mater.*, vol. 58, no. 17, pp. 5848–5857, Oct. 2010.
- [190] O. Engler and V. Randle, *Introduction to Texture Analysis: Macrotecture, Microtexture, and Orientation Mapping, Second Edition*. CRC Press, 2000, p. 488.
- [191] M. Cervenka, “Rolls Royce PLC,” 2004. [Online]. Available: <http://www.msm.cam.ac.uk/phase-trans/mphil/Trent1/sld001.htm>. [Accessed: 10-Jan-2014].
- [192] R. Komanduri and B. Von Turkovich, “New observations on the mechanism when machining titanium alloys of chip formation,” vol. 69, pp. 179 – 188, 1981.
- [193] H. Maier, R. Teteruk, and H. J. Christ, “Modeling thermomechanical fatigue life of high Temperature Titanium Alloy IMI 834,” *Metall. Mater. Trans. A*, vol. 31, no. 2, pp. 431–444, 2000.
- [194] M. Thomas, “On the characterisation of subsurface deformation microstructures in aerostructural titanium alloys,” PhD thesis, The University of Sheffield, 2012.
- [195] C. Ramachandra, A. K. Singh, and G. M. K. Sarma, “Microstructural characterisation of near- α titanium alloy Ti-6Al-4Sn-4Zr-0.70Nb-0.50Mo-0.40Si,” *Metall. Trans. A*, vol. 24, no. 6, pp. 1273–1280, Jun. 1993.
- [196] M. W. Mahoney and N. E. Paton, “The effect of minor alloying element additions on mechanical properties of titanium alloys,” *Rockwell Int. Sci. Cent.*, 1977.
- [197] H. Kestler, H. Mughrabi, and H. Renner, “Influence of heat treatment and microstructure on the low cycle fatigue properties of the hot forged near alpha

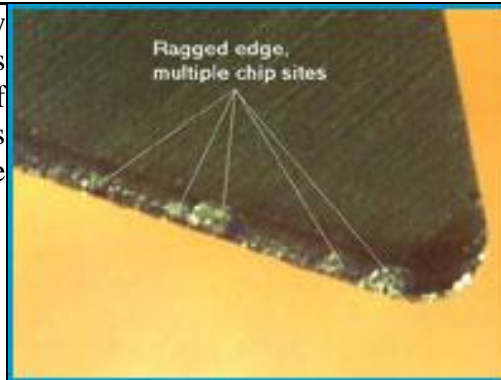
- titanium alloy IMI 834,” in *Titanium '95: Science and Technology*, 1995, pp. 1171–1178.
- [198] J. C. Williams, N. E. Paton, and R. G. Baggerly, “Deformation behavior of HCP Ti-Al alloy single crystals,” *Metall. Mater. Trans. A*, vol. 33, no. 13, pp. 837–850, 2002.
- [199] W. Tirry, F. Coghe, S. Bouvier, M. Gasperini, L. Rabet, and D. Schryvers, “A multi-scale characterization of deformation twins in Ti6Al4V sheet material deformed by simple shear,” *Mater. Sci. Eng. A*, vol. 527, no. 16–17, pp. 4136–4145, Jun. 2010.
- [200] G. Bartarya and S. K. Choudhury, “State of the art in hard turning,” *Int. J. Mach. Tools Manuf.*, vol. 53, no. 1, pp. 1–14, Feb. 2012.
- [201] A. Machado and J. Wallbank, “Machining of titanium and its alloys—a review,” *Proc. Inst. ...*, vol. 204, no. Part B, pp. 53–60, 1990.
- [202] A. Vary, “Ultrasonic Testing, American Society for Nondestructive Testing,” in *Nondestructive Testing Handbook*, vol. 7, 2nd ed., A. S. Biks, R. E. Green, and P. McIntire, Eds. 1991, pp. 382–431.
- [203] K. G. Budinski, “Tribological properties of titanium alloys,” *Wear*, vol. 151, no. 2, pp. 203–217, Dec. 1991.
- [204] *Technical guide: Materials, Specific cutting energy*. Sandvik Coromant.
- [205] G. Sutter and G. List, “Very high speed cutting of Ti–6Al–4V titanium alloy – change in morphology and mechanism of chip formation,” *Int. J. Mach. Tools Manuf.*, vol. 66, pp. 37–43, Mar. 2013.
- [206] W. Li, “Laser ultrasonic method for determination of crystallographic orientation of large grain metals by spatially resolved acoustic spectroscopy (SRAS).” University of Nottingham, 2012.
- [207] “Tool wear examples,” *Asset recovery group*. [Online]. Available: <http://www.asset-recoverygroup.com/tool-wear-examples.html>. [Accessed: 10-Oct-2013].

Appendix

Images obtained via [207]

<p>A built up edge (BUE) is a formation ahead of the tool and can create an integral interface between the workpiece and the tool often serving as a protective barrier to flank and crater wear. The size and shape of the BUE can alter the shape of the leading edge changing the effective rake angle. An unstable BUE can lead to irregular wear on cutting edges that can generate a poor surface finish when fragments of the BUE are dragged under the leading edge of the tool.</p>	 <p>This micrograph shows a cutting tool edge with a prominent, irregularly shaped built-up edge (BUE) at the top. A label 'Build up' points to this feature. Below it, the original tool edge is labeled 'Chipped edge'.</p>
<p>Spalling wear is a gradual wear mechanism occurring early in the life of the tool most commonly observed on the flank edge. Spalling is a precursor to further gradual wear failure mechanisms such as Flank, crater, flaking or fracture wear</p>	 <p>This micrograph shows a cutting tool edge with a coating. A label 'Chips in coating' points to small, irregular fragments of the coating that have broken off from the tool's surface.</p>
<p>Flank (land) / Nose wear is a gradual abrasive wear mechanism and is the most common wear pattern. Characterised by a coarse surface usually on the flank of the tool, visible evidence of burning may also be apparent towards the trailing edges of the worn regions. It is generally of a similar form over these areas of wear, it will increase with temperature gain.</p>	 <p>This micrograph shows a cutting tool edge with a rough, textured surface. A label 'Land / Flank wear' points to this area. Below the image, the text 'Tool Land or Flank area' is visible.</p>
<p>Crater Wear is a gradual diffusional wear mechanism on the tool face occurring in the absence of a BUE. The sustained rubbing of the chip causes crater wear across the face of the tool resulting in a concave depression. Crater wear will ultimately lead to chipping or fracture.</p>	 <p>This micrograph shows a cutting tool edge with a distinct, concave depression. A label 'Crater forming' points to this feature.</p>

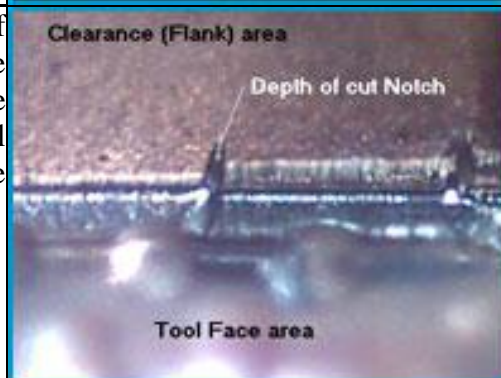
Chipping wear is a precursor to early catastrophic failure when the insert is subjected to high cutting forces. Chipping of the tool leads to multiple irregular sharp edges giving rise to a surface finish of the workpiece that is usually rough and streaked.



Flaking wear can occur abruptly within the early parts of a cutting cycle when the insert is subjected to high cutting forces resulting in large regions of material become detached from either the rake or flank edges of the tool.



Notching Wear is caused by the formation of an individual groove at the same time on the face and flank of the tool whose size corresponds to the depth of cut. Notching will lead to a substandard finish on the workpiece and may lead to fracture of the tool.



Fracture occurs abruptly at the end of a tool's life typically preceded by other wear mechanisms such as Crater, Chipping or Flaking.



This page intentionally left blank